NR-318-073

(6)

LTV REPORT NO. 3-32300/4CR-21
ARPA ORDER NO. 4225
ONR CONTRACT N00014-81-C-0560

AD-A154 260

Thin Film Phase Transition Materials Development Program

17 AUGUST 1981 - 16 AUGUST 1984

LTV AEROSPACE AND DEFENSE COMPANY
VOUGHT MISSILES AND ADVANCED PROGRAMS DIVISION
P. O. BOX 650003
DALLAS, TEXAS 75265-003

DTIC
ELECTE
MAY 29 1985
S D
B

FINAL REPORT
APRIL 1985
PRINCIPAL INVESTIGATOR: W. E. CASE
(214) 266-7628

The views and conclusions contained in this document are those of the authors and should not be interpreted as necessarily representing the official policies, either expressed or implied, of the Defense Advanced Research Projects Agency or the U. S. Government.

DTIC FILE COPY

PREPARED FOR:

DEFENSE ADVANCED RESEARCH PROJECTS AGENCY
1400 WILSON BLVD.
ARLINGTON, VIRGINIA 22209

DISTRIBUTION STATEMENT A
Approved for public release;
Distribution Unlimited

LTV Aerospace and Defense
Vought Missiles and
Advanced Programs Division

85 5 09 036

TABLE OF CONTENTS

		PAGE NO.
1.0	EXECUTIVE SUMMARY	1
1.1	Organization	1
1.2	Background	1
1.3	Objectives and Resources	2
1.4	Technical Highlights	2
1.5	Technical Summary	4

APPENDIX A TECHNICAL RESULTS - VOUGHT MISSILES AND ADVANCED PROGRAMS DIVISION

APPENDIX B TECHNICAL RESULTS - CORNELL UNIVERSITY

APPENDIX C TECHNICAL RESULTS - UNIVERSITY OF ARIZONA

APPENDIX D TECHNICAL RESULTS - THE JOHNS HOPKINS UNIVERSITY

Accession For
NTIS GRA&I ☑
DTIC TAB ☐
Unannounced ☐
Justification
By PER LETTER
Distribution/
Availability Codes
Dist | Avail and/or Special
A-1

1.0 EXECUTIVE SUMMARY

1.1 ORGANIZATION

This document completes the reporting of work performed on the Thin Film Phase Transition Materials Development program (DARPA/ONR Contract N00014-81-C-0560). The following introductory section presents a brief description of the applied research leading to the present contract, and the benefits that further development of thin film phase transition materials under this contract are expected to provide for future military systems and subsystems. Program objectives are presented next as a framework for evaluation of technical results. These results are highlighted in Section 1.4 and discussed fully in Appendices A-D. Section 1.5 summarizes achievements in relation to overall objectives of the program.

1.2 BACKGROUND

For several years this company has conducted applied research on thin films of vanadium dioxide. The material undergoes a thermally induced semiconductor to metal phase transition near 67°C with dramatic changes in both electrical and optical properties. Moreover, injection of energy (about 15 mJ/cm^2) into a small portion of the film causes the transition to occur only in that local region. The resulting local change in properties may be either removed (dynamic operation) or stored indefinitely (memory operation). These options are possible because the material deposited as a thin film exhibits hysteresis, i.e., the curve describing the state of the film vs. temperature is double valued in the transition region.

A number of application concepts have emerged based on the idea that a phase transition thin film such as vanadium dioxide provides a high resolution, two-dimensional format for switching, recording, and processing optical signals. These applications range from high density optical disk recording systems and optical data processing to laser protection devices, infrared FLIRS and seekers,

Cont'd

laser radar systems and IR scene simulators. All application candidates have a potential for providing either a totally new capability, an improved performance, a lower cost, or combinations of the three. Probably of greatest significance is the emergence of "agile" sensor concepts arising out of some of the film's special properties. These are represented by the above FLIRs, seekers and laser radar systems.

1.3 OBJECTIVES AND RESOURCES

A three year research program has been completed to advance the state-of-the-art in the preparation and characterization of selected thin film phase transition materials. The objectives of the program were: (a) to expand the data base and improve operational characteristics of Vought prepared vanadium dioxide thin films, (b) to evolve process chemistry and subsequently characterize several new program materials, including rare-earth chalcogenides, organic semiconductor charge complexes, alloys of transition metal oxides, and metal-insulator cermets, and (c) to spin-off new applications and concepts.

Technical effort was divided between this company and three universities. The participants were Johns Hopkins University/Applied Physics Laboratory, University of Arizona/Optical Sciences Center, and Cornell University/Materials Science Center. In addition, this company performed an applications study to screen all program materials for early exploitation. A summary of activities under the contract is provided in Table 1 at the end of Sec. 1.0; specific task descriptions are found in Appendices A-D.

1.4 TECHNICAL HIGHLIGHTS

Brief statements of technical highlights are given below; details appear in Appendices A-D. Two interim contract reports provide additional information, especially on those activities essentially completed in the first and second years (ATC Report No. R-93000/3CR-6, January, 1983, and LTV Report No. 3-32000/4CR-C, January 1984).

MATERIALS RESEARCH

- A new form of vanadium dioxide has been processed at Cornell University. Unlike "ordinary " VO_2 film, which shows little change in visible optical properties on switching, the new material transforms from blue to red. Accumulated evidence indicates that "blue" VO_2 film is stoichiometric - perhaps electronic grade-material.

- Organometallic charge-transfer complexes compose a rich new materials base for optical switching. These organic solids have been produced in thin film form at Johns Hopkins University (APL) by a new solid-state diffusion process. Enhanced optical properties have been demonstrated. In particular, CU-TCNQ (copper-tetracyanoquinodimethane) and AG-TCNQ transform from blue and violet colors to a pale yellow.

ANALYSIS

- Significant advances have been made in understanding the mixed phase of TFPT materials. In this region, semiconducting and metallic phases coexist. A model proposed for the composite system provides an algorithm for calculating conductivity and effective optical constants of VO_2 films.

- Investigative techniques have been developed for the microcharacterization and composition analysis of TFPT materials. These methods include X-ray diffraction, scanning electron microscopy, Auger electron and X-ray photoelectron microscopy, Raman and far-infrared spectroscopy.

- A new and unique analytical method has been developed to extract thin-film optical parameters from spectrophotometric measurements. Analytical solutions for configurations of more than one film have not been possible until now.

- Good progress has been made on the synthesis of thin-film designs incorporating phase transition materials. Current output is a seventeen layer design with excellent switching performance form 8.0- to 12.0-microns wavelength.

NEW STRUCTURES AND CONTROL METHODS

- Several major avenues of interest with respect to VO_2 transition modification have been explored, including low energy AR-ion bombardment. Definitive correlations have been found between transition temperature and film stress, and between hysteresis loop width and grain size.

- It has been proven that electric field intensity, even at optical frequencies, can provide the switch mechanism in organometallic thin-film systems. Laser induced conductivity is observed; also laser writing and erasure.

- A substantial data base is accumulating on the filamentary nature of electrical switching in VO_2 thin film. Enhancement in laser switching threshold is a primary objective.

In addition, application reports were delivered by Vought personnel in oral presentations to DARPA and ONR representatives on Otober 12, 1982, and on on November 30, 1983.

1.5 Technical Summary

Two significant advances have been made under this program in the preparation and characterization of new phase transition materials. First, a previously unknown form of vanadium dioxide (VO_2) has been fabricated. This development is a consequence of research at Cornell University into reactive evaporation as a technique for the production of VO_2 film. Evidence was gathered to show that the new film is stoichiometric, perhaps electronic grade, material. Since these films in the semiconducting state look blue in both transmission and reflection, the term "blue" VO_2 was adopted. (High quality bulk crystals look blue in reflection, but are opaque). Heating through the transition results in a striking blue-to-red color change as viewed by transmission of room light. In the 600-800 nm spectral range, a nine fold increase in transmittance takes place from the semiconducting to metallic phases as compared to a 50% decrease for ordinary VO_2 film.

A second advance in materials centers on the optical switching characteristics of certain organo-metallic systems, such as copper and silver tetracyanoquinoidimethane (Cu-and Ag-TCNQ). It has been proven that electric field intensity, even at optical frequencies, provides the switch mechanism in this family of films. Further, the reverse transition can be induced on heating. These effects have been observed using laser irradiation for both switching and erasure. The macroscopic properties of CuTCNQ and AgTCNQ films, when irradiated, are dramatically transformed in that the films undergo a change from their respective blue and violet colors to a rather pale yellow, characteristic of neutral TCNQ.

A significant advance has been made also in understanding the mixed-phase of thin-film phase transition materials. For example, a model proposed for the composite system of co-existing semiconducting and metal phases provides an algorithm for calculating the effective conductivity and the effective optical constants of VO_2 films. It is now possible to investigate systematically the effect of individual parameters on the macroscopic properties. In particular, it is concluded from theory that the temperature width of the mixed-phase is controlled primarily by grain size, not film thickness.

The data base on physical properties of vanadium dioxide thin film, both "ordinary" and "blue" types, and a variety of organometallic materials has been expanded under the present contract, with emphasis on electrical and optical measurements. The optical data consists of microwave, infrared, and visible spectra, hysteresis curves, and laser switching thresholds. Electrical conductivity of VO_2 thin film has been measured from 77°K to 370°K. In addition, an effort was initiated to determine for VO_2 film the enhancement in laser switching sensitivity gained with electrical biasing. It is well known that electrical current flow through a VO_2 thin film can induce, due to Joule heating, stable filaments of metallic phase imbedded in unswitched semiconducting phase. It is anticipated that under certain bias conditions a relatively small heat input due to an optical pulse can trigger the filamentary conditions, and external circuitry can be used to provide current for further heating and additional response.

Several major avenues of interest with respect to VO_2 transition modification have been explored, such as alloying with other transition metals, low energy ion bombardment, and substrate and barrier layer effects on the electrical and optical properties of VO_2 films. A data base has been established which demonstrates the strong relationship between transition temperature and the tensile stress induced in VO_2 by film substrate thermal expansion coefficient mismatch; low energy Ar-ion bombardment is proving to be a promising tool for influencing transition properties; and a definitive correlation has been found between grain size in VO_2 film and hysteresis loop width, as predicted by theory.

In support of optical characterization tasks, a new technique was developed under the contract to extract thin-film optical parameters from photometric measurements. Given reflectance and transmittance data at a specified wavelength, polarization, and angle of incidence, the technique is unique in that it is analytical and it yields all solutions for the complex refractive index and thickness of the unknown film compatible with the measurements. The film of interest may lie anywhere within a multilayer structure. Analytical solutions for configurations of more than one film have not been possible until now.

Excellent progress has been made also in the microcharacterization and compositional analysis of thin film phase transition samples. Investigative techniques include x-ray diffraction, scanning electron microscopy, Auger electron and x-ray photoelectron microscopy, Raman and far-infrared spectroscopy. Submillimeter wave spectroscopy of VO_2 films on germanium and sapphire substrates have shown that both the phonon mode frequencies and line strengths depend on sample substrate and thin film production techniques. From the number, position and widths of these modes one can say a greal deal about the crystal symmetry, strain and disorder in the film. Since the VO_2 phonon lines are very sensitive to thin film morphology, this spectral fingerprint may prove to be a simple thin film characterization parameter.

Multilayer design and fabrication of optical thin-film structures incorporating VO_2 were also tasks under the contract. The specific design goal was to produce a thin-film structure switching between one state of high transmittance and a second state of high reflectance over the widest possible LWIR bandwidth. One output of this effort was a nine-layer design exhibiting satisfactory switching performance from 8.7 to 11.4 microns wavelength. In this range, cold-state reflectance never exceeds 0.04, hot- state reflectance averages 0.8, and cold-state transmittance averages 0.82. Fabrication of the structure has been attempted.

TABLE 1. ACTIVITIES SUMMARY
ONR CONTRACT N00014-81-C-0560

ACTIVITY/ORGANIZATION	LTV VMAPS	CORNELL	JOHNS HOPKINS	UNIV. OF ARIZONA
Materials Research				
Vanadium Dioxide	X	X		
Alloys of Transition Metal Oxides			X	
Organometallics			X	
Rare Earth Monochalcogenides				X
Cermets		X		
Analysis				
Optical Characterization	X			X
Electrical Properties		X		
Multilayer Synthesis	X			X
Mixed-Phase Structure		X		
New Stuctures and Control Methods				
Transition Modification	X		X	
Multilayer Fabrication	X			X
Optical Devices	X		X	X
Mixed Phase Effects		X		
Electrical Devices and Effects	X	X	X	
Applications Study	X			

APPENDIX A

FINAL REPORT

LTV AEROSPACE AND DEFENSE COMPANY
VOUGHT MISSILES AND ADVANCED PROGRAMS DIVISION
P. O. BOX 650003
DALLAS, TEXAS 75265-0003

TECHNICAL INVESTIGATORS:

W. E. CASE
D. H. STROME
F. C. CASE
M. K. PURVIS
W. M. TEPFENHART

1.0 TECHNICAL RESULTS - LTV AEROSPACE AND DEFENSE CO., VOUGHT MISSILES AND ADVANCED PROGRAMS DIVISION

1.1 INTRODUCTION

During the first and second years of the program, a number of technical tasks were advanced near to completion and documented in detail.[1,2] These include:

(1) implementation of experimental conditions that lead to the highest possible accuracy in routine spectrophotometric measurements,

(2) establishment of an analysis procedure to obtain thin-film optical parameters from photometric data,

(3) discovery of processing techniques and conditions that influence the phase transition properties of thin-film vanadium dioxide, and

(4) creation of optical switch designs using vanadium dioxide.

Progress in the above technical areas are reviewed in Sections 1.1-1.5 and updated appropriately for work performed during the period October 1983 to August 1984.

In addition, two other tasks were initiated: multilayer fabrication and the characterization of thermal filament formation in vanadium dioxide. Documentation of technical status composes Sections 1.6 and 1.7, respectively.

1.2 OPTICAL MEASUREMENTS

During the first half of this contract a substantial effort was undertaken to achieve a capability for accurate optical measurements (reflectance and transmittance) in support of the determination of thin-film optical constants and the characterization of thin-film multilayer structures.[1,2]

A part of the effort was the integration of a newly acquired UV-VIS-NIR instrument and computer data handling system with existing MWIR measurement

apparatus. Improved, temperature stabilized sample holders were fabricated for use in both spectrophotometers, and calibrated reflectance standards were obtained for both instruments. The development of a protocol for data manipulation and file naming to permit the routine correction of data against the calibrated standards was an important aspect of the work.

Once the measurement apparatus was fully operational and routine use had been established, data was acquired to assess the accuracy and precision of the measurements.

It was found for the case of the MWIR instrument that systematically low reflectance readings did not originate in actual loss of light due to various possible defects in the optical train. Attention was turned to the data acquisition and processing, and it was found that the major source of error was ordinate non-linearity that was very sensitive to the drift of a particular instrument adjustment. A circuit was designed, fabricated and installed to monitor the status of the parameter in question, permitting the operator to keep the instrument optimally adjusted for all measurements. At that time residual measurement error was estimated to be +/- 0.15%.

Subsequent use of the MWIR instrument has shown that significant degradations of accuracy can arise from relatively subtle inadequacies in instrument maintenance, from lack of experience on the part of new system operators, and from the appearance of new error mechanisms over the course of time as the system ages. [illegible] quired to deal with these factors has slowed the implementation of plans to add a variable-angle-of-incidence measurement capability. However this and other further improvements in optical measurements will continue under IR&D funding.

A similar program of accuracy assessment was also begun for the UV-VIS-IR instrument. It was found that substantially greater drift effects required an operating protocol in which reference scans were recorded as often as sample scans, but eventually an accuracy level of +/- 0.5% was achieved. The evolution of optimum operation of this instrument is still in progress; a variable-angle-of-incidence capability and other improvements will continue under IR&D funding.

1.3 Optical Constants Analysis

1.3.1 General Remarks

A homogeneous, planar thin film is generally characterized by its complex refractive index (n and k) and physical thickness (d). The importance of acquiring accurate information on these parameters over a wide wavelength region is well recognized. However, information on bulk materials and newly proposed thin-film materials may not be available. If found, there is no guarantee of satisfaction from "representative" indices: thin-film structures usually differ from the bulk and, moreover, frequently depend on the particular circumstances of the deposition process. These complications inevitably lead each researcher to derive optical constants from measurements in his own laboratory.

The most convenient and widely accepted methods for the determination of optical constants are based on photometric measurements using conventional laboratory instrumentation. For these cases, the problem becomes one of inversion. Instead of calculating reflectance and transmittance at a fixed wavelength, incident angle, and polarization from the given optical parameters of the thin-film, it is necessary to derive the optical parameters from the measured data.

The underlying approach taken by all previous optical constants-from-photometry techniques is based on numerical iteration. Briefly stated, the computer program that calculates optical performance from optical parameters is presented with a search domain of n-k-d space. Suitable starting values are provided along with a method of generating other n-k-d points in the search domain. In successive trials, optical performance is calculated for various combinations of thin-film parameters and a comparison made between predicted and actual data. These procedures will usually converge to a set of optical numbers that represent "a solution," although not necessarily the physically correct one. Other search domains may be tried and the procedure iterated over again, but the number of possible combinations discourages a complete evaluation. In fact, one search space limitation commonly employed is simply not to search along the d-direction at all.

In contrast to the numerical iteration schemes, we have developed an algebraic method to derive optical constants and thickness of a thin film directly from photometric measurements. Because the algebraic expressions needed to predict reflectance and transmittance can be extremely complicated even for the simplest thin-film configuration, the inverse process of mapping optical data into film parameters has not been considered possible. However, given that a method exists, powerful advantages become apparent. There is no requirement for an initial guess solution, and the possibility of not finding any solution vanishes. Most importantly, access is gained to the entire locus of n-k-d points compatible with the measurement data without "a priori" bias.

A first version of the algebraic method was published recently[3]. This report completes documentation of further work under contract. Previous restrictions on the measurement configuration have been removed: the film under investigation may reside at any location in a multilayer, and non-normal incidence of light is now a measurement option.

1.3.2 Theory

1.3.2.1 Approach

The generic measurement configuration is shown in Figure 1. A thin film with unknown optical parameters, hereafter film-X, is part of a multilayer stack connecting two semi-infinite media. Any number of layers may be included in the stack, and more than one layer absorbing.

Measurement data are reflectance R and transmittance T at specified wavelength, angle of incidence, and polarization. The problem is to derive the complex index of refraction $\hat{n} = n + ik$ and thickness d of film-X consistent with R and T.

For the purposes of analysis, the configuration of Figure 1 will be subdivided and separated into the several distinct modules depicted in Figure 2. The input medium and a following sequence of thin-film layers comprises module 1. With the optical constants of the materials and the thicknesses of the layers in module 1 given, (complex) amplitude reflection and transmission coefficients may

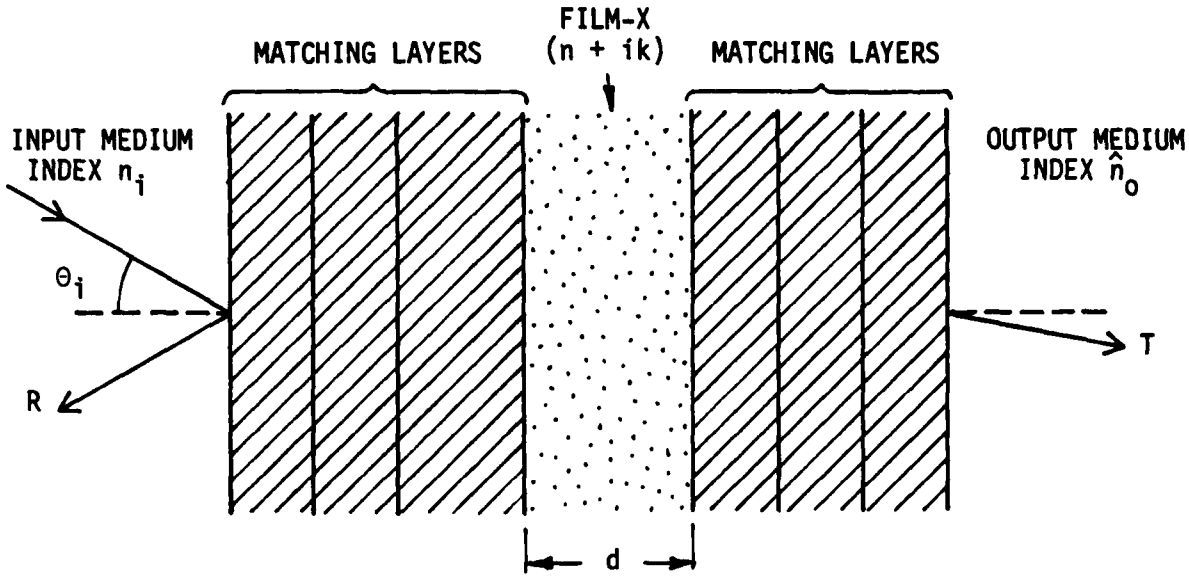

Figure 1. The Generic Measurement Configuration. Light is incident at angle Θ_i in a medium with real refractive index n_i. Measurement data are power reflectance R and power transmittance T at a specified wavelength and polarization state.

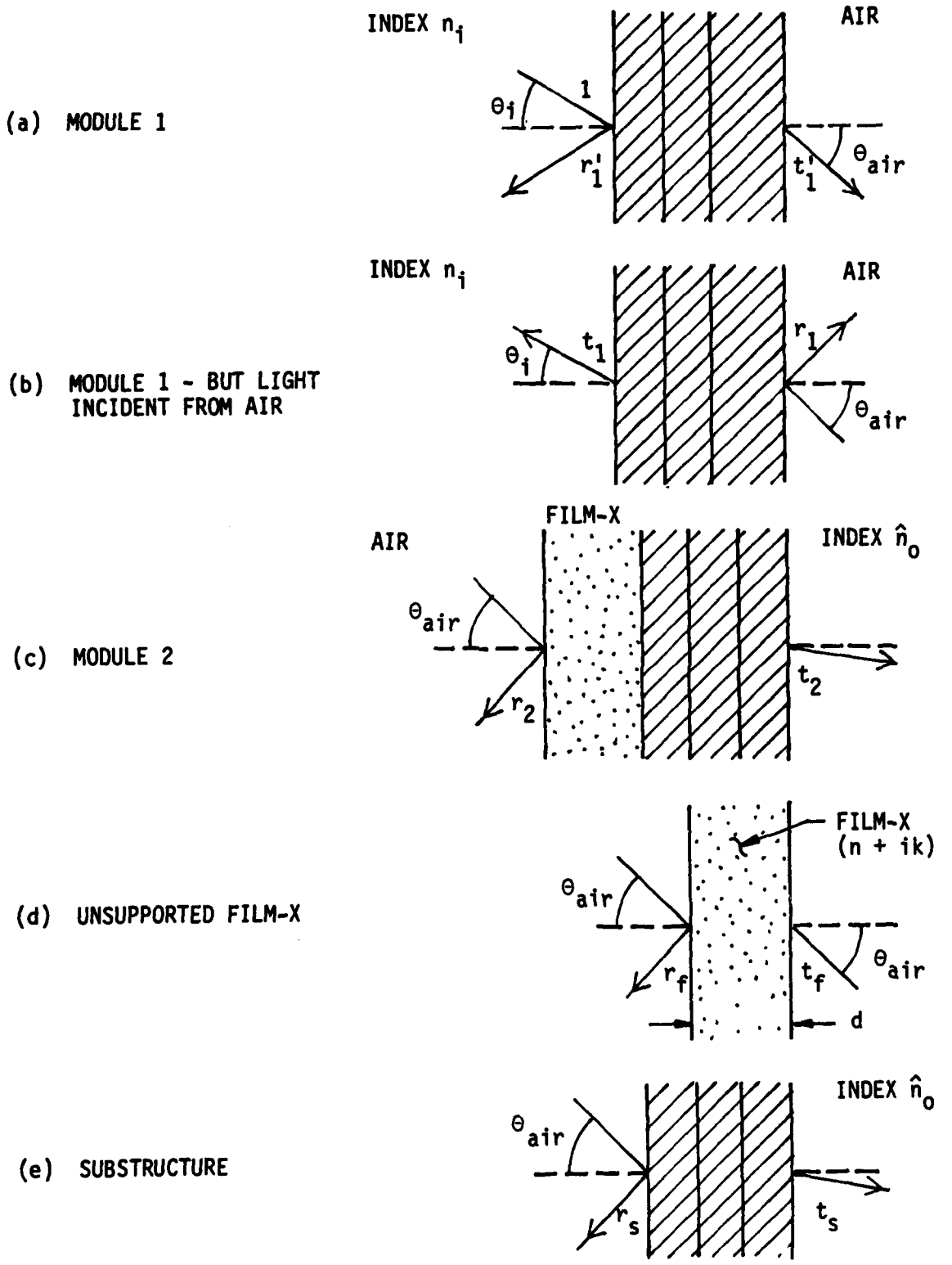

Figure 2. Separation of the Generic Configuration into Modules and Specification of Amplitude Reflection and Transmission Coefficients for Each Part.

be calculated by standard techniques. In general, the reflection coefficient is the ratio of wave amplitudes for reflected and incident electric field components tangential to the input boundary surface; the transmittance coefficient is the ratio of transmitted amplitude tangential to the output boundary surface and the incident amplitude. These parameters are denoted r_1 and t_1, respectively, for light incident from air onto module 1; r_1' and t_1' if light is incident from the massive input medium. Similar parameters r_2 and t_2 are introduced for the thin-film structure, module 2 of Figure 2(c), having film-X as the outermost layer.

In most experimental arrangements, either the input or output media will be air or vacuum. If the input medium is not air, then a difficulty will become apparent in later formulas whenever the incident angle exceeds the critical angle θ_i' defined by $n_i \sin \theta_i' = 1$. In order to avoid complications in the presentation needed for complete generalization, a restriction is placed now on the incident angle, namely $n_i \sin \theta_i < 1$. In addition, photometric measurements in the laboratory include a contribution from the second surface of the massive substrate (either the input or output media). It is assumed here that the back surface contribution has been removed from the data by standard computational procedures.

In a first analysis step, R and T measurement data on the complete multilayer structure are transformed into information about module 2, specifically r_2 and power transmittance T_2 proportional to $|t_2|^2$. The transformation of two given numbers, R and T, into three unknowns, i.e., T_2 and the real and imaginary parts of r_2, implies the introduction of a free variable. Here the variable is an angle φ in the complex reflectivity plane.

In a second analysis step, module 2 is separated into film-X and a substructure of thin-films and the output medium. The optical parameters r_s and t_s defined for the substructure are known (calculated) according to standard multi layer techniques. Thus, formulas for r_2 and T_2 of module 2 transform into

amplitude reflectivity and power transmittance formulas for the unsupported film-X.

The last analysis step is one of inversion. A solution set is found for the index of refraction n, extinction coefficient k, and thickness d of film-X consistent with r_2 and T_2. This set is parametric in the free variable ϕ, i.e., $n = n(\phi)$, $k = k(\phi)$, and $d = d(\phi)$.

1.3.2.2. The Module Feature

The configuration shown in Figure 3 serves as the framework for optically combining two modules. All wave amplitudes indicated on the drawing refer to electric field components tangential to the boundary surfaces. The wave incident at angle θ_i onto the surface S1 between the input medium and the first layer material has unity amplitude. In the absence of the second module, part of this light would be reflected at S1 with complex amplitude r_1' and part transmitted with amplitude t_1' at the exit boundary surface S2.

Now module 2 is added to the existing structure. This addition has the effect of creating a wave of amplitude b incident on module 1 from the back direction. Part of this wave is reflected with amplitude $r_1 b$ at S2 and part transmitted with amplitude $t_1 b$ at S1. Since the separation distance between S2 and S3 is vanishing small, no extra phase factors due to light propagation are needed. Thus the total reflected wave amplitude r at S1 is written as the summation:

$$r = r_1' + t_1 b \quad . \tag{1}$$

The amplitude b is obtained by satisfying a self-consistency condition. That is, given that the reflection coefficient for module 2 is r_2 at surface S3, then

$$b = (t_1' r_2 + r_1 b)\, r_2 \quad , \tag{2}$$

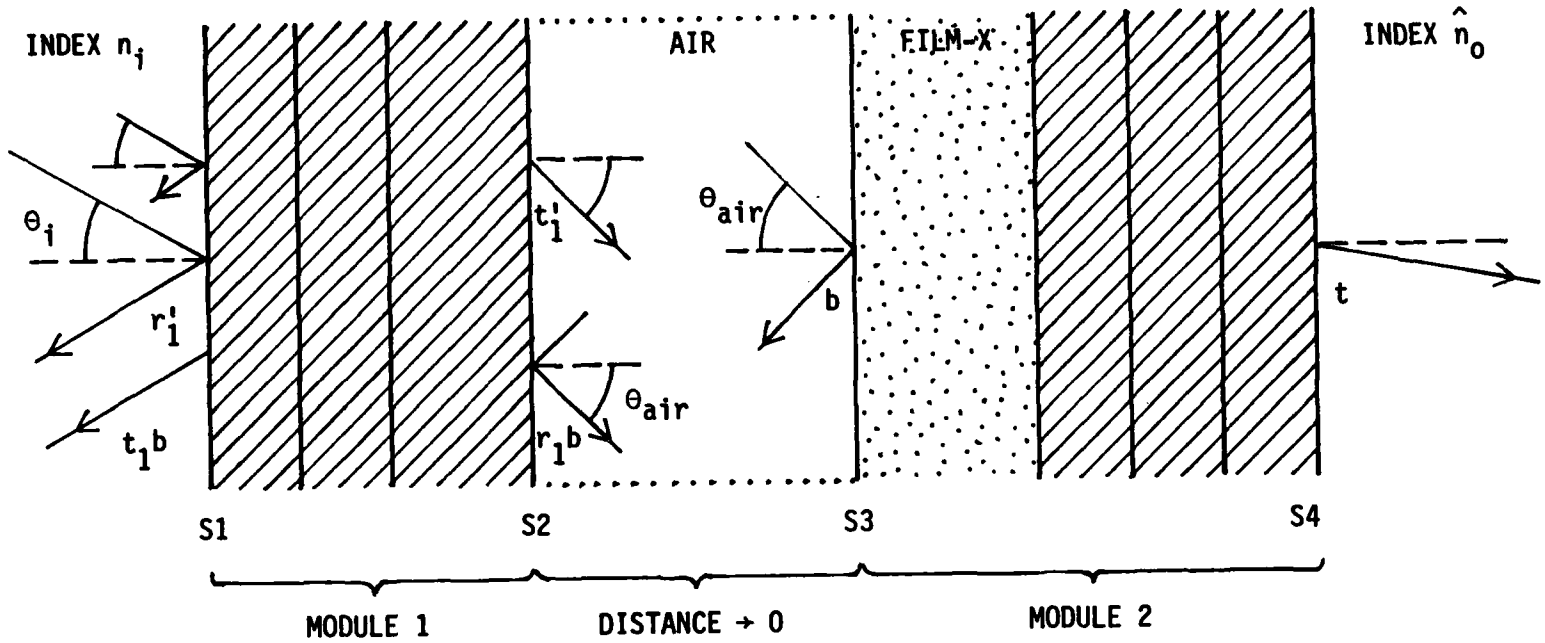

Figure 3. A Configuration Showing the Optical Combination of Two Film Modules into a Complete Multilayer.

or

$$b = t_1' \, r_2/(1-r_1 r_2) \quad . \tag{3}$$

The total amplitude t of the transmitted wave at surface S4 is written as a summation also:

$$t = (t_1' + r_1 b) \, t_2 \quad . \tag{4}$$

Again, t_2 is the transmission coefficient for module 2. Substitution of Eq. (3) into Eq. (1) for r and Eq. (4) for t yields

$$r = \frac{r_1' - (r_1' r_1 - t_1' t_1) \, r_2}{1 - r_1 r_2} \quad , \tag{5}$$

$$t = \frac{t_1' t_2}{1 - r_1 r_2} \quad . \tag{6}$$

The connection to measurement data is made by equating $R = |r|^2$ and exploiting the proportionality of T to $|t|^2$:

$$R = \left| \frac{r_1' - (r' r_1 - t_1' t_1) r_2}{1 - r_1 r_2} \right|^2 \quad , \tag{7}$$

$$T = \frac{T_1 T_2}{|1 - r_1 r_2|^2} \quad . \tag{8}$$

In the latter derivation, constant factors involving the refractive indices of the input and output media and the angle of incidence cancel from the left and right sides of Eq. (8).

1.3.2.3 Reduction

All quantities in Eq. (7) are known except r_2. Following Ref. 3, it is straightforward to show that the complex function r_2 consistent with Eq. (7) is

($\wedge$ denotes a complex quantity explicitly and * denotes complex conjugate)

$$r_2 = \hat{C} + L \exp(i\varphi) \tag{9}$$

where

$$\hat{C} = (r_1' \hat{\mu}_1^* - Rr_1^*)/(|\mu_1|^2 - RR_1) \quad , \tag{10}$$

$$L = T_1 R^{1/2}/(|\hat{\mu}_1|^2 - RR_1) \quad , \tag{11}$$

$$\hat{\mu} = r_1' r_1 - t_1' t_1 \quad , \tag{12}$$

$$R_1 = |r_1|^2 \quad , \quad T_1 = |t_1' t|^2 \quad . \tag{13}$$

Equation (9) is the formula for a circle in the complex reflectance plane. An example circle is depicted in Fig. 4. The center coordinate $\hat{C}$ and radius L are expressed in terms of known (calculated) quantities. Amplitude reference r_2 is a vector connecting the origin of the coordinate system and a point on the circle fixed by the angle φ.

The power transmittance T_2 of modulus 2 is obtained directly from Eq. (8) after specification of r_2:

$$T_2 = TT_1^{-1}|1 - r_1 r_2|^2 \quad . \tag{14}$$

In the case that all films in module 1 are nonabsorbing, it can be shown that

$$\hat{u}_1 = r_1'/r_1^*, \quad |\mu_1|^2 = 1 \quad , \tag{15}$$

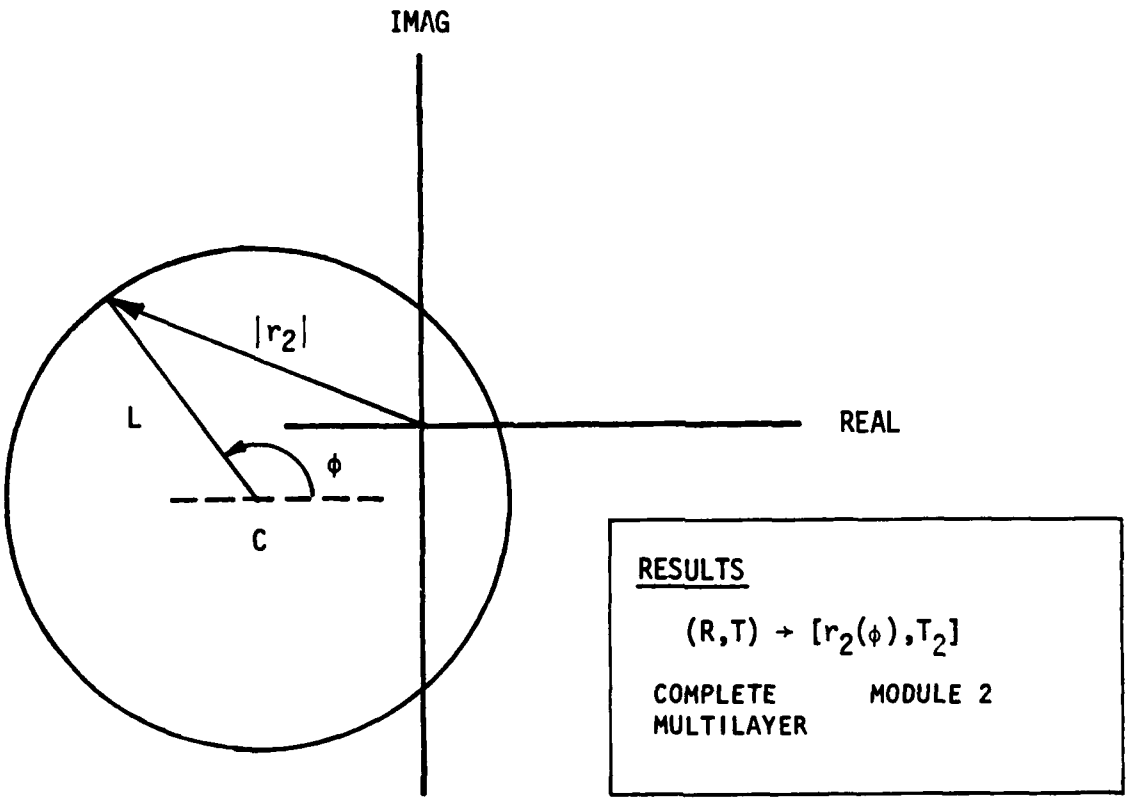

Figure 4. Example Circle Diagram in the (Complex) Amplitude Reflectivity Plane. All Vectors r_2 from the Origin to Points on the Circle are Consistent with the Reflectance Data Point R.

making the following simplifications possible:

$$\hat{C} = (1 - R)\, r_1^*/(1 - RR_1) \quad , \tag{16}$$

$$L = (1 - R_1)R^{1/2}/(1 - RR_1) \quad , \tag{17}$$

$$T_2 = T\,(1 - |r_2|^2)/(1 - R) \quad . \tag{18}$$

Thus, R and T measurement data on the complete multilayer structure have been transformed into r_2 and T_2 information about module 2. The free variable in the reduction is the angle φ.

The second step is separation of module 2 into film-X and the substructure. These elements combine optically according to

$$r_2 = \frac{r_f - (r_f^2 - t_f^2)\, r_s}{1 - r_f r_s} \quad , \tag{19}$$

$$t_2 = \frac{t_f t_s}{1 - r_f r_s} \quad . \tag{20}$$

Here Eqs. (5) and (6) have been rewritten using film-X and the substructure as modules 1 and 2, respectively.

Further reduction depends now on replacement of r_f and t_f with intrinsic optical parameters of film-X. This is discussed next.

1.3.2.4 Inversion

The optical properties of a homogeneous, unsupported thin film in air are described most compactly in terms of the Fresnel coefficient,

$$f = (\hat{n} - 1)/(\hat{n} + 1) \quad , \tag{21}$$

and the phase factor

$$\varepsilon = \exp\,(2\pi\,\hat{\beta}d/\lambda) \quad . \tag{22}$$

One observes that the optical thickness $\hat{\beta}d \neq \hat{n}d$ and $\hat{n} \neq (n + ik)$ except for normal incidence. If light is incident from air at angle θ_{air} onto film-X under different conditions of polarization, then

$$\hat{n} = \hat{\beta}/(1 - \gamma^2)^{1/2} \quad , \text{ s-polarization} \tag{23}$$

$$\hat{n} = (n + ik)^2(1 - \gamma^2)^{1/2}/\hat{\beta} \quad , \text{ p-polarization} \tag{24}$$

where

$$\gamma = \sin\,\theta_{air} = n_i\,\sin\,\theta_i, \tag{25}$$

$$\hat{\beta} = u + iv, \tag{26}$$

$$2u^2 = [(n^2 - k^2 - \gamma^2)^2 + 4n^2k^2]^{1/2} + (n^2 - k^2 - \gamma^2) \quad . \tag{27}$$

$$2v^2 = [(n^2 - k^2 - \gamma^2)^2 + 4n^2k^2]^{1/2} - (n^2 - k^2 - \gamma^2) \quad . \tag{28}$$

In Eq. (25) the second equality relates θ_{air} to θ_i established in the input medium, index n_i. Equations (27) and (28) are solutions of the more general condition on wave propagation

$$\beta^2 + \gamma^2 = (n + ik)^2 \quad . \tag{29}$$

Note that the condition $\gamma \geq 1$ introduced into Eqs. (23) and (24) requires special consideration. This complication is avoided here by imposing the constraint $\gamma < 1$.

Written in terms of f and ε, the amplitude reflectivity r_f and transmittance t_f of the unsupported film-X in air are

$$r_f = -f(1 - \varepsilon^2)/(1 - \varepsilon^2 f^2) \quad , \tag{30}$$

$$t_f = \varepsilon\ (1 - f^2)/(1 - \varepsilon^2 f^2) \quad . \tag{31}$$

It is worthwhile to consider separately the special case of nonabsorbing ($k = o$) film-X. Although the lossless conditions is part of a more general $k \neq o$ treatment to follow, a different solution path here will provide formulas with certain computational advantages.

Start with inversion of Eqs. (30) and (31), viz.,

$$\hat{n}^2 = \frac{(1 - r_f)^2 - t_f^2}{(1 + r_f)^2 - t_f^2} \quad , \tag{32}$$

$$\varepsilon^2 = (1 + f^{-1} r_f)/(1 + f\ r_f) \quad . \tag{33}$$

Then, if $k = 0$, a relation of the type Eq. (15) holds, i.e., $r_f^2 - t_f^2 = r_f/r_f^*$, and $\hat{n}$ is a real number, say n_{eff}. These considerations lead immediately to a solution for r_f from Eq. (19) and n_{eff} from Eq. (32):

$$r_f = \frac{|r_2|^2 - |r_s|^2}{r_2^*(1 - |r_s|^2) - r_2(1 - |r_2|^2)} \quad , \tag{34}$$

$$n_{eff} = \frac{r_f + r_f^* - 2|r_f|^2}{r_f + r_f^* + 2|r_f|^2} \quad . \tag{35}$$

The solution for n_{eff} provides both β and the refractive index n:

$$\beta = (1 - \gamma^2)^{1/2} n_{eff}, \quad \text{s-pol.} \quad , \tag{36}$$

$$2\beta = (1 - \gamma^2)^{-1/2} n_{eff} + [(1 - \gamma^2)^{-1} n_{eff}^2 - 4\gamma^2]^{1/2}, \quad \text{p-pol.}, \tag{37}$$

$$n = (\beta^2 + \gamma^2)^{1/2} \quad . \tag{38}$$

Film thickness d is obtained from Eq. (33) and definition (22): $\varepsilon^2 = \cos(4\pi\beta d/\lambda) + i \sin(4\pi\beta d/\lambda)$.

Thus, for a nonabsorbing film-X, complete analytical inversion is possible. Remembering that $r_2 = r_2(\phi)$ and, therefore, $r_f = r_f(\phi)$, it is seen that a range of optical parameters are found using the free variable ϕ. Thus, $n = n(\phi)$, $d = d(\phi)$, or $n = n(d)$.

The problem with an absorbing film-X is the lack of a simple relation between r_f and t_f. Therefore, the inversion procedure for $k \neq 0$ begins with substitution of Eqs. (30) and (31) into Eqs. (19) and (20):

$$r_2 = \frac{-f(1 + fr_s) + \varepsilon^2 (f + r_s)}{(1 + fr_s) - f\,\varepsilon^2 (f + r_s)} \quad , \tag{39}$$

$$T_2 = \left| \frac{\varepsilon\,(1 - f^2)}{(1 + fr_s) - \varepsilon^2 f(f_f + r_s)} \right|^2 T_s \quad . \tag{40}$$

In the derivation of Eq. (40), recognition is given to the fact that T_2 is known for each $r_2(\phi)$, not t_2 itself. Again, a proportionality factor, based on the refractive index of the output medium, connects amplitude and power transmittance. The factor is the same for both the substructure and module 2, thereby cancelling from the left and right sides of Eq. (40).

Since ε depends on film thickness in an exponential form, this parameter is expressed first in terms of the Fresnel coefficient f by inversion of Eq. (39):

$$\varepsilon^2 = (f + r_2)(1 + fr_s)/(f + r_s)(1 + fr_2) \quad . \tag{41}$$

Then, after eliminating ε from Eq. (40) and substituting $\hat{n}$ for f viz. Eq. (21), one arrives after some algebraic manipulation at

$$\left|\hat{n}^2(1 + r_s)^2 - (1 - r_s)^2\right|^2 T_2^{\,2} = \left|\hat{n}^2(1 + r_2)^2 - (1 - r_2)^2\right|^2 T_s^{\,2} \quad . \tag{42}$$

Following again Ref. 3, Eq. (42) is equivalent to a circle formula for the complex variable $\hat{n}^2$ written as

$$1/2\ \hat{n}^2 = \hat{A} + B \exp(i\psi). \tag{43}$$

Here

$$\hat{A} = \frac{2\,[r_s(1 + r_s^*)^2 T_2^2 - r_2(1 + r_2^*)^2 T_s^2]}{(|1 + r_2|^4 T_s^2 - |1 + r_s|^4 T_2^2)} + 1/2 \quad , \tag{44}$$

$$B = \frac{2T_s T_2 |(r_2 - r_s)(1 - r_2 r_s)|}{\left| |1 + r_2|^4\ T_s^2 - |1 + r_s|^4 T_2^2 \right|} \quad . \tag{45}$$

Each value of the single-angle variable ψ generates a new solution for $\hat{n}$. In turn, each $\hat{n}$ provides separate values of $\hat{\beta}$ and the product $\hat{\beta}d$. The complex number $\hat{\beta}d$ is obtained by means of Eq. (41) and definition (22): $\varepsilon^2 = \exp(i4\pi\hat{\beta}d/\lambda)$. Derivation of $\hat{\beta}$ depends on the polarization condition. Simple inversion of Eq. (23) results in

$$\hat{\beta} = (1 - \gamma^2)^{1/2}\hat{n} \quad , \text{ s-polarization.} \tag{46}$$

For p-polarization, Eqs. (29) and (24) are combined as

$$\hat{\beta}^2 - (1 - \gamma)^{-1/2}\ \hat{n}\ \hat{\beta} + \gamma^2 = 0, \text{ p-polarization} \quad , \tag{47}$$

with (complex) solution

$$2\hat{\beta} = (1 - \gamma^2)^{-1/2}\ \hat{n} + [(1 - \gamma^2)^{-1}\hat{n}^2 - 4\gamma^2]^{1/2} \quad . \tag{48}$$

Two sign possibilities occur with the square root in Eq. (48). The positive root is chosen in order that the solutions for p- and s- polarization converge at normal incidence of light.

The next step is finding the angle ψ in Eq. (43) such that $\hat{\beta}d$ from ε and $\hat{\beta}$ from f are consistent with a real, positive film thickness d. These conditions are written

$$IP(\hat{\beta}d/\hat{\beta}) = 0, \quad d \geq 0, \tag{49}$$

where IP denotes "imaginary part of." A number of numerical interpolation procedures can be used to satisfy conditions (49). The important point is that this solution appears from a bounded set of calculated possibilities, all defined by Eq. (43).

Once $\hat{\beta}$ has been fixed, the complex refractive index is found easily from Eq. (29):

$$n + ik = (\hat{\beta}^2 + \gamma^2)^{1/2} \quad . \tag{50}$$

1.3.2.5 Multiple Solutions

Each value of the free variable ϕ in Eq. (9) generates a different (n,k,d) solution. As ϕ varies between 0 and 2π, a surface is traced in n-k-d space, each point of which is consistent with input reflectance and transmittance data. In general, a number of distinct, non-intersecting surfaces exist under the same measurement conditions of wavelength, polarization, and incidence angle. This multiplicity occurs because the extraction of the complex parameter $\hat{\beta}d$ from the phase factor ε, Eq. (22), is not unique. Accordingly, the real part of $\hat{\beta}d$ must be assigned to separate optical thickness ranges:

$$\frac{(m-1)\lambda}{2} < ud < \frac{m\lambda}{2}, \quad m = 1, 2 \ldots\ldots$$

Finding multiple solutions for n and k at the same film thickness is a direct consequence of inverting nonlinear optical equations. Resolving the ambiquity at a single wavelength requires additional measurements at different angles of incidence and polarization. Other possibilities are to vary sample thickness, or to add other coatings with known optical parameters.

1.4 TRANSITION MODIFICATIONS

Several major avenues of interest with respect to VO_2 transition modifications have been explored, such as substrate and barrier layer effects on the electrical and optical properties of VO_2 films[1] and correlation of grainsize with hysteresis loop width.[1,2] A data base was established which demonstrates the strong relationship between transition temperature and the tensile stress induced in VO_2 by film-substrate thermal expansion coefficient mismatch. A successful attempt at transition modification was made using low energy Ar+ bombardment.[4] Insight was gained as to the nature of factors effecting hysteresis loop width and transition temperature. VO_2 films were prepared by the thermal oxidation of vanadium on three orientation of sapphire substrates, on crystalline and fused quartz, and on ZnSe.

The effects of barrier layers on these films was also investigated; for example, addition of a thin sapphire barrier layer between the substrate and the VO_2 produces very small grains, generally less than .1 micron in diameter, while quartz barrier layers tend to increase grain size. Temperature-cycled optical hysteresis loop data was taken at 3.4 microns with a Perkins-Elmer Model 580 Infrared Spectrophotometer. Resistivity data was taken with an Alessi four-point probe.

It was observed that the width of the transmittance hysteresis loop is dependent on grain size. In the case of sapphire and ZnSe, loop width increased with decreasing grain size. Figure 5 illustrates this behavior. The opposite effect was observed for VO_2 on fused quartz substrates.

Although optical properties were not atypical on fused quartz, the films were poor metals electrically in the hot state and cold/hot resistivity ratios were much lower than those on x-cut crystalline quartz by three orders of magnitude. It was noted that smaller grain size on fused quartz corresponds to larger

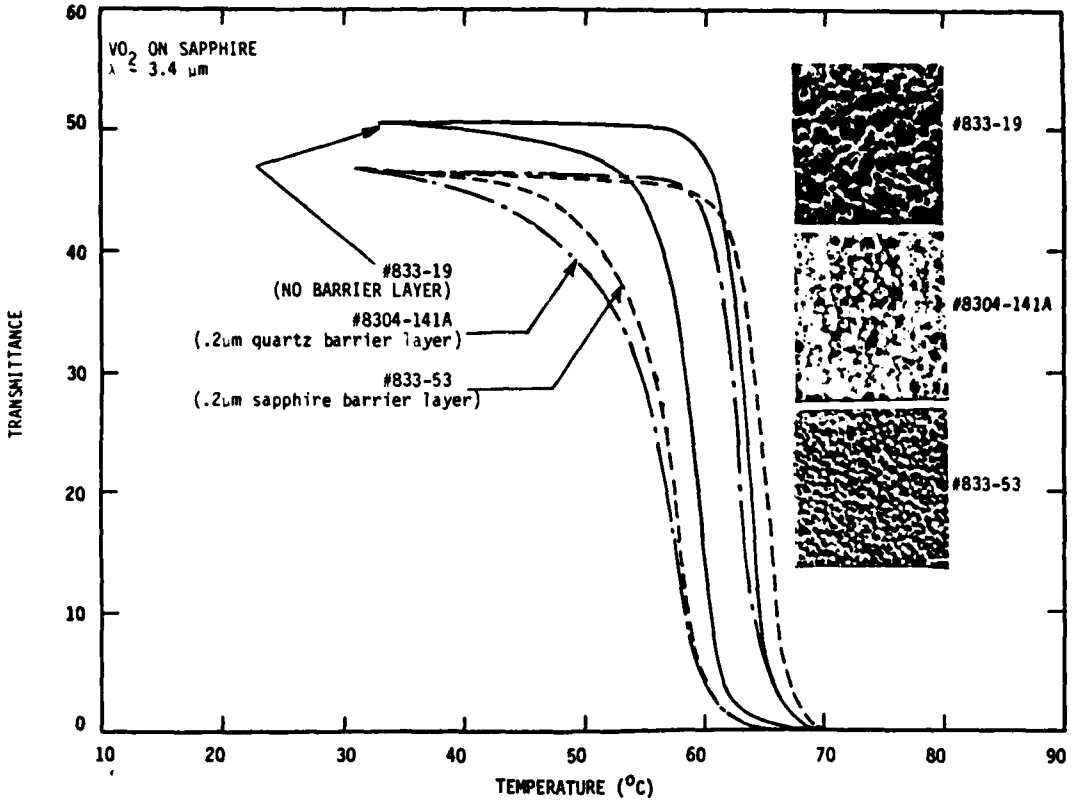

(a)

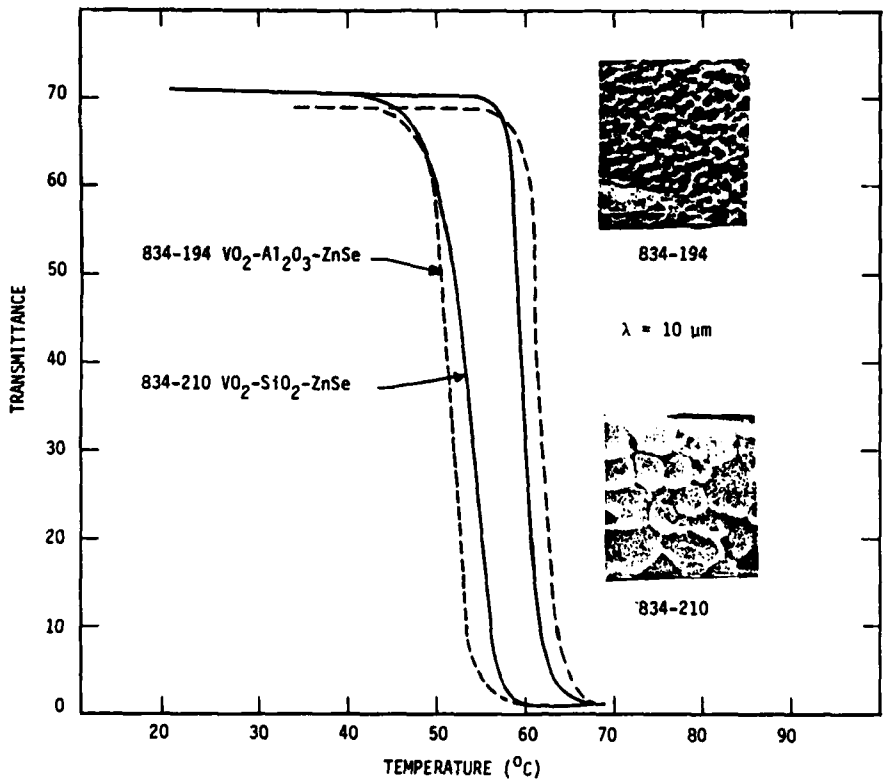

(b)

Figure 5: Transition Modification vs. Grain Size

(a) VO_2 on Sapphire

(b) VO_2 on ZnSe

resistivity ratio. Increasing the thickness of the VO_2 on fused quartz also improved the resistivity ration without the addition of a sapphire barrier layer. The formation of VO_2 on fused quartz under typical process conditions appears to be islandic and conelike in nature. This minimal contact between grains is likely responsible for the high hot-state resistivity. As the film is made thicker or grain size smaller, inter-grain contact increases and so does the resistivity ratio.

VO_2 films on x- and z-cut quartz invariably appeared irregular to the eye. Under SEM examination this translated to regions of widely different grains size and growth patterns, brought about presumably by the non-isotropic thermal conductivity of the substrates. The optical data corresponding to these films is always anomalous, in that the hysteresis loop is not of uniform width. On the assumption that the measured loop is actually a superposition of loops, each characteristic of a particular size of grain growth, a thin sapphire barrier was deposited prior to the VO_2. This resulted in a smooth surface, uniformly small grains, and a symmetrical erect hysteresis loop.

There are two fundamental types of stress introduced into evaporated thin films during deposition. Intrinsic stress is related to atom mobility, with ensuing voids and grain boundaries, and is related to process conditions. Evaporated films of refractory metals typically retain high tensile stress. Extrinsic stress is that introduced by the thermal expansion coefficient mismatch between film and substrate. The effect of the latter on VO_2 transition temperature was investigated.

Shifting of the semiconductor-metal transition temperature in VO_2 was observed for films on different substrates. This was correlated with stress developed between substrate and film on cooling from the deposition temperature, due to the difference in their thermal expansion coefficients. VO_2 on fused quartz, sapphire, and x-cut quartz displayed transition temperatures of 66.2°C, 63.6°C, and 59.5°C, respectively, for films processed under the same conditions. The calculated stresses were all tensile, but decreased in magnitude from fused quartz to sapphire to x-cut quartz. This behavior is consistent with predictions from the literature; namely that transition temperature should decrease as the stress goes from high tensile, thru zero, towards compressive. Figure 6 is a

plot of transition temperature T_t versus tensile stress, including data points for VO_2 on z-cut quartz and calcium fluoride (CaF_2). It was expected that the close match in expansion coefficients between CaF_2 and VO_2 would result in a large reduction in transition temperature, since the calculated extrinsic stress of $.045 \times 10^{10}$ dyne/cm for VO_2 on CaF_2 is substantially less than, say, that for VO_2 on Z-cut quartz. A transition temperature on the order of 50°C was expected to put CaF_2 in line with other results in Figure 6; however, a 54°C transition was observed, suggesting that perhaps intrinsic stress might play an important role as well in affecting the transition temperature. This was then explored by employing the technique of ion bombardment of pre-deposited VO_2 films on several types of substrate materials to ascertain if any effects observed were substrate-independent and attributable primarily to ion-film interaction.

Initial attempts at transition modification by ion bombardment were made using a 500 eV Ar+ beam at 1 mA/cm^2 for 600 seconds. The microstructure after ion bombardment lost its grainy character and appeared amorphous, characterized optically by a collapsed hysteresis loop. Etching of the surface had obviously occured and, therefore, subsequent conditions for bombardment time and energy were reduced. For 146 eV ions at 1.18 ma/cm^2, impacting VO_2 films on fused quartz 125 seconds dramatically reduced the transition temperature by approximately 10°C, with a large change in hysteresis loop width, but no discernable change in either thickness or in surface morphology. The latter behavior was repeated again for bombardment VO_2 films on thin quartz films, which had been put down over a metallization layer on quartz substrates. Absorption did increase, and transmission decreased, but not dramatically in most cases. Results of ion bombardment, at the same low levels, for VO_2 on silicon yielded both a dramatic shift in T_t of 7°C and a narrowing of the hysteresis loop, accompanied by an increase in "effective" extinction coefficient k from .08 to .26. Hysteresis loop width for VO_2 on sapphire was least affected by ion bombardment; however, there were associated shifts in T_t of as much as 4°C. Resistivity data was taken with an Alessi four-point probe while temperature-cycling the samples. Figure 7 shows optical and resistivity hysteresis loops before and after Ar+ bombardment of a VO_2 film on sapphire. AES analysis confirms the presence of a barely detectable Argon signal on the surface. Although metal-state resistivity is unaffected, the semiconducting-state value was reduced by two orders of magnitude. One might expect electrical properties of this sample to be affected in a

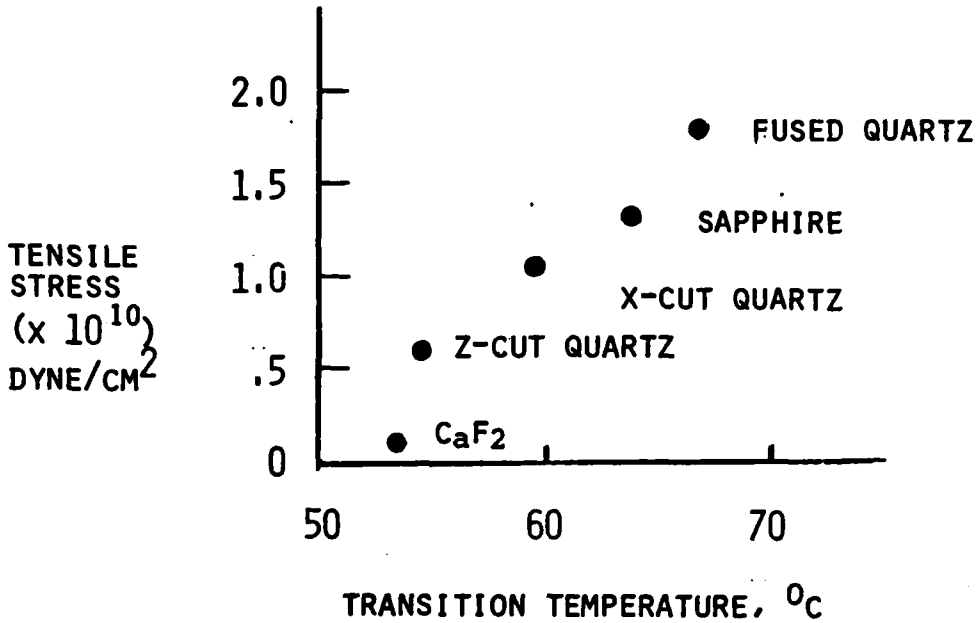

$\Delta\alpha$ = DIFFERENCE BETWEEN LINEAR THERMAL EXPANSION COEFFICIENT OF THE FILM AND SUBSTRATE

ΔT = DIFFERENCE BETWEEN DEPOSITION TEMPERATURE AND ROOM TEMPERATURE

E = YOUNG'S MODULUS OF VO_2 (2×10^{12} DYNES/CM^2)

S = THERMAL STRESS

$S = (\Delta\alpha)\Delta T\ E$

Figure 6: Transition Temperature vs. Extrinsic Tensile Stress

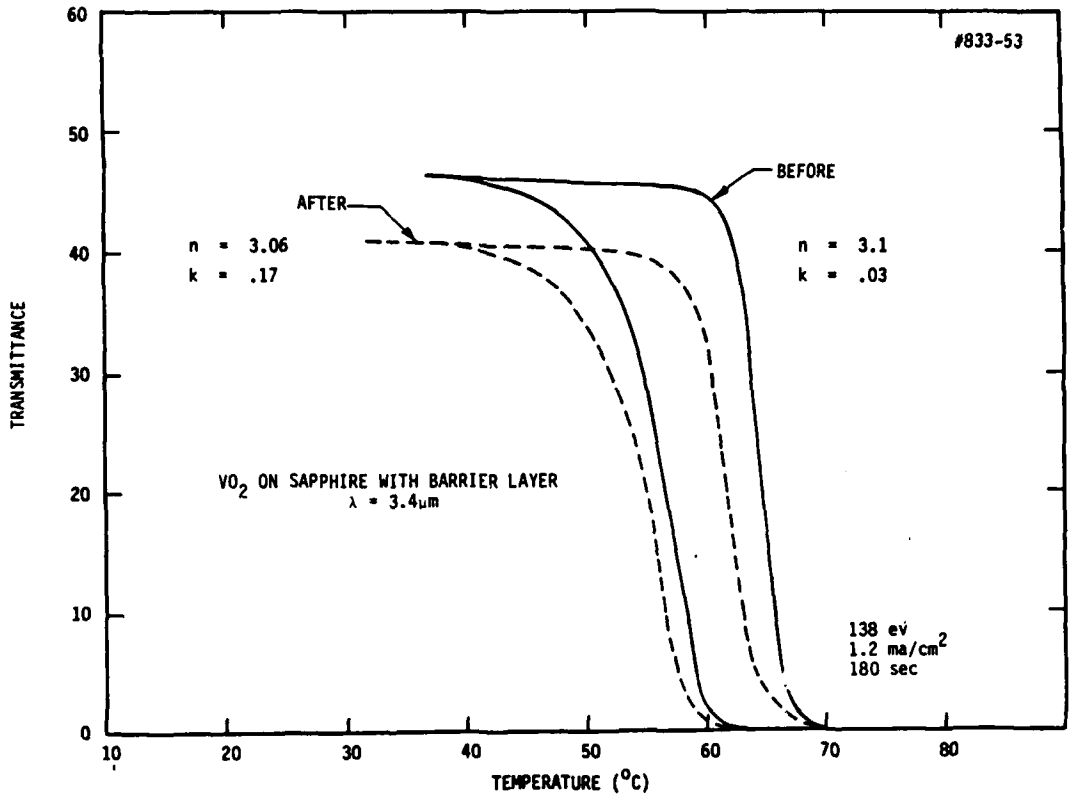

(a)

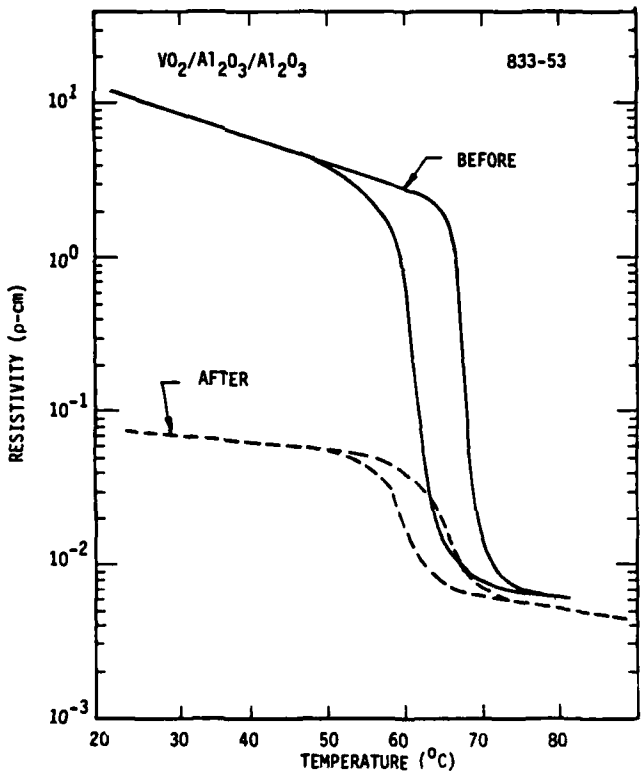

(b)

Figure 7: Effects of Ar^+ Bombardment on VO_2 on Sapphire
(a) Transmittance Hysteresis Loop
(b) Resistivity Hysteresis Loop

more dramatic way than the optical properities if the Ar+ beam reduces the surface oxide of the VO_2, producing a thin metallic layer, which then shorts out the remaining film during the semiconductor-state resistivity measurement. The metal-state value would not change significantly, before and after ion bombardment, due to switching of the underlying VO_2 layer to the metallic state. If this metallic layer is thin enough, the transmission should not be affected greatly, but show an increased absorption, as is the case for most of these samples.

The resistivity and optical transmittance data can be explained by the presence of a thin reduced oxide surface layer. However, this model does not explain the back surface reflectance data, taken from the substrate side, for each of the bombarded films. This data also exhibits identical hysteresis loop narrowing and shifts to lower T_t. One would not expect the thin front surface reduced-oxide layer to be "sampled" strongly from the substrate side, especially in the metallic phase, where only a few thousand angstroms of VO_2 will effectively reduce transmission to near zero. Therefore it is reasonable to ass: : that bulk effects are induced as well by the Ar+ bombardment, and the most likely mechanism is a change in intrinsic film stress. This hypothesis is reasonable in that the transition temperature of VO_2 is a function of total stress, extrinsic due to expansion coefficient mismatch, and intrinsic stress, as brought about by low energy ion bombardment of pre-deposited thin films. It is also hypothesized that hysteresis loop width, although correlated to grain size, may also be somewhat dependent on intrinsic stress.

1.5 MULTILAYER DESIGN

The simplest multilayer in terms of fabrication that includes vanadium dioxide and exhibits good optical switch characteristics has the phase transition material outermost in the structure. Since no design configuration of this type was known to exist for the LWIR spectrum region, the task of developing such a design was introduced into the program.

The design problem is particularly difficulty because of the scarcity of available low index thin-film materials for the LWIR spectral region, and limitations imposed by the presence of vanadium dioxide. That is, fabrication

considerations require that a layer of special buffer material lie just below the vanadium dioxide, and the elevated temperatures present during vanadium dioxide deposition reduce the (already short) list of available design materials. The temperature consideration limits the high and low index materials to just germanium and zinc sulfide, respectively. The general design configuration is shown in Figure 8.

The program goal was to produce a thin-film structure that switches between a state of high transmittance and a state of high reflectance over the widest possible LWIR bandwidth. The fact that vanadium dioxide films thicker than 0.3 microns are essentially opaque when in the hot (metallic) state suggests that a thickness of approximately this magnitude would be appropriate.[2] The transmittance goal is then satisfied when the cold-state reflectance is as low as possible over the wavelength from 8- to 12-microns. Since the design synthesis procedure involves varying the thicknesses of all the films except the vanadium dioxide layer and its adjacent, buffer layer of silicon, these latter two layers are designated as the "fixed module" in Figure 8, and the remaining layers are termed the "multilayer substructure."

A computational design procedure developed in this company was applied to the synthesis problem. The procedure involves successive applications of thin-film modules consisting of a few layers each.[5] For each module a target amplitude reflectance must be provided. The first approach was to determine analytically the target amplitude reflectance for the "multilayer substructure." It had to be such that the overall film stack reflectance (including the fixed module) would be zero. When it became evident after several attempts that more than on design module would be required, various intermediate target amplitude reflectances were considered for the first module. Eventually a nine-layer design was obtained with acceptable switching bandwidth from 9.3 to 10.7 microns (Figure 9).

Subsequently, the computational synthesis procedure was improved so that design targets and merit function evaluations automatically took into account any fixed layers that lay above or below the design modules. This resulted in merit

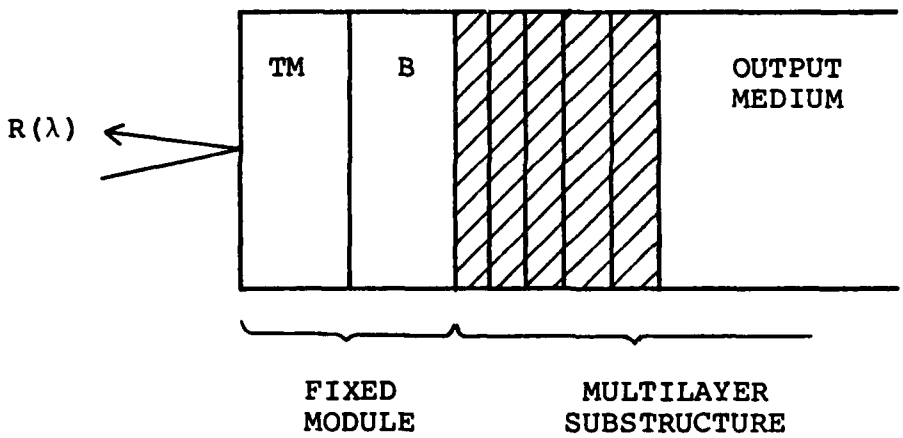

- THE TRANSITION MATERIAL (TM) IS VO_2
- THE BUFFER (B) LAYER IS SILICON
- IF THE VO_2 THICKNESS $\gtrsim$ 0.3 MICRONS, R_{HOT} = 0.8 (R_{BULK} = 0.815) IN THE LWIR SPECTRAL REGION IRRESPECTIVE OF THE SUBSTRUCTURE
- TARGET REFLECTANCE FOR SYNTHESIS IS $R(\lambda) = 0$ FOR $8 \leq \lambda \leq 12$ MICRONS
- FIRST APPROACH - FIND BY ANALYSIS THE TARGET (AMPLITUDE) REFLECTANCE AT THE BOUNDARY BETWEEN THE BUFFER LAYER AND THE SUBSTRUCTURE SUCH THAT ADDITION OF THE FIXED MODULE (BUFFER + TM) BRINGS $R(\lambda) = 0$.

Figure 8. Optical Switch-Design Methodology

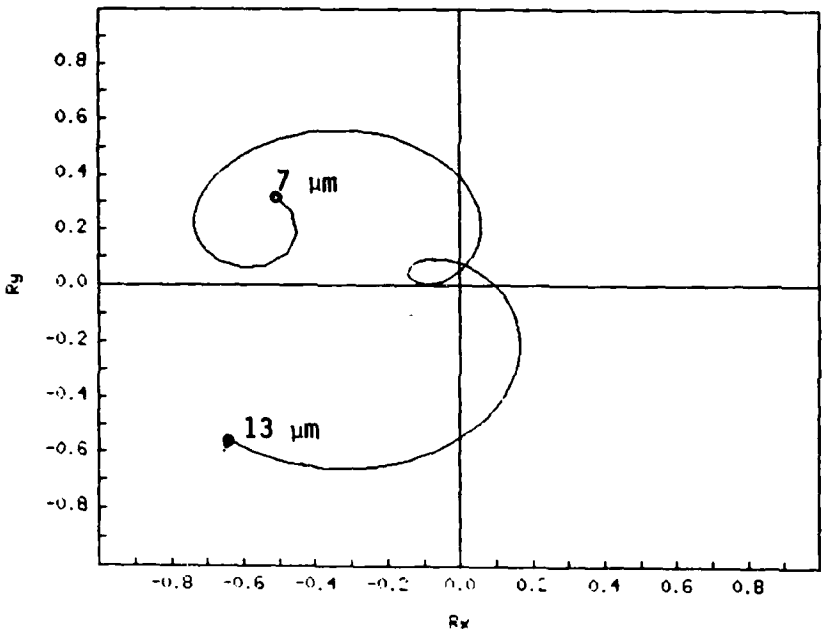

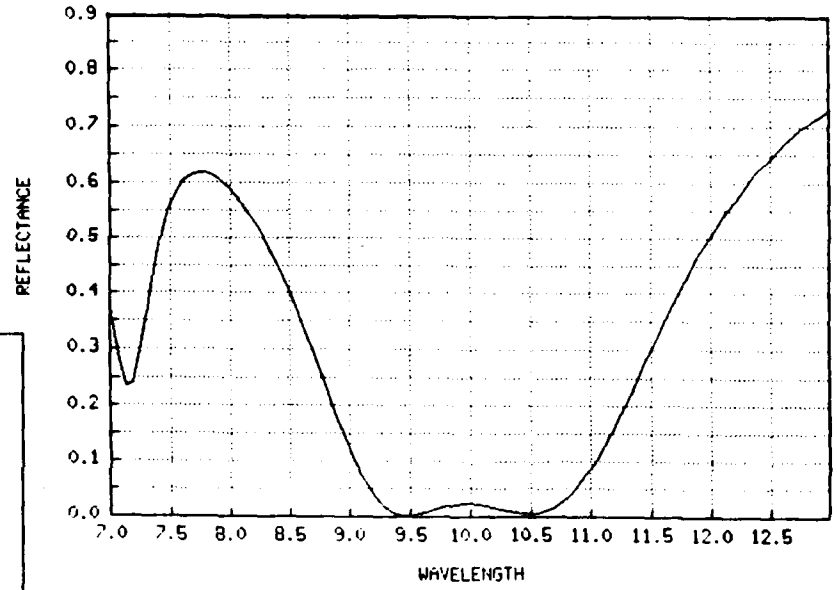

Film Stack:

Layer	N	K	D
<OUT>	4.00	0.00	
1	2.15	0.00	0.175
2	4.25	0.00	0.660
3	2.15	0.00	2.127
4	4.25	0.00	0.950
5	2.15	0.00	0.682
6	4.25	0.00	0.644
7	2.15	0.00	0.381
8	3.43	0.00	0.100
9	2.90	0.20	0.400
<IN>	1.00		

Figure 9. Initial Design Results. The wavelength dependence of both power reflectance and amplitude reflectance is shown. Note the single loop near the origin in the polar plot of amplitude reflectance.

function calculations more precisely correlated with the design goals, and brought about an improvement in the design of Figure 9, but only needed seven layers.

Next, a new module strategy was exploited to further the features of the improved computation synthesis procedure. The bottom two layers of the latest design were taken to be fixed layers, and layers 3, 4, and 5 were replaced by a new five-layer design module. The top two layers were fixed, as usual. With this approach, an improved, nine-layer design was achieved.

Refinement was the final step, accomplished by fixing the final six layers of the current stack and treating the first three layers as a design module. The next iteration in the refinement process was to fix the first three layers at their latest thickness values and to treat the next four layers as a design module. Thus the first three layers and the next four layers alternated as the design module, all others layers remaining fixed for that iteration. This alternating refinement process was iterated several times, until further improvements became insubstantial. The resulting design values and spectral performance are shown in Figure 10. Here, the bandwidth exhibiting satisfactory switching performance covers 2.7 microns.

At this point, the design was fixed for fabrication purposes, but work on the methodology continued into the third year of the contract.

The same improvement strategy described above -- replacing existing three-layer modules that lie somewhere in these tack by five-layer design modules, keeping all other layers fixed, and searching for improved performance -- was applied again, in an effort to obtain a design that would provide satisfactory switching performance over the full 8- to 12-micron spectral band. From these operations, a thirteen-layer design was achieved, and subsequently refined.

The refinement proceeded by an elaboration of the procedure described above. This time any adjacent four or five layers of the multilayer substructure were selected as a "design" module for a given iteration, all other layers remaining fixed. For the next iteration, a different set of adjacent layers would be

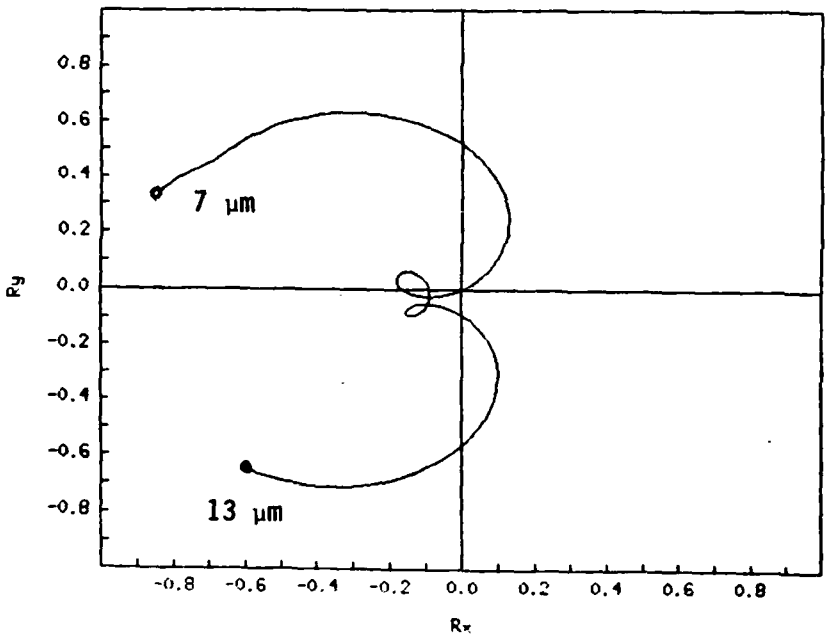

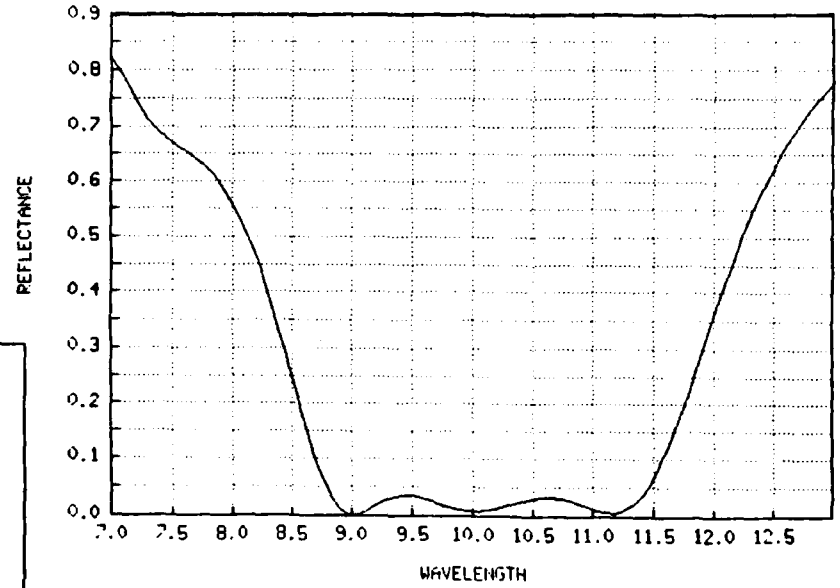

Film Stack:

Layer	N	K	D
<OUT>	4.00	0.00	
1	2.15	0.00	2.067
2	4.25	0.00	1.050
3	2.15	0.00	0.667
4	4.25	0.00	1.305
5	2.15	0.00	0.796
6	4.25	0.00	0.615
7	2.15	0.00	0.409
8	3.43	0.00	0.150
9	2.90	0.20	0.300
<IN>	1.00		

Figure 10. Fabrication Design. Note the double loop near the origin in the polar plot of amplitude reflectance.

selected as the design module. Thus, instead of alternating between two sets of layers as the design module, there were many different sets of adjacent layers taken as the "design" module for a given iteration. The resulting multilayer stack and its performance is shown in Figure 11.

The increasing complexity of the refinement procedure as the number of layers in the design increased led us to consider another approach to refinement, the so-called "N2-scan" method.[6] In this method, for a multilayer of N layers, the thickness of the first layer is varied over a prescribed range, while the remaining layers are held constant. The thickness of the first layer is then set at the value for which the evaluated merit function was minimal. The same procedure is then repeated for the remaining N-1 layers, yielding the first approximation. The overall sequence is now repeated, starting the next iteration with the second, third. ..., Nth layer and ending with the first, and so on. This continues until, in the final iteration, the Nth layer is varied first, then the first, etc. A computer implementation of this procedure was applied to the present problem.

At the same time, it was observed that the number of layers in each of the designs (Figures 9, 10, 11) that had an optical phase-thickness approximately equal to one-half the wavelength of the band center was correlated with the number of "loops" in the polar plot of the amplitude reflectance and the number of relative minimal across the spectral bandwidth. It seemed likely that the performance bandwidth would be increased if another relative minimum could be introduced in the spectral band pattern, and this, in turn, could be achieved by insertion in the design of another layer of material whose optical thickness was approximately five microns.

Therefore, in the course of applying the N2-scan refinement procedure, an attempt was made to insert into the design stack another layer with optical thickness of five microns; specifically, a two-layer module of germanium with a thickness of 1.4 microns (and, hence, an optical thickness of approximately five microns), and zinc sulfide with a thickness of 0.2 microns. Then the N2-scan refinement procedure was applied to the enlarged stack.

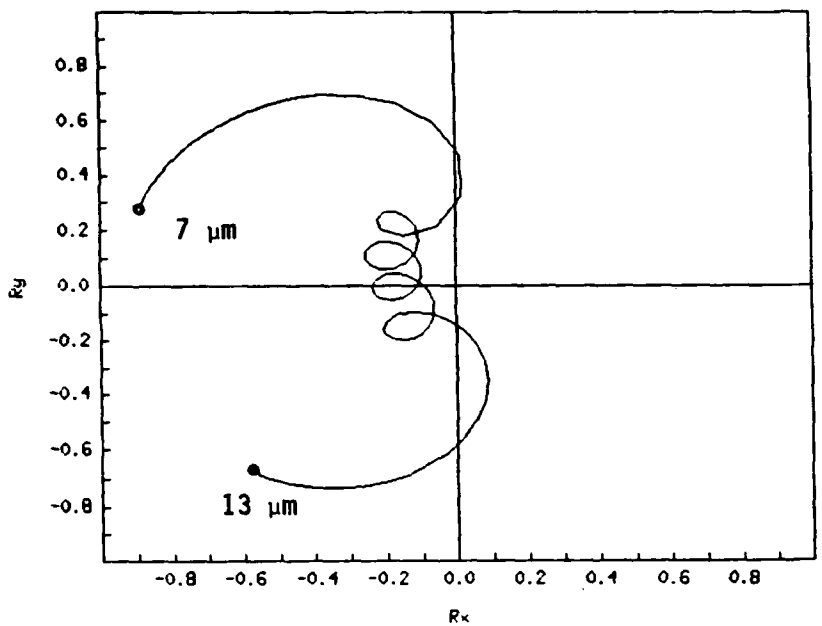

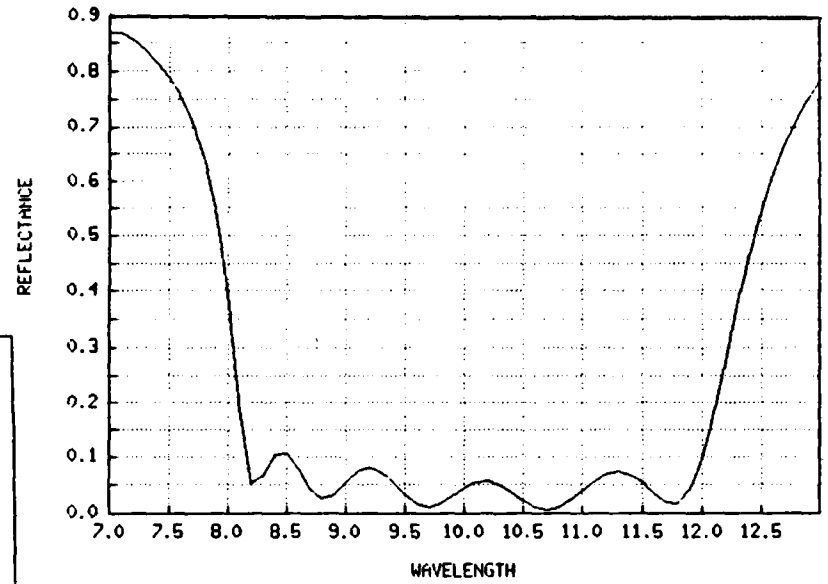

Film Stack:

Layer	N	K	D
<OUT>	4.00	0.00	
1	1.68	0.00	0.040
2	2.15	0.00	2.198
3	4.25	0.00	1.063
4	2.15	0.00	0.035
5	4.25	0.00	1.378
6	2.15	0.00	0.393
7	4.25	0.00	1.409
8	2.15	0.00	0.573
9	4.25	0.00	1.382
10	2.15	0.00	0.511
11	4.25	0.00	0.678
12	2.15	0.00	0.404
13	3.43	0.00	0.150
14	2.90	0.00	0.300
<IN>	1.00		

Figure 11. Initial Broadband Optical Design (prior to refinement). Note the four loops near the origin in the polar plot of amplitude reflectance.

This heuristic design method proved to be successful in developing a seventeen layer stack whose switching performance met the design goals across the full 8- to 12- micron band. Its performance is shown in Figure 12. Notice the increased number of relative minimal in the spectral band performance and the increased number of loops in the polar plot of amplitude reflectance.

In the course of this work, a new design was produced using vanadium dioxide. Additionally, new thin-film design techniques and numerical procedures were developed which, when used in combination, can be effective tools in the design of new multilayer structures.

1.6 Multilayer Fabrication

In this company, fabrication of multilayer structures containing VO_2 employs the electronbeam vapor deposition process. Two 24-inch vacuum bell jars are dedicated to this effort, each equipped with rotary vane high vacuum pumps, thermocouple and ion vacuum guages, quartz microbalance rate control systems, optical thickness monitoring systems, and quadruple mass spectrometer residual gas analyzers. The principal difference between the two systems is in the method of heating the film substrate; in one system, heating is by physical contact to a heated stainless steel surface; in the other system, tungsten-iodine lamps are used to heat the substrates radiantly. In both cases, primary temperature control is by an automatic feedback system employing a thermocouple, with additional temperature readout and subsequent manual adjustment according to a thermocouple attached to the substrate itself. It has been found that the contact heated system optimizes control over the deposition of VO_2, and the radiantly heated system optimizes control over the deposition of dielectrics. Samples of multilayer structures containing dielectrics and VO_2 have been made in both systems separately, and by moving the sample from one to the other when changing from dielectrics to VO_2.

One of the designs discussed in the previous section has been the subject of intensive fabrication efforts during the last year of the contract. Early in this effort, a phenomonoligical pattern was established wherein reasonably good agreement between design and measured performance is achieved for the dielectric substructure (Figure 13), but after the addition of the VO_2 layer, performance is

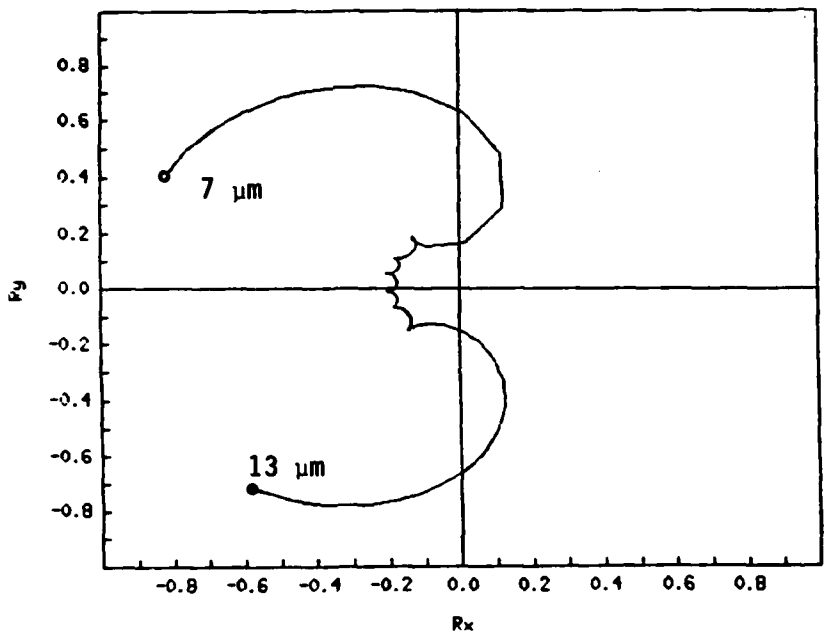

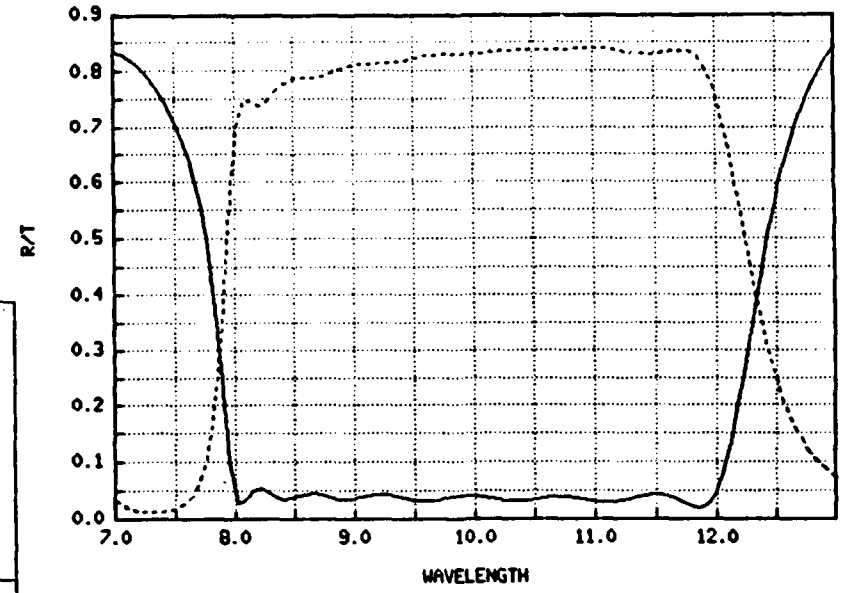

Film Stack:

Layer	N	K	D
<OUT>	4.00	0.00	
1	1.68	0.00	0.040
2	2.15	0.00	0.084
3	4.25	0.00	1.330
4	2.15	0.00	2.172
5	4.25	0.00	1.105
6	2.15	0.00	0.184
7	4.25	0.00	1.350
8	2.15	0.00	0.425
9	4.25	0.00	1.366
10	2.15	0.00	0.575
11	4.25	0.00	1.344
12	2.15	0.00	0.575
13	4.25	0.00	1.402
14	2.15	0.00	0.395
15	4.25	0.00	0.691
16	2.15	0.00	0.449
17	3.43	0.00	0.100
18	2.90	0.20	0.300
<IN>	1.00		

Figure 12. Optimized Multilayer Optical Switch Design.

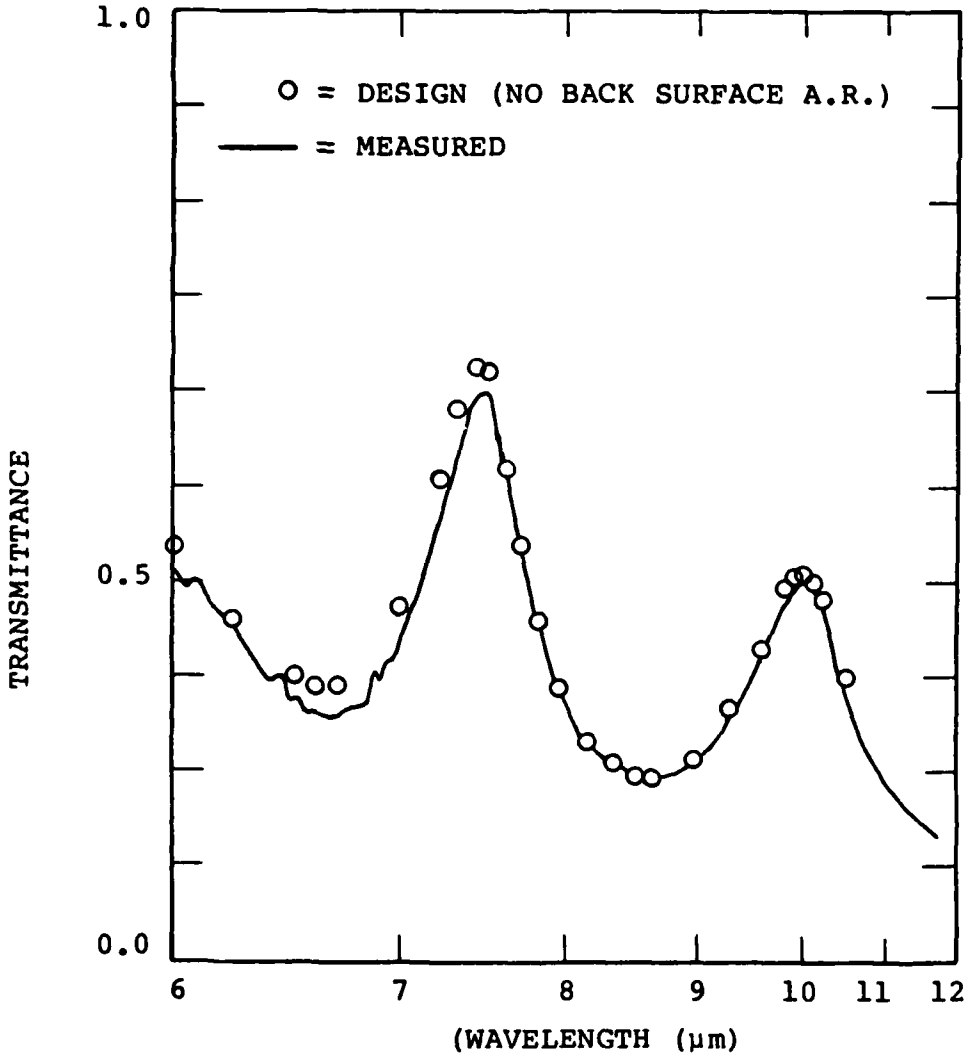

Figure 13. Optical Performance of a Dielectric Substructure Compared to Design

shifted to lower wavelengths (Figure 14). After work began on the design of Figure 10, the same basic phenomenon occurred, and it has been reproduced during numerous subsequent fabrication attempts. Its resolution has therefore been a major concern, one to which a significant variety of probes, both analytical and experimental, have been applied.

Since the accuracy of layer thickness control is a fundamental issue, an important experimental probe was to develop the best possible post-mortem method for determining the actual layer thicknesses deposited, independent of the optical monitoring scheme used during the fabrication. Although both stylus-profilometric and Fizeau-interferometric methods are used for certain thickness measurements, it was found that breaking the sample and viewing it edge-on in a Scanning Electron Microscope gives the best data on layer thicknesses after a complete deposition. Data from such measurements will be discussed shortly.

Another important experimental probe applied to this problem was chemical depth profiling using Auger Spectroscopy during etching by a focussed Argon ion beam. It was hypothesized that the high temperature of the VO_2 deposition process might have altered the dielectric substructure in some way, perhaps through chemical decomposition or interdiffusion among the layers. The results of Auger depth profiling, however, do not show any evidence of such an effect.

Another experimental investigation was undertaken to see if the need to break vacuum to replenish the evaporant materials was in some way affecting the performance of the optical Monitoring system, perhaps through the introduction of impurities, such as water, at the interfaces. The vacuum was broken separately at each of the types of interfaces between materials, but subsequent optical transmission and reflectance measurements did not show any difference from expected behavior.

On the analytical side, one area investigated was the effect of error propagation due to possible differences between the refractive indices assumed in establishing the optical monitoring scheme and the actual refractive indices realized upon deposition of the materials in the multilayer stack. The predicted optical performance of the final structure was computed for a matrix of possible

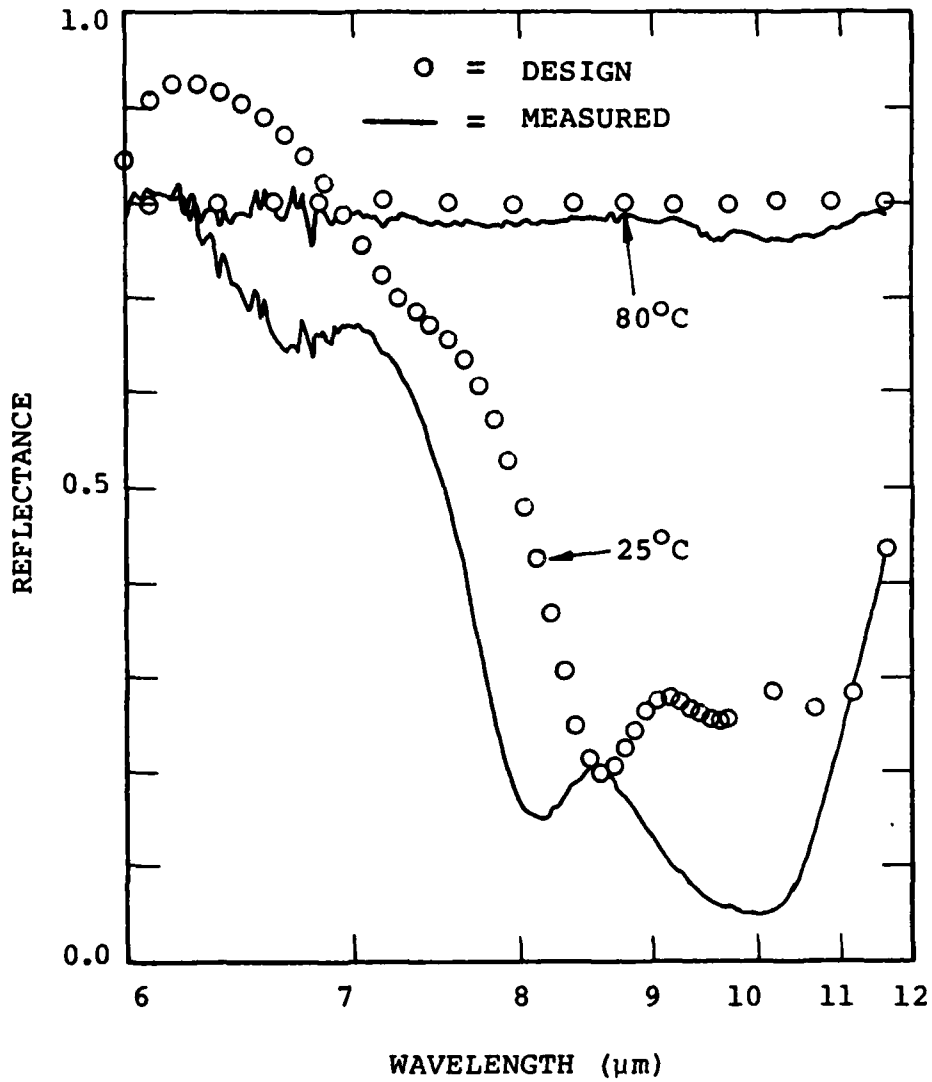

Figure 14. Optical Performance After Adding VO_2

errors of differing magnitudes, and each was compared with the measured performance of the fabricated structure. The technique was among those used to develop the most probable final configurations for the present fabrication effort, as discussed further below.

A related analytical effort was the development of a Monte Carlo simulation routine to assess the sensitivity of multilayer designs to fabrication errors of both the refractive index and thickness in any of the layers of a particular structure. In this routine, each layer was assigned a random thickness and/or index error according to assumed Gaussian distributions of errors. For the present case, random errors with 5% standard deviation in refractive index were found to result in a yield of 74% of final structures whose optical performance fell within 5% of design across the operating and on an RMS basis. For thickness errors with 5% standard deviation, the number of acceptable final structures was 95%. It was concluded that this design is not inordinately sensitive to random fabrication errors.

With these experimental and analytical efforts providing the preliminary background, a detailed analysis of one complete fabrication was undertaken, with major additional emphasis on a comparison of various predictions of the expected power reflectance of the dielectric sub-structure with the actual measured power reflectance. Four bases were used to establish predicted performance: (1) the original design; (2) inverse synthesis (employing the same basic methods discussed in the previous section on multilayer design); (3) fabrication simulation (discussed above); and, (4) SEM thickness measurements. Additionally, each of these methods was further refined using the N2 scan method (also discussed in the previous section), giving a total of eight hypothetical predicted performances for the dielectric substructure. These are shown, in comparison to the photometric data from the fabricated substructure, in Figures 15 through 18. The thicknesses resulting from N2 scan refinement are tabulated in Figure 19.

A noteworthy aspect of these curves is that, whereas all four of the refined curves fit the photometric data equally well, the initial thickness sets from which they are derived are clearly grouped according to the behavior of the last three layers: D4, D6, and D8 are quite similar to each other, while D2 differs

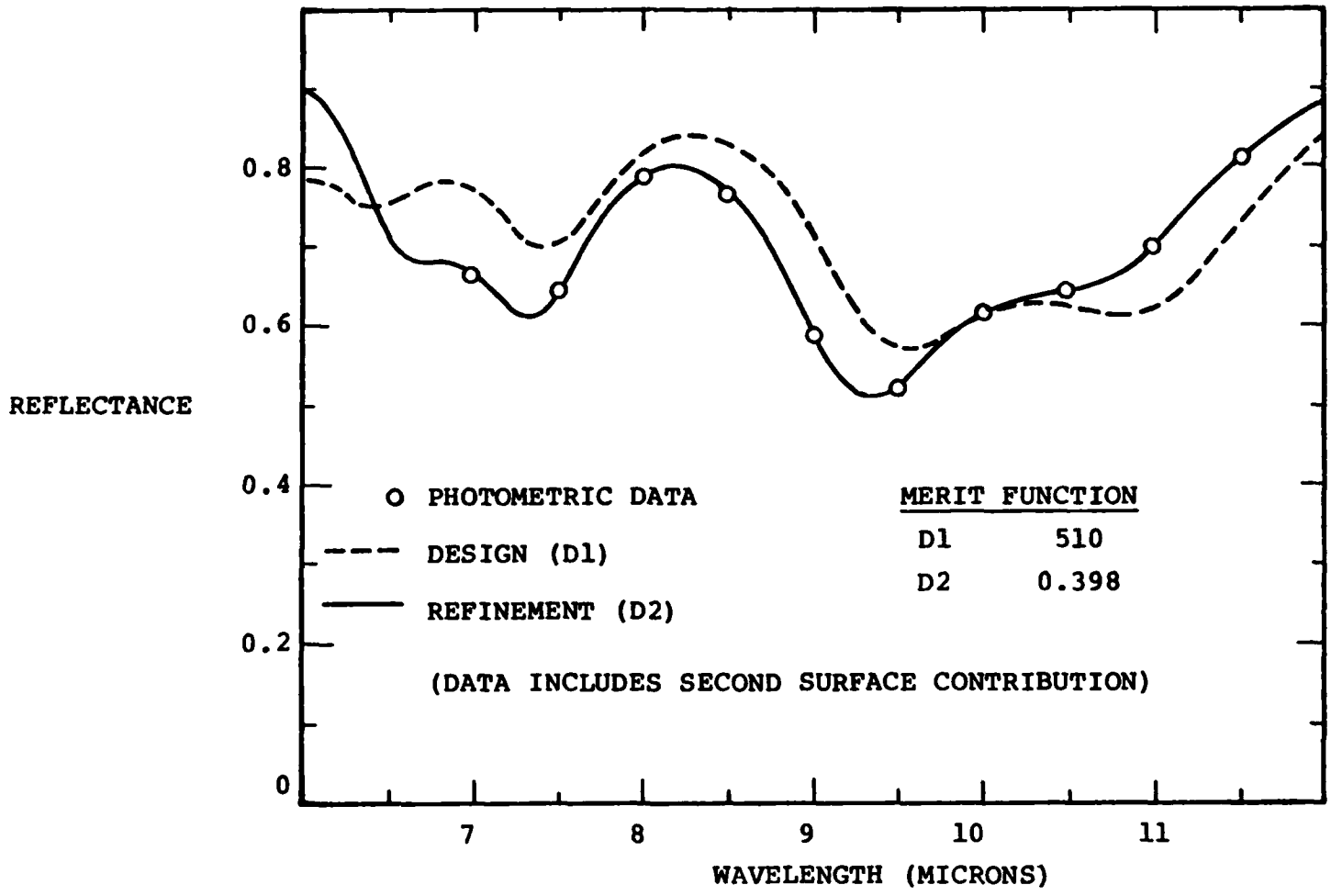

Figure 15. Substructure Spectral Data Analysis (Design Approach)

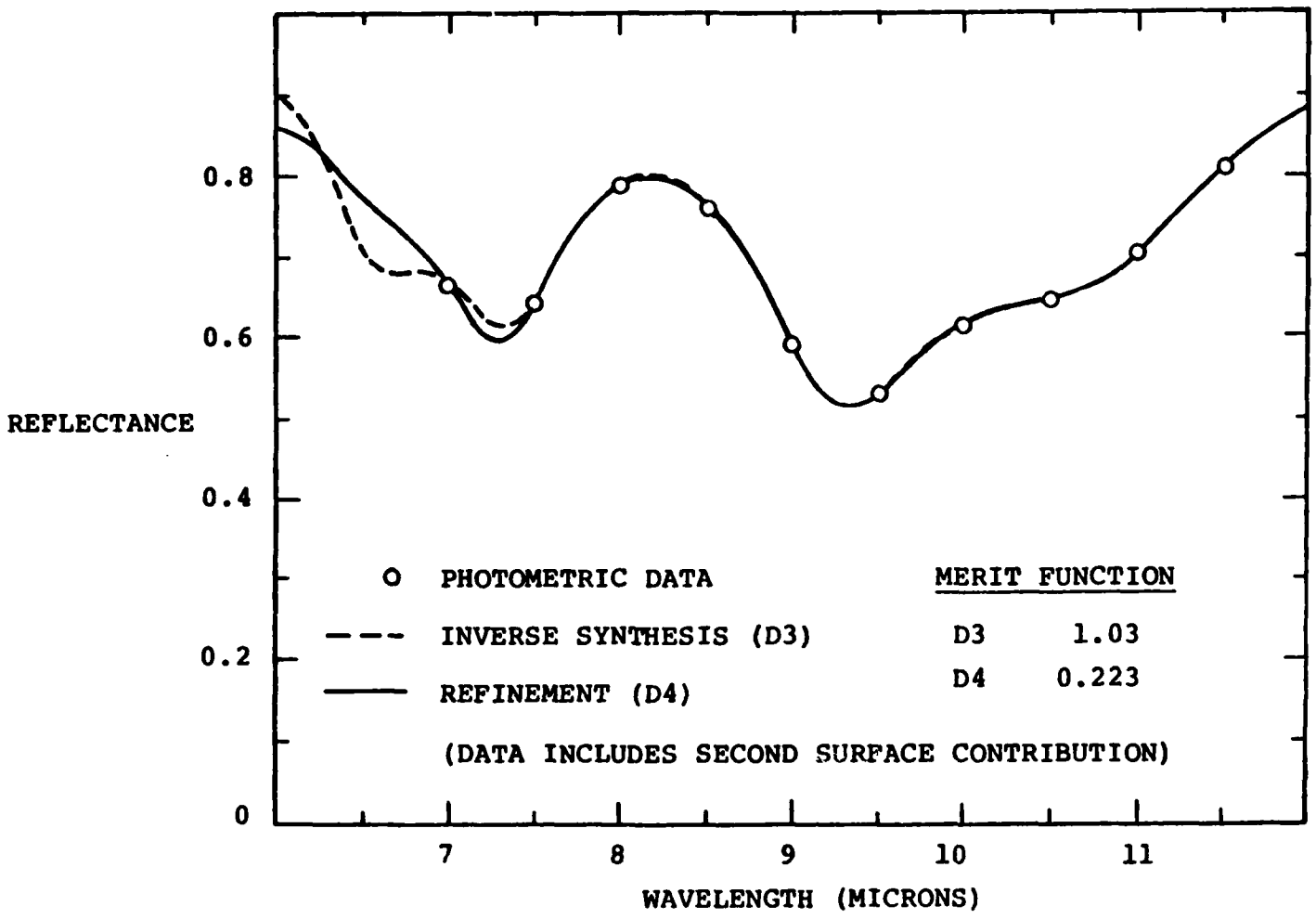

Figure 16. Substructure Spectral Data Analysis (Inverse Synthesis Approach)

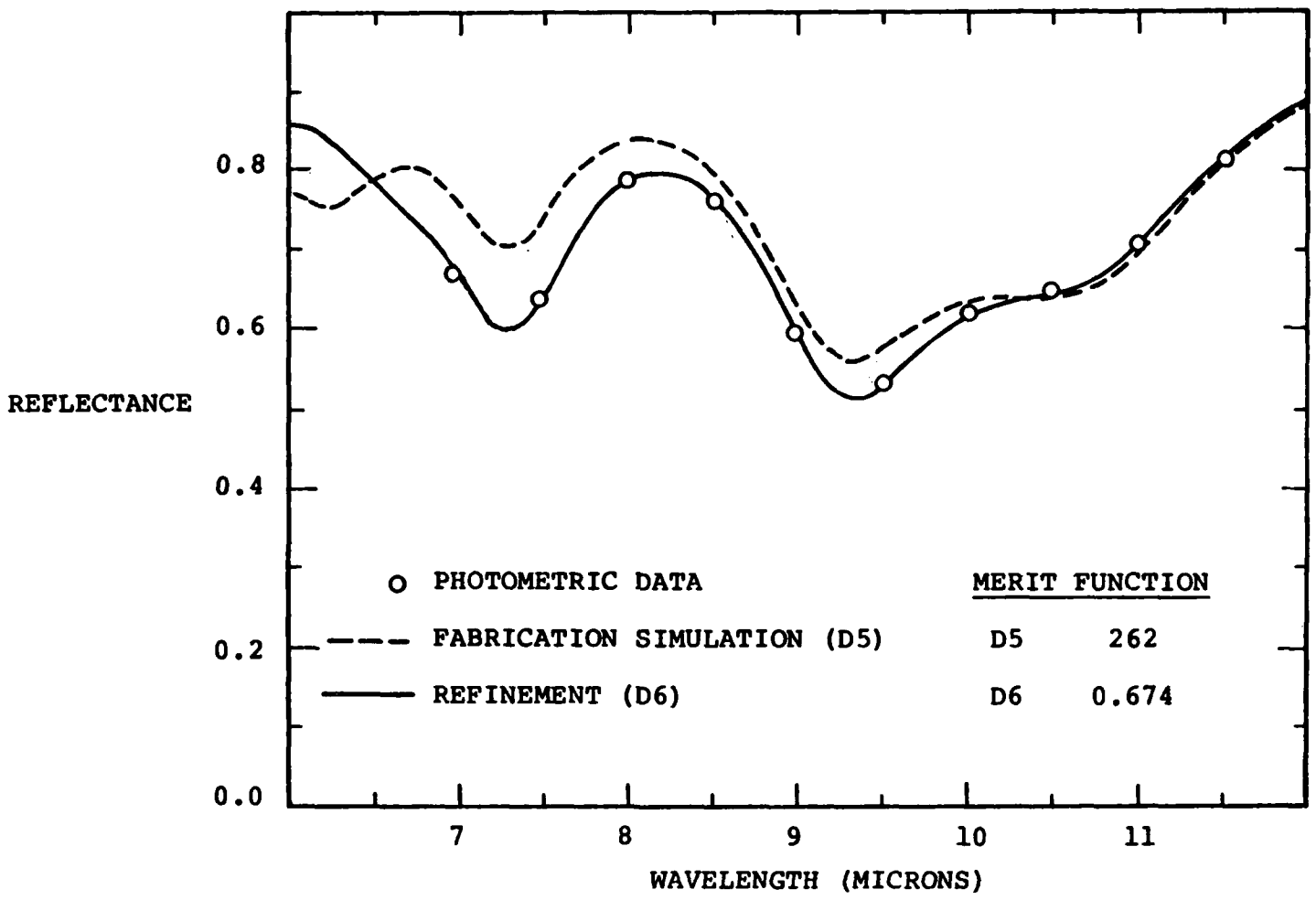

Figure 17. Substructure Spectral Data Analysis (Fabrication Simulation Approach)

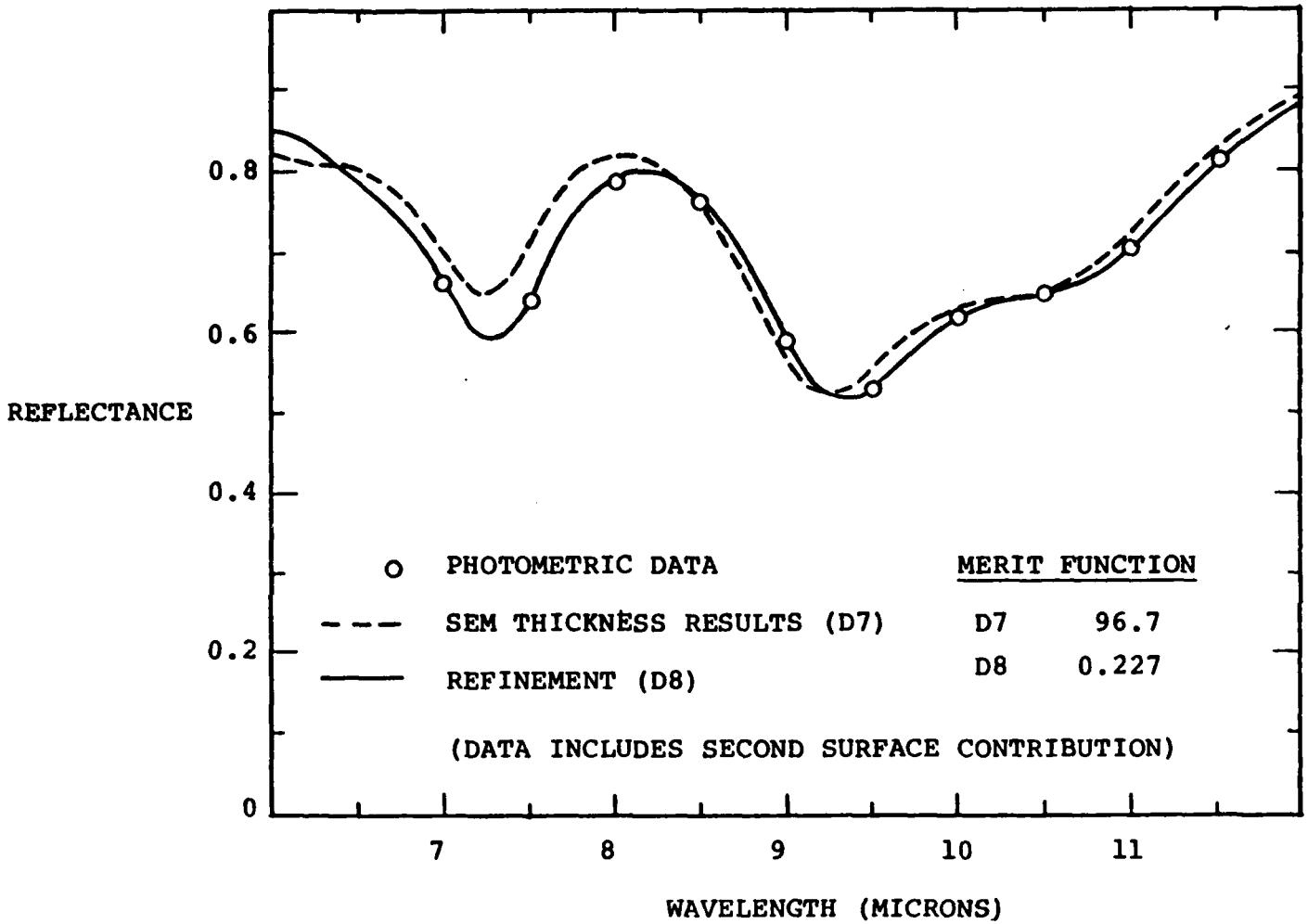

Figure 18. Substructure Spectral Data Analysis (SEM Approach)

(THICKNESS IN MICRONS)

LAYER	N	K	D2	D4	D6	D8
OUTPUT	4.00	0	-	-	-	-
1	2.15	0	2.074	2.087	2.074	2.101
2	4.20	0	1.020	1.010	1.008	1.008
3	2.15	0	0.699	0.686	0.722	0.658
4	4.20	0	1.250	1.225	1.208	1.225
5	2.15	0	0.637	0.823	0.885	0.862
6	4.20	0	0.731	0.625	0.608	0.595
7	2.15	0	0.269	0.463	0.485	0.502

SPECTRAL FIT MERIT FUNCTION	0.398	0.223	0.674	0.227

Figure 19. Substructure Configurations

from them. This grouping is further evident if amplitude reflectivity instead of power is plotted, as in Figure 20.

In the context of investigating why good agreement with design is obtained before VO_2 deposition, and poor agreement after, the existence of the two groups in Figure 19 provides some insight. That is, the degeneracies found in fitting power reflectance are partially removed with respect to its component parts, amplitude and phases. It can be expected that differences in the amplitude reflectivity of these various substructure configuration will lead to differences in the final configuration which includes another layer (VO_2). This is further illustrated by a plot of the analytical addition of a VO_2 layer to each of the four refined configurations, as shown in Figure 21. Upon inspection it is seen that the D2 configuration is much closer to the measured data. It can be speculated that some third group of thickness parameters could be found which agrees well with the data, fully resolving the issue of a shift in performance to lower wavelengths after addition of VO_2.

Continuing the search among degenerate configurations was not pursued further, however, since the range of thicknesses in Figure 19 clearly suggests that more progress must be made in achieving accurate deposition of the substructure. Thus, attention turned to determining at what point in the fabrication process divergence from close agreement with design expectations occurs. The structure was fabricated on a layer-by-layer basis, with power reflectance and transmission measurements made after each layer. This was done both by adding new layers to the sample after each measurement, and by fabricating n layers (for all n less than the complete structure) before a measurement is made. The result is that after the fifth layer deposition there occurs anomalous behavior reminiscent of the original phenomenon: the spectral dependence of the power reflectance is shifted to lower wavelengths. This shift persists for all subsequent layers.

Since degeneracies of the type discussed can occur at any step after the first few layers, progress will be made only with further improvements in both the optical monitoring technique and in the reproducibility of the materials deposition process. Addition of monochromators to the optical monitoring systems

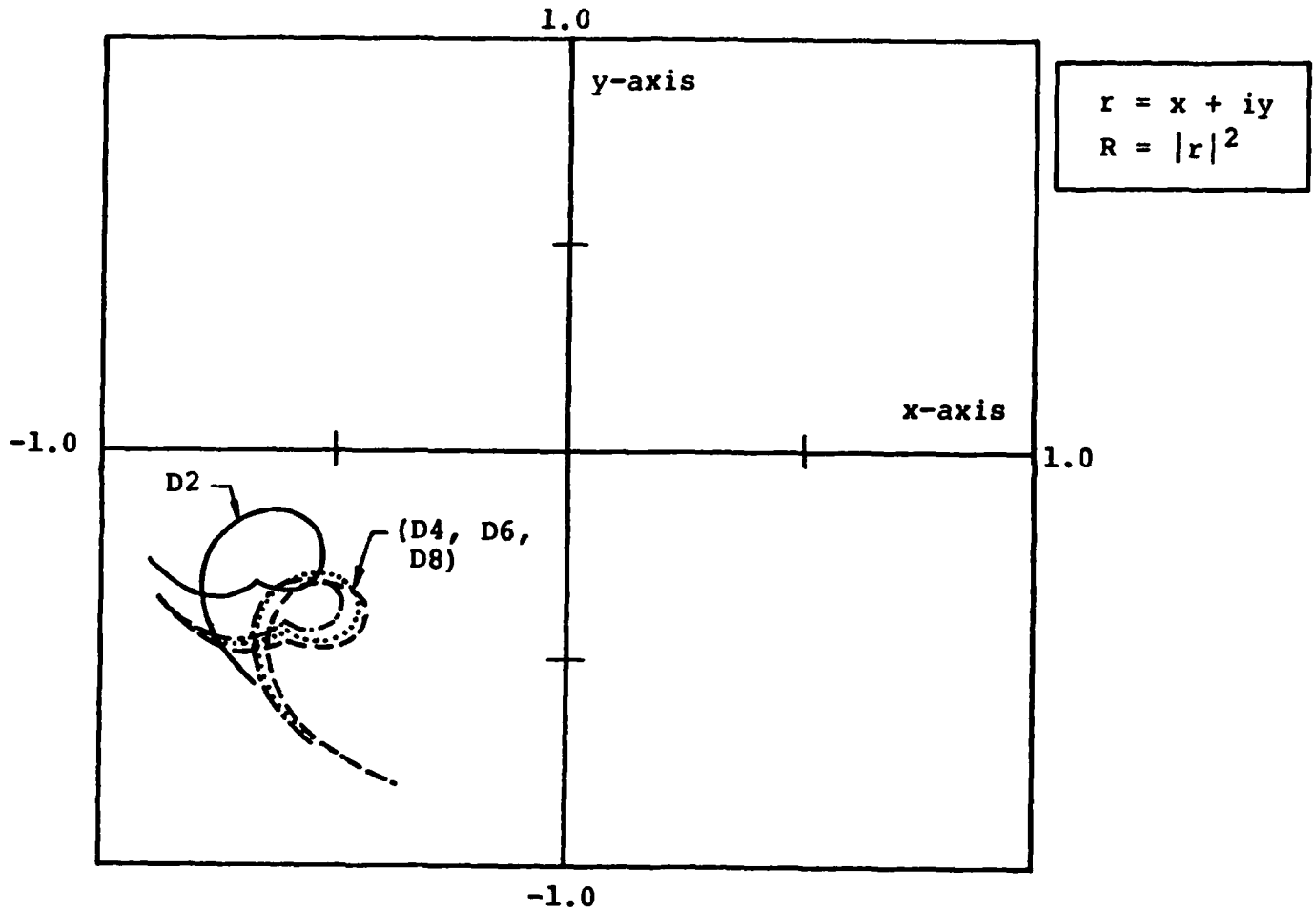

Figure 20. Amplitude Reflectivity Plot (Substructure Configurations)

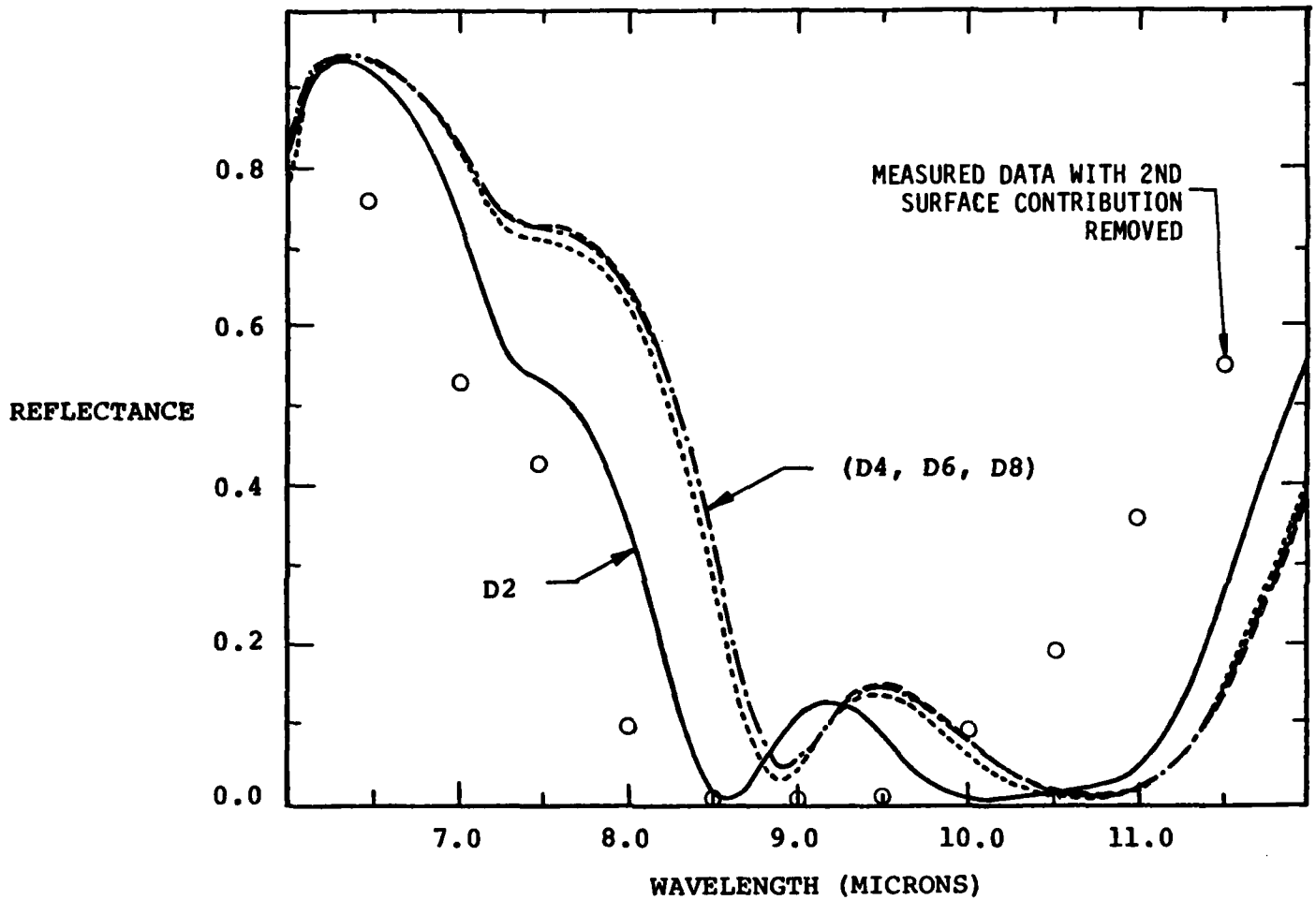

SUBSTRUCTURE DESIGNS

D2 - Design Refinement
D4 - Inverse Synthesis + Refinement
D6 - Fabrication Simulation + Refinement
D8 - SEM Measurements + Refinement

Figure 21. Optical Switch Performance (Predicted)

is one planned improvement. Ongoing work, under IR&D funding, to improve the temperature control of the deposition process, to more accurately measure film indices of refraction and possibly their stress-dependence, and to streamline the computer analysis of spectrophotometric data will also contribute.

1.7 Electro-Optical Devices Based on VO_2

Since both the electrical and optical properties of VO_2 change at its phase transition, it is a natural candidate for a variety of electro-optical device concepts During the first part of the contract effort, work was performed to investigate an electric-field switched optical modulator configuration.[1,2] More recently, the phenomenon of filamentary conduction in VO_2 has been explored in the context of several interesting device concepts.

Electric-field switching of VO_2 has been reported by K. A. Valiev, et. al.[7] using a configuration employing a liquid electrolyte as one of the field electrodes (the electro-reflectance technique). On this basis, work began in this company aimed at achieving electric-field switching in a configuration compatible with existing VO_2 thin film technology. The first structure tested was a thin film of VO_2 between two sapphire thin-film insulating layers and two semi-transparent thin-film metal electrodes, all deposited on a sapphire substrate. For each of several samples fabricated using this approach, high fields up to 2×10^7 V/cm caused the insulating layers to fail before switching of the VO_2 was observed. Subsequently, germanium was used as substrate, so that it could serve as one field electrode, and TiO_2 was used for the insulating layers, since it has a moderately higher dielectric strength than sapphire. The other field electrode was a thick layer of gold (substantially more robust than the semitransparent electrodes of the earlier configuration); the optical response of the VO_2 was viewed in reflection through the substrate. Once again several attempts were made before reaching the electrical breakdown of the insulator, but none of these succeeded in switching of the VO_2.

It was concluded on the basis of this work that the dielectric strength of thin film insulating material does not permit sufficient field strength to switch

VO_2. A report of negative results from a similar, independent effort, has subsequently been received.[8]

Investigations with more positive results were made during the last year of the program, namely thermal filamentary conduction in VO_2. One motivating factor is to further explore the use of thermal filaments as a bolometer, along the lines suggested by Jelks, et al.[9]

As detailed in recent quarterly reports, initial experimentation involved observation of thermal filament phenomena in electrode structures with relatively large electrode gaps (eg., 100 μm - 1000 μm).

On a first device, resistance versus temperature curves and current versus voltage curves were recorded for a .95 mm electrode gap. The latter were found to agree qualitatively with those reported in the literature.[9] Preliminary data was recorded on the temperature and voltage dependence for ignition of the thermal filament, and the filament was observed with an imaging infrared detector system. A visible microscope was used to measure the width of the filament as a function of current. Preliminary measurements were made on the speed of the filament switch-on.

A second sample was fabricated to attempt smaller electrode gaps. One sample with a gap of 118 μm was used for further experiments, including the first reported use of a laser pulse to initiate the ignition of the thermal filament. Laser switching of the filament was characterized with measurements of the power dependence, laser spot size dependence, and temperature dependence of the switching response time.

During the final quarter of the present program, the first submicron-scale devices were fabricated at the National Research and Resource Facility for Submicron Structures (NRRFSS), Cornell University. In exploring the behavior of much smaller devices for the bolometer application, one hopes to find both quantitative (faster response, lower operating voltage) and qualitative changes.

Figure 22 shows a photograph of the sample, fabricated on a one-inch diameter sapphire substrate. The gray circular region is a VO_2 film on the

surface of the substrate, and the darker features are the patterned gold electrode structure (center) with leads to bonding pads near the perimeter. The details of the central electrode-gap region are shown in Figure 23. The six devices left to right in the upper row have gap sizes of 50, 20, 10, 5, 2, and 1 μm, and the lower row is the same, but from right to left. The sample was mounted on a heater ring and wired using silver-laden epoxy, as shown in Figure 24. It happens that both of the 1 μm gaps and one each of the 2 μm and 5 μm gaps were bridged with gold, due to less than optimum performance of the e-beam photo resist processing. It is expected that this problem will not recur on subsequent fabrications.

Current versus voltage characteristic curves were recorded for one of each of the good devices, as shown in Figure 25. The fact that the 2 μm and 5 μm curves do not nest within the others is anomalous compared to experience with larger devices. The reason for this behavior became apparent on examination in the optical microscope, as shown in Figure 26: the region between the gaps is apparently damaged, and the filament traverses a path around the damaged region.

Another anomalous feature of the curves in Figure 25 is that the 10 μm curve shows two switching discontinuities instead of one. This turns out to be due to the formation of two different filaments, in different locations, as shown in Figure 27. The upper photo shows a filament corresponding to the higher voltage switching event; it is buried somewhere in the damaged region of the film. The lower photo shows the second filament which forms after the lower voltage switching event. Presumably the first filament is extinguished when the second one ignites; however, the issue of possible simultaneous existence of two filaments in parallel deserves further investigation.

Attempts to determine the cause of damage were initiated. The first ten filaments ignited in a virgin gap were photographed, and subsequently a photo was taken after each five ignitions up to fifty. The filaments were ignited by manual increase of the power supply voltage, and during the sequences of five the repetition rate was intentionally made as rapid as seemed reasonable (about 0.5 Hz). It was found that no damage occurred during the first ten, but that damage did occur after each subsequent sequence of five. thus, the repetition rate may be a factor in the damage phenomenon. Alternately, the rapid manual operation

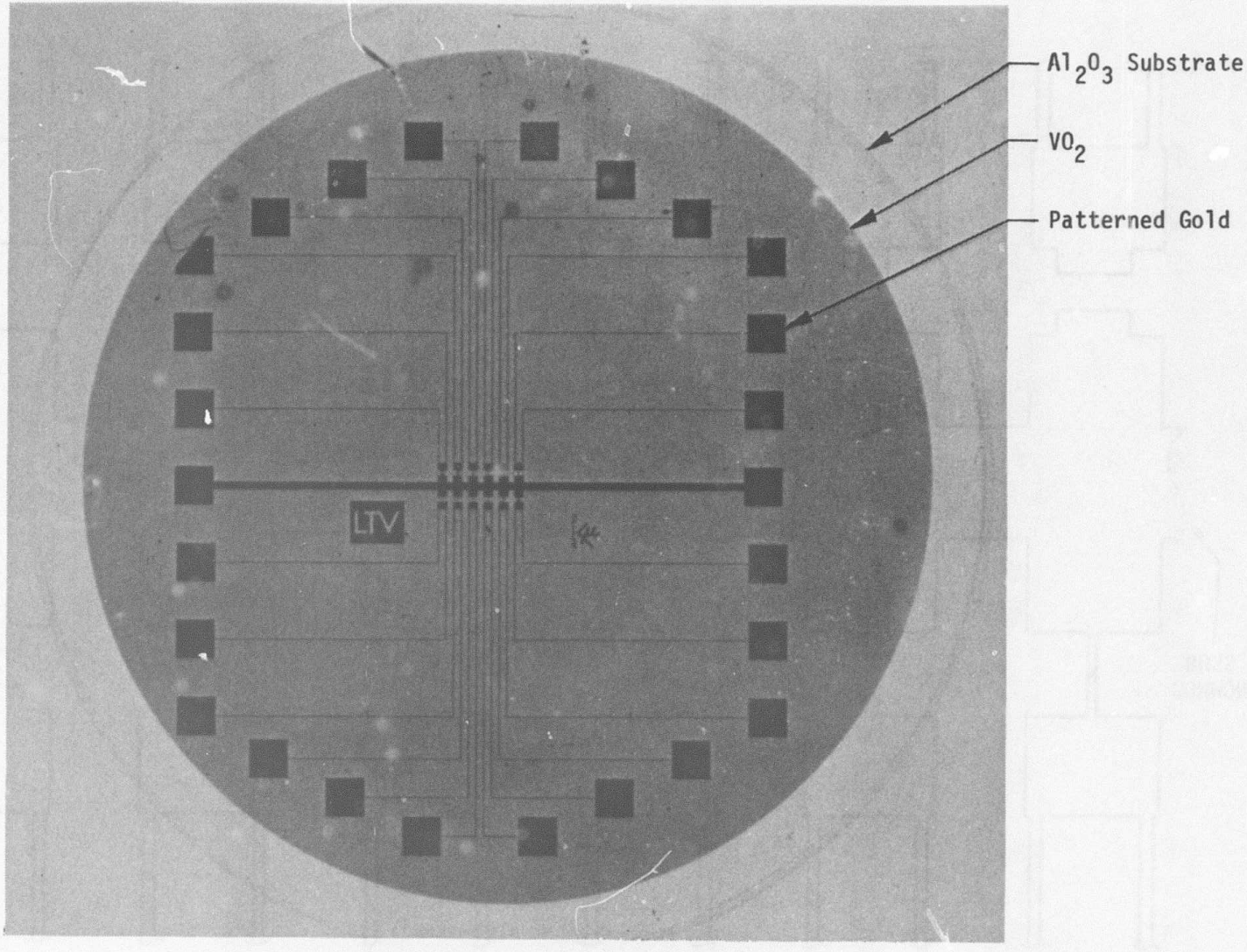

Figure 22. Submicron-Resolution Electrode Structures for Thermal Filaments in VO_2 Fabricated at NRRFSS

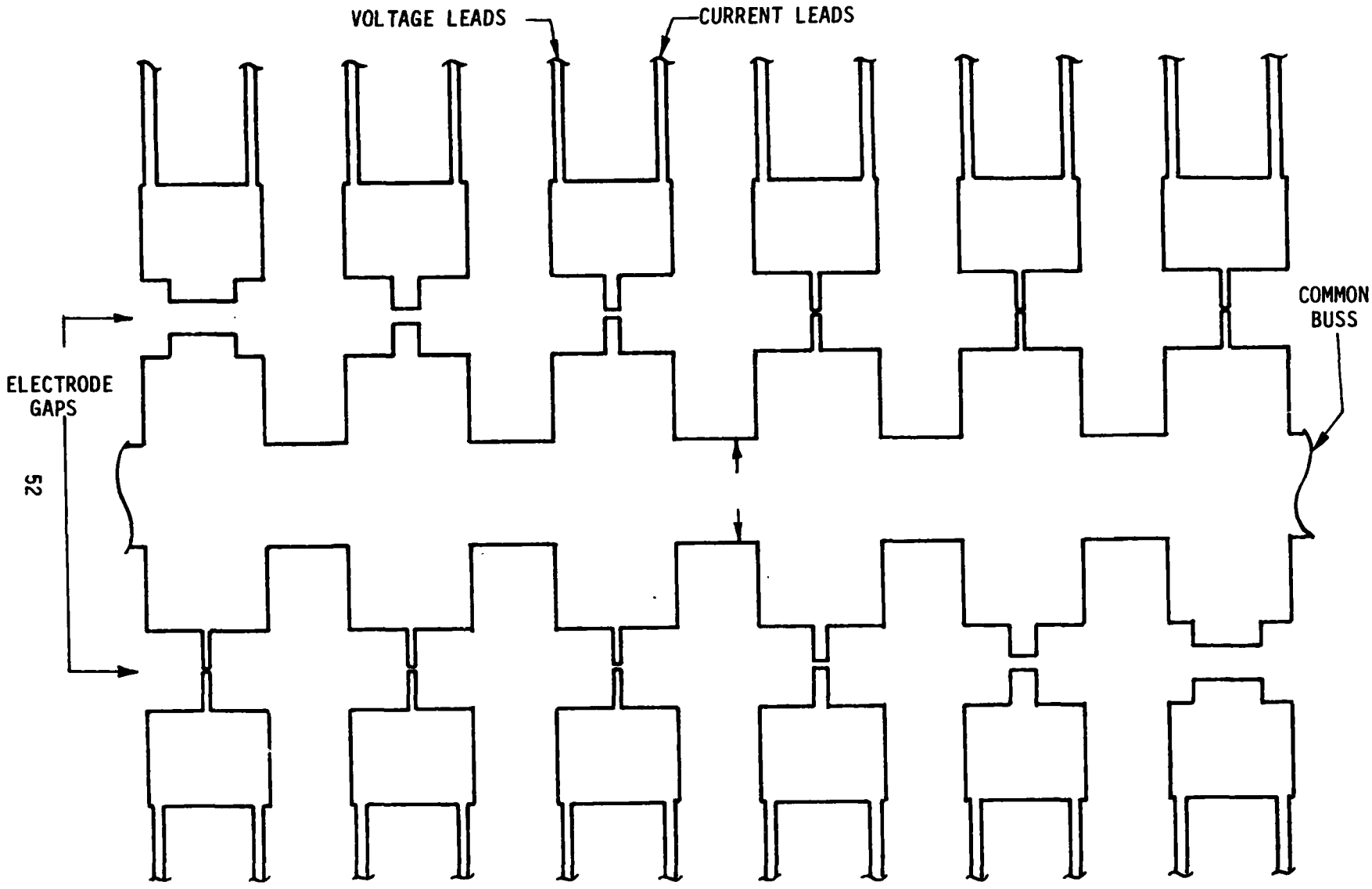

Figure 23. Detail of Central Electrode-Gap Region

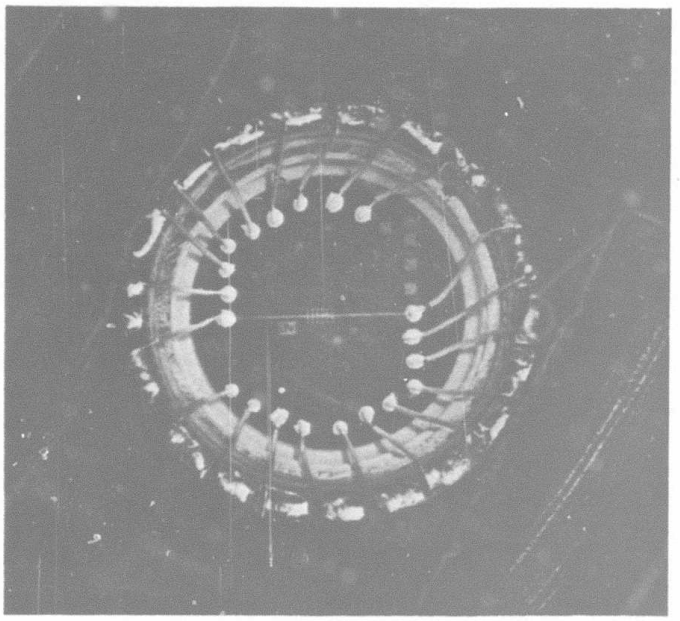

Figure 24. Sample Mounted in Heater and Wired

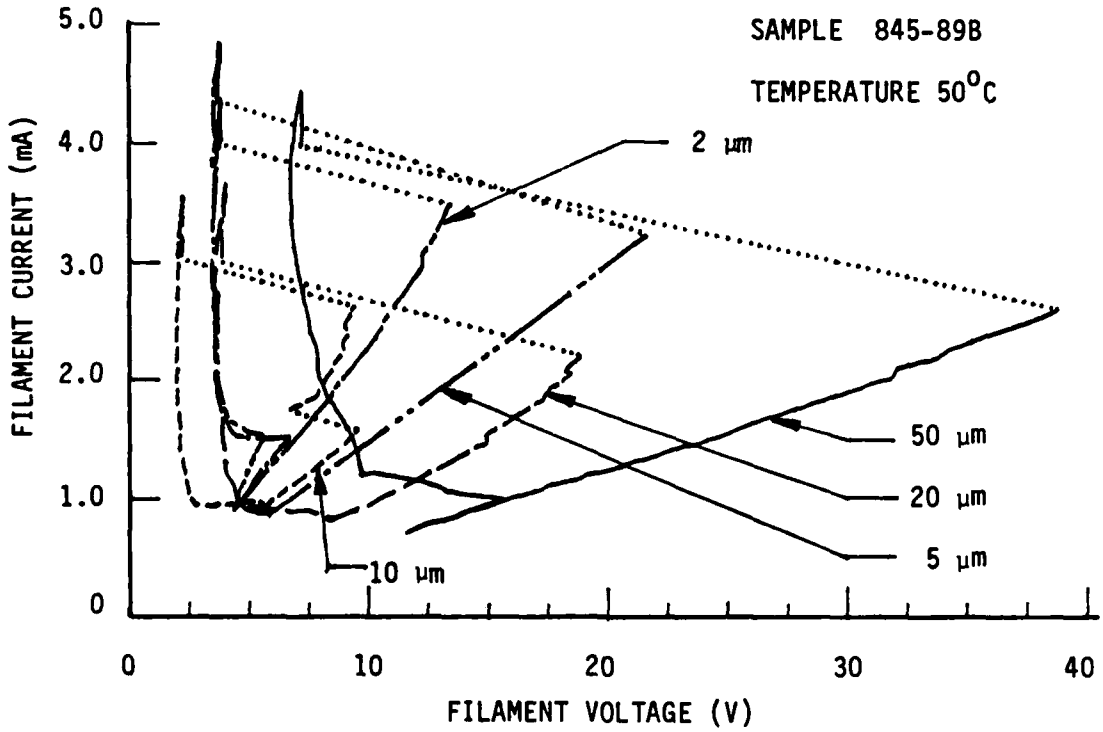

Figure 25. Current-Voltage Characteristics of First NRRFSS Devices

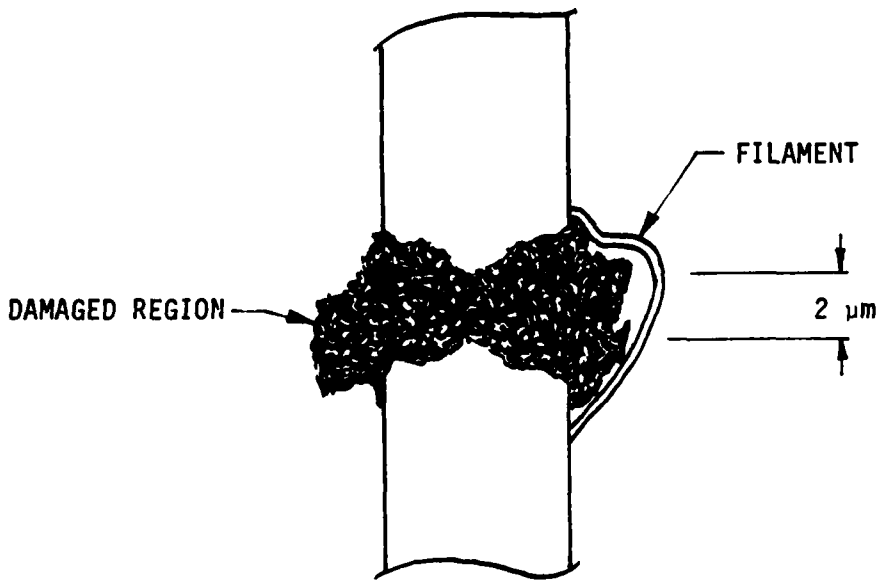

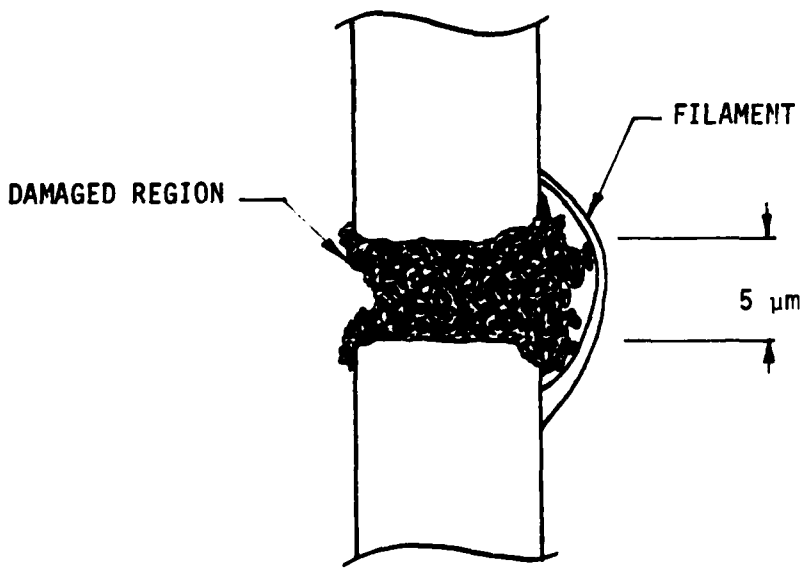

Figure 26. Filaments Avoid Damage Region

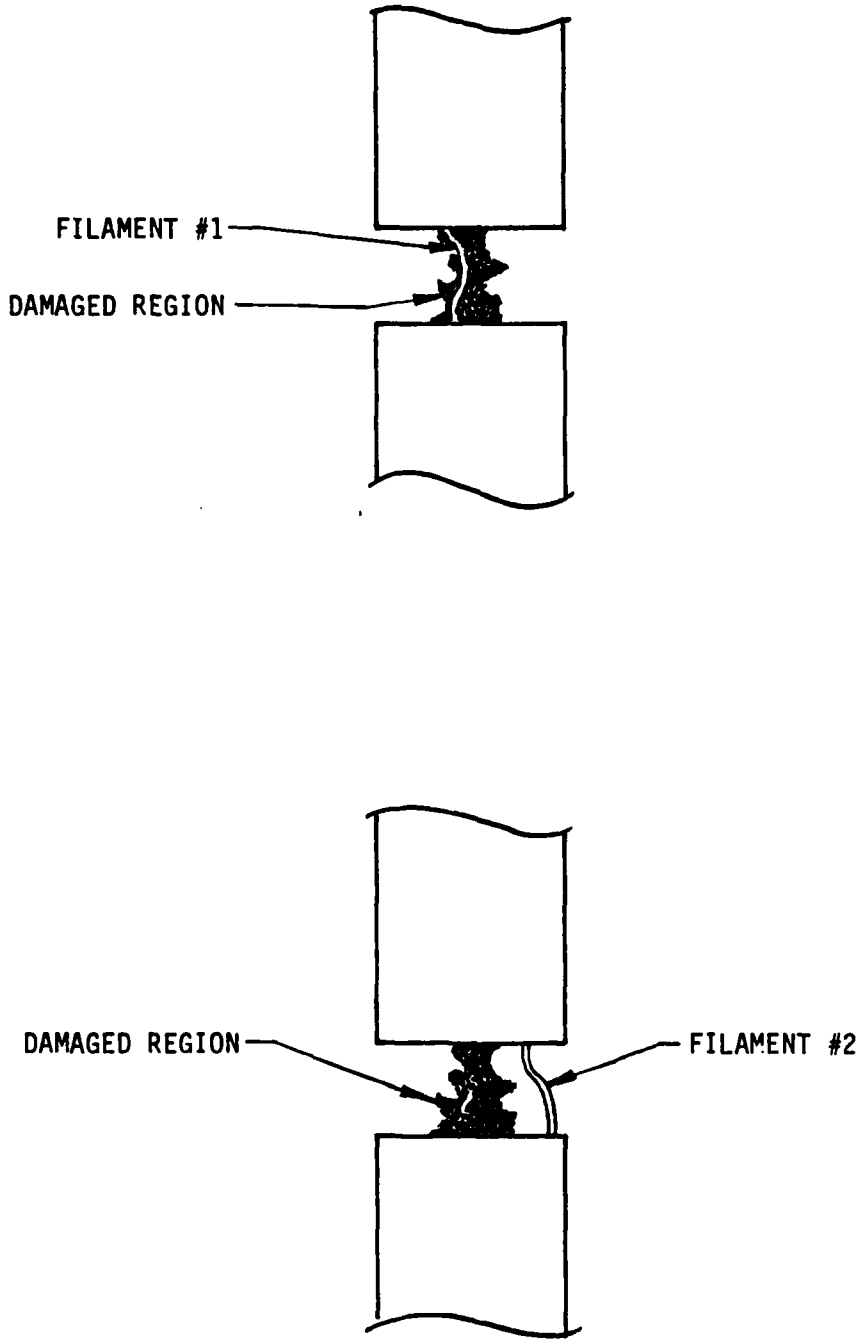

Figure 27. Two Different Filament Locations in Same Gap

·ing the sequences of five led to inadvertently exceeding the minimum voltage ıuired to achieve ignition, resulting in higher than usual current. Another :tor is that the films for this sample were thinner by a factor of two than ›se of earlier samples. Also at issue is the dumping of capacitive energy ›red in the device before switching. Earlier, large gap devices were found to ve a capacitance of about 300 pF. On the assumption that all the energy sorted s converted to heat in the observed filament volume, the temperature rise was nputed to be 200°C. In those devices, no damage occurred; a set of similar asurements for the submicron-scale gaps must still be pursued..

Thus, initial experimentation with thermal filaments in VO_2 has been uitful: much of the data reported in the literature has been reproduced. This boratory, and a start has been made in the exploration of new phenomena, such optical probe response. It is planned to continue investigating the damage enomenon and other behavior of submicron-scale thermal filaments in VO_2 under &D funding.

REFERENCES

- Thin Film Phase Transition Materials Development Program, Annual Report for Period 1981-1982, ATC Report No. R-93000/3CR-6, January 1983.

- Thin Film Phase Transition Materials Development Program, Annual Report for Period 1982-1983, LTV Report No. 3-32000/4CR-3, January 1984.

- "Algebraic Method for Extracting Thin-Film Optical Parameters from Spectrophotometer Measurements," W. E. Case, Appl. Optics 22, (1983).

- "Modifications in the Phase Transition Properties of Pre-Deposited VO_2 Films," F. Cardillo Case, accepted for publication in the December issue of Journal of Vacuum Science and Technology.

- "New Synthesis Method for Optical Thin-Film Coatings, W. E. Case, Appl. Optics 22, 4111 (1983).

- Computer-Aided Techniques for the Design of Multilayer Filters, H. M. Liddell, published by Adam Hilger Ltd, Bristol, pg 82 (1981).

- "Optical and Electrical Parameters of Vanadium Dioxide in a Strong Electric Field," K. A. Valiev, et. al., Sov. Phys. Solid State 13, 242 (1971).

- Infrared Optical Chopper, J. C. Lee, (AFWAL-TR-80-4117).

- E. C. Jelks, R. M. Walser, R. W. Bene, W. H. Neal, II, Appl. Phys. Lett. 26, 355-357 (1975).

APPENDIX B

FINAL REPORT

CORNELL UNIVERSITY
ITHACA, NEW YORK 14850

FACULTY PARTICIPANTS:

R. A. BUHRMAN
A. J. SIEVERS
N. W. ASHCROFT

Introduction

This is the final report of the Cornell Thin Film Phase Transition Group concerning the research which was carried out as part of the Thin Film Phase Transition Materials Development Program, DARPA/ONR Contract N00014-81-C-0560.

This report, as was the research program, is in three parts. There were two experimental components and one theoretical component to program. The projects were: (1) The production and study of VO_2 thin films, (2) Far infrared and Raman studies of VO_2, and (3) Theory of thin film phase transition materials. The final report of each of these projects is presented in turn in the following.

Final Report

1. Preparation and Properties of VO_2 Thin Films

G.A. Nyberg, D. Lathrop and R.A. Buhrman

Cornell University, Ithaca, New York 14853

The basic objective of this research project was to develop a new means to produce improved quality thin films of VO_2 and to investigate the properties of such films.

The technique which was most extensively developed for the production of VO_2 thin films was the reactive evaporation process. This new process consists of electron beam evaporation of vanadium in a controlled, low pressure oxygen gas environment, with the film being deposited onto a high temperature (T > 500 C) substrate. Following extensive development efforts, a sophisticated microprocessor controlled procedure was established which proved capable of producing very high quality VO_2 films. The key to the process was the attainment of very precise control of process parameters. In particular, best results were obtained when substrate temperature was maintained to ± 5°C, oxygen pressure to ± 1% and vanadium evaporation rate to ± 1%. The successful development of this reactive evaporation process constituted a very major portion of our research effort. The description of this process is given in detail in the appendix that follows this report.

Properties of Reactively Evaporated VO_2 Thin Films

Resistivity: The standard measure of the quality of a VO_2 thin film is the amplitude of the resistivity change that is observed when the material goes through the structural phase transition. As indicated in Figure 1, where the

temperature dependent resistivities of two different types of reactively evaporated films are shown along with that of a sample supplied by Vought, the resistivity change is of the order of 10^4 when the films are deposited on oriented sapphire substrates. The largest resistivity change that was observed in this work was 30,000. But perhaps a more important point to notice in Figure 1 is that the high temperature metallic phase of the reactively evaporated VO_2 films has a positive temperature coefficient of resistivity (TCR). A positive TCR is the signature of a true metal, but a positive TCR has seldom if ever been seen before in thin films of VO_2. In our opinion the achievement of a comparably-low metallic state resistivity combined with the positive TCR represents a major improvement in the quality of VO_2 thin films. While the practical implications of this quality enhancement have yet to be established, from a basic science point of view, better material can only lead to a better understanding of the fundamental properties of the VO_2 system.

Optical Properties: Perhaps the most striking result of this research project was the discovery of a new type of VO_2 film, one which, contrary to all reports in the literature, exhibits a visible blue to red color change upon going through the phase transition. To produce this particular type of VO_2 film required very precise deposition conditions: $T_{substrate} = 580 \pm 15°C$, $P_{O_2} = 1.0 \times 10^{-3}$ Torr ± 5%, vanadium deposition rate D = 0.7 Å/sec ± 5%. Deviations from these values would produce VO_2 films with very good resistivity ratios, $\approx 10^4$, but with a dark yellow color which was invariant through the phase transition.

X-ray diffraction studies on the new type of VO_2 film indicate that there is a small amount of suboxide present in this type of film, but the degree of stoichiometry is much higher than that of the ordinary yellow VO_2 films. Oxygen annealing and vacuum reduction experiments have confirmed this hypothe-

sis. By carefully annealing yellow VO_2 film in an oxygen ambient, conversion to the new form was observed. A high temperature vacuum reduction treatment was also found to convert blue/red VO_2 films to the yellow form. Our conclusion is thus that the blue/red film is much closer to stoichiometry than any film previously reported. We must note however that we have not observed any strong correlation between resistivity ratio and optical properties; both yellow and blue/red films were found to have resistivity ratios of the order of 10^4.

To quantify the optical properties of the various types of reactively evaporated VO_2 films, we have made transmission and reflectance spectrophotometer measurements in the visible and infrared spectral region. From such measurements we have extracted the optical absorption coefficient for the various films. Figure 2 shows the absorption coefficient VO_2 films measured by Verleur et al.(1) in the metallic and semiconductor state. The behavior shown in Figure 1 is quite similar to that reported by Verleur et al.(1) for bulk crystals also. In Figure 3 we show the absorption coefficient α for a reactively evaporated, yellow VO_2 film deposited on a quartz substrate. The behavior is quite similar to that seen in Figure 1. with α in the semiconductor state exhibiting a gradual absorption edge in the 0.7 eV region and a second increase at $E \approx 2$ eV. Also note that for $E < 2$ eV $\alpha_{metal} > \alpha_{semi}$.

In Figure 4 we show α for a film which is intermediate in character between the yellow and blue/red type. This film is dark yellow in the semiconductor state but turns reddish upon going into the metallic phase. Notice that here the semiconductor absorption edge at 0.6 eV is much sharper than in Figures 1 or 2 and that the second increase in α at 2.0 eV is less strong. Also note that α metal now dips below α_{semi} in the 1.5 eV region which accounts for the color change.

In Figure 5 we show α for a dark blue/red film. Here the semiconductor absorption edge has been shifted slightly to lower energies and the second edge at 2.0 eV is no longer apparent. Moreover, α_{metal} strongly drops below α_{semi} in the 1-2 eV region accounting for the pronounced color change that we observe. Clearly these various types of films are very different in optical character.

These differences are further illustrated by examining the reflectance of the various types of VO_2 films. Figure 6 shows the reflectance of a 3000 Å film which was calculated from the optical constants of VO_2 films as determined by Verleur et al.[1]. Figure 7 shows the reflectance of a dark yellow/red film and Figure 8 shows the data for a blue/red film. Concentrating on the metallic state we see that both Verleur's results (which correspond to our results for low temperature deposition onto quartz) and our dark yellow/red data have essentially the same limiting reflectivity in the IR. But the yellow/red film has a lower energy reflectance edge which can be considered as a reduction of the plasma frequency of the metal from 3.3 eV (for Verleur) to 2.4 eV (for our dark yellow/red films). Going to the blue/red film we see a very significant decrease in IR reflectivity, from 85% to 65%, while the plasma frequency appears to remain at ≈ 2.4 eV. Thus for an infrared switchable mirror application the less stoichiometric yellow VO_2 film apears to be the better choice. Unfortunately we as yet have no satisfactory explanation for these very intriguing results.

Photoemission Study: In an effort to further characterize these materials we initiated an X-ray photo-emission spectroscopy study. Unfortunately, we were able only to obtain preliminary results in the time available for this study but Figures 8 and 9 illustrate that such measurements could prove very useful in quantifying these materials. Figure 8 shows a high resolution XPS spectrum

of a dark yellow VO_2 film while Figure 9 gives the spectrum for a blue/red film. The shift in the horizontal axis between the two spectra are due to differences in substrate charging during the measurements and are not significant. What is significant is the clear difference in the O_{1S} lineshape. Clearly the oxygen configuration is significantly different in the two films. In our opinion an extensive XPS study of reactively evaporated VO_2 films would be extremely useful in getting a better understanding of these materials. We hope to pursue such an investigation with other funding.

Summary

This project has resulted in the successful development of a new reactive evaporation process for producing very high quality VO_2 films. This process is readily extendable into a high throughput mode, although we have not attempted to demonstrate this aspect of the project. Reactive evaporation is a very flexible process suitable for producing materials for detailed study of the phase transition. The process is also particularly amenable for experiments involving the production of VO_2 films alloyed with other transition elements in an attempt to shift and modify the phase transformation.

In the course of the project a new form of VO_2 film was discovered with strikingly different optical properties. As indicated in this report, these properties have been characterized but not explained. Further work in this area is clearly appropriate.

Reference

1. Verleur, Barker and Berglund, Phys. Rev. 172, 788 (1968).

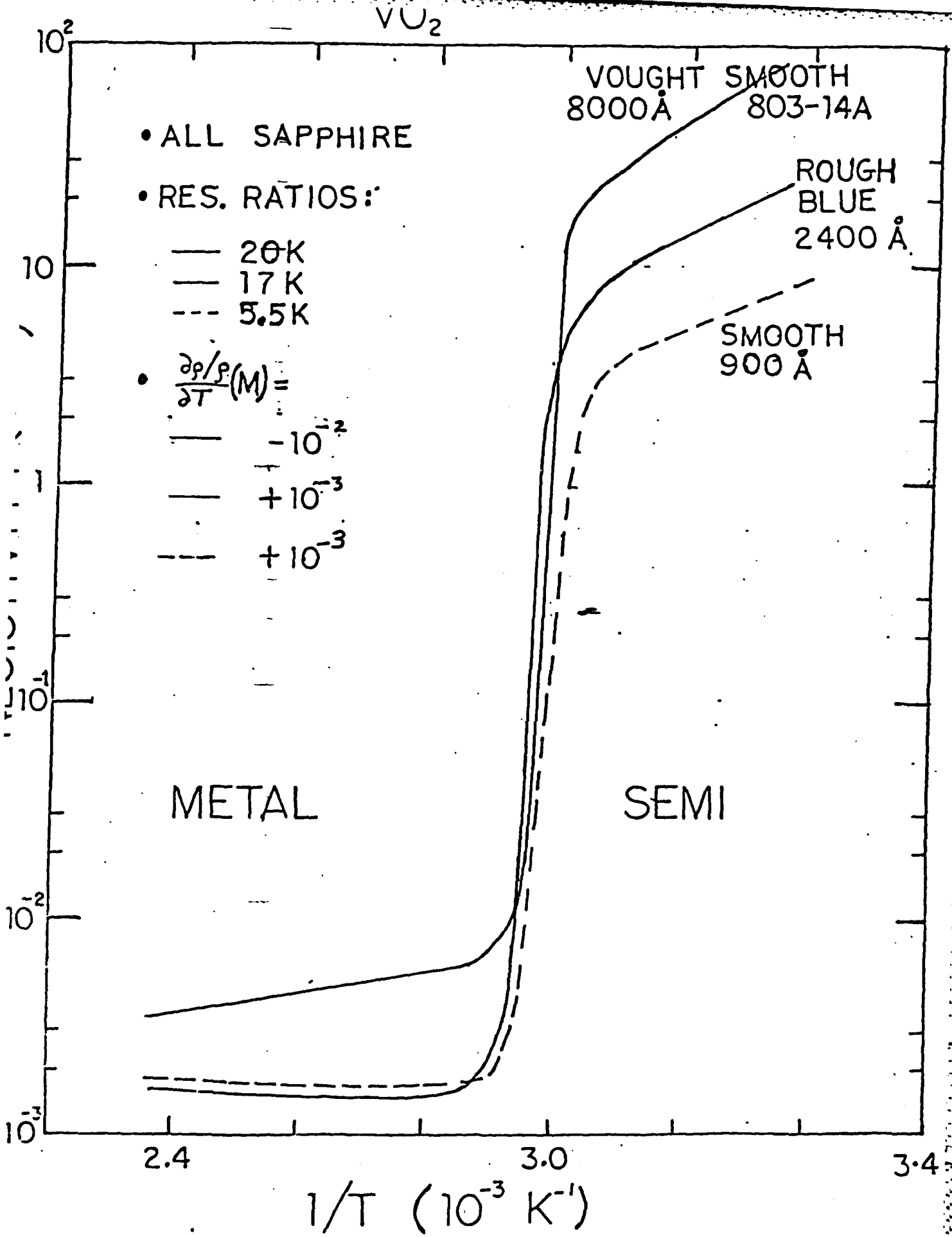

Figure 1. Temperature dependent resistivity of two reactively evaporated VO_2 films and one VO_2 film supplied by Vought. All films are on sapphire substrate.

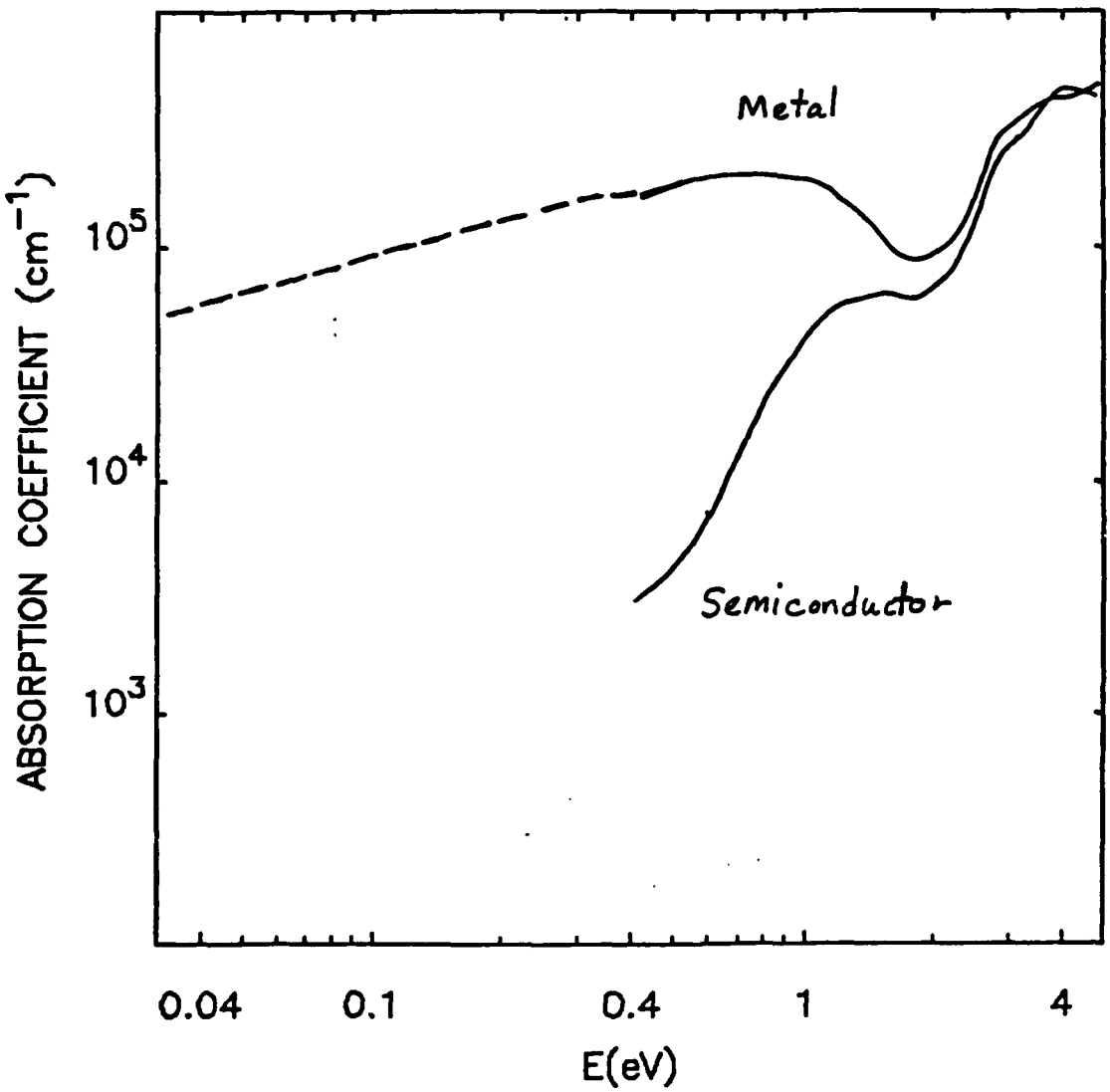

Figure 2. Absorption coefficient for VO_2 thin film, as measured by Verleur et al.[1].

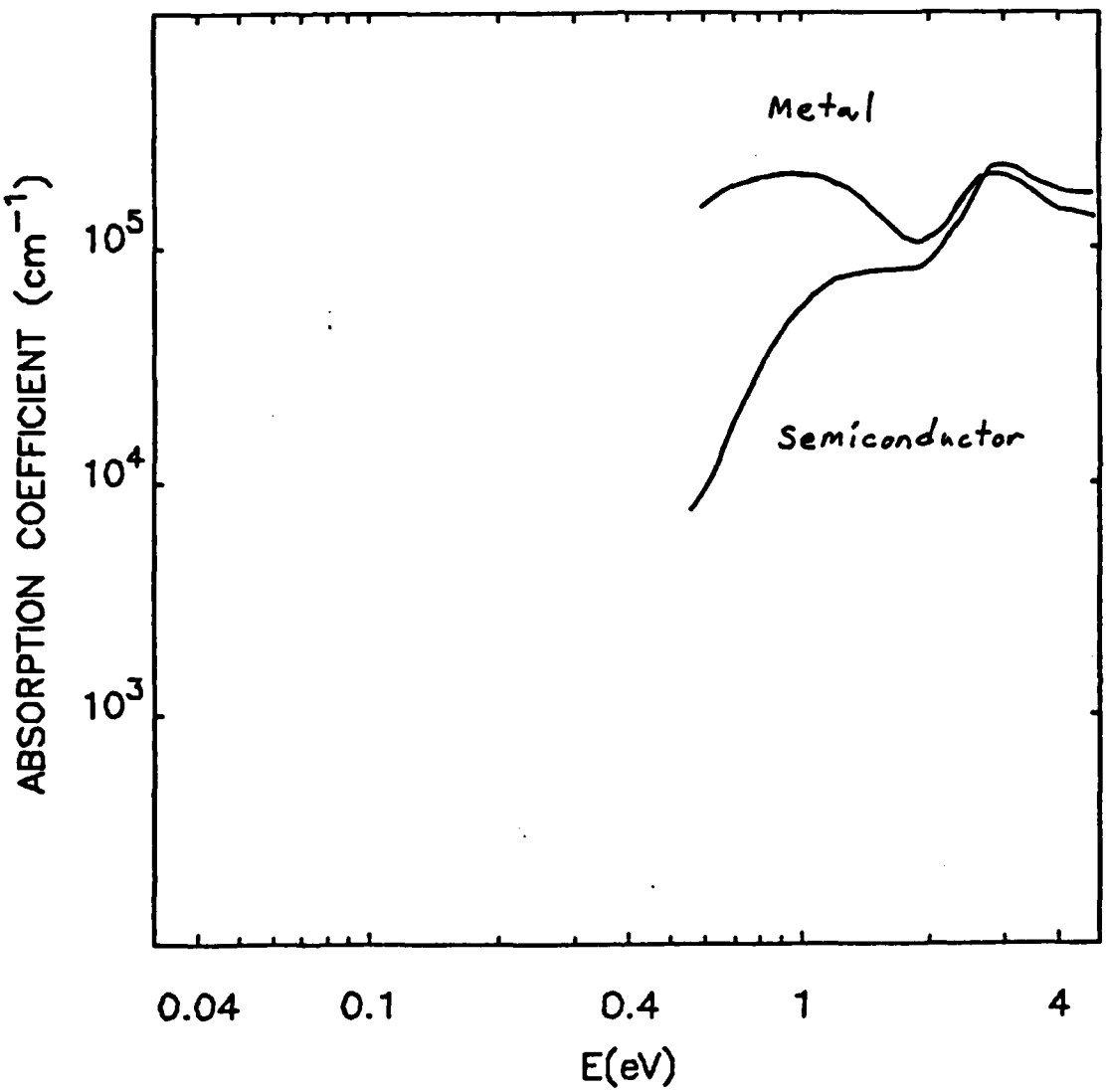

Figure 3. Absorption coefficient for reactively evaporated (yellow) VO_2 on fused quartz substrate.

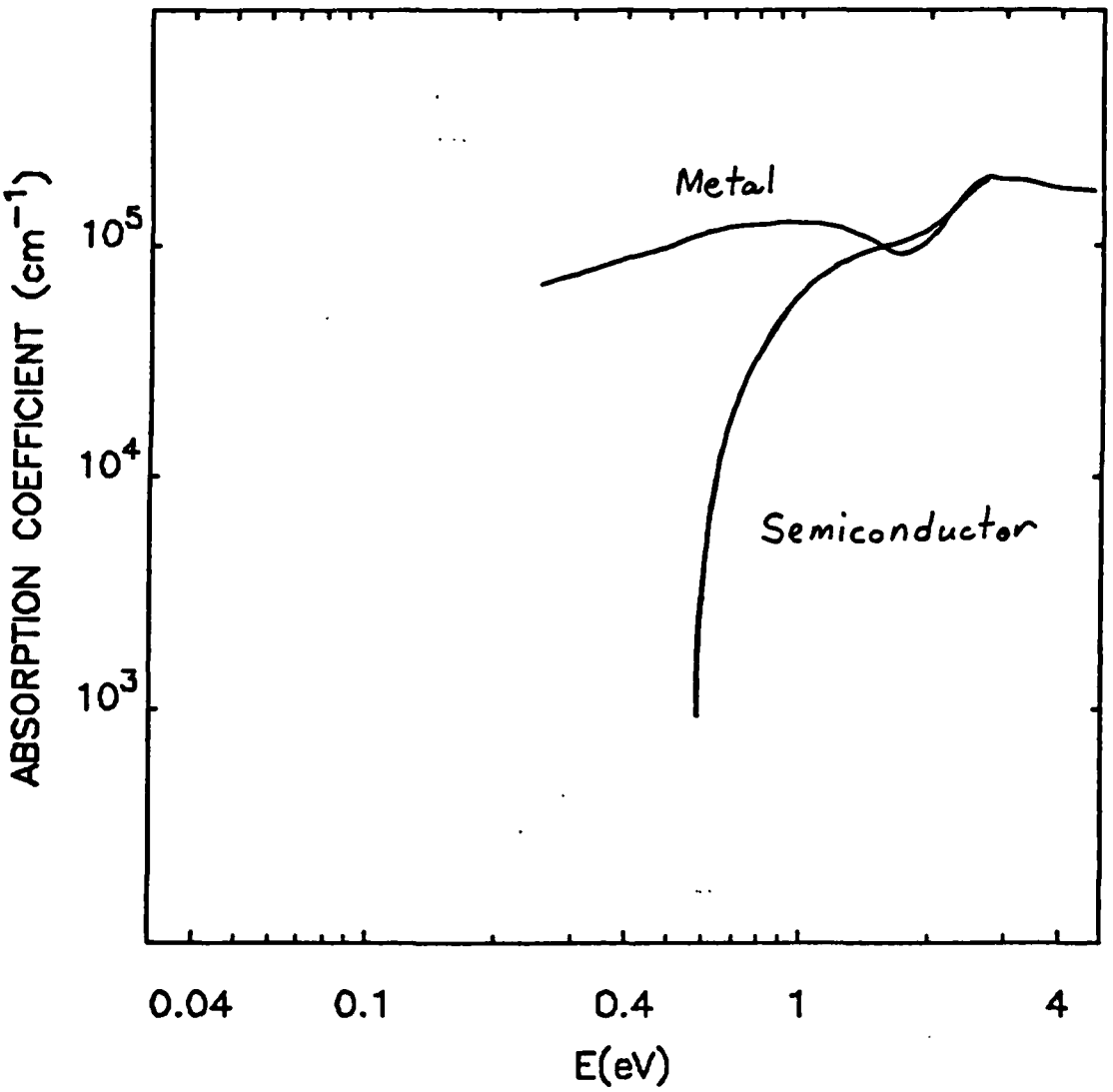

Figure 4. Absorption coefficient, α, for a 3000 Å thick reactively evaporated dark yellow/red film.

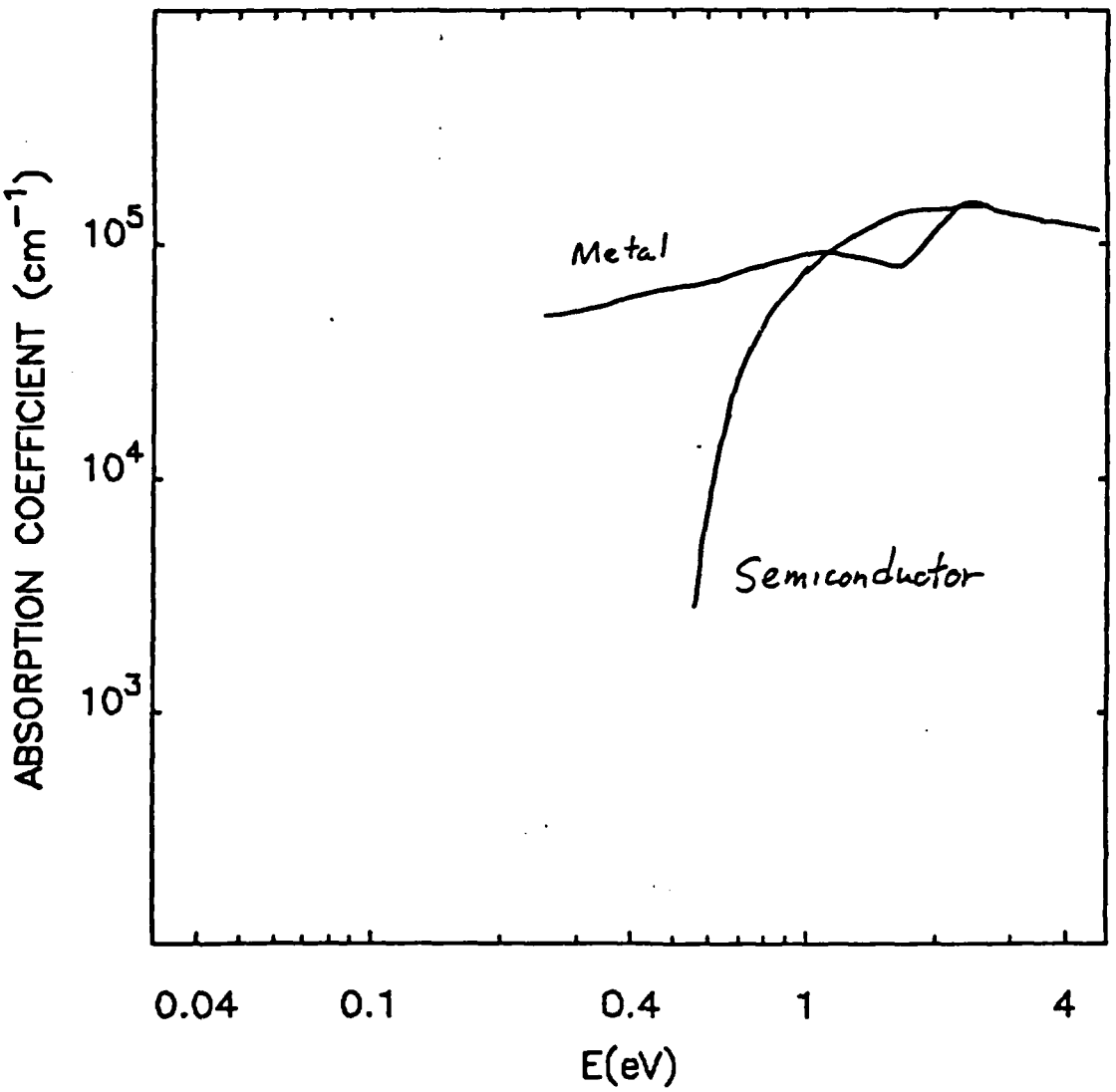

Figure 5. Absorption coefficient, α, for a 2700 Å thick reactively evaporated blue-semiconductor/red-metal film.

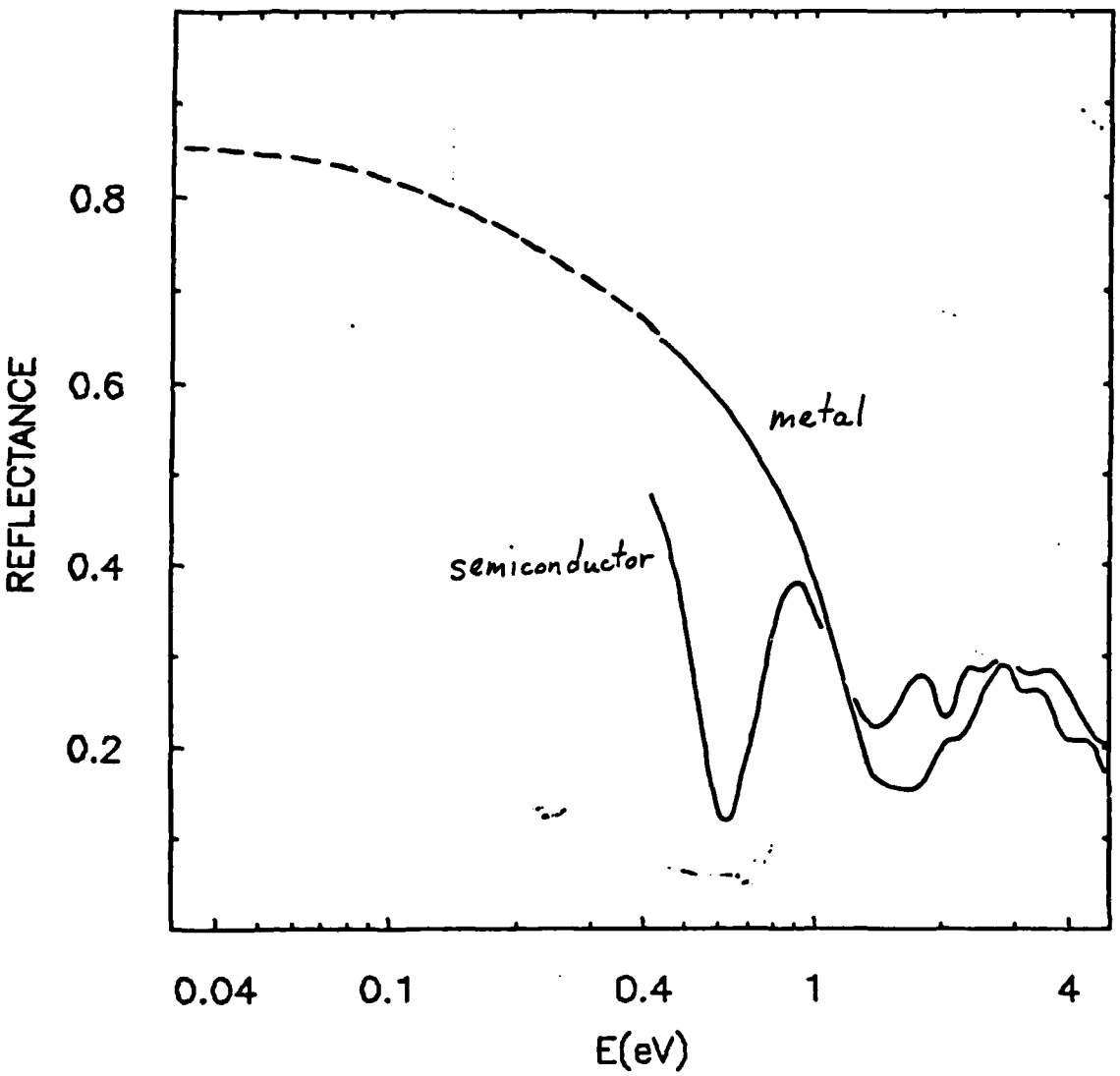

Figure 6. Reflectance data for a 3000 Å thick dark yellow/dark yellow film based on Verleur et al.

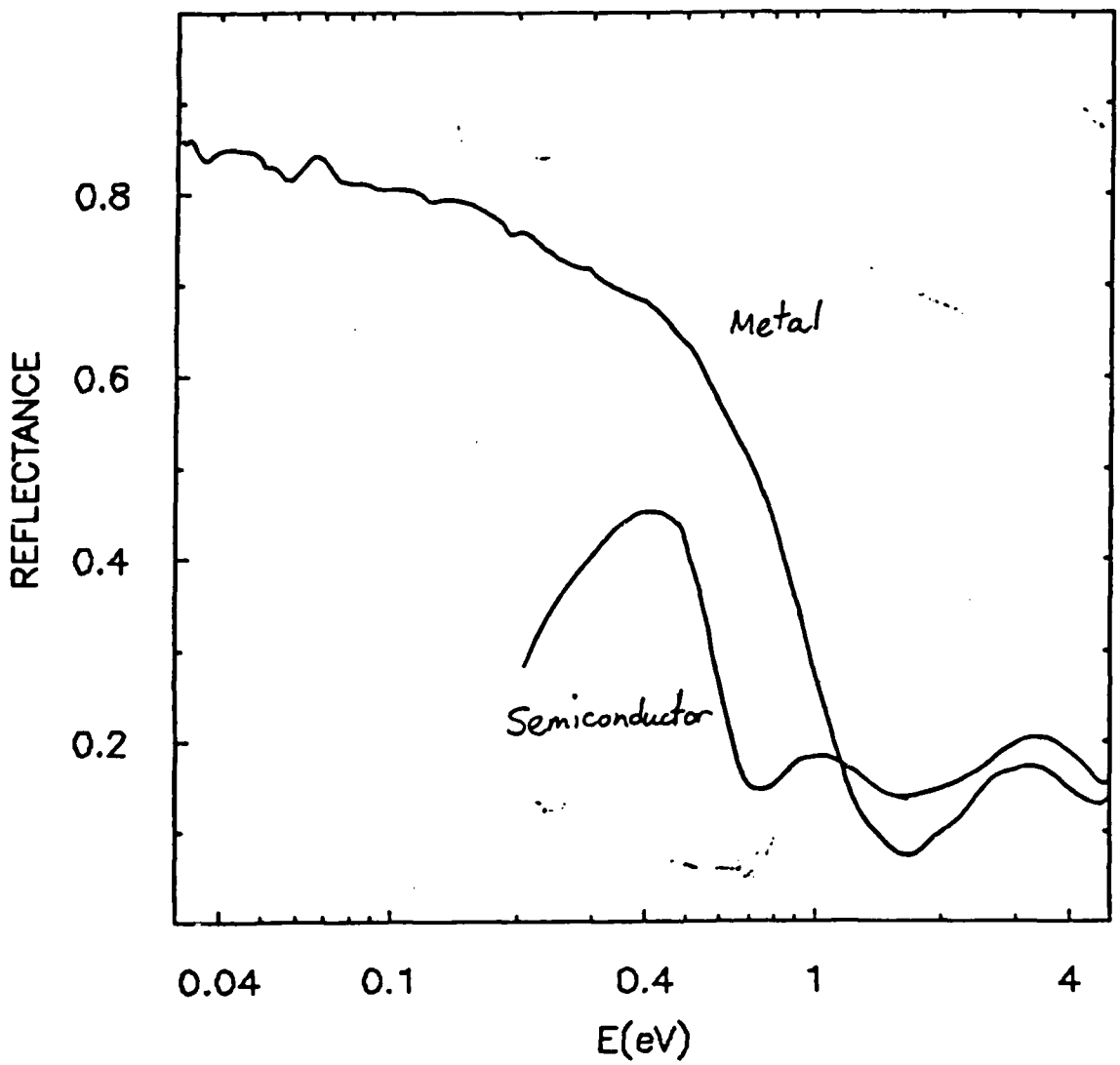

Figure 7. Reflectance data for a 3000 Å thick reactively evaporated dark yellow/red film.

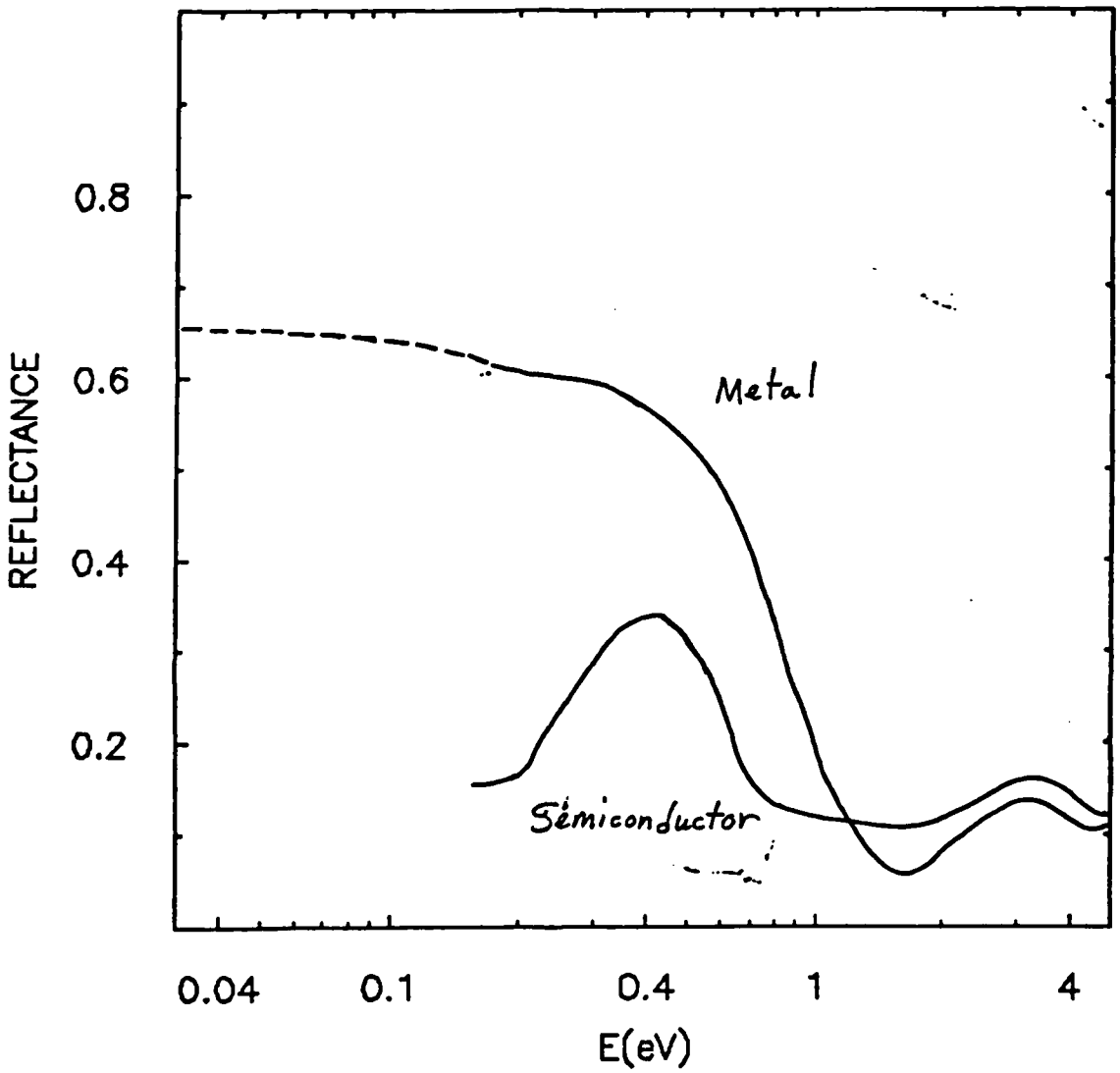

Figure 8. Reflectance data for a 2700 Å thick reactively evaporated blue-semiconductor/red-metal film.

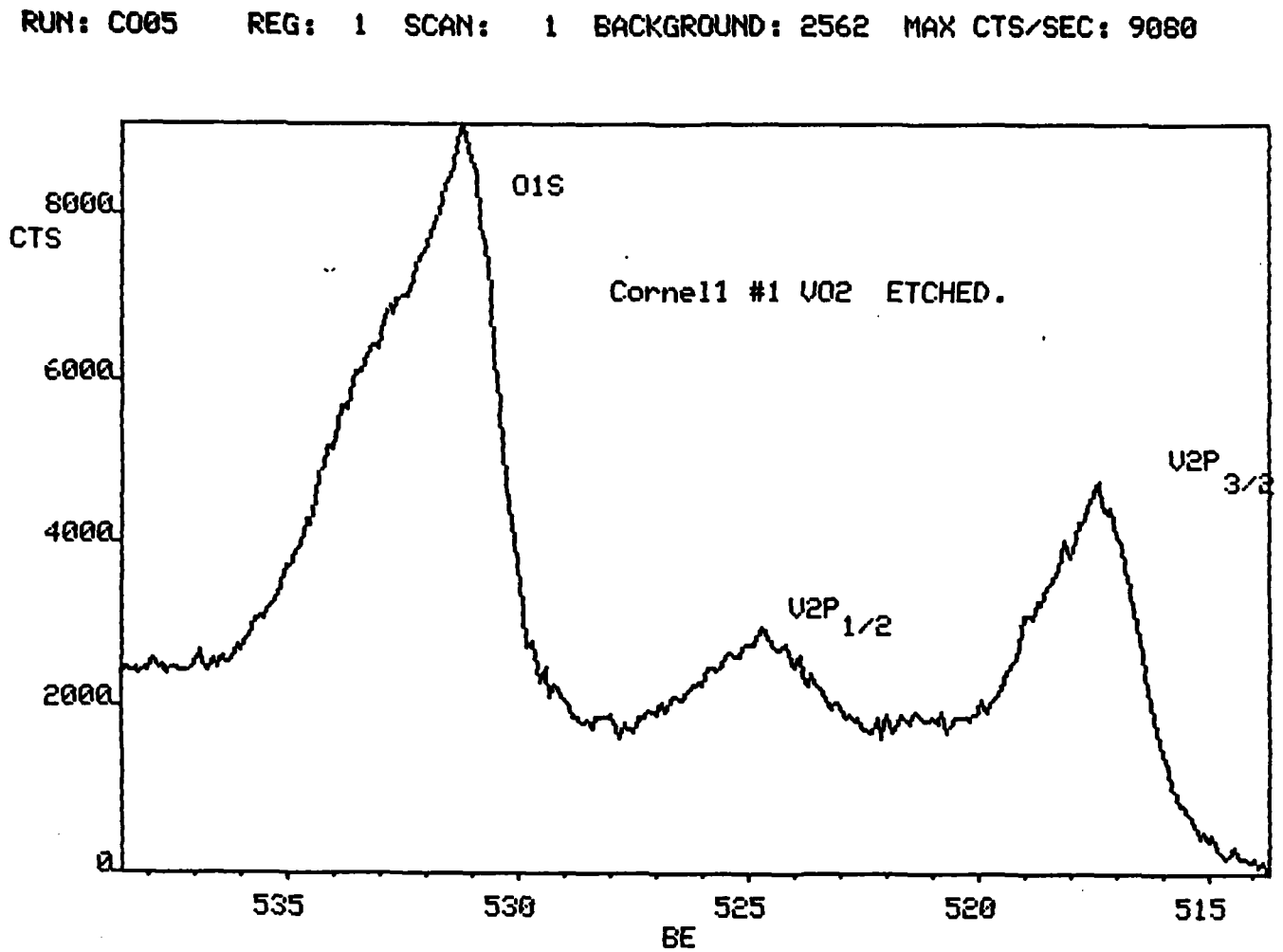

Figure 9. XPS spectrum of a dark yellow VO_2 film produced by reactive evaporation onto sapphire.

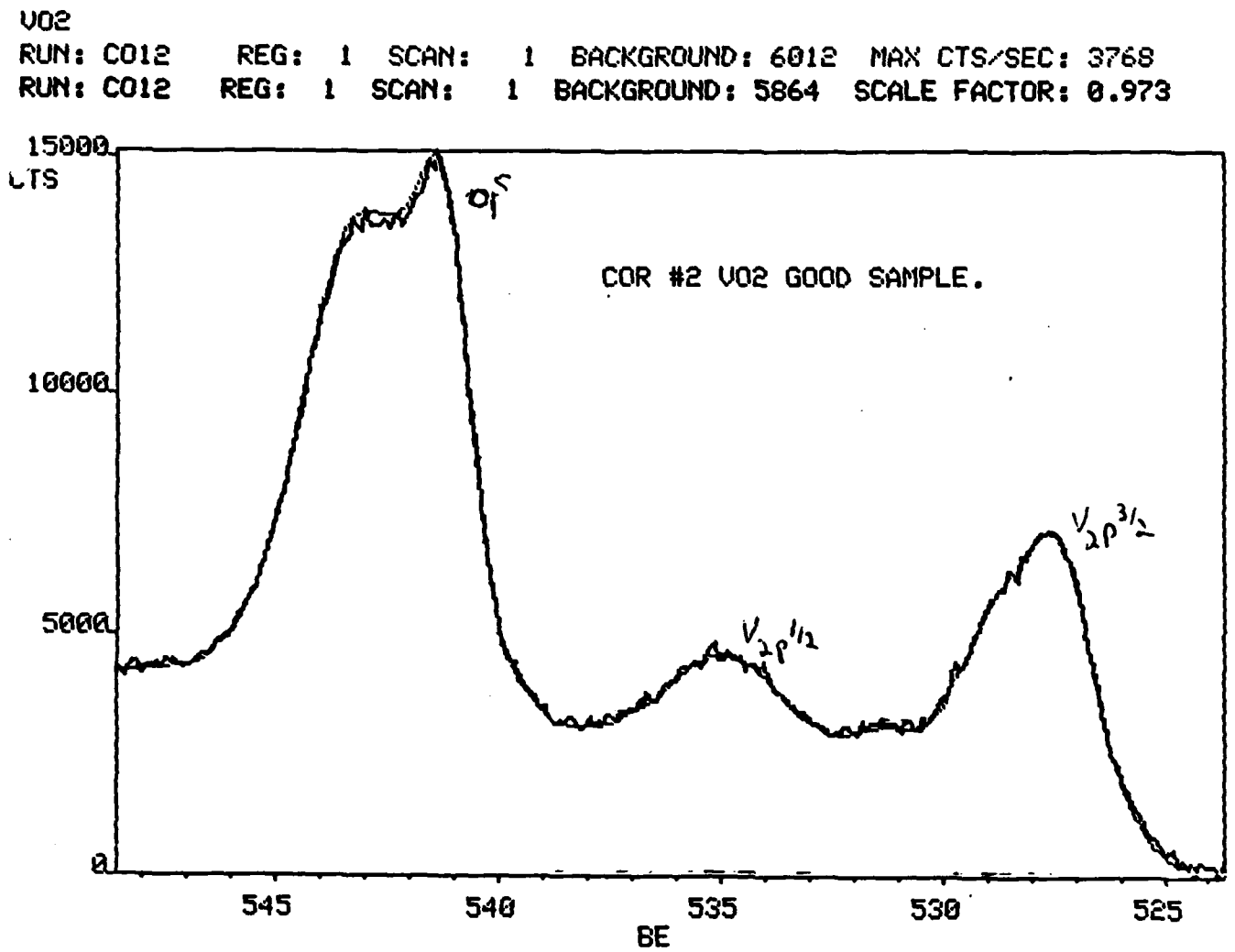

Figure 10. XPS spectrum of a dark blue/red VO_2 film. Note the difference in the O_{1S} lineshape when compared to that shown in Figure 9.

FINAL REPORT

2. Far Infrared Absorption and Raman Scattering Properties of VO_2 Films on Dielectric Substrates

R. C. Spitzer and A. J. Sievers

INTRODUCTION

A measurement of the millimeter and far infrared spectral properties of a semiconductor can provide a great deal of information about both the dynamics and statics of the material. The signature of a low concentration of free carriers in the solid is a plasma resonance in the millimeter wave spectral region. Bound donors and acceptor levels appear as sharp spectral lines which have temperature dependent absorption strengths at low temperatures. Finally the infrared active optical phonon modes can be identified by their temperature independent behavior. From the number, position and widths of these modes one can say a great deal about the crystal symmetry, strain and disorder in the solid. Because all of this information should be especially useful in analyzing the properties of thin semiconducting VO_2 films grown on dielectric substrates, we have concentrated our efforts collecting and analyzing such data.

Millimeter and Far Infrared Spectral Properties

Our first room temperature measurements of VO_2 films on GE substrates did show a large absorption in the mm wave region. A similar frequency dependent absorption was observed for the Ge substrate without the VO_2 film. No low frequency absorption has been observed for a VO_2 film on an Al_2O_3 substrate. Since this millimeter wave absorption is quenched by cooling the Ge samples to helium temperatures, we have identified its source to be thermally activated free carriers in the substrate.

Fir spectra for all the Ge samples were obtained with TE and TM polarized light at a temperature of 1.2°K. Comparison of the VO_2-Ge with the bare Ge spectra has enabled us to identify various features. The absorption lines in the 42-90 cm^{-1} region are produced by electronic impurity transitions in the Ge substrate. Two-phonon absorption bands in Ge which occur in the 225 to 350 cm^{-1} region obscure some VO_2 phonon modes in the thin film VO_2-Ge samples. A sharp absorption line at 190 cm^{-1} is observed for thin VO_2 films on Ge but not for the substrate itself. Because this line also appears in the thin film VO_2-sapphire arrangement discussed below, it is probable that the absorption is associated with the VO_2 film. We used a strong magnetic field to show that line arises from lattice vibrational modes.

The VO_2 film on a sapphire substrate exhibits modes which depend on the light's polarization relative to the plane of the film. Although the same modes are always present, their strengths depend on whether the light is TE or TM polarized, indicating that the film assumes a definite crystallographic orientation with respect to the substrate. The observed phonon frequencies agree well with previously published results for bulk samples.

A high temperature investigation of VO_2 far infrared properties also was made. The semiconductor-metal transition at 68°C involves a crystal change to the rutile structure, which decreases the number of allowed infrared phonon modes in the high temperature phase. Unfortunately, sapphire is opaque in the frequency region of interest at room temperature. Ge is somewhat transparent to far infrared radiation in this region, in spite of its two-phonon bands.

We observe that the semiconductor-metal transition for VO_2-Ge causes an overall transmission drop by at least a factor of 10. A frequency dependence characteristic of free carrier absorption appears in the spectra and the VO_2 lattice modes in the 310-325 cm^{-1} region vanish.

Our first major find was that the phonon mode frequencies and line strengths measured for VO_2 films on Ge and Al_2O_3 substrates depend on sample substrate and thin film production techniques. For small grain films the electromagnetic wave excites phonon sphere modes which are blue shifted from the bulk mode frequencies, while for larger grain sizes the bulk modes can be observed in the thin film geometry.

We also have studies VO_2 films prepared on Si substrates. The reason for switching to Si substrates is twofold: 1) the substrate is now transparent over the entire infrared region where VO_2 phonons occur; and 2) the substrate is transparent in the mm wave region even at temperatures above the VO_2 transition.

To make these measurements, we had to construct a new interferometer mirror drive mechanism which makes the instrument useable up to a frequency of 1500 cm^{-1}, a frequency much larger than the largest VO_2 phonon frequency. The drive makes use of a new position gauge which just became available. These gauges use optically-produced, fine-scale gratings to

provide the accuracy of an optical positioning system. By coupling such a gauge to a translation stage driven by a d.c. motor and screw, the position errors due to the screw can be eliminated. Position errors no larger than a few tenths of a micron can be maintained over the whole travel range of several cm's.

The mirror positioning system is a precision ball-bearing sliding stage driven by a Newport Actuator and coupled to a Heidenhain Corp. MT series length gauge. Homebuilt electronics combines commands from the computer with motion information from the gauge to determine the driving voltage on the actuator motor and thus set the mirror position.

VO_2 films on Si substrates have been prepared both at Vought and at Cornell. IR spectra of cooled samples showed Si donor levels in the VO_2 phonon region. By making the IR comparision between samples at room temperature these donor levels are thermally ionized and no longer contribute in the spectral region. The two samples which were prepared using different thin film production techniques show different mode strengths.

When the sample temperature is raised above the VO_2 transition region, then the relatively sharp phonon modes observed in the low temperature phase are replaced by very diffuse phonon modes in the high temperature phase. In addition, the sample transmission decreases from 50% to about 2 1/2% in this spectral region.

In the submillimeter wave region a complex absorption spectrum has been measured for all VO_2 films. The frequency positions and strengths of the measured features are observed to depend on the film substrate and on the film production technique. Magnetic field and temperature dependence studies have been used to identify both substrate electronic impurity spectra and VO_2 phonon lines. Since the VO_2 phonon lines are very sensi-

tive to thin film morphology, this spectral finger print may prove to be a simple thin film characterization parameter.

IR ACTIVE PHONONS IN VO_2 FILMS

The IR active phonon modes of bulk VO_2 single crystals were first measured[1] in 1966. Group theory applied to the monoclinic phase of VO_2 shows that in the long wavelength limit there are eight infrared active modes for the electric field parallel to the b axis and seven infrared active modes for E directed in the a-c plane. Barker[1] found that distinct spectra were obtained only for E parallel or perpendicular to the a axis. He concluded that this simplification occurred because the crystal had formed a fine grained domain structure in this monoclinic semiconducting phase. He was able to fit the IR reflectivity data with eight phonon modes.

Our low temperature submillimeter wave spectra for VO_2 on Ge did not agree with Barker's mode frequencies, or line strengths. However, similar measurements for VO_2 on Al_2O_3 substrates produced much better agreement with the bulk results. Two of these spectra are shown in Figure 1. The bulk mode frequencies are labeled by $E\perp$ or $E\parallel$ indicating the mode for the E field $\perp$ or $\parallel$ to the a crystal axis. The s identifies the three strong bulk modes.

Because the IR radiation is polarized there are two possible ways of probing the film. Fig. 1(a) shows the spectrum when the electric field is in the plane of the film (TE polarization and Fig. 1(b), the spectrum when the electric field out of the plane of the film (TM polarization). For the Al_2O_3 substrate the two polarizations produce distinct spectra while for the Ge and Si substrates the two polarizations give the same results.

Raman Scattering Properties

Far infrared transmission measurements of VO_2 films on S_i substrates prepared both at Vought and at Cornell show that when the sample temperature is raised above the metal insulator transition region, then the relatively sharp phonon modes observed in the low temperature phase are replaced by very diffuse phonon modes in the high temperature phase. In addition the sample transmission decreases from 50% to about 2 1/2% in this spectral region.

One possible mechanism for this extreme broadening of the infrared active modes near the phase transition is mode softening. It is known that infrared active phonons become extremely anharmonic and go to zero frequency as the temperature of a displacive ferroelectric transition is approached from the paraelectric phase. The Raman active modes remain essentially undisturbed when the IR active modes become unstable at T_c. With this idea in mind we have made Raman scattering measurements of the films in the two different phases.

In the high temperature metallic rutile phase four Raman active phonon modes are to be expected while in the semiconducting monoclinic phase eighteen Raman active phonons are allowed. Since the samples are opaque in the visible region the measurements were done with a backscattering geometry which is shown in Fig. 2. The source was a Coherent Radiation 4 Watt argon ion laser. The flux was monitored with a flux integrator and the counting period was adjusted automatically to maintain a constant flux-time product. The light was focused onto the sample with a combination of a bi-convex spherical lens and a plano-convex cylindrical lens to produce a line image about 2 mm high on the sample. The light backscattered by the sample was collected by an f/1.3 plano-convex lens and image onto the

spectrometer entrance slit with an f/6 bi-convex lens. The collected light was sent through a quartz wedge to scramble its polarization.

In the semiconducting phase all VO_2 film substrate combinations showed essentially identical Raman spectra. Typical data are shown in Figures 3 and 4. Eight phonon modes were observed in the 200 to 700 cm^{-1} and the frequencies and intensities are recorded in Table I and II, respectively. This result is very different from that obtained from infrared measurements where it was observed that the mode positions and strengths depend on thin film morphology. We conclude that the Raman active mode frequencies are independent of production techniques but that the mode intensities are not. The reason that the two kinds of modes behave differently is that the IR active mode properties depend on the local shape depolarization field whereas the Raman mode properties do not.

When the samples are heated up to the metallic phase, the sharp mode structure disappears and is replaced by a single broad resonance at 500 cm^{-1} which persists even to temperatures as large as 300°C. The data are shown in Figures 5 and 6. The corresponding broad resonance in the IR spectrum occurs at 300 cm^{-1}. A comparison of the two types of measurements can be made in Figure 7. The fact that both IR and Raman active modes are broad and remain broad far above the transition temperature indicates that the anomalous width has nothing to do with the transition itself.

Conclusions

1) The far infrared absorption maxima for thin films do not correspond to the measured absorption maxima for bulk VO_2 samples.

2) The far infrared absorption spectra depend on the substrate material.

3) The measured phonon mode frequencies for VO_2 on Al_2O_3 correspond more closely to the bulk VO_2 frequencies than do the modes for VO_2 on Ge and Si.

4) Only one broad IR active mode is observed in the high temperature metallic phase.

5) Since the mode frequencies measured for different film-substrate combinations correspond to different film morphologies the IR technique could be used as a monitor.

6) The IR active mode frequencies depend on surface dipole depolarization fields and hence are sensitive to surface structure; whereas, the Raman active mode frequencies do not depend on the surface dipole field hence they do not provide information about surface morphology.

7) Our measurements demonstrate that the Raman scattering intensities do depend on surface structure hence this probe can also be used as a simple production control monitor.

8) Because the Raman scattering technique does not make use of a large sample area and does not probe the substrate, we conclude that this method is to be preferred for thin film VO_2 work.

9) The broad IR and Raman active bands observed for VO_2 above the metal-semiconductor transition are quite unusual. The behavior has been observed for bulk VO_2 as well but not for V_2O_3 above its transition temperature. The mechanism behind this broadening remains a mystery.

REFERENCES

1. A. S. Barker, H. W. Verleur and H. J. Guggenheim, Phys. Rev. Letters 17, 1286 (1966).

2. R. Ruppin and R. Englman, Rep. Prog. Phys. 33, 149 (1970).

FIGURE CAPTIONS

Figure 1. Far infrared spectra of a VO_2 film on an Al_2O_3 substrate. The phonon modes for bulk VO_2 are labeled by $E\perp$ and $E\parallel$ depending on whether the applied electric field is $\perp$ or $\parallel$ to the monoclinic a axis. The strong modes are identified by the letter s. (a) The spectrum for transverse electric polarization (TE). (b) The spectrum for transverse magnetic polarization (TM). The phonon modes in the Al_2O_3 substrate cut off the transmittance for frequencies greater than 375 cm^{-1}.

Figure 2. Raman backscattering geometry for observing phonon modes in VO_2 films.

Figure 3. Raman scattering intensity versus frequency for VO_2 films on Ge and Si substrates. The measurements are made at room temperature. The mode frequencies are the same for the two films.

Figure 4. Raman scattering intensity versus frequency for VO_2 films on Ge and sapphire substrates. The measurements are made at room temperature. Again the mode frequencies are the same for the two films.

Figure 5. Temperature dependence of Raman scattering near the metal-semiconductor transition temperature of VO_2. The substrate is Ge and Si respectively.

Figure 6: Temperature dependence of Raman scattering near the metal-semiconductor transition temperature of VO_2. The substrate is Ge and sapphire.

Figure 7. Comparison of the infrared and Raman spectrum for a VO_2 film on Si in the high temperature phase. Both modes are extremely broad.

TABLE I

MEASURED FREQUENCIES OF RAMAN ACTIVE MODES

IN BULK AND THIN FILM VO_2

Bulk cm^{-1})	Ge-VO_2 Vought (cm^{-1})	Si-VO_2 Vought (cm^{-1})	Sapp-VO_2 Cornell (cm^{-1})
142	142	142	140
191	194	194	194
222	225	225	224
259	261	261	260
308	310	310	309
335	338	338	336
389	390	390	390
436	442	443	-
497	500	500	498
611	613	613	612

Table II

RELATIVE INTENSITIES OF RAMAN ACTIVE MODES FOR DIFFERENT VO_2 THIN FILM MORPHOLOGIES

MODE FREQUENCY (cm^{-1})	Ge-VO_2 Vought	Si-VO_2 Vought	Sapp.-VO_2 Cornell
142	0.23	0.26	0.15
191	1	1	1
222	0.55	0.61	0.26
259	0.11	0.08	0.02
308	0.18	0.17	0.42
335	0.05	0.07	0.03
389	0.28	0.27	0.31
436	0.05	0.05	-
497	0.11	0.09	0.09
611	0.83	0.81	0.67

(a)

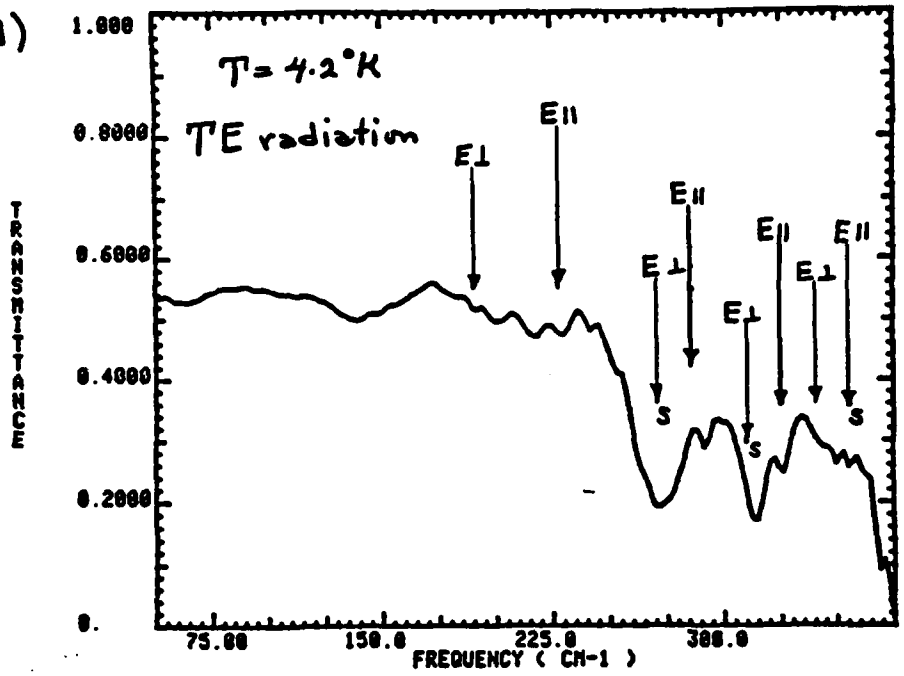
T= 4.2°K
TE radiation
E⊥
E∥
E∥
E⊥
E⊥
E∥
E⊥
E∥
S
S
S
TRANSMITTANCE
1.000
0.8000
0.6000
0.4000
0.2000
0.
75.00
150.0
225.0
300.0
FREQUENCY (CM-1)

(b)

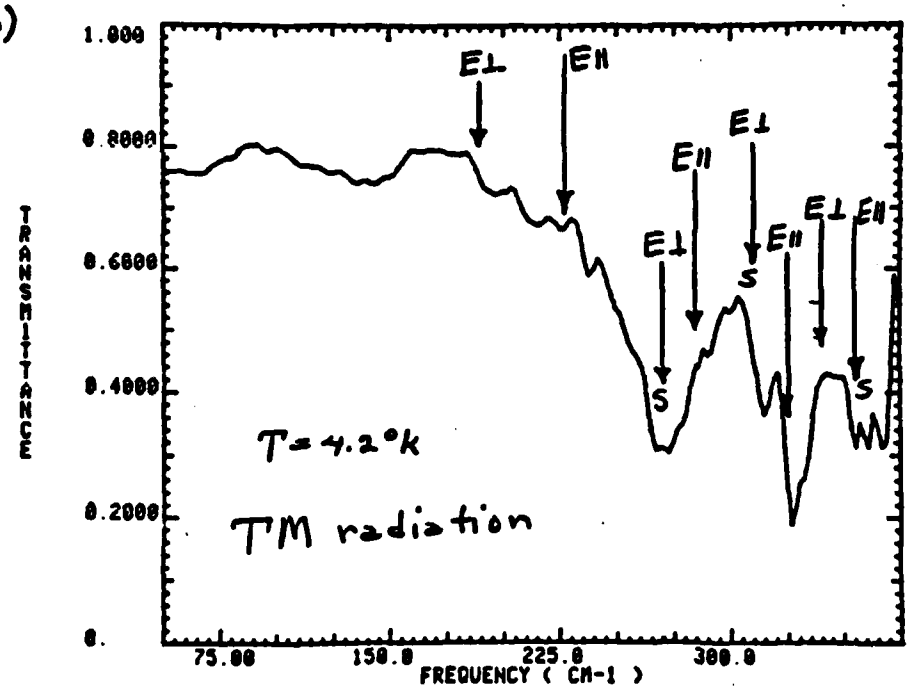
E⊥
E∥
E⊥
E∥
E⊥
E∥
E⊥
E∥
S
S
S
T= 4.2°k
TM radiation
TRANSMITTANCE
1.000
0.8000
0.6000
0.4000
0.2000
0.
75.00
150.0
225.0
300.0
FREQUENCY (CM-1)

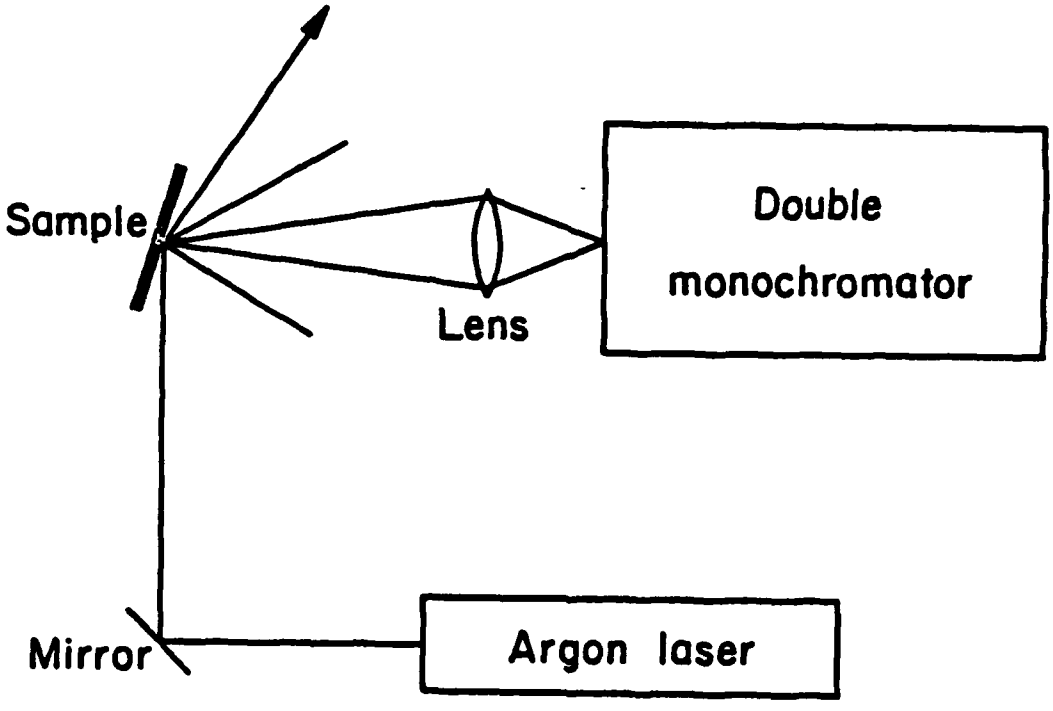
Sample
Lens
Double
monochromator
Mirror
Argon laser

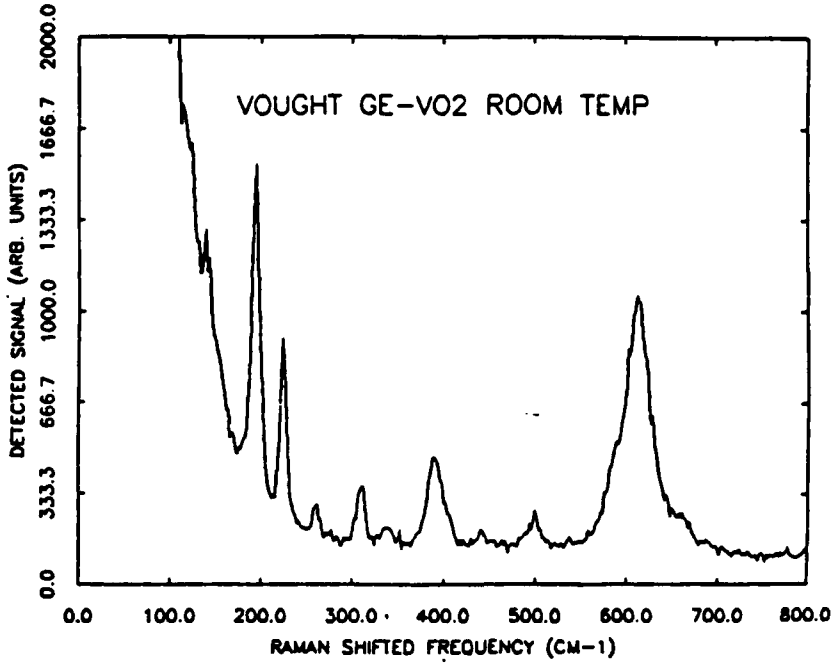
VOUGHT GE-VO2 ROOM TEMP
DETECTED SIGNAL (ARB. UNITS)
0.0
333.3
666.7
1000.0
1333.3
1666.7
2000.0
0.0
100.0
200.0
300.0
400.0
500.0
600.0
700.0
800.0
RAMAN SHIFTED FREQUENCY (CM-1)

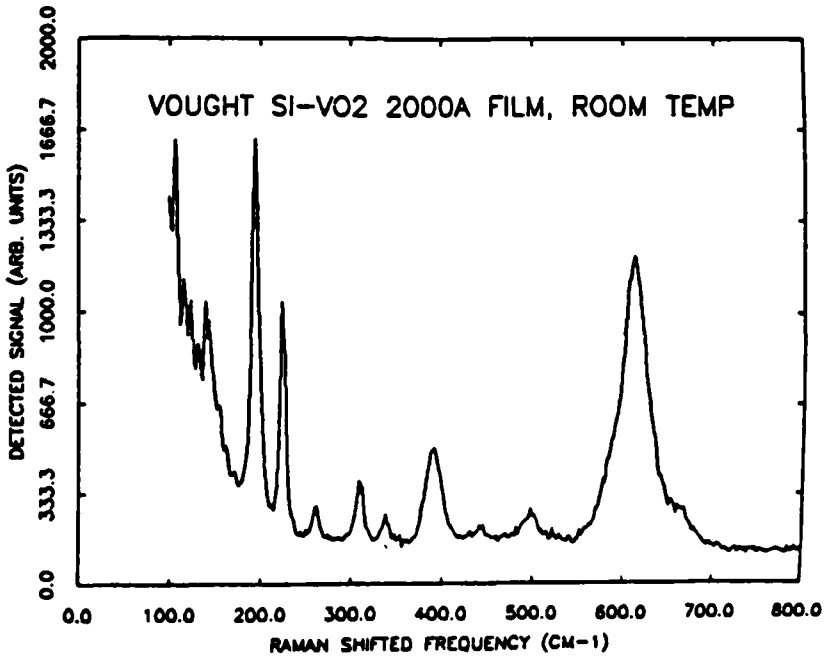
VOUGHT SI-VO2 2000A FILM, ROOM TEMP
DETECTED SIGNAL (ARB. UNITS)
0.0
333.3
666.7
1000.0
1333.3
1666.7
2000.0
0.0
100.0
200.0
300.0
400.0
500.0
600.0
700.0
800.0
RAMAN SHIFTED FREQUENCY (CM-1)

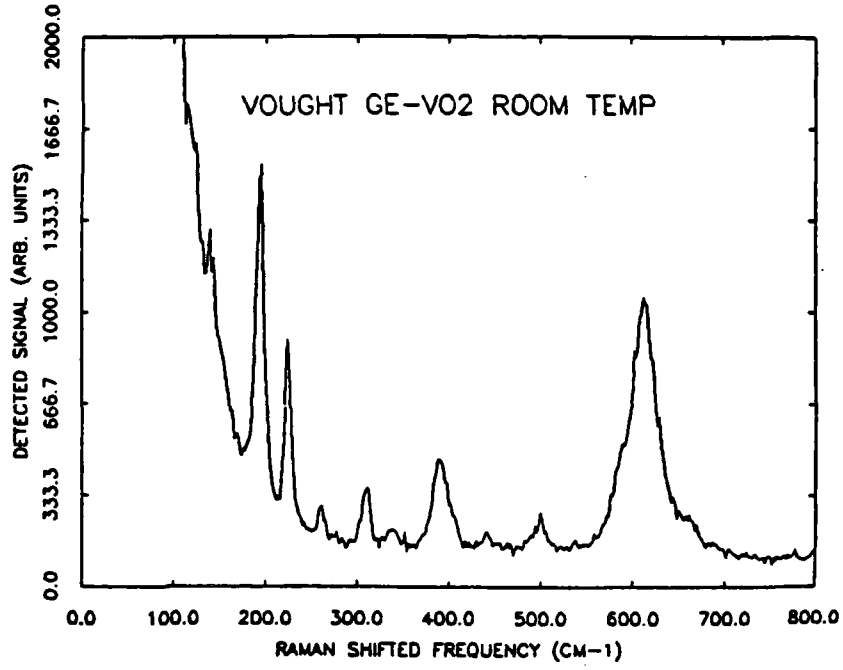
VOUGHT GE-VO2 ROOM TEMP
DETECTED SIGNAL (ARB. UNITS)
0.0
333.3
666.7
1000.0
1333.3
1666.7
2000.0
0.0
100.0
200.0
300.0
400.0
500.0
600.0
700.0
800.0
RAMAN SHIFTED FREQUENCY (CM-1)

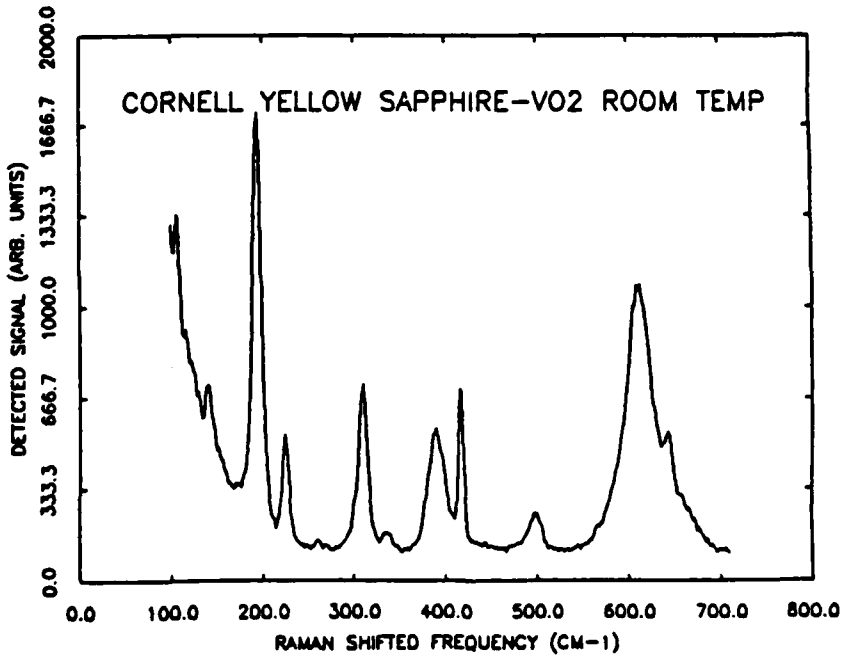
CORNELL YELLOW SAPPHIRE-VO2 ROOM TEMP
DETECTED SIGNAL (ARB. UNITS)
0.0
333.3
666.7
1000.0
1333.3
1666.7
2000.0
0.0
100.0
200.0
300.0
400.0
500.0
600.0
700.0
800.0
RAMAN SHIFTED FREQUENCY (CM-1)

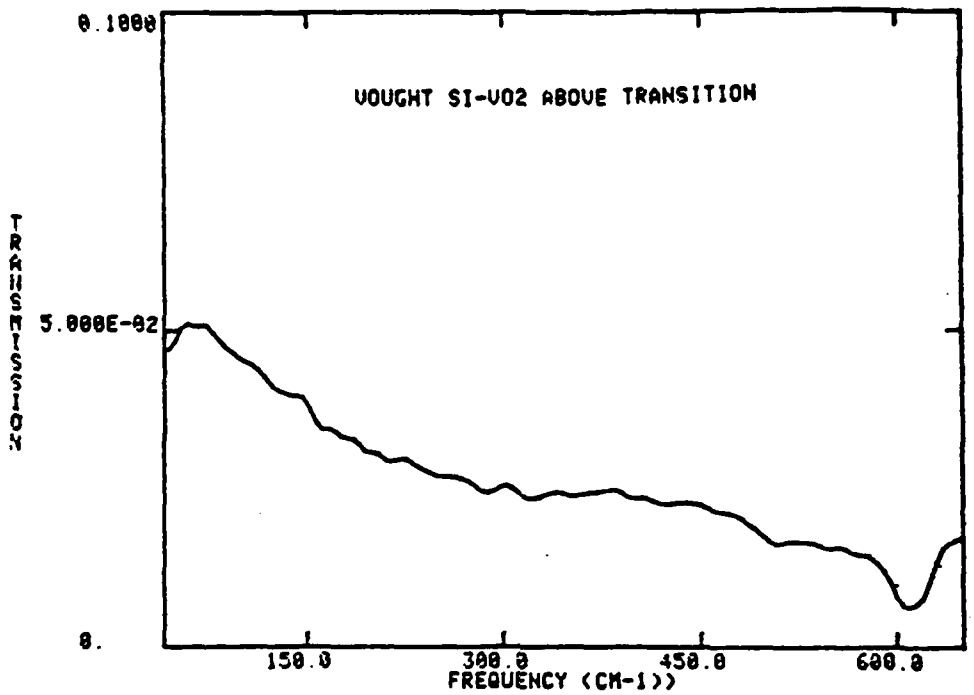
VOUGHT SI-VO2 ABOVE TRANSITION
TRANSMISSION
0.1000
5.000E-02
0.
150.0
300.0
450.0
600.0
FREQUENCY (CM-1))

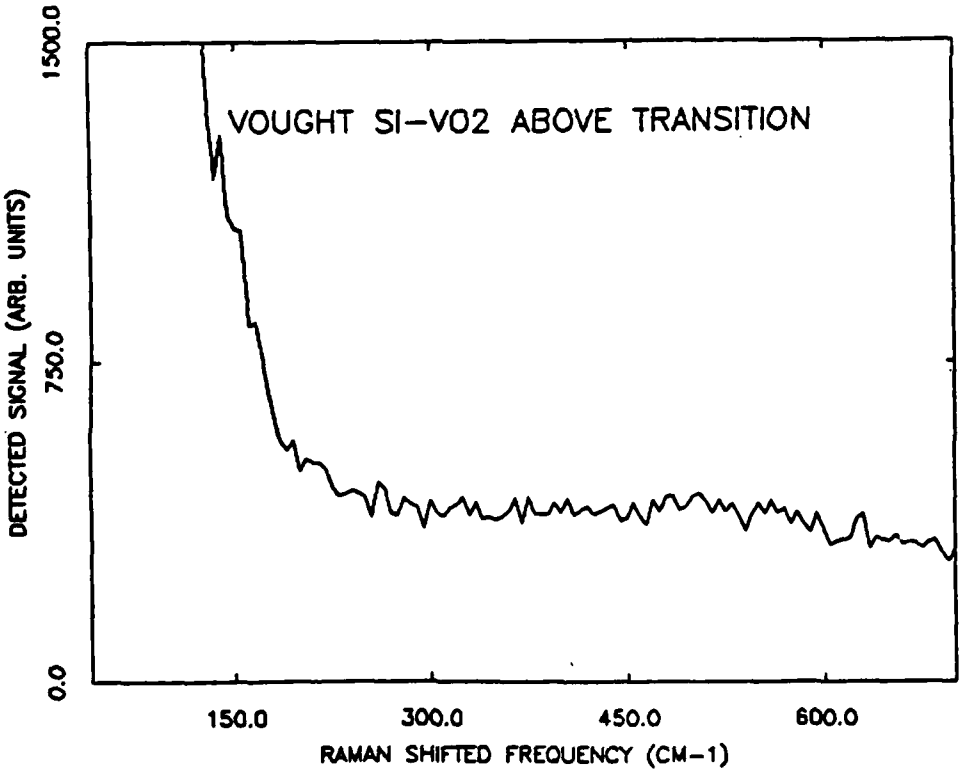
VOUGHT SI-VO2 ABOVE TRANSITION
DETECTED SIGNAL (ARB. UNITS)
1500.0
750.0
0.0
150.0
300.0
450.0
600.0
RAMAN SHIFTED FREQUENCY (CM-1)

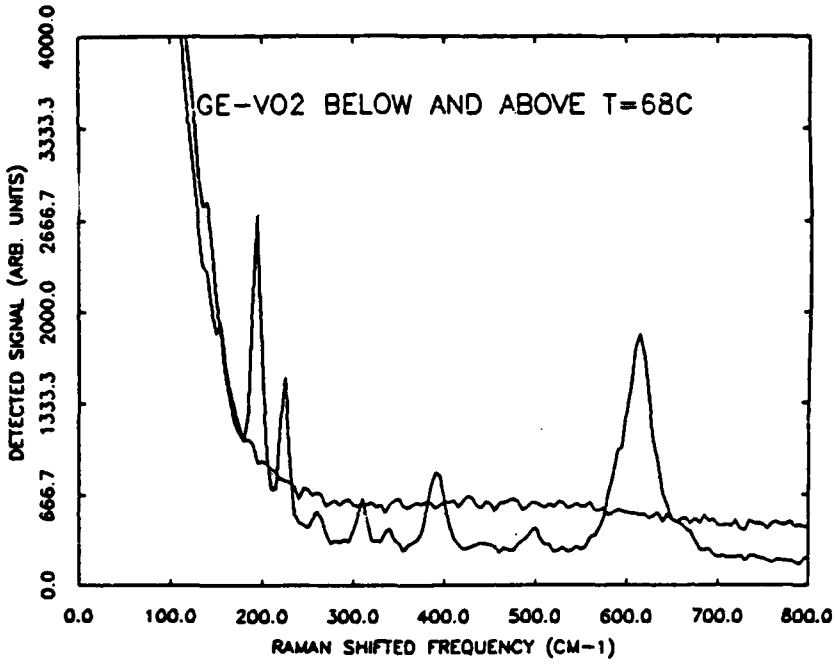
GE-VO2 BELOW AND ABOVE T=68C
DETECTED SIGNAL (ARB. UNITS)
0.0
666.7
1333.3
2000.0
2666.7
3333.3
4000.0
0.0
100.0
200.0
300.0
400.0
500.0
600.0
700.0
800.0
RAMAN SHIFTED FREQUENCY (CM-1)

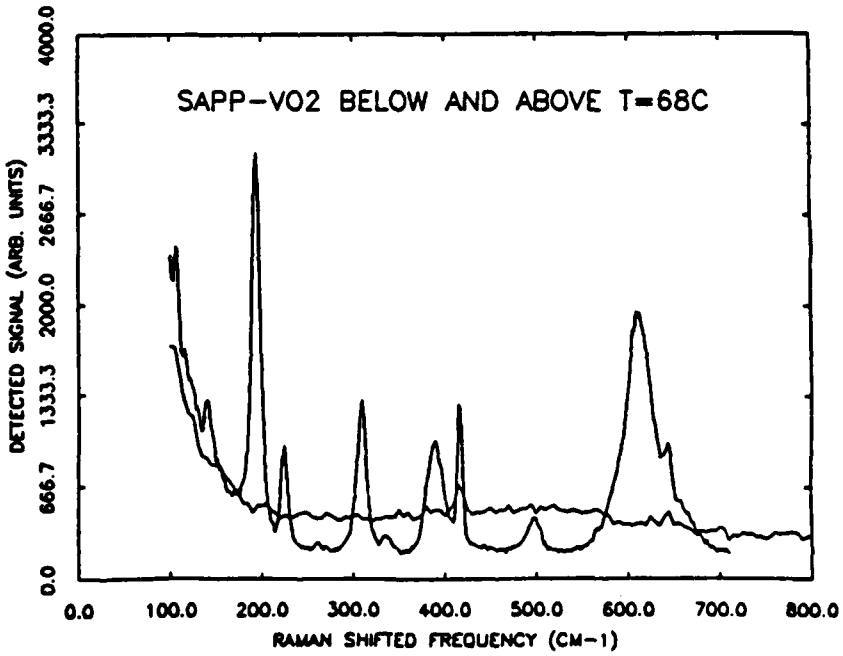
SAPP-VO2 BELOW AND ABOVE T=68C
DETECTED SIGNAL (ARB. UNITS)
0.0
666.7
1333.3
2000.0
2666.7
3333.3
4000.0
0.0
100.0
200.0
300.0
400.0
500.0
600.0
700.0
800.0
RAMAN SHIFTED FREQUENCY (CM-1)

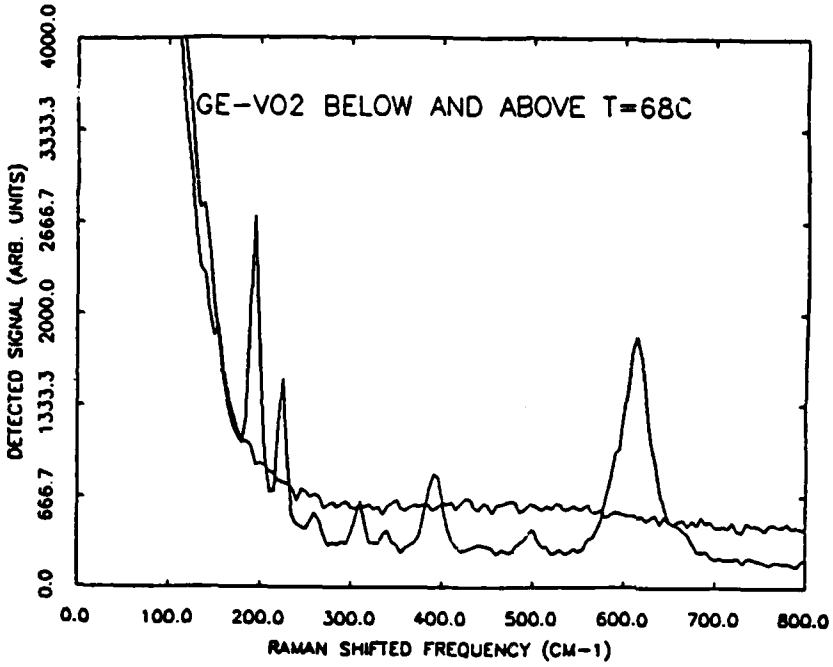
GE-VO2 BELOW AND ABOVE T=68C
DETECTED SIGNAL (ARB. UNITS)
0.0
666.7
1333.3
2000.0
2666.7
3333.3
4000.0
0.0
100.0
200.0
300.0
400.0
500.0
600.0
700.0
800.0
RAMAN SHIFTED FREQUENCY (CM-1)

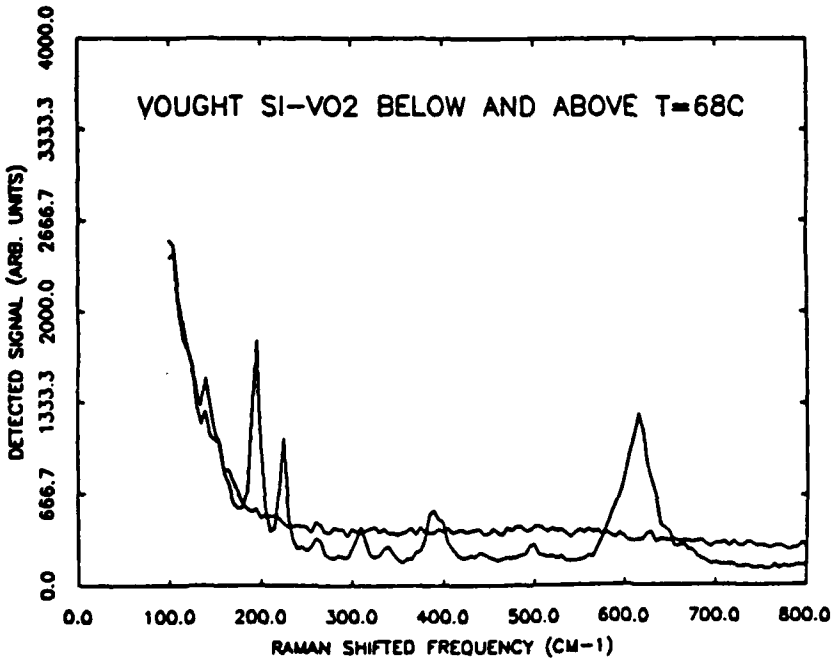
VOUGHT SI-VO2 BELOW AND ABOVE T=68C
DETECTED SIGNAL (ARB. UNITS)
0.0
666.7
1333.3
2000.0
2666.7
3333.3
4000.0
0.0
100.0
200.0
300.0
400.0
500.0
600.0
700.0
800.0
RAMAN SHIFTED FREQUENCY (CM-1)

FINAL REPORT

3. Thin Film Phase Transition Materials: Theory

S. A. Solla and N. W. Ashcroft

Cornell University

Introduction

The semiconductor-metal transition in polycrystalline VO_2 films is diffuse and exhibits hysteresis [1]. The smearing of the transition in thin films is associated with the coexistence of semiconducting and metallic phases [2], and arises from fluctuations in the transition temperature of the individual grains. The transition thus belongs to a class of percolative transitions characteristic of two-component systems such as (i) composite materials prepared by dispersing small metallic particles in an insulating host [3] and (ii) resistance grids with missing bonds or sites [4]. In bulk systems, the parameters that control the effective, macroscopic properties of such heterogeneous systems are (a) the intrinsic properties of the constituents, and (b) the topology or connectedness of the system. An additional feature pertinent to films is the deviation from bulk behavior and attributable to the existence of a restricted geometry.

Model System

We have treated this problem using a model system, as follows: Consider the problem of calculating the temperature dependence of the conductivity of a VO_2 film as it undergoes the metal-semiconductor transition. The percolative mechanism for the phase transition in polycrystalline films

implies the coexistence of metallic and semiconducting grains for temperatures within, say, $\Delta T_t \approx 5°C$ of the transition temperature $T_t \approx 68°C$. In this temperature regime the behavior of the films is characteristic of composite materials in an aggregate topology.

A suitable model for this particular VO_2 composite system is that of a random resistor network but taken to have a slab geometry. The coexistence of a dielectric or semiconducting phase of conductivity σ_D and a metallic phase of conductivity σ_M is represented through a binary distribution of conductances, and the resulting random resistor network then simulates the topology of the original system. The growth of a connected cluster of metallic component, responsible for the macroscopic conductivity transition, is controlled by the volume fraction p occupied by the metallic phase. This volume fraction increases with increasing temperature T, and an explicit relation between p and T immediately follows from assuming a Gaussian form for the distribution of transition temperatures of the individual grains [2]. Another crucial parameter is the film thickness L, and in particular its ratio to a typical linear dimension a_0 of the smallest homogeneous regions.

Hysteretic Effects in the Conducting Transition

The application of position-space renormalization group techniques to the random resistor network model provides us with an algorithm for calculating the effective conductivity of the system. A typical conductivity vs. temperature curve is shown in Fig. 1. The effective conductivity σ is measured in units of the metallic conductivity σ_M and then plotted on a logarithmic scale. The parameters that control the temperature dependence

of the effective conductivity are the conductivity ratio $R = \sigma_M/\sigma_D$ and the dimensionless film thickness $n = 4\ n_0$. The curve shown in Fig. 1 corresponds to R = 5,000 and n = 2.

A systematic investigation of the effects of conductivity ratio $h = \sigma_M/\sigma_D = R^{-1}$ and film thickness $n = L/a_0$ leads to particularly interesting crossover from three-dimensional ($n = \infty$), to two-dimensional ($n = 1$) behavior which occurs as the film thickness n is decreased. The existence of a percolation threshold at a critical concentration $p_c(n)^-$ which increases with decreasing n^- leads to an increase in transition temperature $T_t(n)$, in agreement with experimental observations in polycrystalline VO_2 films [6].

Another consequence of the existence of a percolation threshold at $p_c(n)$ is the nonanalytic behavior of the effective conductivity at h = 0. The corresponding singularities are characterized by critical exponents which are universal in that they depend only upon the dimensionality of the system. Although $\sigma_D \ll \sigma_M$ in VO_2, the conductivity ratio h is not zero. A systematic investigation of the effect of a finite conductivity ratio shows crossover from percolative singularities for $h > 0$ to effective-medium type behavior for $h < 1$ [5]. The effective conductivity in the immediate vicinity of the percolation threshold at $p_c(n)$ is controlled by h. A generalized scaling form describes the effect of both h and n on the phase transition, again in agreement with experimental results [7].

The hysteretic behavior of polycrystalline VO_2 films arise from dynamical aspects of the metal-insulator transition. The width of the hysteresis loop has been observed to increase systematically with decreasing deposition time [1]. The deposition time controls both size and

film thickness: a longer deposition time leads to a thicker, more homogeneous film. Our calculations for films of various thickness at n = 1, 2, 4, show that the width of the resulting hysteresis loop is quite insensitive to film thickness. We thus conclude that grain size is the dominant parameter controlling hysteresis.

Optical Properties

An extension of the renormalization-group formalism into the frequency domain provides us with an algorithm to calculate the effective frequency dependent dielectric constant of the composite VO_2 films. It is thus possible to calculate the effect of temperature and film thickness on the effective optical coefficients of the system. The model incorporates composite effects into a random resistor network, and generalizes the percolation description to include frequency effects. The approach is of interest to the general problem of optical properties of inhomogeneous media [8], since the statistical nature of the model includes disorder effects such as clustering and a size distribution of metallic grains.

We consider a lattice model and allow for a random distribution of an insulating matrix characterized by a dielectric constant ε_D, and a metallic component characterized by a frequency dependent dielectric function of the Drude form, namely,

$$\varepsilon_M(\omega) = 1 - \frac{\omega_p^2}{\omega^2 + i\omega\Gamma}, \qquad (1)$$

where ω_p is the plasma frequency and Γ is an appropriate damping constant. The frequency dependence of the effective dielectric function $\varepsilon(\omega)$ determines the optical properties of the composite material at a fixed

volume fraction p of the metallic component. Of particular interest are the loss function:

$$\beta(\omega) = \mathrm{Im}\left[-\frac{1}{\varepsilon(\omega)}\right], \tag{2}$$

and the absorption coefficient

$$\alpha(\omega) = \frac{2\omega}{c}\,\mathrm{Im}\sqrt{\varepsilon(\omega)}\,. \tag{3}$$

The results for the real and imaginary part of the dielectric function $\varepsilon(\omega)$ shown in Fig. 3 and the loss function $-\varepsilon^{-1}(\omega)$ shown in Fig. 4 correspond to Ag particles embedded in gelatin at 10% filling fraction. The corresponding parameters are [9] $\varepsilon_i = 2.37$, $\omega_p = 9.2$ eV, and $\Gamma = 0.2$ eV. The effective medium results are shown as dashed lines for comparison. The appearance of additional structure and the red-shift of the main peaks are both due to clustering. Results for the absorption coefficient as a function of frequency are shown in Fig. 5 and compared to effective-medium results for 10% and 20% filling fraction. The disorder introduced in this model results in an effective broadening of the absorption peak as well as a shift toward laser frequencies. Such effects are characteristic of composite materials in aggregate topology, and should be observable in VO_2 within the transition region.

Kinetics of the Phase Transition in VO_2

The phase transition in VO_2 single crystals exhibits features of a martensitic transformation [10]. In particular, there is

- a lattice correspondence between the two structures on either side of the transition
- a discontinuity in these lattice parameters
- a change in crystal symmetry
- constancy of composition
- atomic motions smaller than nearest-neighbor distances
- hysteresis (in temperature)

and

- twinning in the low temperature phase.

A martensitic mechanism implies athermal, diffusionless behavior, in which the rate of transformation is independent of temperature while the amount of transformation is virtually independent of time and is a function of temperature only.

A martensitic transformation also results in an intermediate coexistence regime, with domains of one phase forming within the matrix of the other phase. The strain energy arising from phase coexistence controls the amount of transformation at any given temperature [11]. The width of the hysteresis loop is then proportional to the strain energy and to the volume change associated with the transformation [12]. The small volume change ($\Delta V/V = 0.04\%$) for the monoclinic-tetragonal transformation in VO_2 [13] is quite consistent with a rather narrow intrinsic hysteresis loop, $\Delta T_t \approx 2°C$.

Within the transition region both phases coexist and are separated by a coherent interface. Such a process requires a minimum crystallite size d_c. For $d < d_c$ coexistence is not possible, and the transformation must proceed via thermally activated nucleation and growth. The interaction with grain boundaries thus enhances hysteretic behavior. Detailed

experimental studies of the transformation kinetics are not yet available for VO_2, but for ZrO_2 $d_c \approx 1000$ A. This material undergoes a monoclinic to to tetragonal phase transition at 1100°C [14].

References

1. D. Bühling and L. Michalowsky, Le Vide 185, 185 (1976).
2. Y. M. Gerbstein, T. V. Smirnova, E. I. Terukov, and F. A. Chudnovskii, Sov. Phys. Solid State 18, 290 (1976) [Fiz. Tverd. Tela 18, 503 (1976)].
3. D. M. Grannan, J. C. Garland, and D. B. Tanner, Phys. Rev. Lett. 46, 375 (1981).
4. B. J. Last and D. J. Thouless, Phys. Rev. Lett. 27, 1719 (1971); M. E. Levinshtein, J. Phys. C 10, 1895 (1977).
5. S. A. Solla, submitted to Phys. Rev. B.
6. R. L. Remke, R. M. Welser, and R. W. Bené, Thin Solid Films 61, 73 (1979).
7. V. N. Andreev, T. M. Smirnova, and F. A. Chudnovskii, Phys. Stat. Sol. B 77, K97 (1976).
8. For a review, see Electrical Transport and Optical Properties of Inhomogeneous Media, eds. J. C. Garland and D. B. Tanner (American Institute of Physics, New York, 1978).
9. A. Liebsch and B.N.J. Persson, J. Phys. C 16, 5375 (1983).
10. J. A. Krumhansl, Report NSF-ITP-82-30.
11. A. R. Ubbelohde, Quart. Rev. Chem. Soc. (London) 11, 246 (1957).
12. K. J. Rao and C.N.R. Rao, J. Mat. Sci. 1, 233 (1968).
13. D. Kucharczyk and T. Niklewski, J. Appl. Cryst. 12, 370 (1979).
14. E. C. Subbarao, H. S. Maiti, and K. K. Srivastava, Phys. Stat. Sol. (a) 21, 9 (1974).

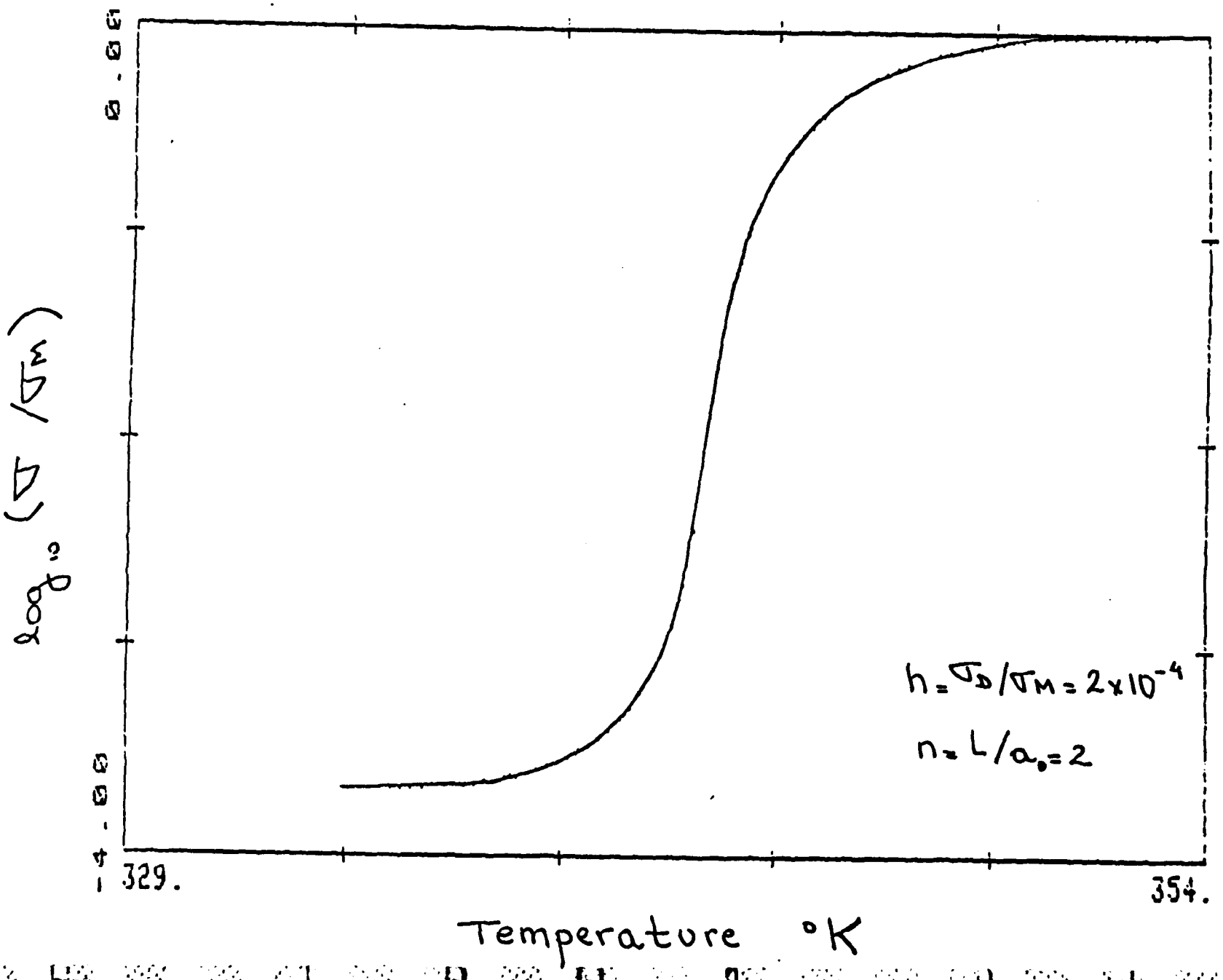
0.00
-4.00
329.
354.
Temperature °K
$\log_{10}(\sigma/\sigma_M)$
$h = \sigma_D/\sigma_M = 2\times10^{-4}$
$n = L/a_0 = 2$

Figure 1

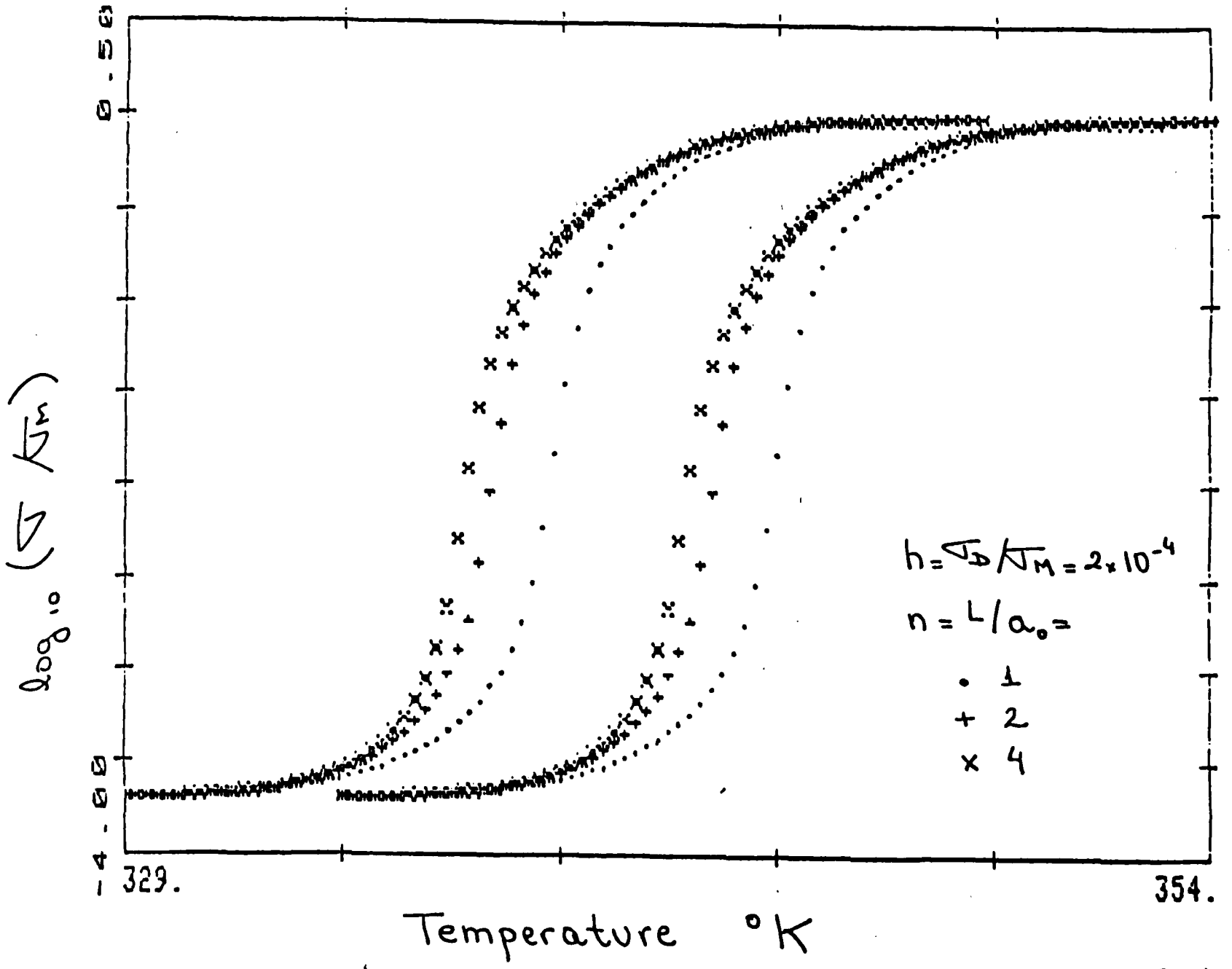

Figure 2

Metal-insulator composite: dielectric function

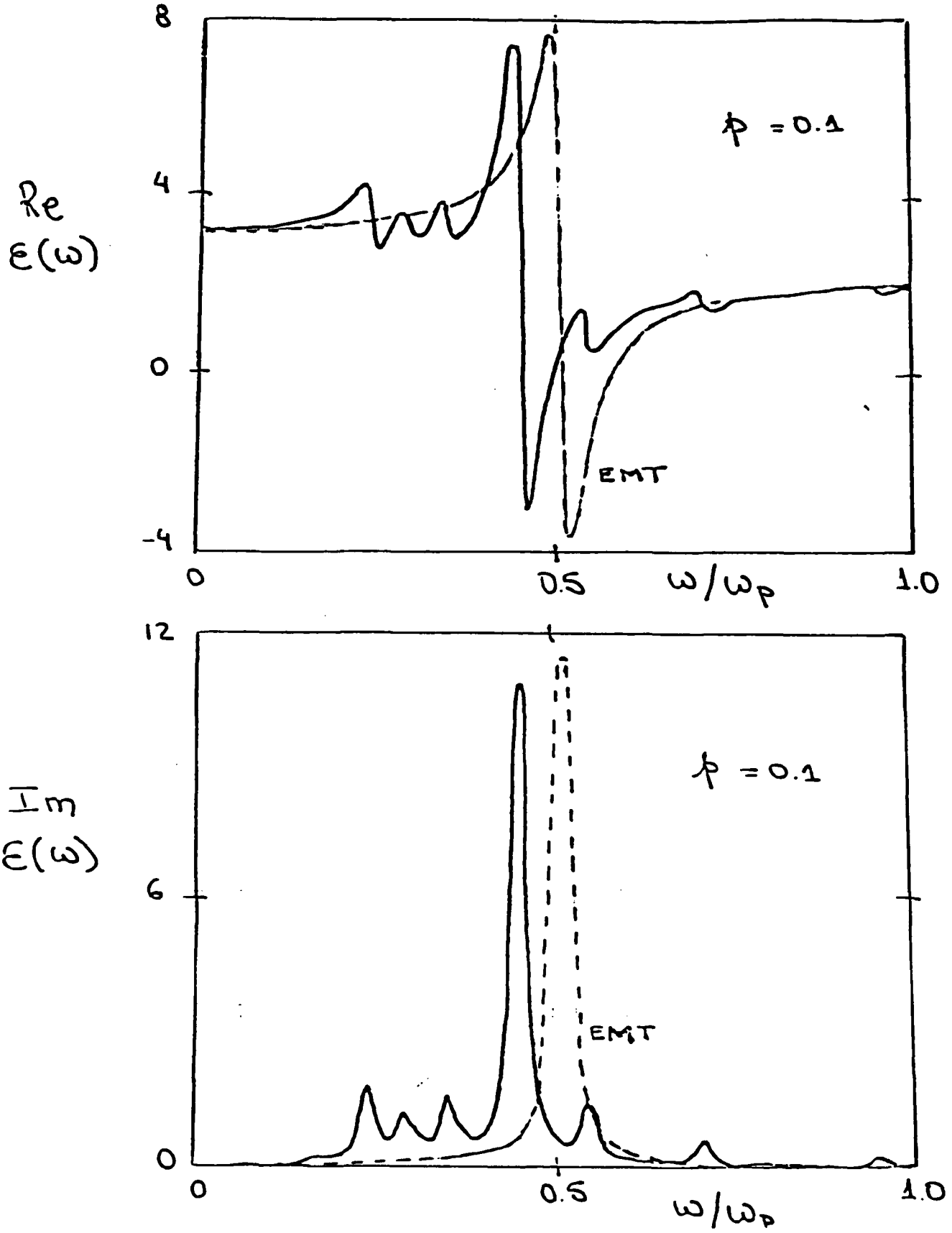

Finure

Metal-insulator composite: loss function

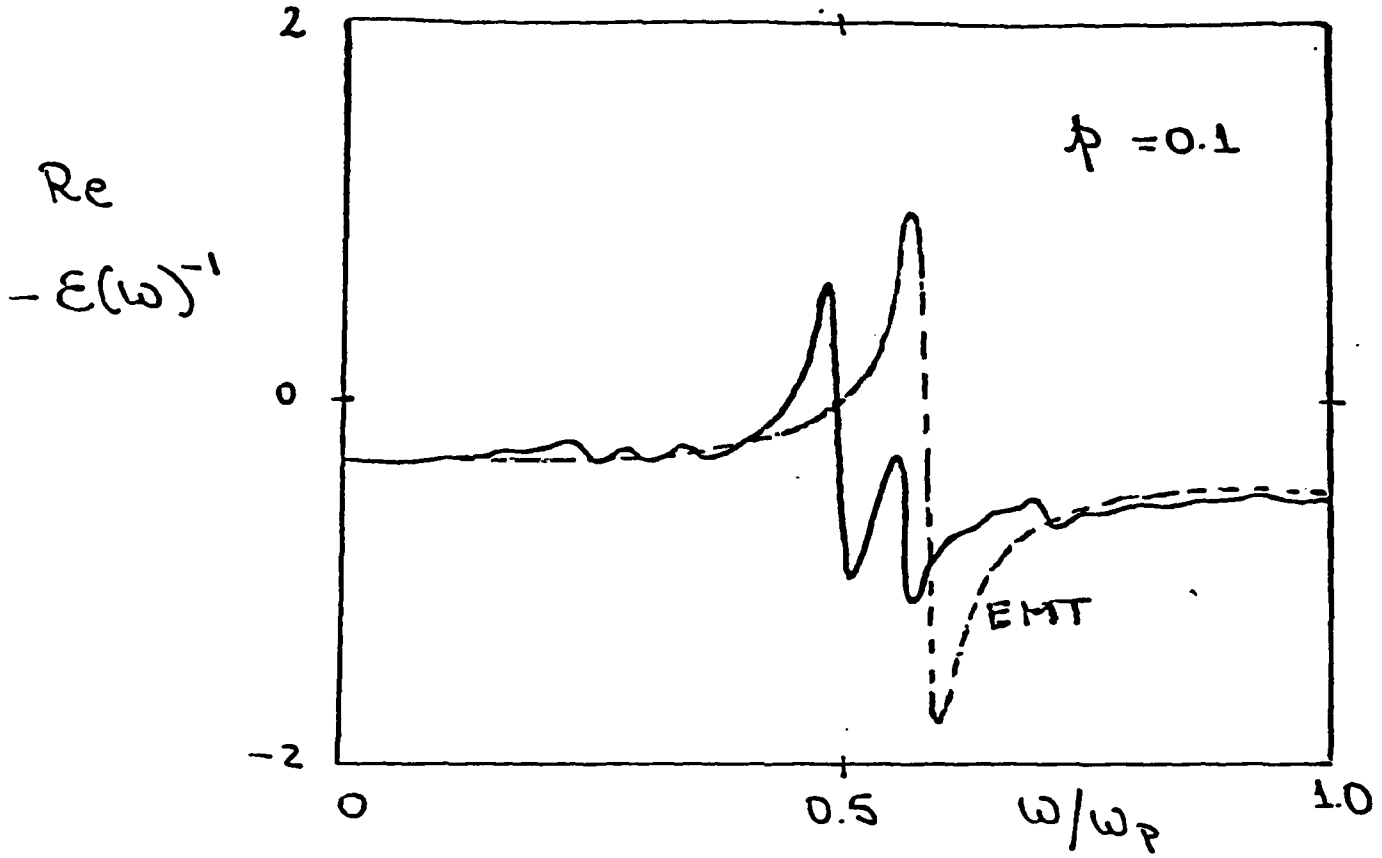

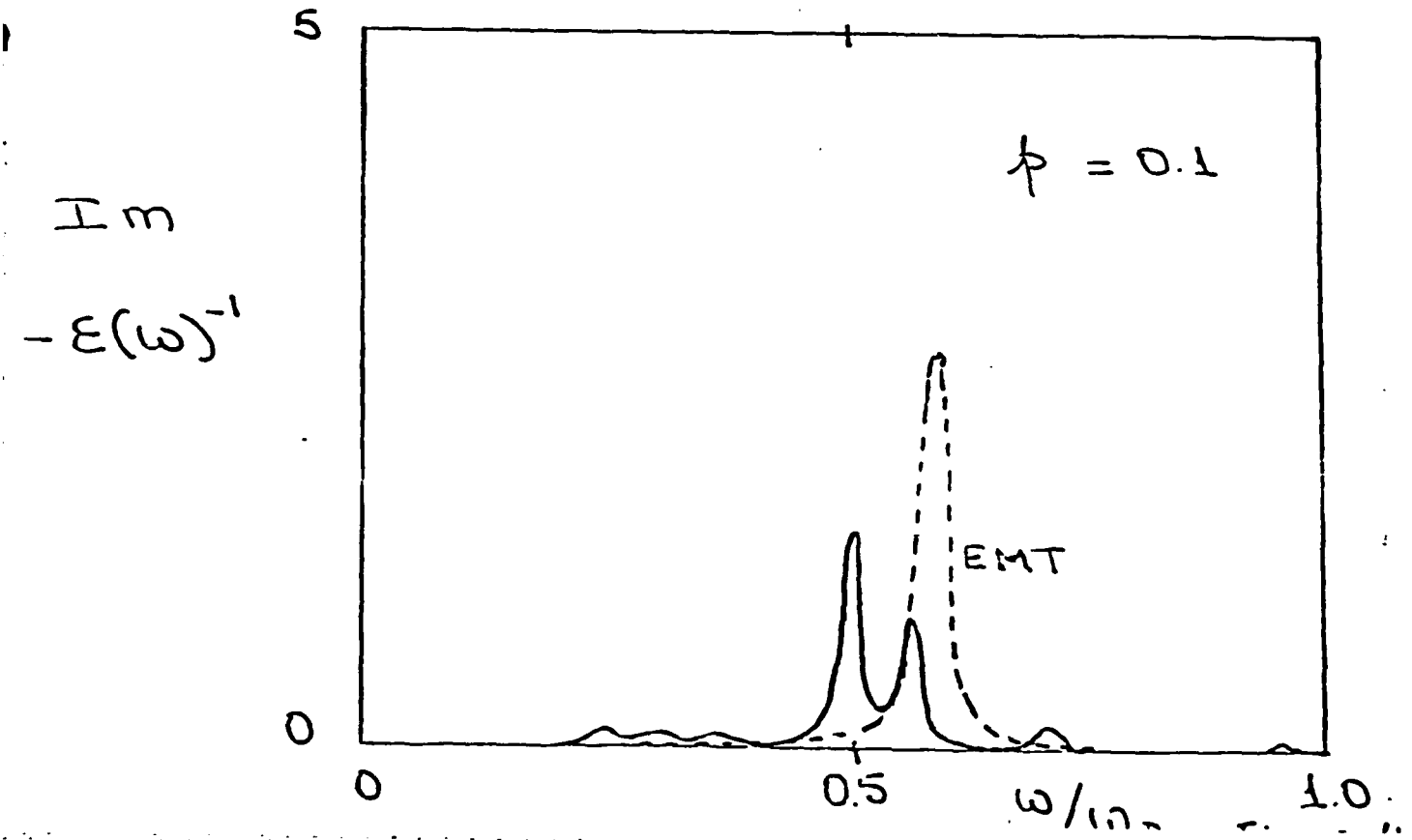

Metal - insulator composite: absorption coefficient

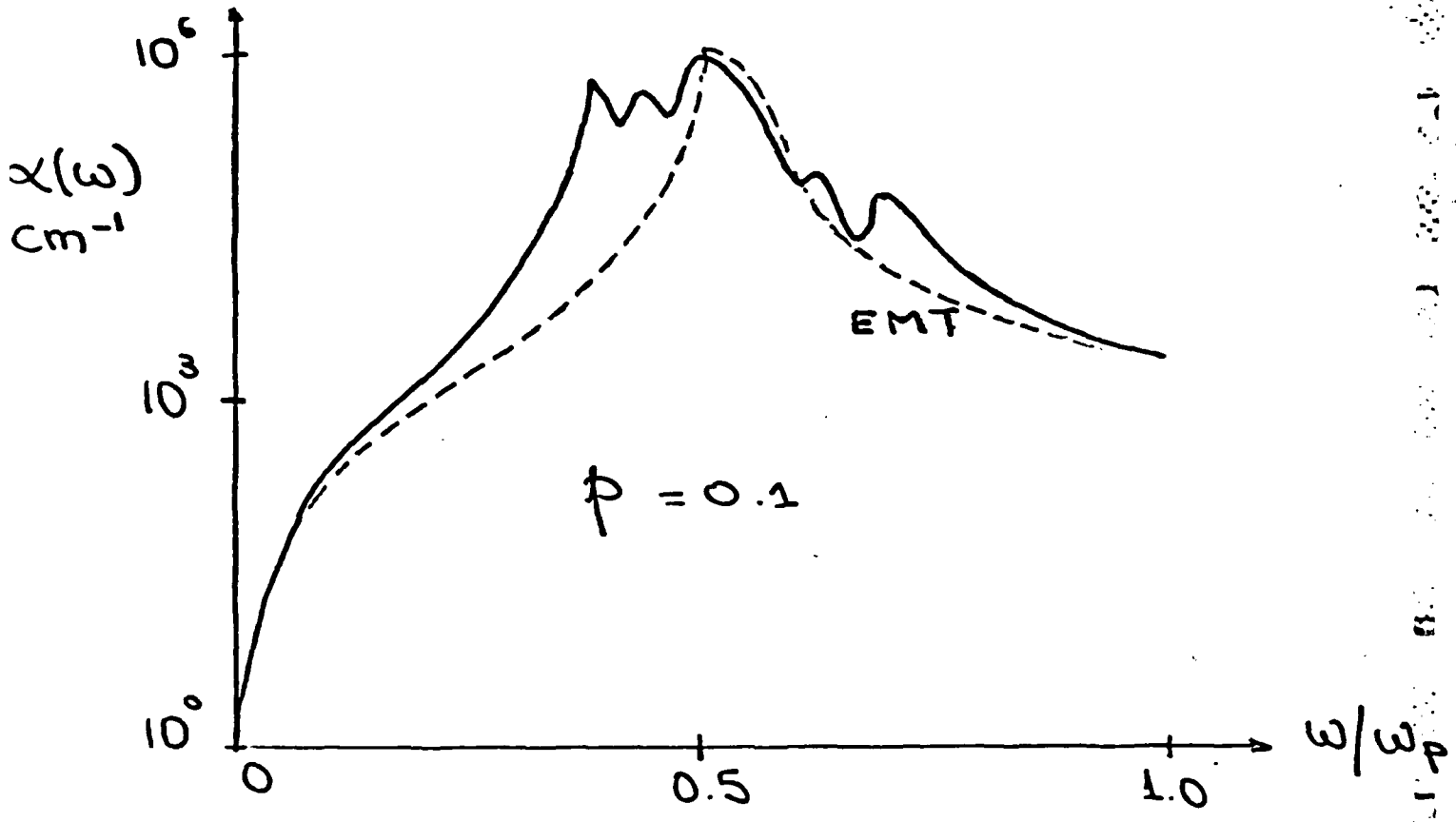

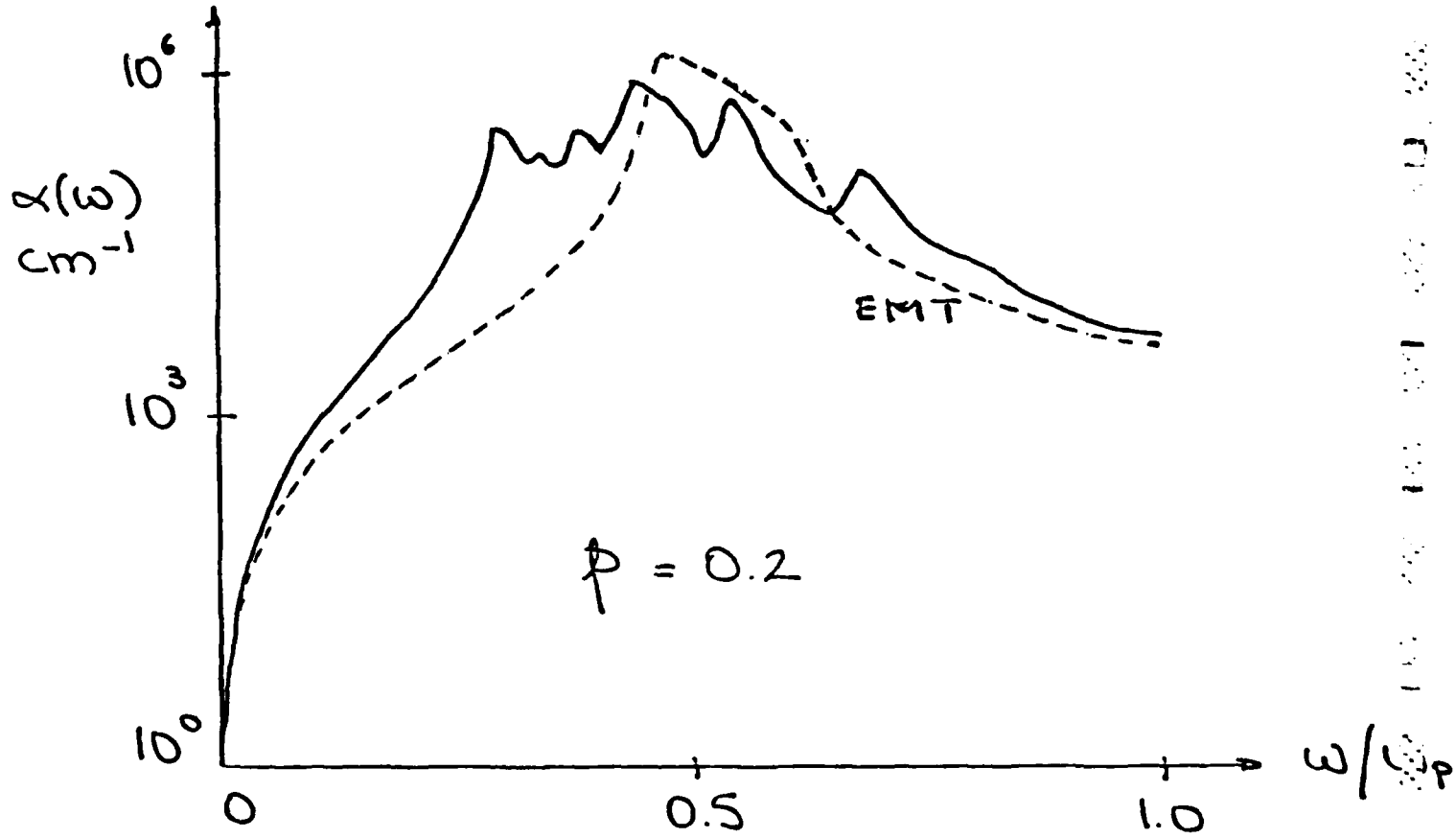

Figure 5

APPENDIX A

VO_2 Thin Film Deposition Procedures

1. Previously Known Methods of Depositing VO_2 Thin Films

There were several known techniques for producing high quality VO_2 films prior to this work. For a review of these techniques prior to 1972, see Fan.[1] Because little qualitative change has been reported since then, only a brief overview of past work will be given here.

The first VO_2 thin films were reported in 1967. They were made by a two-step process: the physical evaporation of vanadium in a oxygen ambient of 5 10^{-5} torr, followed by (high temperature) oxygen annealing. Later, several chemical methods were developed, with the advantages of high deposition rates and thick film capability. DC reactive sputtering was also performed first in a two-step manner. Subsequently it was improved to a one-step process. Since 1970, reactive RF sputtering has been the most frequently reported method.

Although these processes made what were then believed to be high quality films, it was decided that a new approach should be taken. Conceptually reactive evaporation is the simplest way to make VO_2 films: it has the fewest and most independent deposition variables. Henceforth "reactive evaporation" will always mean the one-step evaporation of vanadium in a pure oxygen ambient with the film growing on a

heated substrate.

It is important to use a one-step process because certain applications require a graded stoichiometry as a function of depth.[2] A one-step process permits the addition of other simultaneous processes with the important advantage of easily tailoring the properties of the film as a function of depth. For example it is known that alloying VO_2 with a second metal can lower or raise the transition temperature.[3,4] Evaporating this second metal simultaneously should result in more uniform composition than post-deposition doping which requires a concentration gradient. Also it is known that bombarding a film during deposition with ions can affect the stress in the film.[5] Stress in VO_2 should shift the transition temperature just as hydrostatic pressure is known to.[6] Hysteresis is affected by stress.[7] Furthermore, ion bombardment is an example of activated reactive evaporation[8] which could be used to speed up the oxidation or perhaps enable it to occur at lower substrate temperatures.

Therefore the deposition system shown in Fig. 1 was a very general and powerful one. The set of processes described above supplement the primary process, one-step reactive evaporation. Surprisingly no reports of making high quality VO_2 films by this method were found in the literature. Thus the crucial step here was to successfully reactively evaporate VO_2. In the next section is an overview of

the deposition system used for performing just that.

2. Thin Film Deposition System

2.1 Overall Design

A schematic of the deposition system is shown in Fig. 1.

This deposition system was designed by R. A. Buhrman, and assembled by G. E. Schmidt and the author prior to the latter's work on the optical properties of co-evaporated metal-dielectric (cermet) thin films, which preceded the present project. The overall design of the system was to serve as a very versatile, thin film research instrument.

The stainless steel vacuum chamber used copper gasket-UHV technology except for the large Viton top plate gasket. The vacuum pump was a cryopump which used He as the working gas in a closed cycle refrigeration operation. Its nominal pumping speed for air was 1000 l/s. With a bakeout, the system could be pumped down to a practical base pressure of 1 10^{-7} torr. The pump-to-chamber high vacuum valve was of the swing-gate type.

Two mirrors inside the chamber enabled one to observe the vanadium evaporation charge and the growing film.

The evaporation source was an 8kW-rated power, 270° deflection electron gun source. An electron gun source was used instead of a simpler filament or boat source for several

reasons. Because of the high melting temperature of vanadium (1890°C) and the high oxygen ambient, a refractory metal filament or boat is likely to oxidize, evaporate, or alloy with the vanadium. The electron gun source provides more precise control over the evaporation rate.

Measuring the vanadium evaporation rate was done with two quartz crystal monitors. This redundancy was not absolutely necessary, but it helped to minimize down-time and improve reproducibility. The indicated rates from both of these monitors were averaged to provide the feedback control to the electron gun power supply. The electron gun filament current was varied while the high voltage was held constant at 6500 V. The evaporation feedback loop is shown in Fig. 2.

The oxygen pressure was maintained near 1 mtorr by leaking it through a valve that was controlled in a feedback loop with an ion gauge tube as the pressure monitor, as shown in Fig. 3.

It is not possible to deposit stoichiometric VO_2 onto a room temperature substrate.[9] This applies to all known deposition methods and is a basic consequence of the phase equilibria of the vanadium-oxygen system.[3,10,11] Instead, the substrate must be heated to several hundred °C. This was done here by thermal contact to a specially made molybdenum heater block assembly into which a chromel-alumel thermocouple was mounted. The temperature control feedback loop

was completed by a temperature control unit, as depicted in Fig. 4. The substrate was not rotated.

The system was also equipped with a differentially pumped mass spectrometer for residual gas analysis and process control.

2.2 Detailed Description

The cryopumped system was oil-free except for the conventional (oil-using) mechanical roughing pump. A molecular sieve trap in the roughing line reduced oil backstreaming. As per instructions, its porous beads were replaced only when the pumpdown time increased noticeably above the normal four minutes. Oil backstreaming is more serious when the pressure is reduced to the molecular flow regime.[12] Here, that regime began at roughly 100 mtorr. To be safe, the roughing valve was closed at 300 mtorr according to the thermocouple pressure gauge controller using an air calibration. The high vacuum valve was then opened to begin cryopumping. The cryopump was incapable of operating at 300 mtorr pressures for any length of time. But it could handle the initial opening surge, since most of the gas was absorbed at the pump before the heat load had time to warm the pump. The cryopump temperature (according to its hydrogen pressure gauge) did not surge when it was cooling properly.

The chamber contained Viton gaskets only in the following places: 20'' diameter top plate gasket, roughing

valves, turbopump/chamber quick connect, high vacuum swing-gate valve, cryopump assembly, and cryopump safety relief pop-off valve. The last three were lightly greased with Apiezon H. All other seals were of the copper gasket-conflat flange type.

Vacuum feedthroughs numbered twenty on the deposition chamber itself, and six on the removable top plate. The substrate heater was mounted on hardware that was attached to the top plate. The top plate feedthroughs were dedicated to the substrate, substrate heating, thermocouple, rotary shutter, and one crystal monitor. The thermocouple feedthrough was a special chromel-alumel one, to match the thermocouple type. A large (8'' diameter) glass window enabled observation of internal processes and events. The entire interior wall space was protected from coating by the use of (0.004'' thick) stainless steel shields that could be cut with metal snippers. A ringstand provided many convenient mounting opportunities for internal fixturing.

All internal water lines were either welded, vacuum brazed, RF brazed, or silver soldered. Since the practical base pressure here was about 1 10^{-7} torr, silver solder (on water lines) was acceptable. Although preference was given to stainless steel as a fixturing material, it was not necessary to use that material exclusively.

Stainless steel threads tend to lock-up especially if they are unlubricated or are taken to high temperatures.

Several precautions successfully avoided such problems. All threads (internal and external) were lubricated with MoS_2, except for those on the substrate heater. The system was deliberately designed to avoid tapped holes of any kind. Instead its fasteners were machine screws and nuts, kept to size 4-40 or smaller. This permitted any reluctant bolt to simply be sheared off.

Prior to installation, all parts were cleaned similarly: scrubbing with Scotch-Brite, soap, water, ultrasonic agitation in acetone (sometimes recycled), and ultrasonic agitation in unused AR grade isopropyl alcohol (2-propanol). A tremendous savings in time resulted from emphasizing the first steps, followed by visual inspection. As an alternative to a hazardous solvent like acetone, a commercial parts washer (Graymills, with Agitene detergent) was used. This was especially suitable for large objects. Trichloroethylene was rarely used because of its toxicity. Isopropyl alcohol was used as the final rinse because it removed the acetone residue, left no residue of its own, was less toxic than methyl alcohol, and air dried quickly. Distilled water was deliberately avoided because of the unreliability of local supplies and because of the necessarily long drying time.

It is in the nature of a thin film evaporation system not to remain long in a pristine state. The surface area of accumulated coatings was enormous and increased the pumpdown time noticeably. Therefore the accumulated coatings

(especially on surfaces that were heated during the deposition) were removed after every deposition by scraping with a spatula and vacuuming out.

The chamber was always vented by backfilling with dry nitrogen gas. That was done because cooling upon expansion of the input gas was sufficient to condense water in the inlet valve. Usually, the chamber was baked out at half power while being flushed with dry nitrogen during the entire substrate removal and replacement time. This expedited pumpdown because it reduced the amount of water sticking to the walls and allowed the pumpdown to begin with the chamber at an elevated temperature.

One of the biggest obstacles in daily operation was the long pumpdown time. The cryopump did not have a sufficiently high pumping speed for this system's large internal surface area, fixturing, shields, and accumulated coatings. Under the conditions here, the electron gun radiated about 200 watts into the chamber during a deposition, which increased the background pressure (mostly H_2O) tenfold.

To overcome this problem, the vacuum chamber was baked out during pumpdown. Chemi-desorption of water vapor has an exponential temperature dependence,[13] so the main idea was to use higher temperatures than those occuring during a deposition. The parts that were heated by the evaporation process were given priority in designing the bakeout system. A practical base pressure for this system was 1 10^{-7} torr.

An adequate pumpdown and bakeout was judged as one that enabled the reactive evaporation to proceed while raising the base pressure to less than 10^{-5} torr. Using this criterion, the minimum pumpdown, without a bakeout, was 24 hours.

One very convenient bakeout procedure employed two Watlow steel heating bands that girdled the center of the vacuum chamber. They were powered with 900 watts each. Three other Watlow heater bands (400 watts each) were mounted on ports of the chamber. Additionally the flexible stainless steel bellows (through which the differentially pumped RGA connected to the chamber) was heated by 400 watts from flexible heater tapes. These external tapes reduced the pumpdown time to five hours.

There were several limitations to external heating of this type. First, the thermal contact between the heater band and the chamber was not good. The heater tapes dissipate much of their heat into the room rather than into the chamber. Secondly, the heating proceeded slowly due to the low thermal conductivity of the steel. An additional inefficiency of external heating resulted from the use of the internal stainless steel shields. If the entire chamber was at 100 ^{o}C, it would have radiated only 400 watts into the steel shields which in turn would have consumed more time before they were heated enough to heat internal parts.

Obviously the bakeout was expedited by an internal source of heat. Any source more powerful than 400 watts was

more effective than the external heater bands. The fastest pumpdown (2 hours) was achieved with a specially designed, internal, quartz lamp, radiant heater. A schematic is shown in Fig. 5. The radiant heater had a maximum power of 3 kW, using six 500-watt (Sloan Technology Corporation, Santa Barbara, Ca.) quartz lamps. The only metal used was molybdenum. The insulators were Macor which tolerates continuous use at 1000 ^{o}C. To avoid cracking, Macor piece thicknesses were never less than 3/16''. The lamps were driven in parallel by a Variac, so that a burnout did not increase the power to the survivors. The Sloan lamps were specifically chosen because the lamp ends were encased in molybdenum from which a wire lead extended. Reliable high temperature contacts were obtained because the lamp ends were inserted into tight-fitting slots machined into the hexagonal end blocks. The wire leads extended through tight fitting holes in these blocks. Therefore electrical contact was ensured by gravity alone. No troublesome bolts or screws were used. This method proved to be far superior in operation and much simpler in construction than an earlier design that used spring-actuated contacts which were susceptible to failure at high temperature. Replacing lamps was easy. The heater assembly was supported by a U-shaped copper frame which rested on the chamber floor. No radiation reflector was used since it was beneficial to heat the entire chamber and floor. The assembly was shielded from the electron gun source to

avoid frequent lamp cleaning. Since the coatings on room temperature surfaces were V_2O_5, cleaning was done by rinsing the complete assembly in hot water.

Finally some precautions need to be noted: damage to other vacuum chamber parts was possible if the heater used more than 1500 watts for more than two hours. In particular the crystal monitor cooling water had to be used. Also, the radiant heater must not illuminate any windows. Other precautions during bakeout included ensuring that the Viton top plate gasket not be heated over 125 ^{o}C. Although Viton can be baked out to 180 ^{o}C, pushing this limit caused softening.

3. The Reactive Evaporation of VO_2

3.1 Procedural Summary

The substrate heater was demounted from the chamber fixturing and taken to a laminar flow hood for substrate mounting. During this time, the vacuum system bakeout heater bands were run at half of their usual power. A metal lid was placed on the chamber while it was purged with dry nitrogen gas. Several cleaning and maintenance steps were performed.

The clean substrate and thermocouple were mounted and then the substrate heater was then reattached to the vacuum system. The thermocouple and heater leads were attached. Immediately before lowering the top plate, the substrate was blown off with filtered dry nitrogen gas for the last time.

The chamber was roughed down to 400 mtorr before switching over to the cryopump. The shutter was locked in the closed position. Before the pumpdown and bakeout proceeded any further, all aspects of the deposition process were tested out. A typical bakeout took at least five hours. The chamber took one hour to cool. It was beneficial but not absolutely necessary to run the electron gun (for 30 minutes) at a power safely under that needed to cause vanadium evaporation. During the cooling down of the chamber, the electron gun was run at twice the power used during deposition for about three minutes. The beam was defocussed for this. This step melted and flattened the vanadium.

The substrate was heated to its final temperature in about 10 minutes. During this time the oxygen pressure was brought up to the final setting. Both oxygen and substrate temperature control were begun. The electron gun was at low power during the substrate warm-up. It was very important for it not to be evaporating vanadium during this time, because the substrate would have been contaminated, even with the shutter closed.

The electron gun power was gradually increased to the deposition set point and then the shutter was opened to commence the deposition. After 10 seconds, the deposition rate control was initiated.

A mirror inside the chamber permitted observation of the growing film. During the first 20 minutes of the deposition,

a highly textured film could be identified as such. This allowed decisions to be made on a change of the deposition parameters or the length of the deposition.

Shutdown was performed in the order: shutter closed, electron gun switched off, substrate heating ended, and oxygen input closed. The chamber could be vented for substrate removal in about 30 minutes.

3.2 Residual Gas Analysis

The differentially pumped quadrupole mass spectrometer (RGA) was capable of process control and residual gas analysis. Here we discuss typical residual gas spectra during system bakeout, after bakeout, and during deposition. With the exception of H_2, all important residual gases have about (to within 10%) the same instrument sensitivity, so no distinction is made between raw data and absolute pressures.

During the bakeout, the chamber pressure was typically 5 10^{-5} torr. The RGA showed that 90% of this was H_2O. A typical spectra after bakeout and prior to deposition with all deposition processes shut off showed that water vapor was still the largest single contaminant, being about 70% of the total pressure. Such is not the case for well baked UHV systems. But serious UHV bakeouts heat the entire chamber to over 300 ^{o}C. It was verified that the system contained no H_2O leaks. The thermally activated nature of chemi-desorption causes any cold spot to dominate the baked surfaces. It

is recommended that future users make an effort to locate and heat these cold spots. The second largest peak was mass=28 which is N_2 and CO. The He and H_2 peaks were quite small. He was not a large contaminant here because of the use of a rotary roughing pump instead of a liquid N_2 cooled, molecular sieve cryosorption pump.

During non-evaporative electron gun bakeouts the H_2 peak typically increased up to 20% of the H_2O peak. It is not known how much H_2 is transferred in and out of the vanadium, which like most transition metals has a large solubility for H_2. The cryopump pumps H_2 at roughly the same speed as air. However the number of activated sites that can cryosorb H_2 is much lower than for air. The rating for this pump is a H_2 saturation at 7 10^3 torr-liters. However, decreased H_2 pumping was observed after 4 months of daily use.

When the vanadium began evaporating, the H_2, mass 28, and O_2 pressures dropped, while H_2O and CO_2 pressures increased. Typically the total pressure dropped a factor of three but then slowly began rising due to the increasing H_2O desorption from heated surfaces.

The hydrocarbon contamination integrated to less than 1% of the total pressure. This sum has not increased over the years, which proves the effectiveness of the methods described above of avoiding contamination from the roughing pump. Also the cryopump was <u>never</u> exposed to the roughing pump or roughing line when it was <u>cold</u>. During cryopump

regenerations it was necessary to rough down the warm cryopump to less than 10 mtorr before cooling. But the rotary pump was only used to 1000 mtorr. After that a single cryosorb pump pumped the cryopump and chamber into the mid 10^{-4} torr range in about 15 minutes. This continued for the first 45 minutes of the cooldown. The procedure was quite safe because the cryosorption pump was never exposed to the oil rotary pump or its line.

Prior to the deposition, the liquid nitrogen shroud which surrounds the cryopump was filled. Failing to do so would result in chamber H_2O pressures in the low 10^{-5} torr range, which is about 2% of the oxygen pressure. This was considered excessive since 1% oxygen control was sought. The orifice in the throat between the vacuum chamber and the cryopump did not impede water pumping by the trap. Using the trap reduced the water partial pressure (during deposition) at least a factor of two, that is, kept below 10^{-5} torr. The trap froze shut with ice unless it was corked after filling.

3.3 Fine Tuning the Deposition Control

In this section is a discussion of the subtleties of using these basic building blocks to reactively evaporate VO_2. Although some of these points might also apply to reactive evaporation of thin oxide films in general, only those issues which are unique to the problem at hand will be emphasized. For background information on thin film tech-

nology, the reader is referred to Ref. 12 and 13.

3.3.1 Stabilizing the Evaporation

One of the problems of electron gun evaporating a metal like vanadium with a high oxygen gettering rate is the positive feedback loop shown in Fig. 6. When vanadium was being deposited on the substrate at roughly 1 A/s, its gettering lowered the oxygen pressure by 20% (with the oxygen input flow rate, 4 sccm, being held constant). Compared to a system with no oxygen input, the presence of 1 mtorr of oxygen requires a 33% increase in filament power to maintain a constant 1 A/s rate. Minimizing the gettering of oxygen was an important reason why the deposition rate was chosen to be only 1 A/s. To achieve that rate, only 6500 V X 0.08 A = 500 watts were required. This is less than 1/10 the rated power of the electron gun system.

The feedback instability occurs only if the electron gun source is operating in the regime of temperature-limited thermionic emission as governed by the Richardson-Dushman equation. The electron gun began showing space charge limited emission for cathode (filament) voltages less than 5700 V. All depositions used 6500 V which is in the temperature-limited regime. In this regime oxygen is a well known "poisoner" of thermionic cathodes[14,15]: when it chemisorbs, the oxygen atom forms a negative ion. This results in a surface dipole layer with the negative pole on

the outside, which raises the surface potential barrier. Thus the filament's work function is increased and the emission decreases exponentially. The well known remedy is the use of thoriated iridium or thoriated tungsten filaments. However, the manufacturer offered no such product. If it were possible to acquire thoriated iridium filaments for the electron gun, this issue would be greatly ameliorated.

As an alternate way of avoiding the positive feedback problem, one might experiment more with space charge limited (lower voltage) operation of the electron gun. VO_2 films were not made in this way because of the trade-off required: higher filament temperature and presumably shorter life. Also the emission increased sharply with voltage (e.g., Langmuir-Child's law), which makes the deposition more susceptible to high voltage instability. Nevertheless by monitoring the filament's resistance, one could determine the temperature and ensure that it was not excessive. Operating in the space charge limited regime is certainly not the orthodox method of electron gun deposition. But that is because of the lower emission currents and evaporation rates, which was not the issue here. Some compromise between the space charge and temperature limited regimes might indeed be the best mode of operation.

In addition to the emission control problems discussed above, high voltage instabilities must be avoided. This is why the low (6.5 kV) gun voltage was used. Initially the

high voltage leads inside the vacuum chamber were sheathed in insulating pyrex tubes. But it was observed (visually) that the pyrex tubes occasionally discharged.

The largest source of instability was fluctuation in the emission current due to the flaking of oxide material in the cavity surrounding the filament. The oxide actually flaked from the "beam former" which was made of tantalum. It was learned that tantalum oxidizes very badly under the deposition conditions here. A more stable deposition and less tedious maintenance work would probably result from using a molybdenum beam former or at least coating the tantalum one. It was verified that the high voltage was stable during these fluctuations. Furthermore one alumina insulator became coated before any of the others. The remedy was to remove the filament assembly prior to <u>every</u> deposition, sandblast, and nitrogen blast the offending parts. These tedious precautions resulted in long term operation with little, if any, arcing. The <u>weak link</u> in the deposition control was invariably evaporation rate instability that resulted from ignoring these precautions.

The "hearth" is the depression in the water-cooled copper brazement of the electron gun into which the vanadium chunks were inserted. No hearth liner was used because it was difficult to avoid hitting it with the electron beam. Other potential problems were oxidation of the liner and alloying with the vanadium. Generally hearth liners are used

to weaken the thermal contact between a low melting point evaporant and the copper electron gun. This is not an issue with vanadium which melts only directly underneath the beam.

The geometry of the vanadium in the hearth was absolutely critical to successful reactive evaporation. The diameter (1'') of the evaporating region on top of the vanadium is 1/9 of the source-substrate distance. So the electron beam's position substantially influenced the geometrical relationships between the source, substrate, and rate monitors. This was particularly true when the vanadium chunk was diminished in size or had holes in it. A four minute, 1200 watt warmup burst (while sweeping the electron beam over wide areas, and with no oxygen in chamber) smoothed and levelled the vanadium. It would also help to use vanadium chunks that are smaller than those used here (0.25'' diameter by 0.5'' long). Sweeping the beam during the deposition over the entire hearth was helpful because it retarded the formation of a trench in the semi-molten vanadium. The "lateral" sweep was actually unnecessary.

Under typical deposition conditions, the filaments lasted about six hours. An aging filament produced a beam that was distended laterally, which then required a higher emission current.

A future improvement of the evaporation control (without any hardware changes) would be to study the angular distribution of the evaporation rate and its dependence on the

electron beam's area (due to the sweeping). It is plausible that the distribution profile of the evaporation rate might be broadened due to wider sweeps. Since the substrate is directly above the gun its deposition rate would be lowered with respect to the crystal sensors.

It helped to attach three layers of steel plates ("shunt bars") to the sides of the electron gun to redistribute the permanent magnetic field lines and thus defocus the electron beam into the largest possible area (Fig. 7). Deposition rate control was degraded by having a vanadium charge four times larger than the electron beam size. The vanadium charge should have a smaller area than the beam, thus minimizing the geometrical irreproducibility. If it is not possible to enlarge the beam further, a feasible improvement is to machine a new copper brazement with a smaller hearth. This would also reduce the radiative heating of the vacuum system and crystal monitors.

A one hour long deposition consumed on the order of 1 gm of vanadium. However, impatience in the pre-deposition warmup typically splattered out three times that much. The hearth, kept full for reasons discussed above, contained about 30 gm. Only acetone and isopropyl alcohol were used to clean a new chunk of vanadium. The entire electron gun assembly was cleaned occasionally by removing it from the vacuum system and glass beading or sandblasting it, without further dismantling.

The state of oxidation of the vanadium in the hearth was not precisely known. Post-deposition inspection revealed that the vanadium was shiny. The top of the vanadium chunk was melted. At the melting temperature of vanadium, the only stable vanadium oxide phase is the alpha phase of vanadium in which there is dissolved less than 1% oxygen.[11]

This was verified by closing the gate valve, and monitoring the amount of oxygen that was required to saturate the vanadium charge. The vanadium was not evaporating because it was heated to only 2/3 the power that it received during depositions. The flow was adjusted to maintain the same oxygen pressure used during depositions. Defining saturation somewhat arbritrarily as the point when the input flow fell from 0.3 sccm to 0.1 sccm, saturation typically occurred in about 45 minutes. This integrates to about 1% of the 0.5 mole of vanadium in the hearth.

Since the vanadium was cooler near the edges it is possible that vanadium oxides were present and were evaporating. A worthwhile improvement on the electron gun configuration, would be to mask off the periphery of the hearth.

In 1 mtorr of oxygen, the collisional mean free path (at room temperature) is about 7 cm. But the oxidation mean free path will be longer. Therefore it is assumed that most of the vanadium is arriving at the substrate as atomic vanadium.

3.3.2 Deposition Rate Monitoring and Control

The basic problem of rate monitoring in the presence of oxygen, is the fact that the crystal monitors measure the rate of mass that is deposited onto them. In 1 mtorr of oxygen, this mass is VO_x. The true vanadium deposition rate could not be monitored completely independently of the oxygen pressure. This compromised one of the most important advantages of reactive evaporation, independent control over the deposition parameters.

The various oxides of vanadium have densities that differ from each other by as much as 50%.[16] If the VO_x film on the quartz crystal changed abruptly from one single phase to another as a function of deposition conditions, this monitoring scheme would be useless.

An Auger depth profile was performed on one of the sensor crystals after deposition. The nominal atomic composition of vanadium was 30% (the rest being oxygen). This agrees very closely with the 28% atomic composition of V_2O_5. The excess vanadium might be another oxide phase or perhaps vanadium metal. The addition of a small amount of metal to V_2O_5 would comprise a cermet which would be expected to be black considering the thickness. Indeed they were always opaque black. It is likely that they appeared black to the eye because light has to make a double pass through the film. The material on the calibration film should be quite similar to that on the crystal. Further evidence of

V_2O_5 comes from glass slides (mounted close to the crystal monitor) which were usually (greenish) yellow and insulating. Slightly higher oxygen pressure caused the film to turn more yellow. V_2O_5 is an amber colored insulator.

To improve reproducibilty, the two quartz crystals were cleaned after every deposition, and reused in the next. The crystals were etched clean of VO_x by a 4 second submersion in a mixture of 45% nitric acid, 27% acetic acid, and 28% HF (diluted with ten times as much water). The gold film electrode was not damaged by such a brief cleaning. Following this came a brief distilled water and then isopropyl alcohol rinse. Ultrasonic cleaning was not used because it dislodged the gold. The manufacturer did make silver coated crystals as well, but gold was chosen because it does not oxidize.

Recall that the VO_x film on the crystal was a V_2O_5 cermet. A cermet deposited on top of a metal is a very good absorber of light from the electron gun source. So another benefit of cleaning the crystals was that the reflectivity was increased five-fold. This was helpful because the crystal monitors were sensitive to changes in the crystal temperature. Shutting off the electron gun abruptly destabilized (raised the rate to 10 A/s) the sensor for only about five seconds. Small changes in the power radiated from the electron gun source would have had much smaller effects than the previous example. Thus heating effects on the

crystal were not a serious problem.

Excessive roughness prevented the accurate measurement of the thickness of the VO_x film on the crystal. This was due to the poor adhesion to the gold electrode. But its thickness is estimated to be about 20% greater than the calibration film.

The two crystal monitor sensors were of different types: "bakeable" and "sputtering". The sputtering sensor included a teflon coated coax cable that could not be used over 105 ^{o}C. This restriction was overcome by threading the coax around the water lines and covering both with aluminum foil. If the cooling water was turned on, the usual vacuum chamber bakeout could then be performed safely. It was essential to orient the sputtering sensor perpendicular to the electron gun source because of the sensor housing's shadowing. The sensor tubing's mechanical flexibility enabled optimum positioning.

The bakeable sensor was mechanically rigid, but suffered no practical restriction on bakeout temperature. It malfunctioned less often than the sputtering sensor because of better contact hardware. However the crystal's thermal contact to the water cooling lines of the bakeable sensor was inferior to that of the other sensor. It helped to insert a 0.002'' thick copper washer between the crystal holder and the sensor body.

The crystals' positions relative to the substrate and

electron gun was very important. The IC-6000 resolution and zero offset noise was on the order of 0.1 A/s. Since the actual deposition rate was roughly 1 A/s, this represents a serious problem unless the crystal sensors receive a rate several times higher. (Programming a false density into the unit can multiply the indicated rate but it also multiplies the noise.) So the source-to-crystal sensor distance was chosen to be roughly 2/3 of the source-to-substrate distance. The resulting three-fold increase of the evaporation rate at the crystal was helpful. It was equally important not to install the sensor too close to the source because of heating effects as discussed above. The sensor destabilized when it was placed closer than 5'' from the source.

The angle between the source-to-sensor line and source-to-substrate line was important in minimizing the irreproducibily in the angular distibution of the vanadium evaporation. The angle for both of the sensors was roughly 20°. There was no danger of heating the sensor by radiation from the hot substrate because the crystal sensor was mounted below the substrate heater and the water cooled housing was the top part of the sensor's body.

3.3.3 Thickness Calibration

There were several problems in obtaining a thickness measurement that could check the vanadium deposition rate. Most VO_2 films were too textured for thickness measurement.

Even if they weren't, their thicknesses were functions of other deposition variables and not just of the vanadium evaporation rate.

To circumvent this problem, a "calibration" substrate was used as shown in Fig. 8. It was an ordinary microscope slide, cut to 0.25'' by 1'', and mounted 2'' from the sputtering sensor. The calibration substrate was greased (Apiezon H) to a copper block which was machined to clamp around (using Apiezon H grease, as well) the water cooling lines of the sputtering sensor. It was very important that alignment was identical for every deposition because the thickness of the calibration film could sometimes vary by 20% over a distance of 2.5 cm.

The result was a very smooth VO_x calibration film whose thickness was measured on a Tencor Alpha-Step (stylus type) surface profiler. All measurements were performed on the same full scale range (100kA). A sharp and reliable edge was obtained by simply scraping the calibration film from the glass with a new razor blade. For an 80 minute deposition at a nominal (non-physical) rate of 5.3 A/s, the thickness of the VO_2 sample was about 2800 A. The calibration film was about 2.9 microns thick.

In the narrow range of evaporation rate and oxygen pressure that were used to make good VO_2 films, it was found that this calibration film's thickness divided by the deposition's duration, the "calibration rate", could be correlated with

the vanadium deposition rate. So by this rather circuitous route, it was indeed found that the reactive evaporation process offered "independent" control of the vanadium deposition rate.

But more importantly, it was learned that the calibration film's color provided extra fine tuning of the vanadium evaporation rate. Within the "good VO_2" range as defined by the calibration film, it was possible, with some experience, to inspect the calibration film's coloration, and then to adjust the oxygen pressure in the next deposition. In the restricted range that made good VO_2 films, the calibration film was yellow-green. Raising the oxygen pressure by two percent or lowering the rate by five percent caused its color to become more yellowish. This trick was very important to the success of this project because the Alpha-Step measurements on the calibration films were only reproducible to 5% which was larger than the capabilities of the rest of the process. Subjective judgement of the color succeeded only because nearly equal thicknesses were compared. For a quantitative treatment, the calibration film's coloration (and reflectance maxima) could have been measured on a spectrophotometer, but that was not necessary. This entire calibration procedure was completely independent of the substrate temperature.

Referring to Fig. 2 we see that two independent complete crystal monitor systems were used. The control unit

(IC-6000) was microprocessor based, and had programmable, feedback parameters. Their output control voltages (0-10 V) were averaged before being received by the electron gun control module. A possible improvement might have been to average the two input signals (from the sensors) at one IC-6000. But the control units could not monitor two sensors simultaneously. The two control units were programmed with identical process control parameters except for the evaporation rate set points since the two sensors received different leposition rates. The mean set point was constant throughout the entire deposition. It was determined by the calibration procedures of the previous paragraph. Each individual set point was adjusted periodically during the deposition to that value which caused its output control voltage to equal that of the other sensor under the constraint that the mean set point remain fixed. The 10% drift between the two monitor's set point was proof of the unreliability of this scheme of rate control. This is thus the weak link in the entire system and must be overcome before there is any substantial improvements in the success of the method.

Reactive evaporation was stable only for the very lowest gain setting of the IC-6000. A 10% change in evaporation rate required only a 1% increase in the electron gun filament current. This was due to the exponential temperature dependence of electron emission from the filament and the exponential temperature dependence of the vanadium

evaporation rate. Therefore it is highly recommended that future work insert a simple logarithmic amplifier between the crystal monitor control unit and electron gun control module. This would exploit the wide dynamic range of the IC-6000.

It has been mentioned that the V:O flux ratio at the substrate had to be controlled to 5% to make good VO_2. This means that the semiconductor-metal transition decreased tenfold if the mean set point of the crystal monitors was varied by more than 5% from the ideal settings as determined by the last calibration. But on a shorter time scale the indicated vanadium evaporation rate varied about 10% on a time scale of 3 secs. During that time less than a monolayer of VO_2 was deposited on the substrate. Control over the evaporation rate is more important over longer time spans. To achieve this the integrated thickness output from the crystal monitor electronics unit was plotted on a chart recorder to compare it directly to a 100 second linear ramp. Trends on this longer time span would then be used for periodic adjustments of the <u>mean</u> set point. This latter technique was only occasionally used.

During the deposition, the throat connecting the vacuum chamber to the cryopump was constricted, or throttled, by a variable orifice. Used in its nominally closed position, it reduced the effective pumping speed at the chamber by 250%. This reduced the oxygen consumption and lengthened the interval between cryopump regenerations. The disadvantage of

reducing the oxygen flow was that it caused the gettering by the vanadium evaporation to be larger relative to the other flow rates. It was unnecessary to throttle the pump to avoid warming up the cryopump as is mandatory for sputter deposition. This was a significant potential advantage of the reactive evaporation process: residual gas pumping need not be diminished during the actual deposition. Nevertheless the pump was throttled as described above, mainly for historical reasons. Using the orifice thusly, dozens of deposition hours separated cyopump regenerations.

3.4 Oxygen Pressure Control

3.4.1 Monitoring Methods

Three oxygen measurements were performed by: an ion gauge tube on the chamber, the differentially pumped mass spectrometer (RGA), and an MKS flowmeter on the inlet.

With such a high pressure, the oxygen pressure was to a good approximation equal to the total pressure as read by the ion gauge tube. The background gases summed to less than 10^{-5} torr if the liquid nitrogen trap was used. The day-to-day variations in the H_2O:oxygen ratio were 1% absolute (again, using the cold trap). Without using the cold trap, the water vapor could more than double. Recall that visible changes in the VO_2 samples resulted from changes in the nominal oxygen pressure of only 1%, so the water vapor was an important factor.

The ion gauge tube was a hot cathode, Bayard-Alpert tube. Even though the ion gauge tube had a thoriated iridium filament, its reliability was questioned because of the high oxygen pressure. The controller was set to its lowest emission current (0.01 mA). It was degassed for 3 minutes before every deposition. The tube lasted for at least 150 hours at 1 mtorr of oxygen.

A better choice might have been a tube of the Schulz-Phelps design which is meant to work at higher pressures.[12] Or it might have been advantageous to avoid hot filament tubes altogether and use a Penning gauge.[12]

Instead, a readily available alternative was studied: an MKS capacitative manometer. It had an unacceptably large zero offset drift of roughly 1%, when operating at 1 mtorr. How much of this was due to the cryopump vibrations is unknown. When operating near 1 mtorr, the manometer also had fewer display digits than the ion gauge controller.

The ion gauge tube readings of the total (mostly oxygen) pressure were supplemented by the RGA. The latter sensed the pressure only 1'' from the substrate through a flexible bellows interconnect (Fig. 9). The RGA was by necessity differentially pumped, here, by a small turbopump mounted immediately next to it. This method had the advantage of operating at an oxygen pressure 100 times lower than the vacuum chamber. Still it was found that the hot tungsten filaments were unstable, necessitating the use of thoriated

iridium filaments. Because of the close sensor-substrate distance and the ability to differentiate partial pressures, this RGA scheme was extremely helpful.

Thus there were two pressure monitoring methods in use on a regular basis. Either one could have been used in the oxygen control feedback loop shown in Fi. 3. But usually the ion gauge tube was used in the loop, due to its more rapid response. The effective conductance between the turbo-pump (and RGA) and the substrate was determined to be 0.8 l/s. Therefore the time constant was about 5 seconds.

Normally the ion gauge controller displayed the pressure mantissa with only 2 significant digits (2 1/2 in overflow mode) The rear panel output signal which was proportional to the pressure mantissa had one more significant digit.

The oxygen flow (roughly 4 sccm) was controlled in proportional mode with a Granville-Phillips APC flow control valve, which performed superbly. The controlling electronics was the Granville-Phillips Series 216 controller. The controller was used with a derivative setting of 3 which corresponded to a 2 second time constant. The time constant of the vacuum chamber itself was much faster: its volume (100 liters) divided by the throttled pumping speed (300 liters/sec), is 0.3 sec. The time constant of the tubing between the oxygen control valve and the chamber was 0.04 seconds. The time constant of the controller was chosen to be 3 seconds because it resulted in slower response than the

evaporation control loop, which was desired. In other words, the oxygen control loop was a low frequency loop on top of which was the higher frequency evaporation loop.

A possible future improvement would be to feed the electron gun emission current back into the pressure control loop. The control valve would be able to respond as quickly as the upcoming change in evaporation rate (and hence pressure, see Fig. 6). Thus the positive feedback loop could be broken.

The pressure controller's reset rate setting was set at about one-third maximum. Its gain setting was about 80% of the maximum. Such a high setting was necessary because the flow (about 4 sccm) was an appreciable fraction of the valve's maximum throughput (30 sccm for an 85 psi inlet pressure). The flexible steel bellows used between the oxygen cylinder (Matheson, UHP, 99.99% pure) and the valve were rated for 100 psi maximum.

Flow rate monitoring was done with an MKS Model 254 Pressure/Flow unit. The operating principle of the rate - meter was the measurement of the temperature difference between two thermocouples with one mounted downstream of the other. A heater is placed between the two controllers. The flow is proportional to the reciprocal of the temperature difference. The flow meter was MKS model 258, rated for 100 sccm. The instrument was not used to <u>control</u> flow but only to monitor it.

The process as described above used strictly upstream control. It is possible to set a steady input flow and maintain a constant pressure, by adjusting the variable orifice between the chamber and the pump (downstream control). This was done in the following way: the deposition was begun with the orifice completely closed. After 5 minutes of completely upstream flow control, the orifice was opened slightly every 5 minutes to maintain a constant flow (the pressure was being controlled automatically on a much shorter time scale). Thus there was a long time constant, manual downstream flow control supplementing the continuous and automatic upstream control.

3.4.2 Fine Tuning the Oxygen Set Point

RGA peak heights were unreliable and inconsistent with the readings of the chamber ion gauge, another ion gauge mounted at the turbopump, and the total pressure readings of the RGA itself. This was true even after careful maximization of the peak. The heights fell 10%/hour even though the total pressure was constant. This could not be corrected by decreasing the mass resolution. It probably follows from the fact that the integrated area under the peak, not the height alone, was proportional to pressure. The mass resolution was permanently set at 1.5 atomic mass units (an instrument setting of 7.5).

Oxygen was of course the main gas at the RGA, too. It

was about 95% of the total pressure and varied from day-to-day by about 1%. The largest irreproducibility was the water partial pressure. This was minimized by filling the cold trap, by careful and consistent bakeouts, and internal cleaning after every sample. Since the base pressure of the turbopump was in the low 10^{-8} range, the RGA spectra should be very similar to the chamber. (The turbopumping speeds of the important gases were similar.) Thus the RGA total pressure reading was a good measure of the chamber total pressure. The consistency between the RGA total pressure and the chamber ion gauge was about 2% on a day-to-day basis. Thus inconsistency larger than this was evidence for some vacuum system problem such as the misalignment of the oxygen inlet tube (Fig. 9) or a decrease in cryopumping speed.

It was decided that the oxygen pressure would be measured primarily by the chamber ion gauge supplemented (or fine tuned) by the RGA data. In other words the oxygen pressure was taken as being equal to a constant multiplied by the chamber ion gauge reading. That constant was near unity, and was determined from the RGA spectra. The higher the sum of the non-oxygen partial pressures <u>relative</u> to the oxygen, the smaller was the proportionality constant. In that way only relative RGA peak heights were used.

The RGA and turbopump station were separated from the chamber by a shutoff valve. When not in use, the RGA was

always pumped on by the turbo. It was left in the total pressure mode which kept the filaments warm. The total pressure mode regulated the emission current at .745 mA. The partial pressure mode used a 1.89 mA emission current which was near its optimum range, that is, the region in which the ion current was least sensitive to the emission current. The partial pressure readings were done with a very low, "Channeltron" electron multiplier voltage (13.0 V on the instrument test point). The gain was quite low: 770 for water. The pressure was so high at the RGA, that a higher gain would have saturated the detector electronics.

During a deposition (with the pressure and throttle adjustment constant) the flow decreased about 8% if the vanadium charge had been saturated in the manner described below. This decrease in flow was due to saturation of the vanadium charge at the higher power. The gettering by the vanadium on the walls was constant during a deposition.

It was important to use a pre-deposition warmup procedure that resulted in reproducible flows but avoided substrate contamination. Saturating the vanadium charge with 2/3 the deposition power was not sufficiently efficient to justify the time. If full deposition power had been used, the substrate would have been contaminated even with the shutter closed. This was actually verified, and might seem surprising considering that the shutter was very large. But the mean free path was 7 and the electron gun to substrate

distance was four times this. In fact a one hour deposition coated surfaces that were completely out of line-of-sight and even facing away from the electron gun.

The flow can be accounted for as follows: about 15% was gettered by vanadium deposited on the chamber walls. Roughly 2% was consumed by the vanadium charge itself. The remainder was consumed by the cryopump.

The relationship between the RGA total pressure and the chamber ion gauge can be illustrated as follows:

1. High vacuum valve closed.
2. Chamber backfilled with oxygen and everything saturated.
3. RGA total pressure reading the typical deposition value (1.63 10^{-5} Amp).
4. Then chamber ion gauge reads 9 10^{-5} torr.

As a second case the system could be under conditions identical to a deposition except that the electron gun is off. The two pressure readings were virtually identical to the above.

Thirdly, during the deposition, with the same RGA total pressure as above, the chamber ion gauge read 12 10^{-4}, which is 33% higher than when the electron gun was off. In other words, the evaporation of vanadium significantly lowers the local substrate pressure with respect to the average chamber pressure. The reason is that the gettering is more intense closer to the electron gun. This undesirable effect is

minimized through the use of the oxygen inlet tube (Fig. 9).

3.5 Film Temperature Control

The physical properties of VO_2 depend critically on the substrate temperature. Therefore the design of a suitable substrate heater was a critical part of this work. Because of the high temperatures needed (over 500 ^{o}C) and the high oxygen ambient (1 mtorr), the heater had to be specially designed.

3.5.1 Substrate Heating Schemes

In general, substrate heaters fall into two categories: radiant or thermal contact. The first type uses an internal quartz lamp that is radiating several hundred watts. The light is focussed onto the substrate as tightly as possible with a metal reflector behind the lamp. Such units are available commercially. Since the tungsten filament is inside the lamp, it will not be destroyed by the high oxygen pressure. Lamp replacement results in little down-time. The radiant heater is of course electrically isolated from the substrate which is important for RF or bias sputter deposition and ion plating deposition. Radiant heating heats the <u>film</u> directly. Therefore the heat flow into the film and underlying substrate is relatively uniform laterally. It is relatively easy to scale up the substrate size when using this technique. Being mechanically isolated from the sub-

strate, the substrate can be continuously spun during deposition to improve film uniformity. Large scale continuous feed coating systems and planetary carousel deposition systems therefore almost always use this type of heating.

On the other hand, the high oxygen ambient is likely to oxidize and darken the reflector unless its surface is coated with platinum. The focussed light is not likely to be strictly limited to the substrate. So one can expect considerable outgassing from the needlessly heated reflector and other internal hardware. A radiant heater takes up much more space than a small thermal contact heating block. It requires an unobstructed line of sight through which it makes relatively normal incidence on the substrate. Any change of that angle of incidence requires a separate temperature calibration. The radiant heater must be shielded from being coated by the evaporation source or it must be cleaned after every deposition.

The fraction of incident radiation that is absorbed by the film, the absorptivity, is a function of the intrinsic optical properties of the film, its thickness, and morphology. All of these are changing during the deposition. A tungsten filament at 2800 K has a peak in its blackbody distribution at about 1.2 microns. At that wavelength, the reflectance of a growing metallic VO_2 film will rise sharply with wavelength, and the position of this edge will vary sharply with film thickness. Radiant heating is not less

affected by the separate question of how to monitor the <u>film</u> temperature.

The second scheme, thermal contact to a heated block, has different trade-offs. The block can be heated by either thermal conduction or radiation from a filament or lamp. Thus one can have a hybrid system in which the film is primarily but not exclusively heated by thermal contact to a block. But let us keep the two categories separate and discuss substrate heating by one mechanism alone: thermal contact to a heater block. The issue of how that block is heated is a separate one and will be discussed later.

It is easy to assure lateral uniformity in the block temperature by making the slab thick enough and by using a high thermal conductivity metal. But it is difficult to maintain lateral uniformity across the substrate and film. Thermal contact heating has the advantages of requiring little space, the capability of achieving higher maximum temperatures on small substrates, and being independent of the film's optical properties.

The lateral uniformity of the substrate and film is made difficult by the simple fact that two solid pieces make thermal contact over a very small area. This effective contact area can be lowered drastically by dust, poor polishing, warping, and non-flatness. These factors are very irreproducible from sample to sample. However, they are fairly constant during the deposition, unlike the problems with the

radiant heater. The substrate must be clamped onto the heater block here because of the configuration of an evaporation system (Fig. 1) and for better thermal contact. Since we are concerned with substrate temperatures above 500 ^{o}C, the linear thermal expansion coefficients must be chosen to be nearly equal. Good thermal contact can not be assured with any known thermally conductive grease. Liquid metal schemes were not used because of the inconvenience possibility of contamination. The substrate heater will oxidize and perhaps evaporate, contaminating the film. Although thermal contact heating does not depend of the growing film's changing optical properties, the emission from the film will change.

The problem of measuring the film temperature is not easier with one type of heating than the other. Although one sometimes encounters in the literature the argument that thermal contact heating suffers the drawback that film temperature is lower than the heater block, this is not in itself a serious disadvantage as long as that gradient is reproducible. At least the film on a contact heater is always cooler than the heater block. However, for a radiantly heated film, the film could be hotter or cooler than its mounting plate depending of the relative absorptivities and emissivities.

If an optical pyrometer could measure the film temperature, one could control the power going to either type

of heater to maintain constant film temperature. But for this system, a pyrometer would have been very awkward to use because of geometrical constraints. It must be admitted that pyrometers which use optical fibers are becoming commercially available so that the geometrical problems could be surmounted more easily. But one is still left with the problem that the pyrometer needs to be calibrated according to the film's optical properties which are changing. A possible remedy is to focus the pyrometer on a corner of the substrate which is shielded from being coated. In any case, preference was given here to thermocouple schemes because they were more readily available. Measuring the temperature of the heater block was easy. A thermocouple was inserted into a hole in the block. To ensure tightness, it was jammed in with a copper wire.

In summary radiant heaters are preferred for large substrates: they provide better sample-to-sample reproducibility than intra-sample uniformity. Thermal contact heaters are preferred for small substrates, very high temperatures, and offer better uniformity during a deposition than consistency from sample-to-sample. Both heating schemes will suffer the problem that the film temperature will be different than any metal plate in contact with it. The problem at hand therefore is devise a better thermal contact heater in which one can better control and measure the film temperature.

3.5.2 Specially Designed Substrate Heater

Fig. 10 show a schematic of the substrate heater used for all samples. It is a thermal contact heater which can operate routinely to 1000 ^{o}C. The materials were specially chosen. The small gold blob melted onto the substrate prior to pumpdown enabled accurate film temperature measurement. Alternatively aluminum foil was placed between the substrate and the heater block.

The heater's design evolved from a more conventional design: a copper block, drilled through with many holes which contained thermocouple tubes, and resistive wire threaded serially through all the tubes. Earlier it was found that a heater such as this could not be used routinely over 500 ^{o}C in vacuum: the copper annealed, and it showed poor reproducibility of the film/block temperature difference. In 1 mtorr of oxygen, it would have burned out in minutes, even if the resistive wires had been stranded. The latter required the time-consuming rethreading of the tubing array. The turns at the ends of the loop were a constant source of hot-spots and burnouts.

The heater of Fig. 10 was built out of molybdenum. A refractory metal like molybdenum has a high melting temperature (2617 ^{o}C), so that it does not anneal in the 500-1000 ^{o}C range. Also its thermal expansion is low, as is that of the dielectric substrate. Molybdenum is hard, resists scratchs, and machines easily. Machining speeds were 30% faster than

typical stainless steel speeds. Molybdenum (Teledyne Wah Chang, Huntsville, Alabama) with a purity of 99.7% was only 15 times more expensive than machine shop quality stainless steel. Its thermal conductivity is high: one-third that of copper.[17]

Molybdenum will oxidize in this system's environment. This is not an issue as long as the temperature is not too high. MoO_3 evaporates near its melting temperature of 795 °C.[18]

The heater consisted primarily of two hollowed-out blocks. The tungsten filament was mounted through holes in the "front" half of the heater (the half with the substrate mounted on it). The thermal contact between the filament and heater was no doubt poor and irreproducible, but this did not matter because the other half of the heater served as a reflector. Thus the radiated power from the filament was trapped in the box-like heater, minimizing wasted power and unnecessary outgassing.

The heating element was a tungsten filament evaporation source. These filaments (R. D. Mathis Co., Long Beach, Ca.) were very inexpensive and easy to replace. The helicity helped the filament to resist sagging (and shorting out). The increased length increased the radiation and resistance, the latter enabling a lower current power supply. The filament was chosen to be large in diameter and multi-stranded to avoid hot spots. It had three strands, each 0.025'' in

diameter.

The filament was consumed after seven hours of usage. Replacement required the dismantling of the heater. At this opportunity, the assembly was sandblasted. The substrate mating surface was ground with 600 grit SiC paper. It is important to note that polishing on a metal polishing wheel is likely to produce non-flatness. So glass discs were used as discussed later. To avoid pinching off pieces of disposable plastic gloves during the reassembly, it was done bare-handed and then cleaned. Ulrasonic cleaning would have loosened the bolts, so cleaning consisted of boiling in isopropyl alcohol.

Electrically, the heater was single-ended: one end of the filament was grounded to the heater block. To heat a substrate to 600 ^{o}C, the power required was 20 watts (1.3 VAC, 15 A, 0.09 Ohms). Using the calibration tables in the back of the Mathis catalog, the filament temperature is estimated at 2000 ^{o}C. The current was brought to the heater through a flexible braided copper sheath that had been stripped from an RG-8 coax cable. The small block in Fig. 10 was also molybdenum but its screws were 0-80 stainless steel. Because of expansion and the usual bad contact between two hard pieces, a 0.003'' thick piece of Mo foil was inserted between the filament and this small block. The same was done on the grounded end of the filament. This improved electrical stability considerably. (Although

tantalum is softer than molybdenum and might have seemed a better choice, it was found that it completely oxidized and disintegrated.) The filament was insulated from the block on the one end by using a short piece of alumina thermocouple tubing. The second piece of alumina was a thin annulus. (It was cut from a high voltage stand-off of the electron gun filament assembly.) It supported the weight of the small molybdenum block and current input cable. Although this insulator became coated with VO_x, its resistance was still several orders of magnitude higher than the tungsten filament.

The screws and nuts that clamped the substrate to the heater's front half were machined out of molybdenum. All others were ordinary stainless steel (0-80), including the bolts connecting the two halves of the heater block. These bolts extended to a stainless steel plate which supported the heater and completed the circuit to the chamber (ground). They had sufficiently low thermal conductivity and sufficiently high electrical conductivity. The one steel screw in the tapped molybdenum hole shown in Fig. 10 did not lock-up because the hole had been drilled oversize.

Originally steel bolts were also used to clamp the substrates. But upon heating to 400 ^{o}C, the steel's relative expansion released the substrate. Ideally the bolts should have a linear expansion slightly less than that of the substrate. Again a refractory metal was needed. Ti bolts were

available commercially, but molybdenum ones were not. Because molybdenum has a thermal expansion slightly lower than sapphire, it was the metal of choice. The holes for the molybdenum bolts and nuts were made two sizes oversized to avoid lockup. The two molybdenum mounting bars were machined to catch the substrate as shown in Fig. 10.

Because of the small amount of tightening of the molybdenum with respect to the sapphire, overtightening would have damaged the bolts or broken the substrate. To overcome this, a 0.001'' thick piece of soft aluminum foil was placed between the substrate and heater. This actually served a much more important function. It was seen to deform and compress. This increased the thermal contact and made it more uniform laterally.

3.5.3 Film Temperature Measurement

Only 1 mwatt was conducted away by the thermocouple wires (0.005'' diameter). The effective thermal contact between the gold blob and substrate was very high. From now on, the film temperature will be considered identical to the thermocouple reading.

Estimating the emissivity of the film and substrate as 0.3, only 2 watt/cm^2 was radiated at 600 ^{o}C. Therefore there was a heat flow of only 2 watts from the heater, through the aluminum foil, substrate, and film, and into the chamber. To conduct 2 watts through the substrate with a 10 ^{o}C

(front-to-back) difference, only 0.01% of the block-foil-substrate interface had to be making contact. Two watt/cm^2 through the 0.025'' thick sapphire substrates requires a 2 ^{o}C gradient. The gradients for fused quartz and TiO_2 substrates will be slightly higher because of their lower thermal conductivities.

A second thermocouple was inserted into the heater block, close to the substrate. Comparison of the two thermocouple readings correlated the different substrate mounting schemes. When the substrate was mounted directly on the heater block, it was found that the film was 80-120 ^{o}C lower than the block. This occurred because of the poor thermal contact between two solid, hard flats. The large irreproducibility was due to dust, surface polishing, waviness, etc. If the emissivity of the heater block surface could have been fixed at the sum of the emissivities of the film and the (inside) face of the substrate, a small temperature gradient could have been assured by radiation alone. However, these values changed during the deposition and from sample-to-sample.

When 0.001'' thick aluminum foil was inserted between the substrate and the block, the film temperature was only 4-9 ^{o}C lower than the block. The aluminum foil worked so well because of its softness and its high thermal expansion. The melting temperature of aluminum is 660 ^{o}C, which is only 60 ^{o}C higher than the block. However, the vapor pressure of

aluminum is only 10^{-9} torr at 600 ^{o}C.[13] (No appreciable evaporation occurs until the vapor pressure reaches 10^{-2} torr.) It is possible that thicker or pre-annealed aluminum foil would have worked even better.

As long as the substrate temperature did not exceed 610 ^{o}C, the aluminum foil did not stick badly (for a one hour deposition). The aluminum foil was easily removed with mixture of 2:1, H_2O:NaOH applied with a cotton swab. It is likely that a clamping box instead of two parallel rails would have reduced this gradient. But here, the gradient was not altogether undesirable. Care was taken to ensure that the aluminum foil was flat and uncreased when it was being installed.

Since the sapphire substrates stuck to the aluminum foil for depositions longer than one hour, it was necessary to coat one side of the foil with a thin film of niobium. About 3000 A of niobium was sputter deposited onto the aluminum foil. Alternatively, copper (0.001'' thick) was used instead of aluminum. But this resulted in a 10-15 ^{o}C temperature difference between the block and the film.

4. Extending the Deposition Process

It would of course be desirable to accelerate the 1 A/s deposition rate used here. No effort was made to increase the deposition rate since uniformity and perfect VO_2 stoichiometry were more important. Earlier work showed that

a higher oxygen pressure was necessary with a higher deposition rate. Tolerance of this higher oxygen pressure is then the main question since it affects almost every aspect of the system adversely.

For example, the electron gun arced for any oxygen pressure higher than 2 mtorr. Above 5 mtorr the electron gun initiates a very pronounced DC glow discharge which makes it impossible to evaporate. Therefore for pressures even 30% higher than the 1.2 mtorr used here, the system's configuration would have to be changed. Most trivially, a shield could be inserted between the substrate and the electron gun, with the oxygen being injected above the shield. This compartmentalization of the chamber into high and low pressure cells could be carried further by a different chamber design that essentially differentially pumped the two cells.

The problem of positive feedback with the electron gun filament operating in the normal temperature limited emission region would get worse at higher oxygen pressures without a differential pumping scheme. So use of the electron gun in the space charge limited should be used.

The ion gauge tube should be replaced with one of the higher pressure tubes as discussed earlier. Alternatively, one could rely totally on the differentially pumped RGA. The cryopumping would not be seriously affected until the oxygen flow increased by a factor of four. After that tighter throttling would be necessary.

In summary, the deposition rate could at most be doubled with only minor modifications of the present system. Further increases are certainly possible but only if the system was redesigned.

References

1. J. C. C. Fan, Ph.D. thesis, Harvard University, 1972.
2. A. A. Gur'yanov, and E. I. Terukov, Sov. Phys. Tech. Phys. 25, 538 (1980).
3. J. B. MacChesney and H. J. Guggenheim, J. Phys. Chem. Solids 30, 225 (1969).
4. J. B. Goodenough, J. Sol. St. Chem. 3, 490 (1971).
5. T. Takagi, Thin Solid Films 72, 1 (1982).
6. L. A. Ladd and W. Paul, Sol. St. Comm. 7, 425 (1969).
7. C.N.R.Rao and K. J. Rao, Phase Transitions in Solids (McGraw-Hill, New York, 1978).
8. R. Bunshah, Thin Solid Films 80, 255 (1981).
9. C. H. Griffiths and H. K. Eastwood, J. Appl. Phys. 45, 2201 (1974).
10. J. B. MacChesney, J. F. Potter, and H. J. Guggenheim, J. Electrochem. Soc. 115, 52 (1968).
11. J. Stringer, J. Less Common Metals 8, 1 (1965).
12. J. F. O'Hanlon, A User's Guide to Vacuum Technology (Wiley, New York, 1980).
13. L. I. Maissel and R. Glang,editors, Handbook of Thin Film Technology (McGraw-Hill, New York, 1970).
14. W. B. Nottingham, in Handbuch der Physik, vol. XXI, ed. S. Flugge, (Springer-Verlag, Berlin, 1956).
15. I. G. Hermann and P. S. Wagener, The Oxide Coated Cathode (Chapman and Hall, London, 1951), p. 55.
16. M. Neuberger, Data Compilation on Vanadium Oxides (Electronic Properties Information Center-IR-79, Hughes, 1971).
17. Y. S. Toulokian, Thermophysical Properties of Matter (IFI/Plenum,New York, 1970), vol. 1.
18. E. A. Gulbransen and W. S. Wysong, Metal Technology 14, 628 (1947).

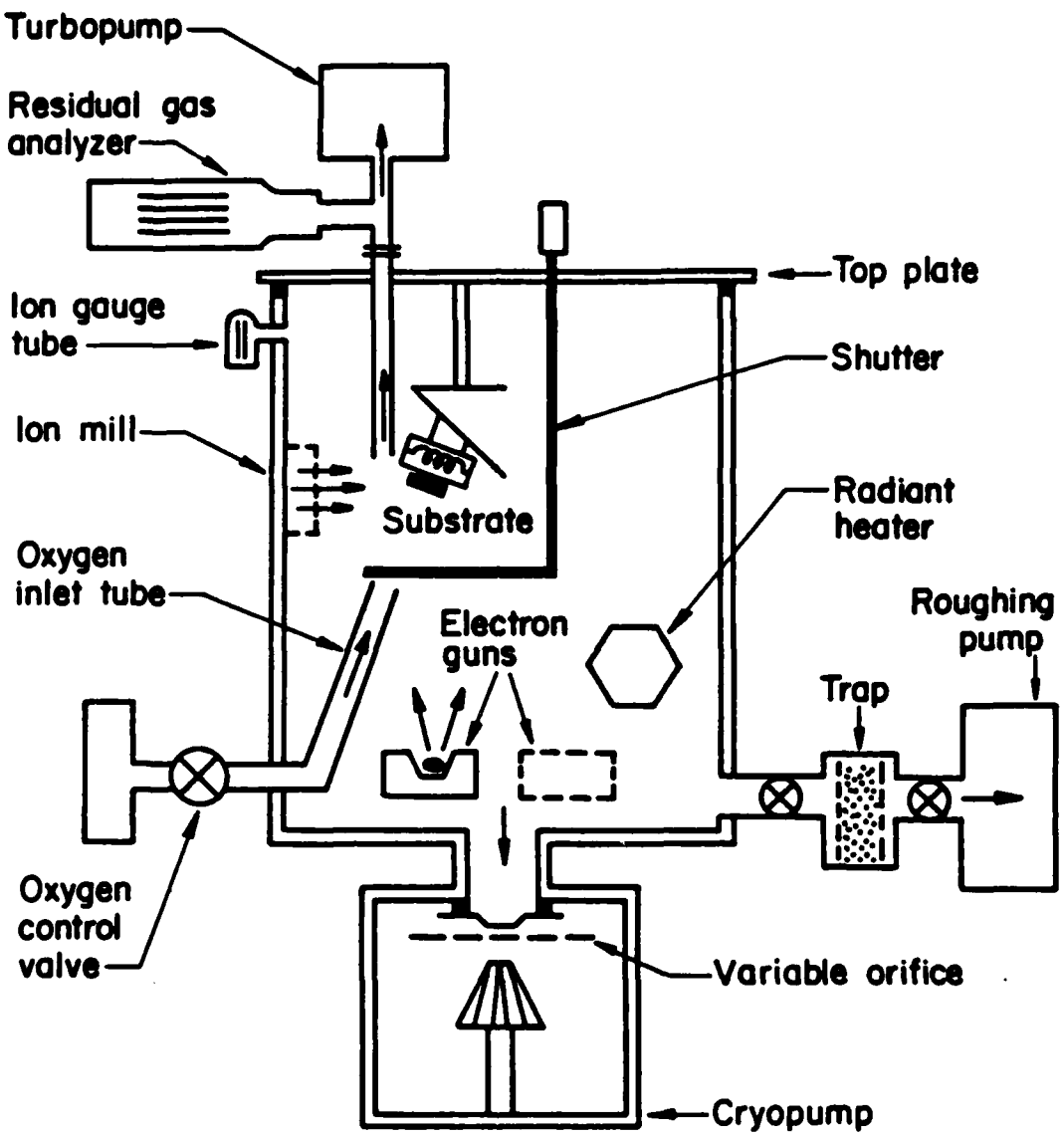
Turbopump
Residual gas analyzer
Top plate
Ion gauge tube
Shutter
Ion mill
Substrate
Radiant heater
Oxygen inlet tube
Electron guns
Roughing pump
Trap
Oxygen control valve
Variable orifice
Cryopump

Figure 1.

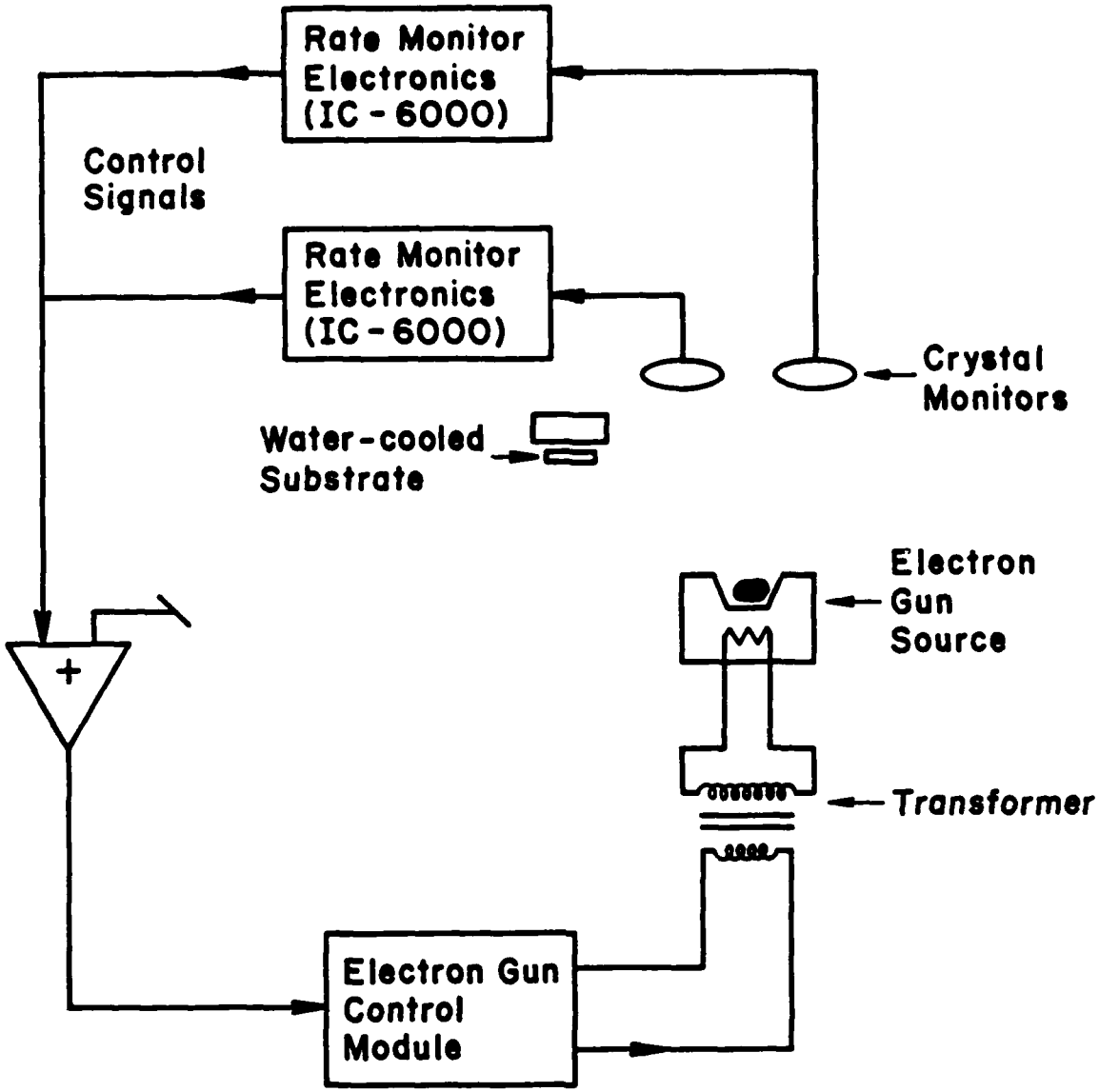
Rate Monitor
Electronics
(IC - 6000)
Control
Signals
Rate Monitor
Electronics
(IC - 6000)
Crystal
Monitors
Water-cooled
Substrate
Electron
Gun
Source
+
Transformer
Electron Gun
Control
Module

Figure 2.

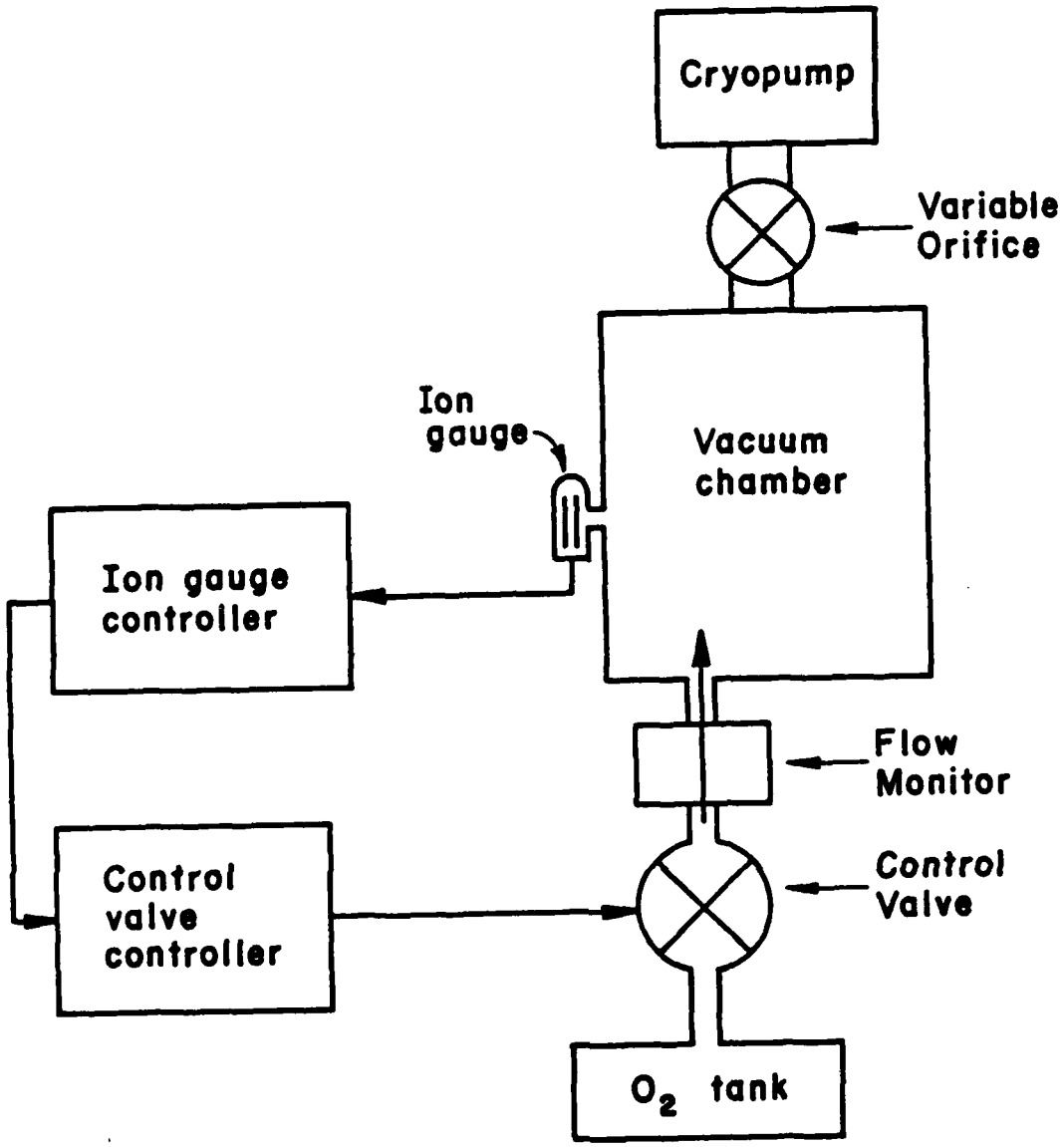
Cryopump
Variable Orifice
Ion gauge
Vacuum chamber
Ion gauge controller
Flow Monitor
Control valve controller
Control Valve
O_2 tank

Figure 3.

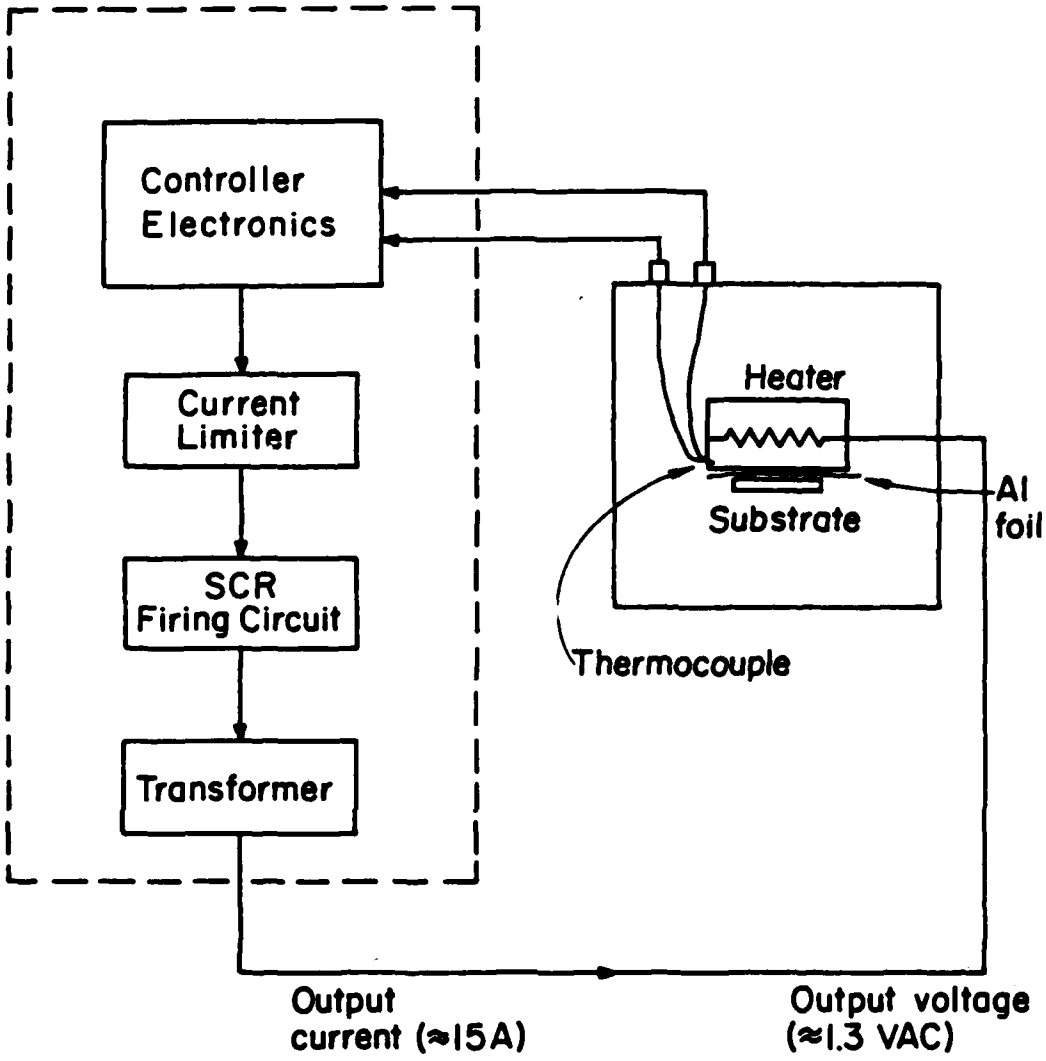
Controller
Electronics
Current
Limiter
SCR
Firing Circuit
Transformer
Heater
Substrate
Al
foil
Thermocouple
Output
current (≈15A)
Output voltage
(≈1.3 VAC)

Figure 4.

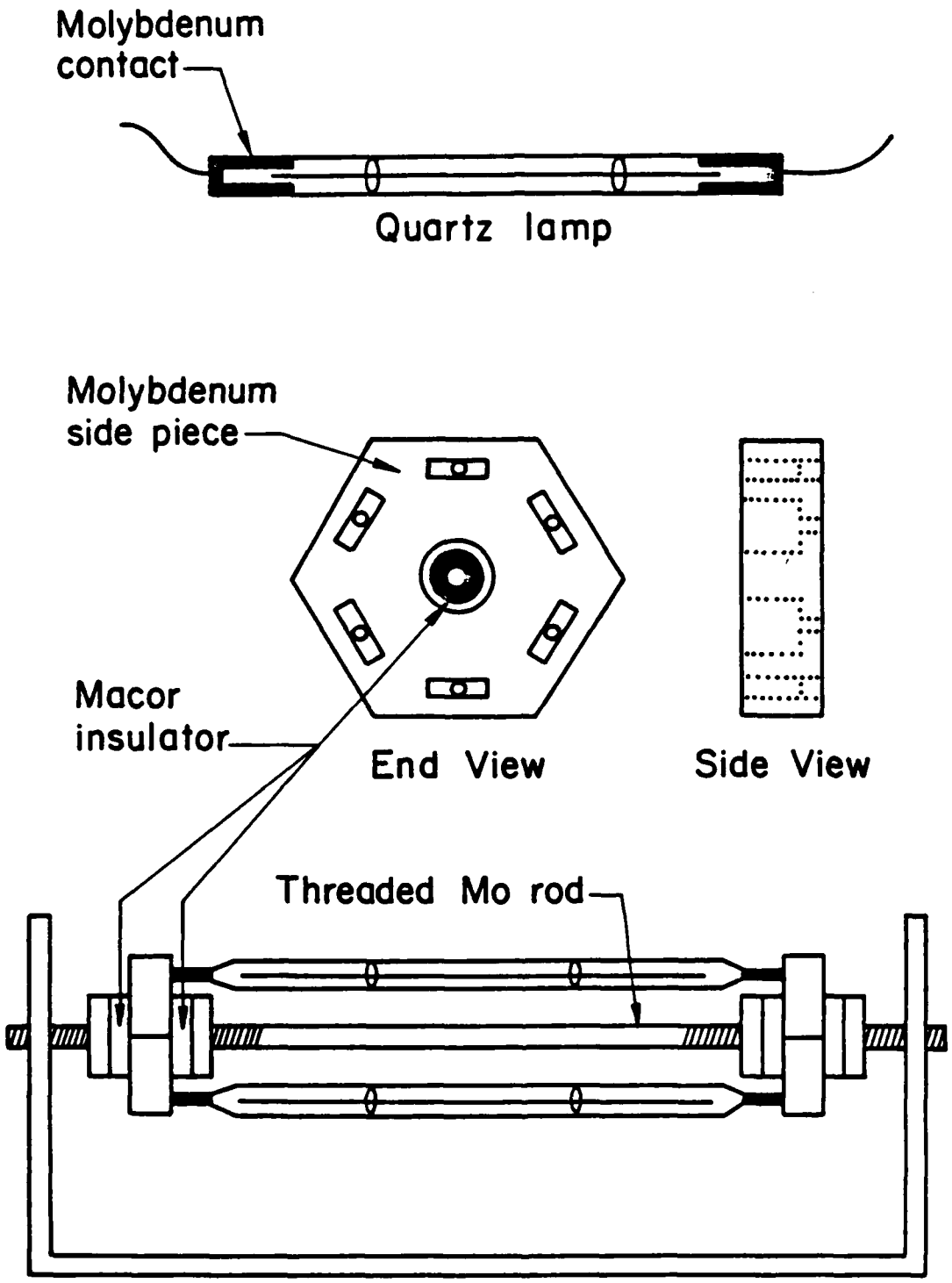
Molybdenum
contact
Quartz lamp
Molybdenum
side piece
Macor
insulator
End View
Side View
Threaded Mo rod

Figure 5.

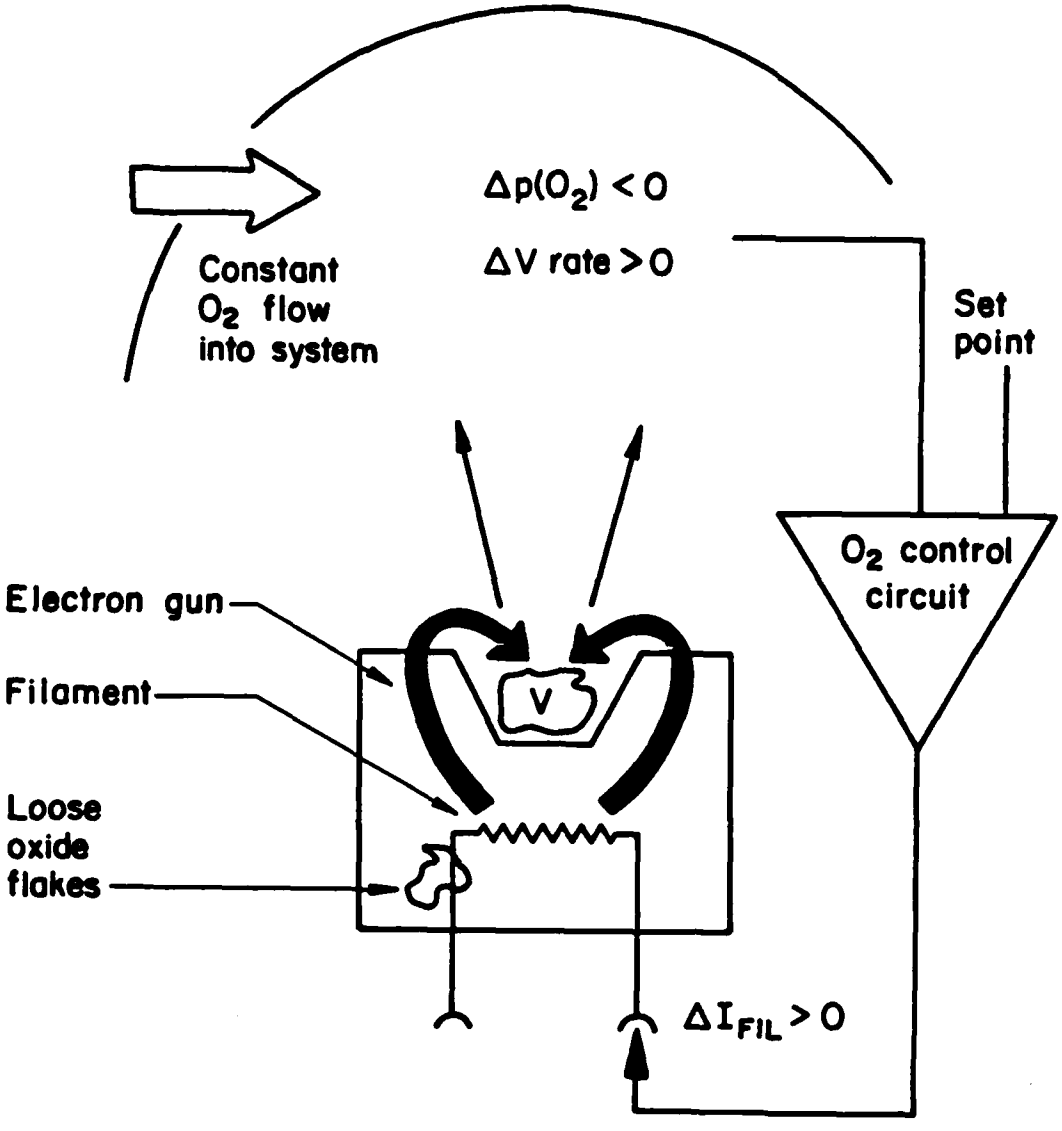
Δp(O2) < 0
ΔV rate > 0
Constant
O2 flow
into system
Set
point
O2 control
circuit
Electron gun
Filament
Loose
oxide
flakes
V
ΔIFIL > 0

Figure 6.

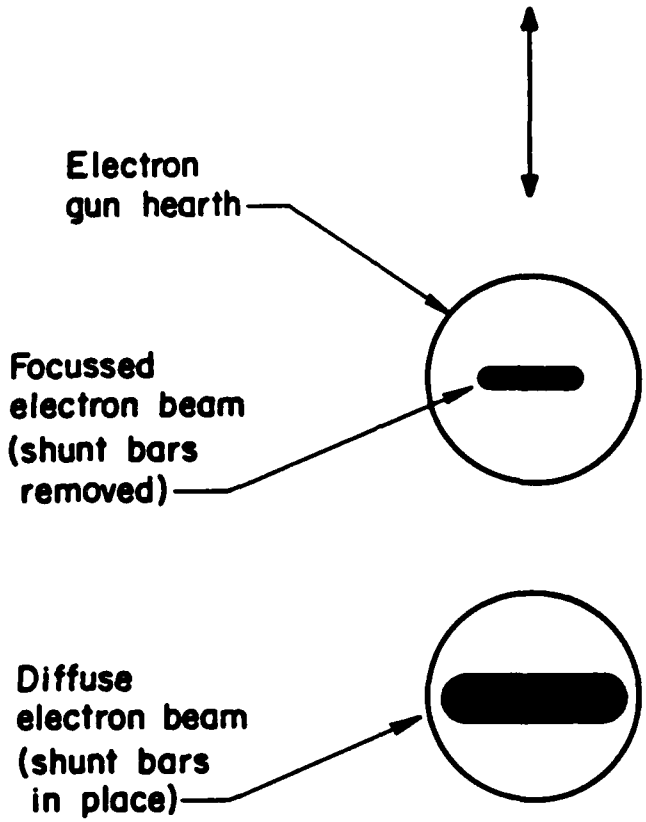
Electron
gun hearth
Focussed
electron beam
(shunt bars
removed)
Diffuse
electron beam
(shunt bars
in place)

Figure 7.

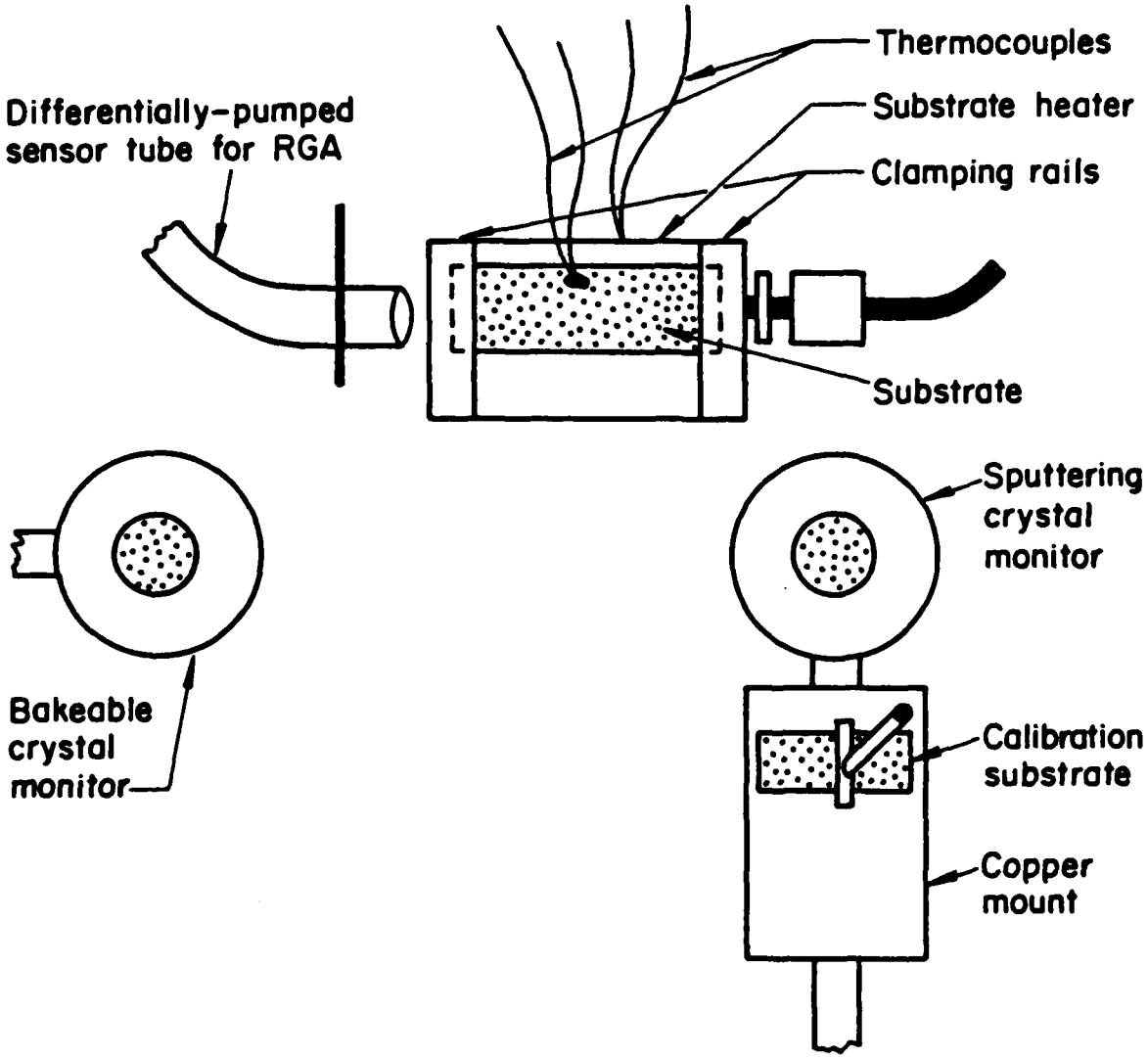
Thermocouples
Substrate heater
Clamping rails
Differentially-pumped
sensor tube for RGA
Substrate
Sputtering
crystal
monitor
Bakeable
crystal
monitor
Calibration
substrate
Copper
mount

Figure 8.

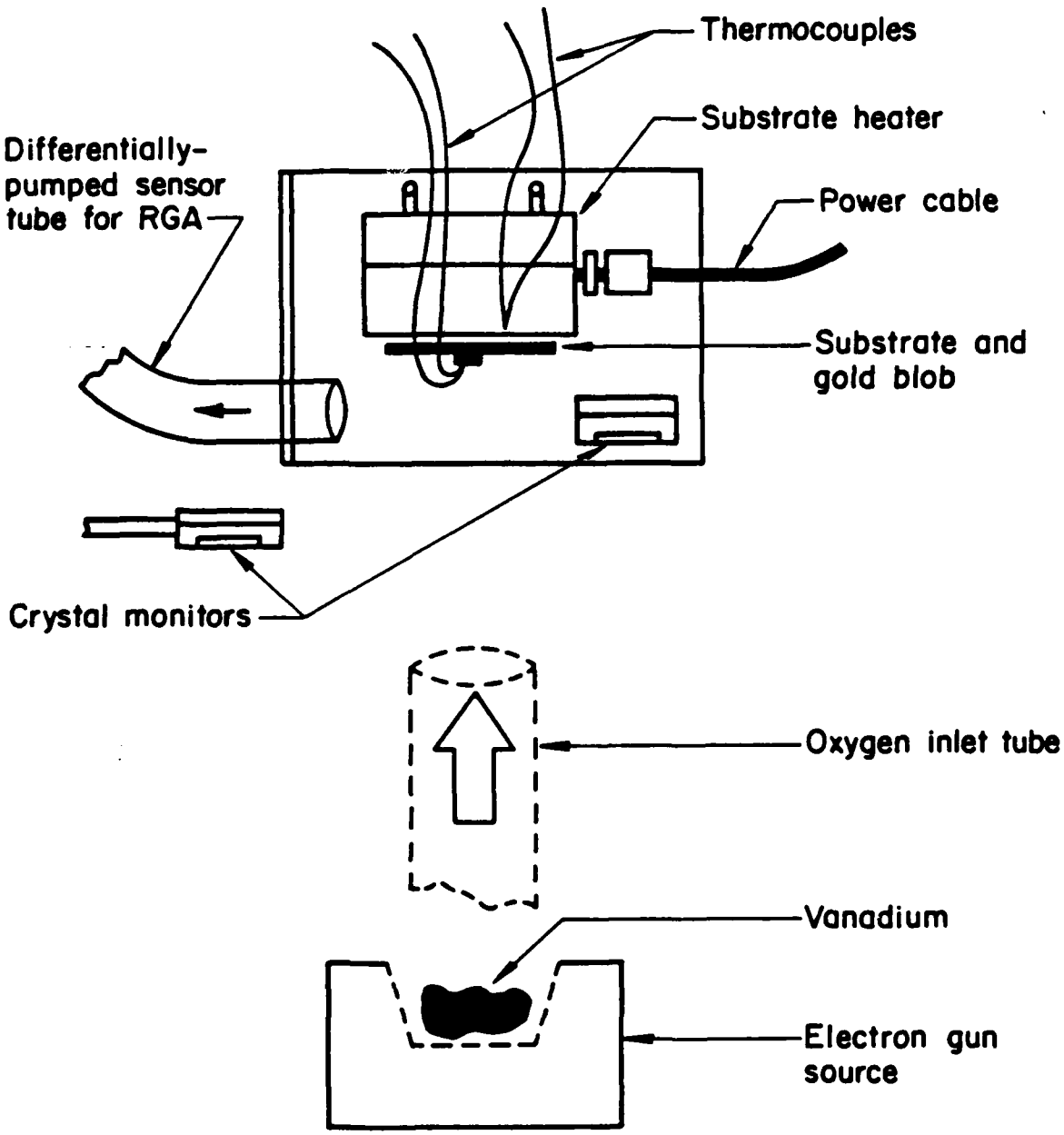
Thermocouples
Substrate heater
Differentially-
pumped sensor
tube for RGA
Power cable
Substrate and
gold blob
Crystal monitors
Oxygen inlet tube
Vanadium
Electron gun
source

Figure 9.

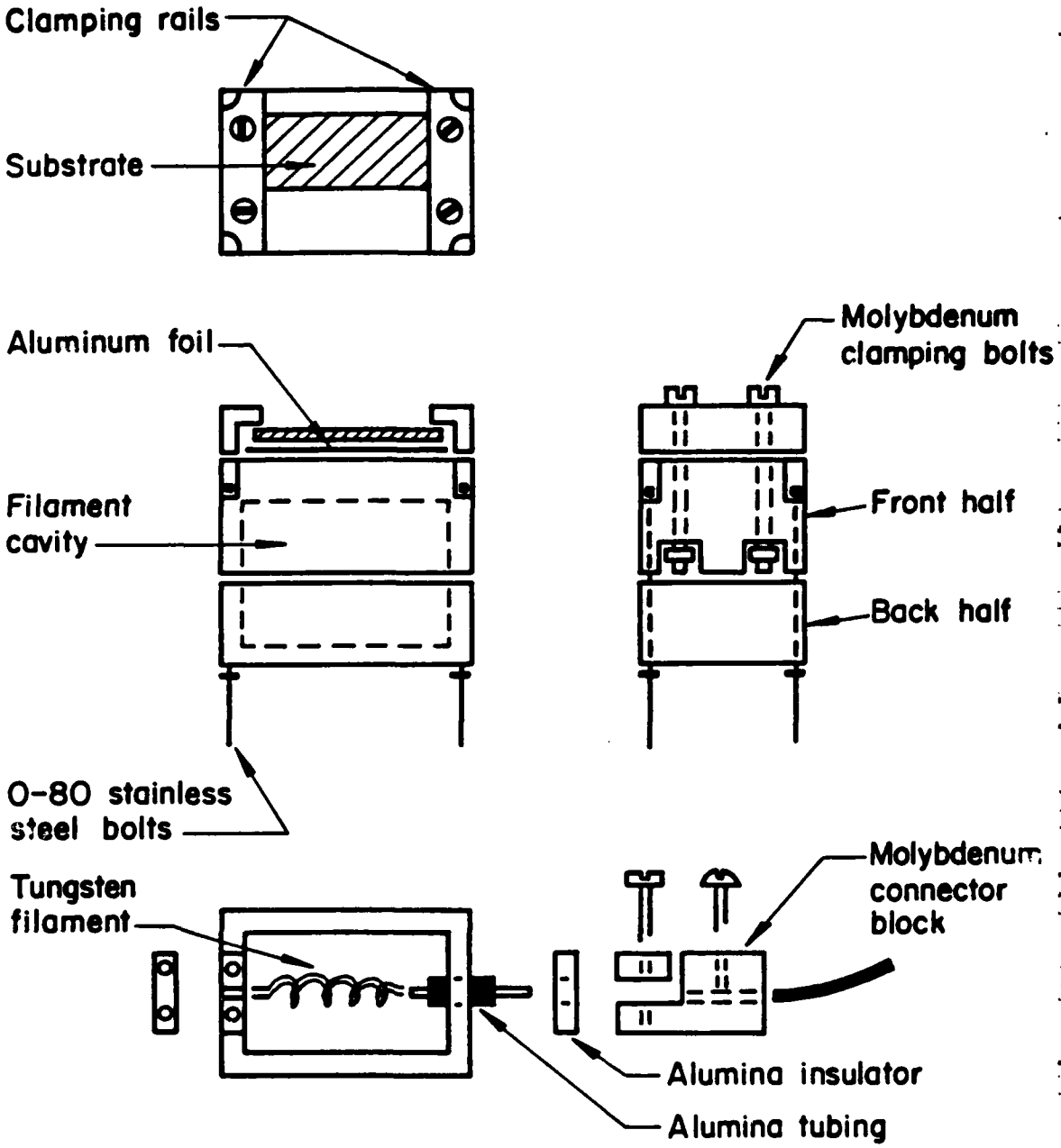
Clamping rails
Substrate
Aluminum foil
Molybdenum clamping bolts
Filament cavity
Front half
Back half
0-80 stainless steel bolts
Tungsten filament
Molybdenum connector block
Alumina insulator
Alumina tubing

Figure 10.

APPENDIX C

FINAL REPORT

UNIVERSITY OF ARIZONA
OPTICAL SCIENCES CENTER
TUCSON, ARIZONA 85721

FACULTY PARTICIPANTS:

U. J. GIBSON
M. R. JACOBSON
H. A. MACLEOD
B. O. SERAPHIN

TABLE OF CONTENTS

I. INTRODUCTION AND SCIENTIFIC BACKGROUND 1
- I.1. SmS as a Phase Transition Material 1
- I.2. Phase Transition in SmS Single Crystals 2
- I.3. Thin Films of SmS Prepared by Physical Vapor Deposition (PVD) 9
- I.4. Characteristic Features of Chemical Vapor Deposition (CVD) 10

II. EXPERIMENTAL FACILITIES AND THE SELECTION OF REACTANT MATERIALS 16
- II.1. CVD Reactor 16
- II.2. Selection of the Reactant Materials. 17

III. CHEMICAL VAPOR DEPOSITION OF THIN FILMS. 21
- III.1. Thermodynamical Modeling of the CVD Reactions 21
- III.2. History of the Deposition Program 23
- III.3. Stresses in CVD Films 27

IV. ANALYSIS 29
- IV.1. X-Ray Diffraction (XRD). 32
- IV.2. Scanning Electron Microprobe Quantometry (SEMQ). . . . 35
- IV.3. Rutherford Backscattering Analysis (RBS) 36
- IV.4. Other Results 37

V. OPTICAL AND ELECTRICAL RESPONSE OF SmS FILMS 38
- V.1. Application of Pressure 39
- V.2. Summary 41

VI. THE DESIGN OF COATINGS INCLUDING A PHASE TRANSITION LAYER . . 42
- VI.1. Maximum Cold Transmittance 43
- VI.2. Zero Reflectance in the Cold State, Maximum Reflectance in the Hot State 45
- VI.3. Zero Reflectance with High Transmittance in the Cold State 59
- VI.4. Zero Reflectance in the Hot State 59

VII. SUMMARY, CONCLUSIONS, AND RECOMMENDATIONS. 64
- VII.1. Choice of the Reactant Material. 65
- VII.2. Recommendations Concernign the Reaction Vessel and Process Parameters 66
- VII.3. Recommendations Concerning the Analysis of the Films . 67
- VII.4. Recommendations Concerning the Determination of the Physical Properties of the Films 69

VIII. REFERENCES 70

IX. APPENDIX 71

Abstract

Single crystals of samarium monosulfide (SmS) exhibit a first-order semiconductor-to-metal transition near a pressure of 6.5 kbar. The technological promise of this transition is considerable, in particular for optical applications based on thin films. However, thin films of SmS show only a gradual change in their properties as pressure is applied; the change is not always reversible and shows hysteresis, which impedes the application of these films.

The inferior properties of SmS films are attributed to internal stress, impurities, small grain sizes, and improper stoichiometry, many of which can be traced to their preparation by physical vapor deposition (PVD). In contrast, work by this group on the chemical vapor deposition (CVD) of thin films has shown that some of these detrimental conditions were not observed in elemental films such as molybdenum (Mo), tungsten (W), and silicon (Si) deposited by the pyrolytic decomposition of a single reactant.

The CVD of SmS films challenged our group for two basic reasons. First, the available thermodynamic and kinetic data on rare-earth compounds in general were sparse, and those for Sa in particular were even more limited. Second, the sulfidization reaction is difficult because it competes with oxidation, and Sa itself can adopt several valences other than the desired divalency when it combines with other elements. A careful study suggested organometallic compounds of Sa as starting materials for CVD that would involve a reaction with hydrogen sulfide (H S) in the reaction chamber. The reaction proved impossible to

control during the time period available to us. Films of related oxysulfides were reproducibly deposited and were characterized by minimum internal stress, but they contained large amounts of O and C, either introduced from the organometallic reactant material or from impurities in the carrier gases. Another starting material, free of O, still produced films with O, so the hypothesis that the starting material was entirely responsible had to be qualified. Processes based on O-free reactant materials with the Sm atom attached to several S atoms were attempted at the very end of the third year, and could not be developed to procedural maturity.

This report presents the choices available and the decisions made at the key points in the program, and traces the suspected reasons for failure, so that future work will not repeat procedures proven unsuccessful. Our presentation is meant as a summary; the reader in need of more detail is directed to the quarterly and annual reports submitted during the course of the contract. We also attach two publications and a detailed doctoral thesis that resulted from this project.

I. INTRODUCTION AND SCIENTIFIC BACKGROUND

I.1. SmS as a Phase Transition Material

All optical properties of materials result from an interaction of photons with the electron assembly. Consequently, the classification of materials with respect to their electrical properties - metals, semiconductors, and insulators - extends to their optical properties as well. Materials that move from one category to another in response to a changing external parameter, such as temperature, pressure, or electric field, exhibit a correlated modification of their optical behavior as well.

More than 800 materials are known in which application of pressure induces a transition from one category, or phase, to another. The monosulfide of samarium (SmS) and its alloys with some other lanthanides attract attention for a number of reasons. The sharp first-order transition from the semiconductive to the metallic state occurs at the moderate pressure of 6.5 kbar. The reverse transition occurs at somewhat lower pressures. This significant hysteresis is due to large remnant effects, producing a state of optical bistability. Near the transition pressure, SmS undergoes striking changes in its optical properties, which are associated with the transition from semiconductor to metal. Unlike most other pressure-induced phase-transition materials, these changes are most prominent in the visible region of the spectrum. This distinction originates in the peculiar electronic structure of SmS: The phase transition is isostructural so that the optical consequences are not based on a change of lattice structure but

are electronic in character. As a result, SmS shows particular promise for optical switching.

It is significant in this context that the transition consists of an intrinsic change of the optical properties that depends on optical polarization, thus making it superior to piezo-optical modulators based on birefringence. The broadband character of the optical change also sets the phase transition apart from the modulation of the spacings of resonators, such as Fabry-Perot etalons, which are the more effective the smaller the wavelength range to be switched.

I.2. Phase Transition in SmS Single Crystals

The pressure-induced phase transition of single crystals of SmS was discovered in 1970 at Bell Telephone Laboratories by A. Jayaraman [1]. The profound changes in the electrical and optical properties of the material are depicted in Figs. 1 through 3, taken from early work on single crystals of the material. Note the significant change from the semiconductor reflectance of about 10 to the metallic value of nearly 90, extending over the wavelengths ranging from 500 nm to the infrared. As Fig. 2 shows for 800 nm, the change occurs abruptly as the pressure approaches 6 kbar, but persists to values below 2 kbar as the pressure is decreased again. The electronic basis for the optical change is seen in the equally drastic change of the electrical resistance plotted in Fig. 3; the corresponding hysteresis loop is also observed as the pressure is reduced.

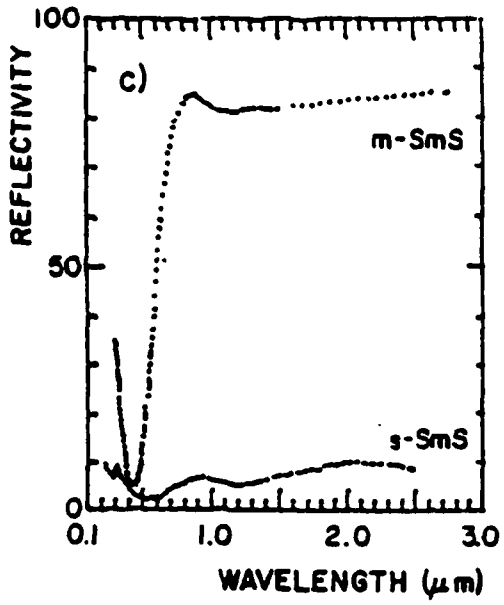

Fig. 1. Reflectivity of a single crystal of SmS, before (s-SmS) and after (m-SmS) application of pressure (Ref. 2).

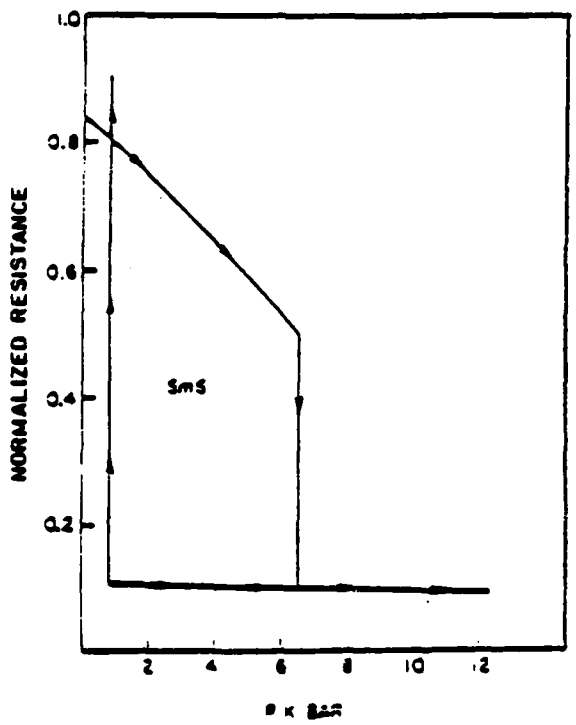

Fig. 2. Normalized electrical resistance versus pressure for single crystal SmS. The actual resistivity at pressures greater than 6.5 kbar is ≈ 3-4 x $10^{-4}\Omega$cm (Ref. 1).

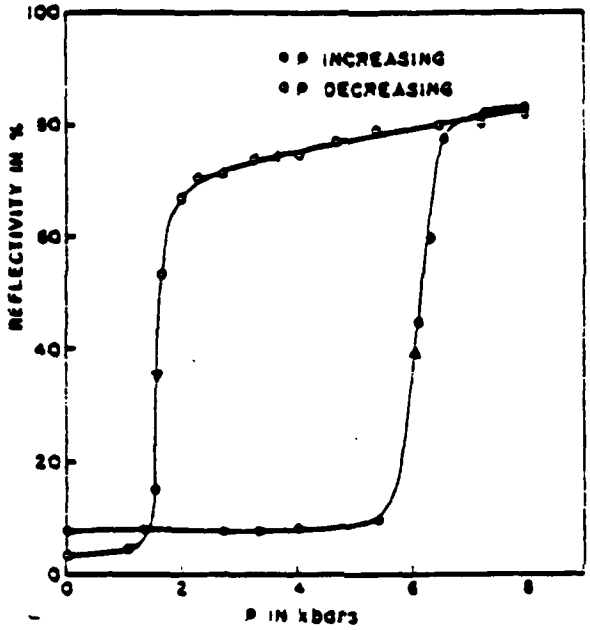

Fig. 3. Room temperature change in reflectivity at the semiconductor-metal transition in SmS at 0.8 μm (Ref. 2).

The exact nature of the transfer of electrons from semiconductive to metallic states is still not yet known in detail. The standard measurements for mapping the electronic bandstructure have been performed on SmS single crystals, but interpretation of the results is ambiguous. In particular, the metallic state requires further investigation through low-temperature measurements under high pressure. Variations among samples aggravate the situation. The basic electronic concepts underlying the phase transition have emerged, however. We will sketch them briefly, since their character demonstrates the difficulties encountered in moving from single crystal samples to thin films.

Figure 4, taken from Kaldis [3], plots a bandstructure before (left) and after (right) compressing a rare-earth monochalcogenide sample. Without pressure, the Fermi level is situated between the uppermost filled 4f level and the empty 5d band. The sodium chloride (NaCl) lattice structure assumed by these compounds is characterized by a crystal field generated by neighboring atoms that splits the 5d band into two sub-bands. Variations in this field caused by the pressure-induced atomic displacements influence the separation of these two sub-bands. At the threshold pressure in SmS, the lower band, designated t_{2g} in Fig. 4, is displaced downwards from the band center far enough to cross the Fermi level and match the energies of the previously filled 4f level. These electrons can then move freely in the empty t_{2g} band causing metallic conductance and the related change in the optical properties.

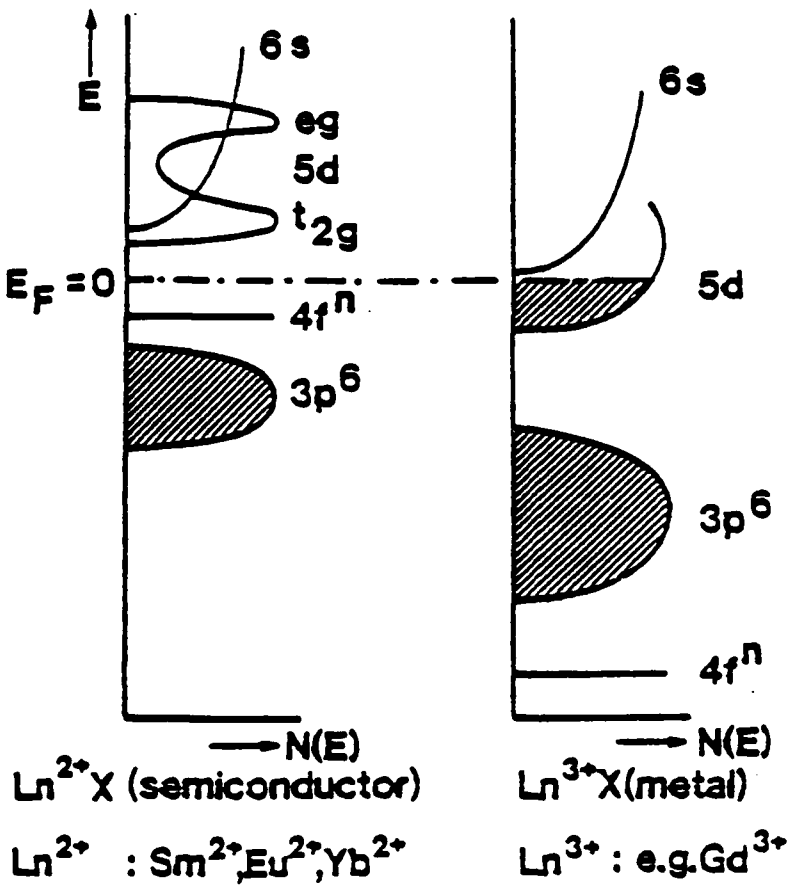

Fig. 4. Schematic comparison of the band structure of divalent (semiconducting) and trivalent (metallic) rare earth monochalgenides (Ref. 3).

Notice the strong difference between the position of the $4f^n$ levels. The figure shows X = sulfur. If m-SmS assumes the band structure on the right the lowest level would be $4f^{n-1}$.

Since a structural parameter - the crystal field determined by identity and configuration of the lattice atoms - controls the energies of the uppermost bands, it is apparent that internal stress, impurities, voids and internal surfaces influence the crystal field at every point inside the lattice. Consequently, the crossover of the bands depends on these structural properties. For this reason, alloys of rare-earth monosulfides have significantly shifted transition parameters, as shown in Fig. 5 for alloys of SmS and gadolinium sulfide (GdS). This suggests the tailoring of transition parameters to match a given application. The ease of adding alloyants to the growing film in CVD is one of the advantages we anticipated for the method once it was under control.

As the deposition of thin films, rather than bulk crystals, is attempted, the influence of the configurational parameters that determine the crystal field splitting becomes more complicated. Physical vapor deposition methods tend to create films with non-uniform structures, so that the threshold condition is reached at different values of the external pressure in different locations of the lattice. Therefore, the unpredictable dependences of the physical and optical properties on pressure are difficult to utilize technologically. We will describe these difficulties in the next section.

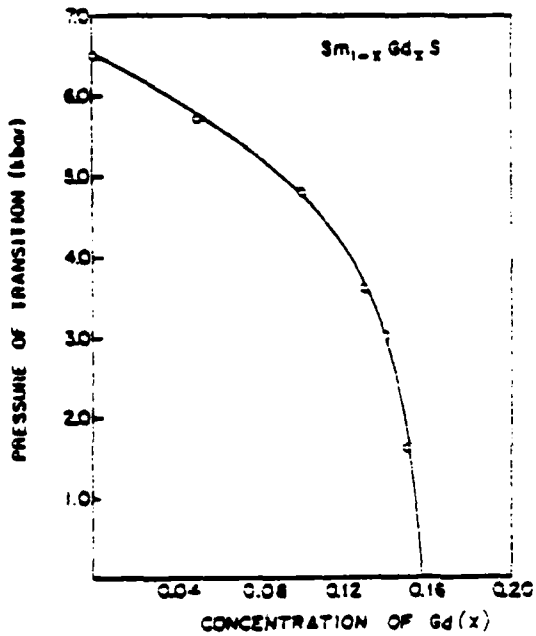

Fig. 5. Pressure of the semiconductor-metal transition for $Sm_{1-x}Gd_xS$ alloys as a function of Gd concentration (Ref. 4).

I.3. Thin Films of SmS Prepared by Physical Vapor Deposition (PVD)

Exploitation of the phase transition for optical applications requires that the material be fabricated in thin film form with tight control over homogeneity, in particular with respect to stress, purity, stoichiometry, porosity, grain size and post-deposition oxidation. Thin films are needed because technological problems preclude the production of crystals with the area needed for optical applications. No less important is the possibility of incorporating an active thin film into a stack of layers that amplifies the intrinsic change of reflectance and transmittance and selects a specific spectral region of operation.

In response to these requirements, thin films of SmS have been deposited by special evaporation techniques, including flash evaporation, electron beam evaporation, simultaneous thermal evaporation of Sm and S, and thermal evaporation of Sm in a chamber with a low background pressure of H_2S. Other methods such as thermal evaporation from solid SmS, heating a Sm film in an H_2S atmosphere, and reactive sputtering of Sm into a small background pressure of H_2S have not succeeded.

Under hydrostatic as well as uniaxial pressure, such films display a much more gradual phase transition than do single crystals, with lower values of reflectance and electrical conductance on either side of the transition. One reason a sharp first-order transition cannot be observed lies in the attachment of the films to a substrate with different mechanical and thermal properties. A second reason may be the intrinsic stress in the deposited films due in part to irregularities such as grain boundaries, voids, and impurities. A strong dependence upon the grain

size is observed, and oxidation of surfaces, external as well as internal, is important. These effects not only handicap thin films relative to single crystals, making the exploitation of the effect less promising, but render fabrication less reproducible. The shortcomings of the available SmS thin films at the outset of this project provided the main incentive for its initiation. Since the method proposed, CVD, had demonstrated that simpler elemental films could be deposited with a minimum of the detrimental features associated with PVD, we shall relate the major features of conventional thin film techniques to the factors that influence the phase transition, in particular the various causes of internal stress. We will then sketch the experiences with CVD that made us anticipate an improvement over PVD SmS films, relying on the expectation that we could repeat the control over the deposition parameters accomplished in our previous work.

I.4. Characteristic Features of Chemical Vapor Deposition (CVD)

Chemical vapor deposition differs from physical vapor deposition in a number of ways. While CVD films are often superior in some respects, control of the deposition process can be more difficult. The critical step is the promotion of a chemical reaction on the surface of the substrate of the form

$$aAC(a) + bBD(a) \rightleftharpoons cAB(a) + dCD(a)$$

where (a) represents a phase adsorbed on the substrate surface, and the lower cases are the stoichiometric coefficients. This critical step is

preceded by the generation and transport of the reactant vapors. It is followed by the desorption of byproducts and their removal from the reaction chamber. We schematically represent the entire sequence of equilibrium processes in Fig. 6; P_x denotes the pressure of x in the gas phase, and R_i denotes reactions.

The complicated chain of reactions can be steered successfully to the deposition of the desired end product by the proper choice of process parameters at every junction and fork of the diagram. If the thermodynamic and kinetic data are well known, the process parameters can be appropriately selected, so that the desired reaction takes place in the designated location, leaving the solid film on the substrate. It is one of the advantages of CVD that the sequence of sharply defined chemical events establishes a selectivity that results in an extremely pure end product, since competing reactions are strongly discouraged in the chosen process parameter space.

The situation changes profoundly and the complex chain of chemical events turns into a handicap once

a) the thermodynamic and kinetic data base is sparse, so that reaction phenomena cannot be predicted, and

b) impurities are present at certain points in the diagram that permit reactions that are not part of the designed sequence.

The schematic representation in Fig. 6 demonstrates the point we want to make in view of our failure to deposit SmS. As will be explained later in greater detail, the addition of O in particular at the left-hand side of the diagram in either the inert diluent gas, carrier

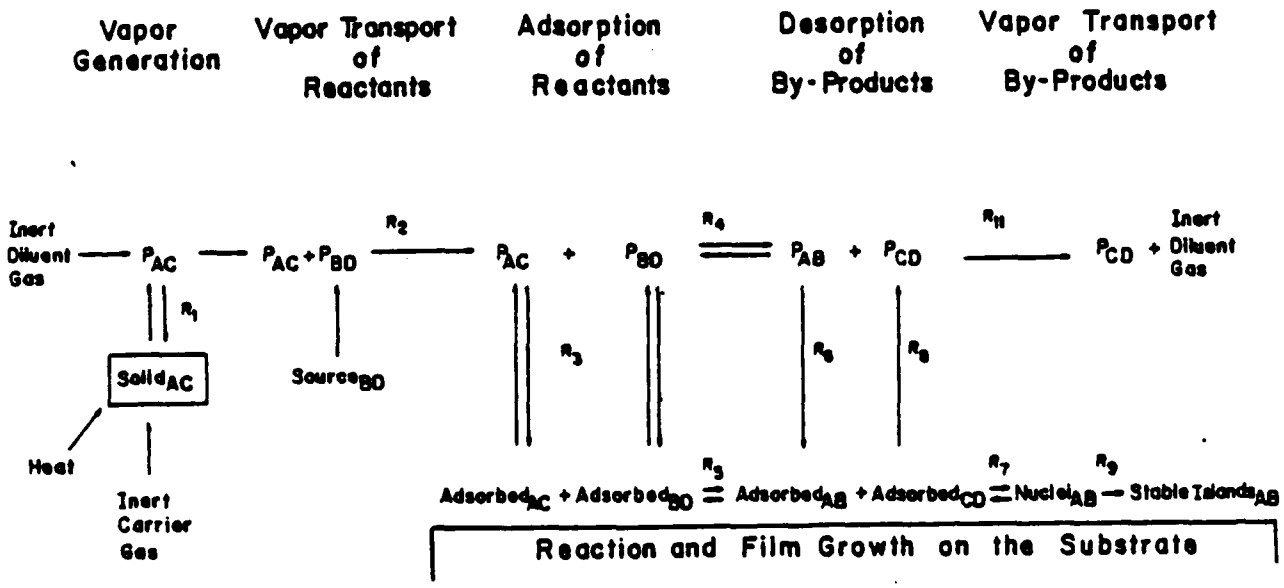

Fig. 6. Schematic representation of the equilibrium steps in the chemical vapor deposition process (Ref. 5).

gas, or the solid reactant material, allowed competing reactions to occur in the subsequent steps. These unforeseen reactions apparently completely removed the desired sequence leading to the monosulfide of Sm from the planned chain of events.

It is apparent from the diagram that at most junctions parallel or even counteracting reactions can occur. To select one and preclude others requires data that are not available for the family of rare-earth compounds. As a result, the process parameters had to be approximated by considering the results from the desired compounds in reactions between undesired phases or by extrapolating from reactions between the desired phases for similar compounds. Unfortunately, the reactions did not go into the planned direction, and the correct end product was not obtained. Choosing an organometallic Sm molecule that would dissociate into an isolated Sm ion and the remaining ligand was particularly difficult. As it turned out, the Sm presumably remained bound to O and C atoms, so that the reaction with the S from the H_2S molecule was more complicated. In Fig. 6, this reaction product would appear in the first position on the line printed along the surface of the substrate.

Both O and C were incorporated into the solid film. The inclusion of C probably promoted deposition of the amorphous phase, which in turn prevented us from obtaining structural information by x-ray analysis. The difficulty was undoubtedly aggravated by Sm's very strong affinity for O, which disappointed our intent to promote sulfidization over oxidation.

The problems of selecting and controlling the many process parameters through all the steps of Fig. 6 were appreciated at the outset. However, the advantages to be gained from CVD are considerable, so an attempt appeared justified. We will briefly summarize these advantages.

Control of the internal stress in SmS films loomed as the primary problem since PVD films did not resemble the single crystal with respect to the sharpness of the transition. We attributed this distinction to the divergent characters of the deposition processes. In PVD, the impinging particles arrive at temperatures greater than the substrate and the nucleation begins before the adsorbed atoms, or adatoms, and the substrate are in thermal equilibrium. In CVD the reactants are cooler than the substrate and must approach equilibrium with it to initiate the reaction; consequently, the film grows in thermal equilibrium with its substrate. Such films, as our previous work has shown, display very low internal stress levels, as measured by transmission electron microscopy.

For CVD films, stress levels depend primarily on film-substrate expansion coefficients; if these are chosen to match, other stress-enhancing mechanisms are minimized by the dense film structure engendered by the thermal equilibrium nature of the deposition process. Previous work on SmS films had established the important role of grain size as a source of stress. In CVD the substrate temperature high is enough to permit stress relief during deposition by diffusion of lattice vacancies, dislocations, and impurities to the surface of the films, with the subsequent relaxation of lattice and grain boundary stresses. Our

molybdenum work had shown that the grain size in CVD films can be controlled, and the optical properties significantly improved, by preferentially depositing grains large enough that optical electrons could freely oscillate and rarely encounter boundaries.

As we have mentioned, the selectivity of the chemical reaction that deposits the film tends to reject impurities. This consideration determined our course at the outset, especially since our previous work had produced, for example, Mo films of superior purity-dependent properties such as the infrared reflectance and the electrical conductance. For these properties, the CVD films were better than any reported results on PVD films. In this case, unfortunately, this effect worked against us.

Last but not least, CVD facilitates alloying by appropriate preparation of the gas phase. Since the temperature and threshold pressure for the phase transition can be widely varied by incorporating other lanthanides, which affect internal stress through their different atomic sizes, into SmS, the ease of building them into the lattice during film growth appeared as an advantage of CVD.

The firmly documented benefits for films deposited by simpler CVD processes are as promising as they were at the start of our program. Should competing thin film technology still not give promising results, the search for a better starting material and a proper set of process parameters for CVD should be continued, avoiding the territory that our work already covered without success.

II. EXPERIMENTAL FACILITIES AND THE SELECTION OF REACTANT MATERIALS

II.1. CVD Reactor

Based on our previous CVD experience, we built a radiatively heated horizontal cold wall reactor to attempt the deposit of SmS. The reaction chamber consists of a quartz vessel that tapers at one end to a 2.5-cm tubulation that mates with a quick-disconnect fitting on the end of the source line. The other end of the vessel is a round quartz flange sealed with an O-ring that mates with an end cap. The end cap contains ports through which the exhaust, heater power, and thermocouple lines are fed. A stainless steel source chamber feeds the reactant, carrier, and diluent gases through stainless tubing to the reaction chamber. Teflon tubing and valves were originally used to maintain the design flexibility of the system, withstand some of the corrosive chemicals, and survive temperatures at which gases enroute to the reactant chamber would not condense. The plumbing included flowmeters and valves to monitor and control the individual flow rates of all gaseous components. The graphite susceptor inside the reaction chamber was heated either by a 5-kW RF generator or by four 500-W cartridge heaters.

As stated, the initial design was considerably modified in the course of our work. Teflon plumbing, initially employed to provide flexibility and corrosion resistance, was prone to leak at joints, and was gradually replaced by glass and stainless steel when hunting for leaks became too time consuming. The source chamber was modified to

present greater surface area of the solid reactant to the carrier gas, while providing better temperature uniformity and control. Another impediment was the premature decomposition of the organometallic source material in the reaction chamber at some distance from the substrates, probably due to the RF glow discharge originating at corners of the susceptor. Since the RF heating was triggering the discharge, we replaced it with simple resistance heating.

Nothing in the initial or final design of the CVD reactor is unconventional, so we shall dispense with further detail here. Two restrictions may have been of minor influence on the program. The source lines could not be heated above 200 C until stainless steel was installed during the third year, so vaporization temperatures had to be kept below that level to prevent condensation. The upper temperature limit was not imposed by the plant; rather, deposition above 700 C shifts the equilibrium strongly toward higher sulfides of Sm, precluding the preparation of the desired monosulfide.

II.2. Selection of the Reactant Materials

An extensive literature search did not produce any information on the CVD of rare earth metals or their compounds, so it was not possible to start with a known CVD reaction and optimize the deposition conditions to produce films with the required stress and optical properties. Facing many unknowns with respect to the proposed process, we had to survey the chemistry of Sm and its compounds and their possible reactions to identify potential starting materials. Even the general chemistry of Sm

compounds is not known well enough to select reactants with confidence, and lead them through the chain of chemical events portrayed in Fig. 6.

There are four general requirements for a suitable reactant material:

1) thermodynamical feasibility of the proposed reaction, i.e. each step in the chain of reactions must have negative free energy,
2) reactant compounds that are either gaseous under the proposed deposition conditions, or reactant compounds that can be volatilized without decomposition, giving a sufficient vapor pressure in the order of 1 mm Hg,
3) reaction byproducts that are volatile so that the probability of their incorporation into the deposit as impurities is small,
4) stability of the starting material under handling and loading conditions.

The list of requirements is largely determined by our decision to use CVD at atmospheric pressure, as in all our previous work. A number of reasons can be cited for the superiority of working at atmospheric versus low pressures. However, atmospheric operation encounters limitations as well. The vapor pressure of the source materials must be fairly high to be volatilized, and feeder lines must be heated to prevent condensation. Future workers may be advised to consider low-pressure CVD as an alternative approach, easing these two requirements.

The widespread CVD of transition metals, their compounds, and some of the standard semiconductors from halides drew our attention to the four stable Sm halides. Detailed analysis of the meager information,

and circuitous calculations of the necessary steps, indicated that the change in free energy would indeed be negative, and the chain of chemical events thermodynamically feasible. In all four cases a temperature in excess of 1100 C was apparently necessary to obtain vapor pressures above 1 mm Hg and to prevent condensation in the source lines. We expected that at such high temperatures the deposition reaction would occur before the susceptor was reached, and if this could be prevented by generating even higher substrate temperatures, the deposit would not be SmS but a higher sulfide.

The quest for a higher vapor pressure at manageable temperatures led us to the organometallics. We found several that met the above criteria and that reacted in the recommended 200 to 700 C temperature range. These organometallics have not produced a wealth of thermodynamic data, due to their limited engineering applications, but their volatility at moderate temperature, and their reactivity with H_2S, appeared secured.

The organometallic $Sm(thd)^3$ appeared to satisfy the above criteria best. Since it was not commercially available, it had to be synthesized in collaboration with our Chemistry Department. Because the structure of the molecule and its derivative reactant materials are important, we show it schematically in Fig. 7. Note that the organometallic ligands are bound to Sm through an O atom. We describe the results of using this configuration in the next chapter, pointing out that our evidence seemed to indicate that decomposition did not break the Sm-O bond, but carried the O into the growing film. No variation of the process

prevented this pattern of dissociation.

Since the incorporation of O appeared to prevent the deposition of the monosulfide, we switched to an organometallic that did not contain O at all. The use of Sm(tcp) improved the situation only slightly, however, and analysis still indicated large amounts of O and C in our films.

In a third step, we attempted to shift the chemical equilibrium toward the monosulfide by using an organometallic that not only did not contain O, but in addition surrounded the Sm center by six S atoms as the links to the organometallic ligands. We have no results on this reactant material, since our preliminary attempts left no films, suggesting that we missed the set of process parameters that produced films for the other reactant materials. This samarium dithiocarbamate starting material, again prepared with the help of our Chemistry Department, did not lead to detectable film deposition. Even varying the substrate and source line temperatures through the accessible range led only to simple recrystallization of the reactant material on the cooler [illegible] the reaction chamber. The reactivity of the samarium dithiocarbamate with H_2S is apparently not sufficient to prevent recrystallization. However, we have not invested sufficient effort into this approach, and recommend that this reactant material be investigated in future programs.

III. CHEMICAL VAPOR DEPOSITION OF THIN FILMS

The deposition of SmS films by CVD could not be guided by broad experience since the preparation had apparently never been tried for any rare-earth sulfides. As a consequence, our work had to consider the multi-dimensional space of the process parameters that might influence composition and microstructure of the deposit. Orientation was received from two sources. We relied on feedback from analyses of the samples from each run; analysis techniques will be addressed in the following chapter. We also employed simple thermodynamic modeling, a description of which follows.

III.1. Thermodynamical Modeling of the CVD Reactions

While empirically exploring combinations of process parameters, we made observations that provided input for thermodynamic modeling of the partial processes taking place during deposition. One result was identification of the mechanisms that determine the deposition rate. By correlating the initial process parameters with the observed deposition rate, we concluded that the deposition process was limited by kinetics - the adsorption of the reactant species on the substrate and the speed of their reaction with each other - rather than by diffusion of the reactants from the gas phase to the substrate. This result streamlined the variations of the process parameters that were to follow.

When in a later phase, the deposition processes strongly favored the formation of Sm_2O_2S over SmS, we simulated the partial processes possible in the Sm-O-S ternary phase diagram using a thermodynamic

equilibrium program that reproduced some of the observations made during the parameter variation and the post-deposition anneals. Calculating the equilibrium formation of the six possible compounds and their areas of dominance in parameter space, we could predict the relative stability of Sm_2O_2S with respect to other compounds such as Sm_2S_3 as a function of temperature and S:O ratio. The results were somewhat frustrating: At regular temperatures Sm_2O_2S is stable unless the S:O ratio above the growing film is greater than 10^4, exceeding by far the purity levels of commercially available gases. At temperatures above the range we had used up to that time, the ratio dropped below 10^3, but then the formation of Sm_2S_3 was favored over SmS.

Although qualitatively helpful, our thermodynamic modeling has severe limitations. First, we are not operating in thermodynamic equilibrium, and second, the reaction occurs at the surface where the rate is limited by the kinetics and not by diffusion from the gas phase above. Finally, the precision of the program depends critically on the thermodynamic data input. CVD involves a complex chain of chemical reactions leading to deposition; at every step, numerous competing reactions are possible. The prediction of which route is taken at each step is decided by the relative reaction rates that must be known for the reactants in their various phases at a range of temperatures and pressures. Other constraints imposed by kinetics and diffusion enter as well.

While this complexity impedes the development of a CVD process, it offers greater flexibility in the choice of the parameters and

conditions. These aspects of CVD even affect reactions between materials for which parts of the reaction sequence are already known, and for which extensive thermodynamic data are available. For our program, however, the difficulties were amplified. Not only is the CVD of Sm compounds unknown, but the rare-earth group has largely been ignored by the chemical technologist, resulting in a scarcity of data in contrast to the wealth available for most other materials. As a consequence, our process parameters were selected and modified on the basis of extrapolations of data from the solid phase to the gas, from room temperature to 400 C, and from one compound to a possibly similar one. Only by iterating the deposition processes with different parameters could the initial extrapolations be improved—a time-consuming process indeed.

III.2. History of the Deposition Program

Once we had adjusted our process parameters to the point where solid films were deposited, we began to subject the films to analyses which are described in the following chapter. It soon became apparent that the x-ray diffraction signatures obtained did not match the Sm compounds we had originally expected. A more thorough search led to the discovery that we had deposited an oxysulfide, Sm_2O_2S, rather than SmS.

Several sources for the unwanted O were suspected. At first, we presumed that the O was incorporated along with the Sm when the $Sm(thd)_3$ pyrolyzed at a point that left the Sm-O bond intact. However, the problem was not solved when we changed to a starting material free

of O. It is quite possible that the O enters through very low levels of O contamination in the diluent and H_2S gas supplies, or through real or virtual leaks of air or water vapor.

At any rate, while still working with the first starting material which did contain O, we performed gas chromatography to determine the nature of the exhaust gases. We did not detect the H compounds of the unbroken chain, but rather fragments of the dissociated reactant molecule. We also began to vary the process parameters to attempt to eliminate the O. A four-dimensional array of parameters was modified, each variation consisting of a separate run with subsequent analysis. Educated guesses on the reaction kinetics - we have addressed the scarcity of data on the chemistry of Sm above - suggested that first raising the substrate temperature T_s should increase the Sm:S ratio, and favor deposition of O-free compounds such as Sm_2S_3. The result was gas phase reactions producing "snow" above the substrate. Second, we increased the H flow rate to bind the O in water molecules. While the results taught us our reaction was limited by the kinetics rather than by diffusion, the desired result was not obtained. As a third variation, we increased the H_2S flow to augment the S:O ratio; this was equally unsuccessful. Finally, we varied the Ar flow rate and employed ultrapure gases with only small effects; with small changes in growth rate and free-S content, we continued to deposit Sm_2O_2S.

As a second approach, post-deposition anneal was suggested approach its psuccess in our Mo work. After years of fighting an oxidation tendency similar to the one observed here, we employed a post-deposition

anneal in H to reduce the O and C content in our chemically vapor deposited (CVD) Mo films. At 750 C the H extracted O and C so effectively that the annealed Mo films changed crystal structure and grain size, resulting in a material of higher infrared reflectance and electrical conductance than had ever been reported. Anneal of our Sm_2O_2S films in H at temperatures up to 800 C did not succeed. Some amorphous samples crystallized, but without change of composition. The Sm-O covalent bond could not be broken in this manner, and an exchange of O for S also proved impossible. Raising the temperature further initiated reactions and diffusion into the substrate.

We also tried vapor transport for the deposition of SmS. Although not truly a chemical vapor deposition, the method shares with CVD its thermal equilibrium nature. By depositing SmS in the closed system of a sealed-off quartz ampoule, contamination by O or other impurities is limited. We did not go beyond setting up the apparatus and performing a few trial runs that did not give convincing results. The new O-free reactant material Sm(tcp) had arrived and we were ready to use it in a modified, resistance-heated reactor that we hoped would eliminate the suspected "shredding" action of an RF glow discharge on the reactant gas that might break the source material into numerous small fragments with unpredictable effects on the total reaction.

Deposition runs using this new reactant material took up the remaining year of the program. Thicker films were deposited more reproducibly and uniformly due in part to a newly installed gas deflector, or spoiler, which directed the flow over the substrates.

Film analysis still lacked precison; qualitatively, however, the O content decreased with respect to that of the films deposited from the $Sm(thd)_3$. Again, we attribute the considerable amounts of remaining O on the strong tendency of the Sm atom to bond to O rather than to sulfur, even if the latter is abundantly present at the 10^6:1 ratio that our calculations predict.

The importance of removing the large C content goes far beyond the production of a material that is predominantly SmS. Without exception, our CVD work of the last 10 years has shown that C stabilizes the amorphous phase in thin films, preventing their crystallization. Incorporating C into films of amorphous Si, for instance, raised the crystallization temperature from 550C to 1000C. In molybdenum films, C stabilized the fcc structure alien to the bcc bulk material. Generalizing these previous results, we expect that lowering of the present C level will result in the crystallization of our films, and their subsequent characterization by a much stronger x-ray signature than is presently observed. In fact, many samples which displayed no intrinsic x-ray pattern showed strong Sm_2O_2S lines after anneal, indicating crystallization with no C compounds. This indicates that the C incorporation, though serious, may be rendered less harmful by anneal. However, anneal seems only to strengthen the position of O in the product.

Returning to basic approaches, we attempted to improve the probability of S incorporation by searching for a suitable reactant material that places S next to Sm. With the help of our Chemistry

Department we synthesized samarium dithiocarbamate, and used it in the final runs of the program. No films were deposited, since the dithiocarbamate condensed in recrystallized, unreacted form on cooler areas of the chamber. Apparently, recrystallization was preferred over reaction with H_2S under the set of process parameters we used. A search for a better suited set should be the first process to be tried under an extension of the work.

III.3. Stresses in CVD Films

The magnitude of the problems and the time required to solve them must be compared to the promise of CVD. We proposed a program that derives its value and uniqueness from CVD and from our previous experiences with thin CVD films. The thermal equilibrium characteristic of the process has in all cases resulted in films of much lower internal stress than is typical for PVD films. This experience has been confirmed in our present work: We did deposit films of Sm_2O_2S instead of SmS, but x-ray analysis confirmed that their internal stress corresponds to an external pressure of less than 0.8 kbar. This is a remarkable result in view of the switching characteristics of PVD SmS films, which indicate internal stresses corresponding to twice the threshold pressure of 6.5 kbar. We cannot extrapolate the stresses in Sm_2O_2S to those of SmS, since the Young modulus of Sm_2O_2S is not known.

In the next chapter, we will discuss some features of our surface analytical program. We should mention here that we are able, through x-ray diffraction, to measure stresses down to a corresponding pressure of

0.8 kbar, slightly over 10 of the threshold pressure for switching SmS. The quality of this analysis is of special importance, since the characteristics and performance of PVD SmS thin films are not representative of a true semiconductor-to-metal transition.

IV. ANALYSIS

Implicit in any attempt to deposit films of exotic materials is a parallel analytical effort. Our work on SmS coatings was no exception. The problems of characterization were multiple. Because the switching effect depends both on structure and composition, we had to apply techniques that would provide both types of information. Secondly, the problem of O and C contamination demanded that the analysis be sensitive to these elements. The lack of adequate data on Sm compounds was a third difficulty. Of course, the appropriate instrumentation had to be available on campus so that the analytical feedback could be rapid enough to guide further preparation. In some cases, the instruments were operated by our own researchers after brief training; in practice, efficient and discerning use of these instruments required months of experience. Finally, the affordability of certain techniques had to be included in some cases.

Our choice of x-ray diffraction analysis (XRD), scanning electron microprobe quantometry (SEMQ), and Rutherford backscattering analysis (RBS) for our analytical arsenal was guided by the following considerations. Because Sm and S must be arranged in a cubic lattice to switch, a measured Sm:S ratio of unity was not sufficient to indicate the presence of polycrystalline SmS. XRD not only distinguishes between crystal configurations, but by accurately determining spacings between planes and comparing the spacings with an extensive database, identifies the elemental constituents.

We used SEMQ, semiquantitatively, to reveal the chemical makeup of our films. The SEMQ technique directs 10 to 15 keV electrons at a sample that interact with and scatter off the lattice atoms. Although the electrons have short mean free paths, multiple scattering allows them to reach depths of several micrometers. When x rays are produced by de-excitation, they carry energies characteristic of the emitting atom; since they interact with the lattice much less than the electrons, they can escape from considerable depths. The x rays are dispersed by either energy-dispersive spectrometers (EDS) or wavelength dispersive spectrometers (WDS). The latter use crystals that disperse x rays over specific wavelength ranges. SEMQ is fairly accurate for heavier Z elements, such as Sm and S, but C is difficult to measure and O is very difficult, due to the proximity of important O lines to other, much stronger lines. Calibration requires standards that are observed in each run before beginning sample analyses.

The third technique we employed was RBS. Rutherford backscattering employs He ions accelerated to several megaelectron volts. The system at the University of Arizona uses a Van de Graaff accelerator for this purpose. Some ions collide elastically with film ions and are backscattered out of the film with an energy that depends only on the masses of the two colliding species, on the incident energy of the scattered ions, and on the energy losses in the film that occur on the way to and from the collision. As an absolute technique, no calibration is necessary. Collision cross sections and backscattered energies are a

direct function of the atomic weight of the film constituents. Thus, RBS is more sensitive to heavier elements. Moreover, because the large ion penetration depth leads to detection of the substrate for most films, and any detected element typically has a tail that extends to lower energies, the substrate tends to obscure lines from elements of lower Z. Therefore, the films are typically deposited on C substrates, since C is a convenient, low Z element. However, interference from C makes its detection in the film difficult.

The instrumentation for XRD, SEMQ, and RBS was available at the University of Arizona at costs our contract could bear. The three techniques are fundamentally different, in that they use photon, electron, and ion probes, respectively, providing somewhat complementary data sets with regard to sensitivity and penetration depth. For example, SEMQ and RBS had different sensitivities to C and O; they were complementary in that SEMQ was less responsive to O, and RBS to C.

On one occasion, we made use of an Auger electron spectrometer (AES) at a national facility at the University of Montana at Bozeman. Use of an AES system at the University of Arizona was prohibitively expensive. The following sections will deal with data from each technique in turn. Recommendations and a summary are found in Chapter VII.

IV.1. X -Ray Diffraction (XRD)

X-ray diffraction was our most critical technique, since it could directly evaluate the film's crystal structure and tell us whether or not we had deposited SmS. We verified this ability by obtaining evaporated SmS films from A. D. Little and from Bell Laboratories and subjecting these "standards" to XRD. In both cases, the pattern matched that of a bulk SmS standard, one of the nearly 40,000 compiled by the Joint Committee on Powder Diffraction Standards (JCPDS). Knowing that the procedure would work for reasonably thick films, we routinely employed XRD analysis after each run. For the first two years of the program, we used Optical Sciences students and staff to gather x-ray data with instruments in the Metallurgy and Physics Departments. In the final year, we relied on an advanced Siemens diffractometer in the Geosciences Department operated by Mr. Wesley Bilodeau, an experienced and responsible staff scientist, who provided accurate, reliable traces usually the day after submission. During the course of the research, we also were able to perform XRD on instruments at the Duval and Anaconda Corporation Research Laboratories, which support copper mining operations in Arizona. Both of their machines included software for compound identification. While our sessions there were inconclusive, our work would have been expedited had we more access to the JCPDS files through search programs.

X-ray traces were obtained by placing sample fragments of about 1 cm^2 into a groove machined into a 3-mm-thick Al sample holder. The groove depth equalled the substrate thickness, so that the top of the sample was at the proper level to eliminate the nominal offset error in the diffractometer. Scans were made by rotating the sample through a set of angles θ from grazing incidence. Results were plotted with diffracted x-ray intensity as a function of 2θ. The range in 2θ was typically about 10 to 85 degrees. X rays have considerable penetrating power, so they easily detect the substrate. The size and power of the beam are usually large enough to sense the sample holder as well. In our case, the Al appeared as a familiar group of about seven moderately strong lines.

The need for XRD traces with low background levels influenced our choice of substrates to some extent, since crystalline or polycrystalline substrates display sharp lines with little background, while amorphous materials produce high background levels over a broad range in 2θ. We chose Si wafers, Si wafers coated with silicon nitride (Si_3N_4), calcium fluoride (CaF_2) windows, and polished quartz as substrate materials, which produced exceedingly strong lines in the traces. These lines also provided calibration and confirmation that the system was working.

In the second year of this program, a line pattern appeared in many of our films that resisted classification for some time. Eventually, a paper by Eick [8], complete with a table of x-ray lines, revealed our

compound's identity: samarium oxysulfide (Sm_2O_2S). This alerted us to the presence of O as more than a contaminant, but as a constituent of the dominant compound in our films. The detection of Sm_2O_2S also told us that Sm was present trivalently. Since Sm is divalent in SmS, any movement toward divalence would have been an improvement.

As mentioned elsewhere in this report, the particular chemistry required to produce SmS was certainly not favored by the range of conditions we could produce in the CVD reactor. Sm reacted preferentially with O and remained trivalent. Our best efforts to eliminate O and vary the concentrations of H_2S to control S incorporation were not sufficient to create detectable amounts of SmS. In some cases, films lacking XRD lines not from the substrate or sample holder were annealed in reducing atmospheres. In every case, Sm_2O_2S appeared in XRD after anneal. This indicated that we either had additional O incorporation during anneal, or the more likely situation that O already present in the matrix combined with Sm and S to make the oxysulfide.

While a few lines are still unidentified, they do not indicate the presence of either SmS or any of the most likely Sm compounds. Access to the entire JCPDS files would probably help. The most reliable data, generated during the third year of the program, are contained in an Appendix.

IV.2. Scanning Electron Microprobe Quantometry (SEMQ)

In contrast to XRD, SEMQ detects x-rays emitted by atoms in the film matrix excited by the electrons. Samples were prepared by taking small fragments, about 2 or 3 mm on a side, and attaching them to a cylindrical Al sample holder with a dab of electrically conducting silver paint. The small sample size is possible due to the tiny electron beam, which we typically set at about 30 μm. The silver paint conducts excess negative charge from the sample surface to the grounded sample holder. About 20 small samples shared the sample holder surface, which is inserted with four other holders, many bearing standard materials, into a sample block, which, in turn, is bolted onto a stage in the vacuum chamber. The chamber is evacuated, and after a lengthy procedure for calibrating, centering, and focussing the beam, standards and samples are observed. We primarily used the wavelength dispersive spectrometers (WDS). For a given element, the spectrometer with the appropriate crystal must be selected and moved to the estimated line position. A quick scan follows; if a line is detected, a slower scan is performed. The length of the process is inversely proportional to the line intensity.

Software manipulates the data and produces tabulated estimates of sample composition. Since x rays emerge from depths as great as a few micrometers, and our films were never thicker than about 1 μm, the substrate was always detected by SEMQ. The strength of the substrate lines was inversely proportional to film thickness, as one would expect.

This was demonstrated in one instance when the film thickness varied greatly on a single sample. While some programs were available to compensate for the presence of the substrate, too many assumptions were required. Our data emerged without subtractions. Since the substrates, such as CaF_2, often contained elements other than those intentionally deposited, substrate detection created little confusion, except in the case of O. Oxygen was an element we wished to detect, but its presence in the quartz substrates was a handicap in that instance. On the other hand, detection of the substrate lines was often helpful in checking the overall performance of the SEMQ.

While Sm and S are relatively easy to detect by SEMQ, C and O are much harder. To calibrate Sm and S levels, we used both evaporated SmS films from A. D. Little and Bell Laboratories as well as small pieces of bulk SmS. Many of our samples had SEMQ ratios of Sm:S close to the desired value of unity, but since no structural information was present, no insight into the phases of Sm and S in the film could be gained. Results from the latter part of the three year program are found in the Appendix.

IV.3. Rutherford Backscattering Analysis (RBS)

With the third technique, RBS, we intended to determine the extent of the C and O contamination of the films and to gain more quantitative information on Sm:S ratios. The graphite substrates we used severely limited our sensitivity to C; the corresponding film peak appears as a

tiny bump on the far more massive plateau representing the substrate. Oxygen, on the other hand, produces a small but clear signal above the background. As atomic weights increase to those of S and Sm, the cross sections rise quickly, so small amounts of these heavier elements produce far larger signals. By tilting the film relative to the ion beam, the profiles shift and diminish to an extent proportional to the distance from the surface. The overall effect is to increase the relative contribution of the surface material to the total profile.

Typical results for Run 46 showed Sm and S at 18 and 14 at.%, respectively. The films were composed mostly of C and O, each comprising about a third of the film.

IV.4. Other Results

The Auger results were obtained for us during a trip made by a graduate student, now Dr. Peter Hay, to the Auger Electron Spectroscopy (AES) facility at the University of Montana at Bozeman. Again, the elements we expected were found, with Sm and S in roughly the right proportions and with C and O again dominating the films. In one instance, the film was depth profiled. The resulting curve displayed great uniformity with depth.

V. OPTICAL AND ELECTRICAL RESPONSE OF SmS FILMS

Measurements were made on the optical transmission and the electrical resistivity of the CVD films and on SmS films produced by other means. These measurements are straightforward at ambient pressure, but significant difficulties were encountered in making reliable measurements at high pressures. This section describes the measurements and the methods employed in attempts to induce the phase transition in the films and discusses the results.

The films deposited by CVD were studied optically at ambient pressure and compared with films of SmS obtained from the A. D. Little [ADL] laboratory. Reflectance and transmittance measurements were made in a Cary 14 spectrophotometer in the visible and near-infrared regions. The films supplied by ADL showed a gradual adsorption edge at short wavelengths in the semiconducting state. The cutoff is significantly less abrupt than that of a single crystal sample but occurs in approximately the same wavelength region. The reflectance of these samples was quite low at all wavelengths. After mechanically switching the films by abrading them with a pencil eraser, the long-wavelength reflectance rose by about a factor of two. This is less than would be expected from a single crystal of comparable thickness, but the change of the reflectance in this spectral region is consistent with measurements made on single crystals undergoing the transition. It was clear that these films, although differing somewhat in crystalline nature from the bulk, were undergoing the phase transition we wished to study.

The films prepared by CVD were also measured in this fashion. These films did not show strong short-wavelength absorption, and throughout the visible and near infrared, showed interference fringes consistent with their identification as a dielectric, namely Sm_2O_2S. Mechanical abrasion of the CVD films did not produce any significant change in their optical appearance.

Resistivity measurements were made on the ADL and our CVD films by two methods: a conventional semiconductor four-point probe tester, and a four-point measurement made by depositing strip electrodes onto the sample. The ADL samples yielded values consistent with published resistivities for SmS in the semiconducting state, about 10^{-1} to 10^{-3} Ω-cm. Measurements on the CVD films consistently yielded values above 10^{4} Ω-cm, indicating that there was a radical difference between these films and those of ADL.

V.1. Application of Pressure

Since mechanically abrading the films to induce the transition, while effective, is largely uncontrolled, and certainly not amenable to calibration, other methods for applying pressure to the films were assessed. These included the use of a sapphire anvil and a large hydrostatic "bomb." Both methods have some serious drawbacks for thin film measurements.

The use of a small anvil is attractive from two standpoints: The pressure applied should be directly proportional to the spring compression, and the device is small and can be incorporated into a

spectrophotometer. Unfortunately, these ideals were not realized. The simple design of the anvil with which we were supplied did not assure that the sapphire faces were parallel, leading to a gradient across the sample, and perhaps more significantly, the pressure of the anvils shattered the substrates in most cases before the desired pressure was achieved. In addition, the pressure on the films with this type of device is explicitly uniaxial. As the lattice collapse is isotropic, there has been some controversy as to whether application of pressure in this fashion should be expected to induce the transition.

We therefore investigated the use of a large hydrostatic cell to apply pressure to the films. Despite the advantages of such a system, the pitfalls are also numerous. The approach is desirable in that it accommodates a fairly large sample, and the pressure can be read accurately over the 0 to 10 kbar range from a manganin wire gauge remote from the actual sample cell. However, the long optical path inside the cell and the unwieldy nature of the support equipment make such a system difficult to operate. Multiple reflections and the critical nature of the alignment of the cell make a good baseline very hard to obtain. As pressure was applied, the tubing leading to the cell applied a torque to the "bomb" causing some misalignment and causing transmittance changes, even with no sample present. In addition, the pressure fluid in the 2.5-cm optical path had a long time constant after each change in pressure. After a great deal of effort, the system was stabilized sufficiently to allow the measurement of the ADL films, already known to switch under mechanical abuse. The result of this

measurement was disappointing, as the changes observed in the transmission were not large enough to indicate a phase change in the film. The substrate apparently locks the film in place and inhibits the lattice collapse.

Measurements of the resistivity in a sapphire anvil are, in principle, possible if the presence of the substrate can be indentified and eliminated. No attempt was made to measure the resistivity change in an SmS film in the hydrostatic pressure cell, as this also was fraught with difficulties. Gold contacts were deposited onto the film, and silver paints and epoxies were attached to the gold. However, none of the contact materials used were able to withstand the pressure, and the contacts came loose during the runs. Ultimately, we bonded a gold wire to the film with silver paint and sealed the joint with epoxy before loading.

V.2. Summary

The results of the measurements of the optical and electrical properties of the films indicated that the ADL films underwent a phase transition from semiconductor to metal. However, those we deposited by CVD were not SmS, but a dielectric with no phase transition we could induce either by a sapphire anvil or in a high pressure chamber.

VI. THE DESIGN OF COATINGS INCLUDING A PHASE TRANSITION LAYER

Although automatic computer synthesis is a powerful tool for the design of optical coatings, it does not provide any understanding of the designs that it produces. Such understanding is necessary in practice because the real behavior of thin films is more complicated and their properties less predictable than the simple models assumed in the design process. Designs must be trimmed to suit real materials, and this adjusting process demands that the influence of the various design parameters, especially layer thickness and optical constants, should be well understood. The work under this contract has therefore concentrated on analytical rather than automatic methods, and the approaches used are, as far as possible, extensions of the methods used for conventional filter design. Vanadium dioxide (VO_2), a temperature-sensitive phase transition material at 10 μm, has been adopted as the model material for this study, but the techniques described are not limited to it. The optical constants of VO_2 are assumed to be:

Cold state:	2.9 - i0.25
Hot state:	3.0 - i7.0

VO_2 is usually deposited over a thin layer of Si in order to achieve satisfactory properties. To render these design examples more generally applicable than just to VO_2, the Si layer was omitted. It can readily be inserted and the designs trimmed accordingly.

The cold and hot states of the coating are characterized by either high or low absorptance, transmittance, or reflectance. The particular switching arrangements investigated comprised:

Cold State	Hot State
Maximum transmittance	Low transmittance
Zero reflectance	Maximum reflectance
Zero reflectance and high transmittance	High reflectance
High reflectance	Zero reflectance

In each case certain parameters were specified as a starting point for the design. These parameters included such things as the switching layer thickness, theoretical zero reflectance in one of the two states, maximum possible reflectance, and so on. The design procedure then involved the optimizing of certain other aspects of performance characteristics. The complete design was then realized by adjusting the dtails of the complete multilayer design.

VI.1. Maximum Cold Transmittance

The starting point for this arrangement is taken as a given thickness of Vo_2. The design technique is based on the concept of potential transmittance and is similar to the design of induced transmission metal-dielectric interference filters. It is assumed that

only the switching layer is absorbing.

The potential transmittance of an absorbing layer is defined as

$$\Psi = T\,(1-R)$$

where T is tranmittance and R is reflectance, and can be shown to depend only on the optical admittance of the structure on the side of the phase transition layer farther from the incident light, which can be called the exit admittance. Once Ψ is fixed, then the maximum value of T will be equal to Ψ and will be obtained only if dielectric layers are added to the front surface of the phase transition layer to reduce R, the reflectance of the assembly, to zero. Ψ is a maximum for an optimum value of exit admittance that can be calculated. The design procedure then consists of treating the cold VO_2 layer as an absorbing layer and finding the optimum value of exit admittance and the corresponding value of (Ψ_{max}). $T_{max} = \Psi_{max}$ can then be achieved by designing the appropriate matching layers surrounding the Vo_2 layer. Since the Vo_2 layer in its cold state is now perfectly matched to its surrounding medium, the match in the hot state will be far from ideal and the transmittance will be low. A typical design uses a thickness of 750 nm of VO_2:

Air | LG 1.676L VO_2 1.676L | Ge

where H and L indicate germanium (Ge) and zinc sulfide (ZnS) quarterwaves, respectively. The performance is shown in Fig. 7. The transmittance in the hot state is less than 1 throughout the range shown.

VI.2. Zero Reflectance in the Cold State, Maximum Reflectance in the Hot State

Here the starting point is zero reflectance in the cold state. The thickness of Vo_2 is found that gives maximum reflectance in the hot state. There are features of the deposition process that encourage placing outermost the VO_2 layer; this is therefore a constraint imposed on the initial design.

The admittance diagram was used. This is a complex plane in which the locus of the optical admittance of the multilayer is usually plotted from the exit interface through to the front interface. Here, however, the reverse locus was first plotted. For zero reflectance to be obtained, the locus must end at the point (1,0) corresponding to the admittance of air, the incident medium. Given any thickness of VO_2, the unique starting point for its locus can be found in order that it should terminate at the point (1,0). The reverse locus is the complete set of such starting points as the thickness is permitted to vary from zero. The mechanism for drawing a reverse locus is simply to replace the starting point by the desired end point and to draw a normal locus but with negative thicknesses. If a multilayer rather than a single layer is

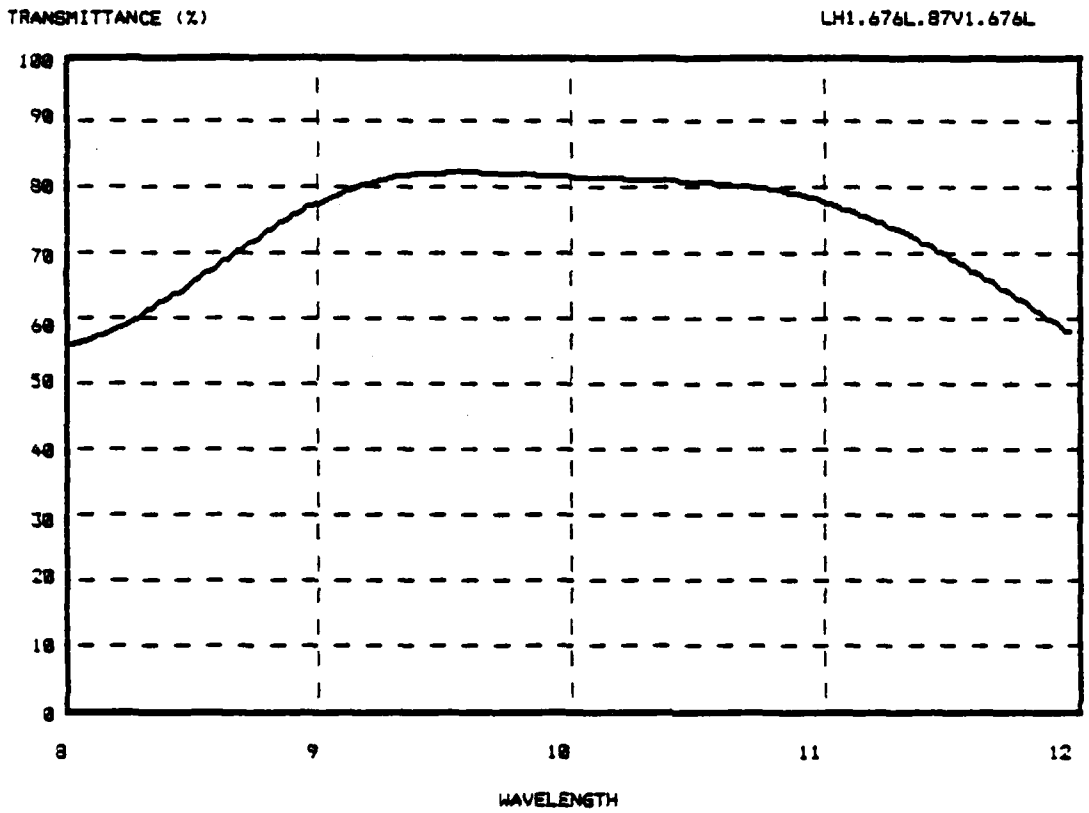

Fig. 7. Cold transmittance of VO_2-based switching coating.

involved, then the order of the layers should also be reversed. The reverse locus of the VO_2 layer is a definitely unambiguous curve with one and only one starting point, the exit admittance, associated with each value of thickness. To complete the design for any thickness, the appropriate exit admittance must be matched to the substrate. Assume that in any particular case this has been done so that the coating in the cold state has zero reflectance. Now consider the coating as switched to the hot state. The matching assembly contains no switching layers and so remains unchanged and, in particular, the exit admittance of the VO_2 layer remains at its cold-state value. This exit admittance is the starting point for the hot layer, and since its thickness is still fixed, so too is the final termination point and, therefore, its reflectance. Therefore, the unambiguous value of hot-state reflectance can readily be calculated. If this operation is repeated for each possible value of thickness of VO_2, the hot-state reflectance is recorded as a function of VO_2 thickness given zero reflectance in the cold state. The optimum value of thickness will be that value that gives maximum hot-state reflectance. Such a curve is shown in Fig. 8, and includes a weak maximum at a thickness of 0.7 μm. As far as matching is concerned, the VO_2 layer, whatever its thickness, can be matched fairly well by a quarterwave of ZnS next to the Ge substrate followed by a layer of Ge. Its thickness would depend on the VO_2 thickness by usually greater than a quarterwave unless the VO_2 is very thick. This can be seen from the reverse admittance locus of VO_2 in Fig. 9 to which a forward locus of

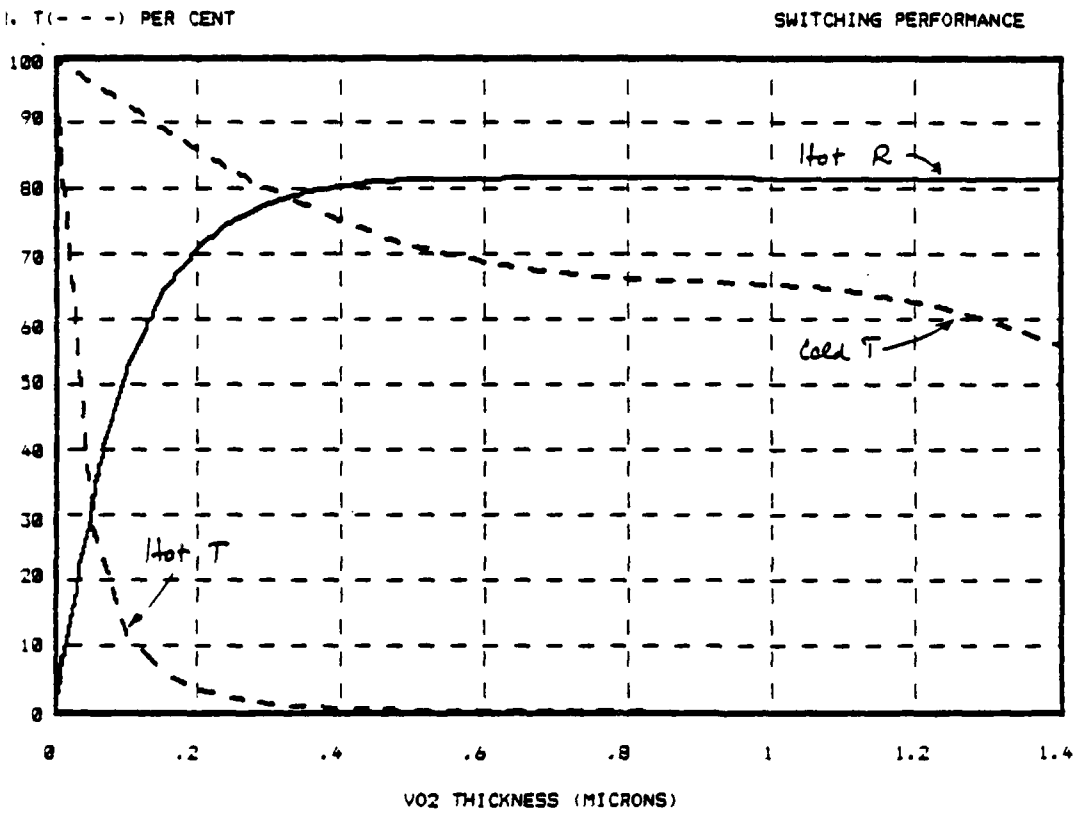

Fig. 8. Performance of switching coating with VO_2 layer outermost given that the cold reflectance is zero.

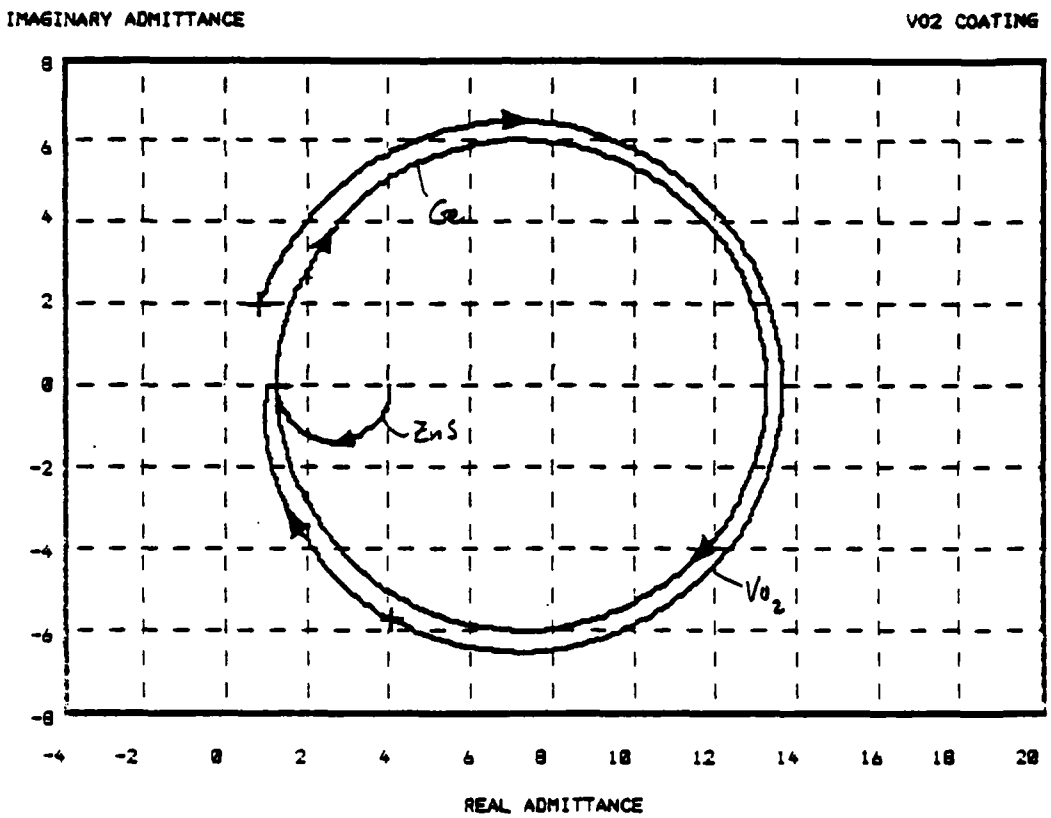

Fig. 9. Admittance locus of matching stack of ZnS and Ge added to the reverse admittance locus of VO_2.

the ZnS-Ge combination has been added. The optimum thickness of VO_2 is 700 nm,and this can be matched fairly well by the structure:

1.3H L | Ge

so that the final design is:

Air | VO_2 1.3HL | Ge.

The performance is shown in Figure 10.

This design technique has so far yielded only a single wavelength design. To flatten the performance over a wider region, halfwave layers can be inserted. Unfortunately, inspection of the admittance plot for the multilayer reveals that a halfwave of index less than 1.0 is needed at the Ge/ZnS interface or greater than 4.0 at the ZnS/Ge (substrate) interface. Neither is readily possible. Therefore more complicated flattening arrangements have to be used that will not be as effective over a wide region. Symmetrical periods can be used to act over a limited range as layers having thickness equal to an integral number of halfwaves. These can be of the form LHHL, for example, acting as a layer of very high index. Here we use the combination LHLLHL is used as a very low index layer so that the complete design becomes:

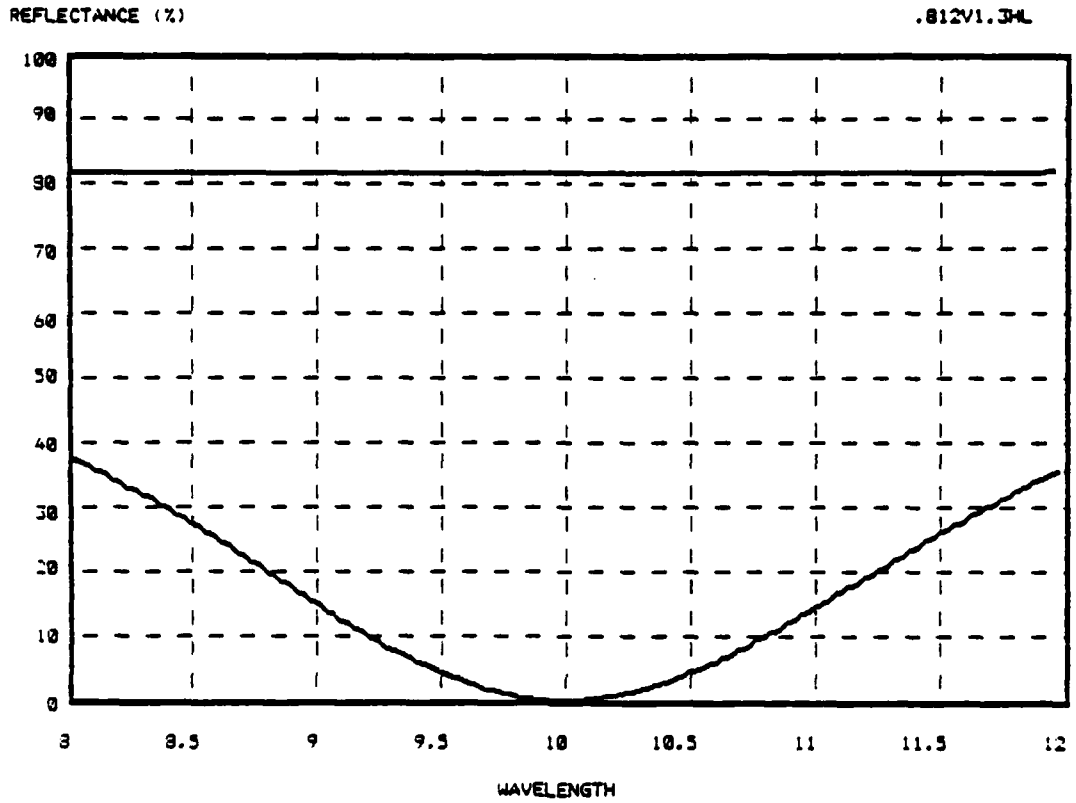

Fig. 10. Air | VO_2 – 700nm | 1.3H L | Ge

H – Ge n = 4.0

L – ZnS n = 2.2

Switched (upper) and unswitched (lower) performance

Air | VO_2(700nm) 1.3H LHLLHL L | Ge .

Figure 11 shows that the addition has flattened the performance somewhat but is not powerful enough. An alternative approach involves using a Ge halfwave layer as a high-index flattener, but in the basic design there is nowhere to insert it. Therefore a halfwave of low index was added next to the substrate, which does not affect the performance around λ_0 but which affords a place for the insertion of the Ge layer. Trial and error show that full waves rather than halfwaves for both these layers are required, giving the final design:

Air | VO_2(700nm) 1.3H L 4H 4L | Ge

and the performance shown in Fig. 12.

The end point of the reverse locus of the VO_2 is in a particularly unfavorable place in the admittance diagram for matching over a broad wavelength range with dielectric assemblies. Metal layers, on the other hand, have loci that can directly link the Ge substrate to the VO_2 locus. The problem is that at 10 μm only a very thin metal film is required. A search of published figures for metal optical constants in the 10-μm region suggests that titanium might be suitable. Figure 13 shows a titanium (Ti) locus crossing the reverse locus of VO_2. Ti has optical constants of 9.1-i17.8 and the crosses on the diagram are spaced at intervals of 100-nm optical thickness so that the match point is at a geometrical thickness of 34.4 nm. The cross on the VO_2 layer represents

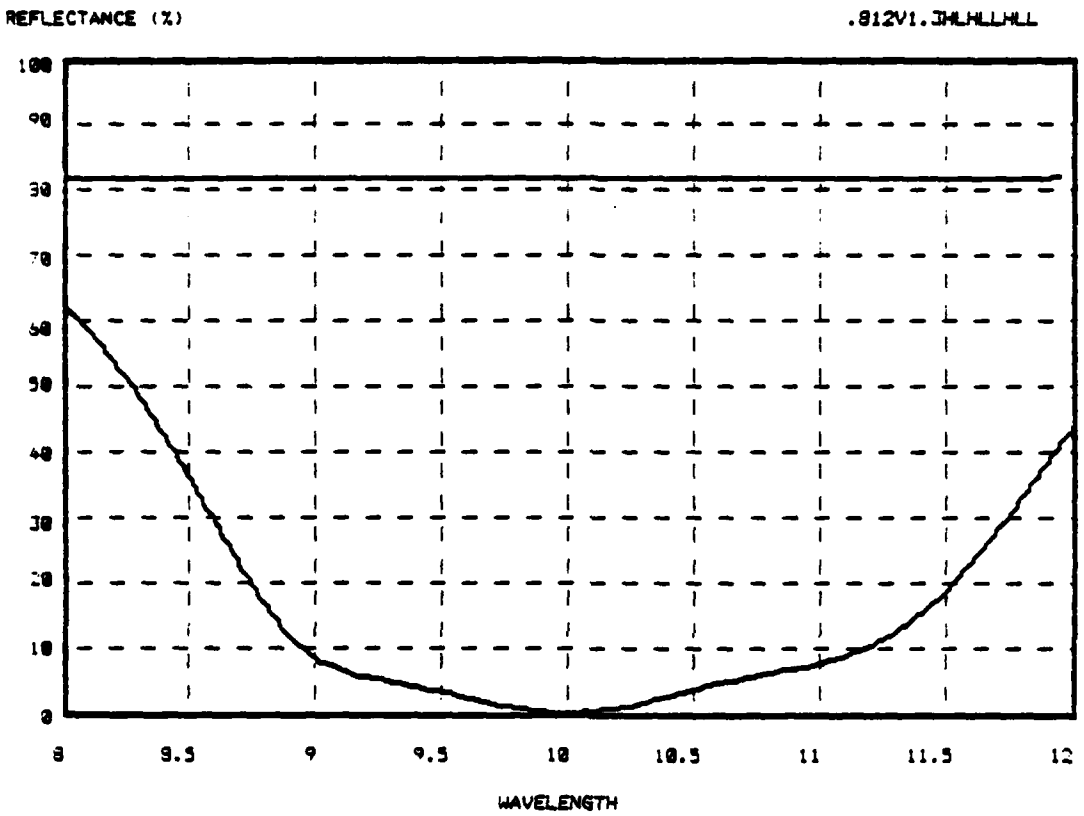

Fig. 11. Air | VO_2 - 700nm | 1.3H LHLLHL L | Ge

H - Ge n = 4.0

L - ZnS n = 2.2

Switched (upper) and unswitched (lower) performance

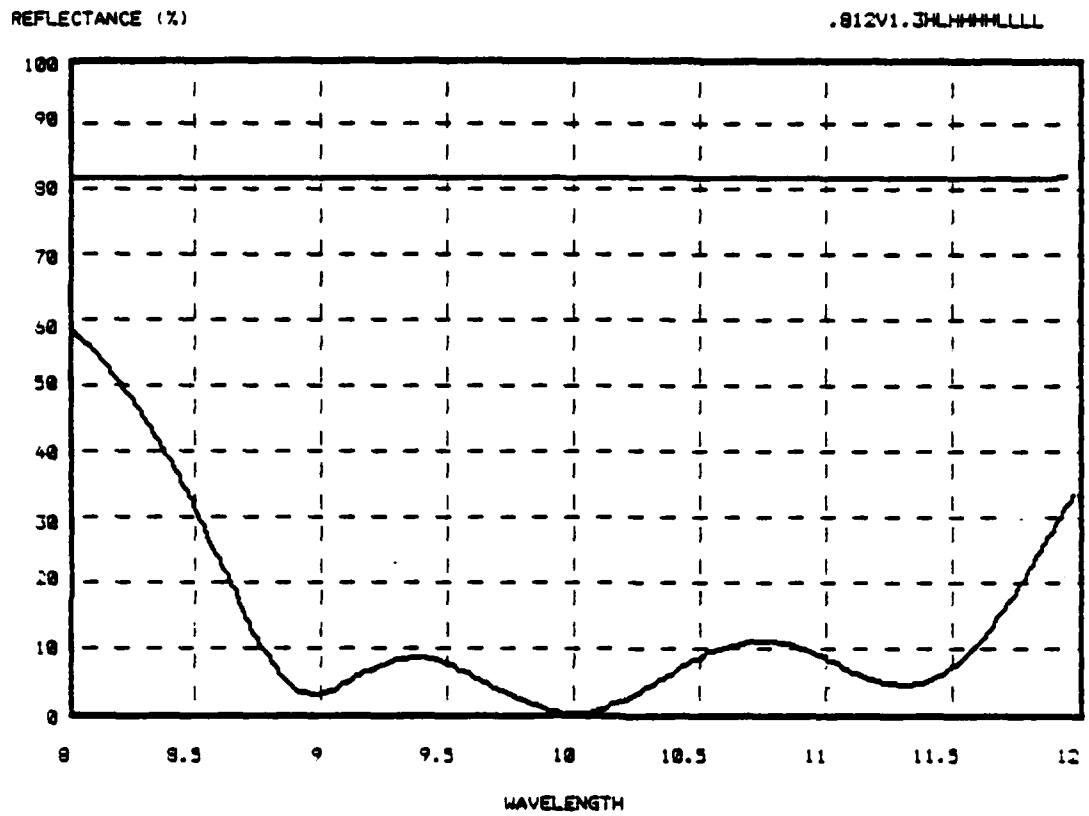

Fig. 12. Air | VO_2 - 700nm | 1.3H L 4H 4L | Ge

H - Ge n = 4.0

L - ZnS n = 2.2

Switched (upper) and unswitched (lower) performance

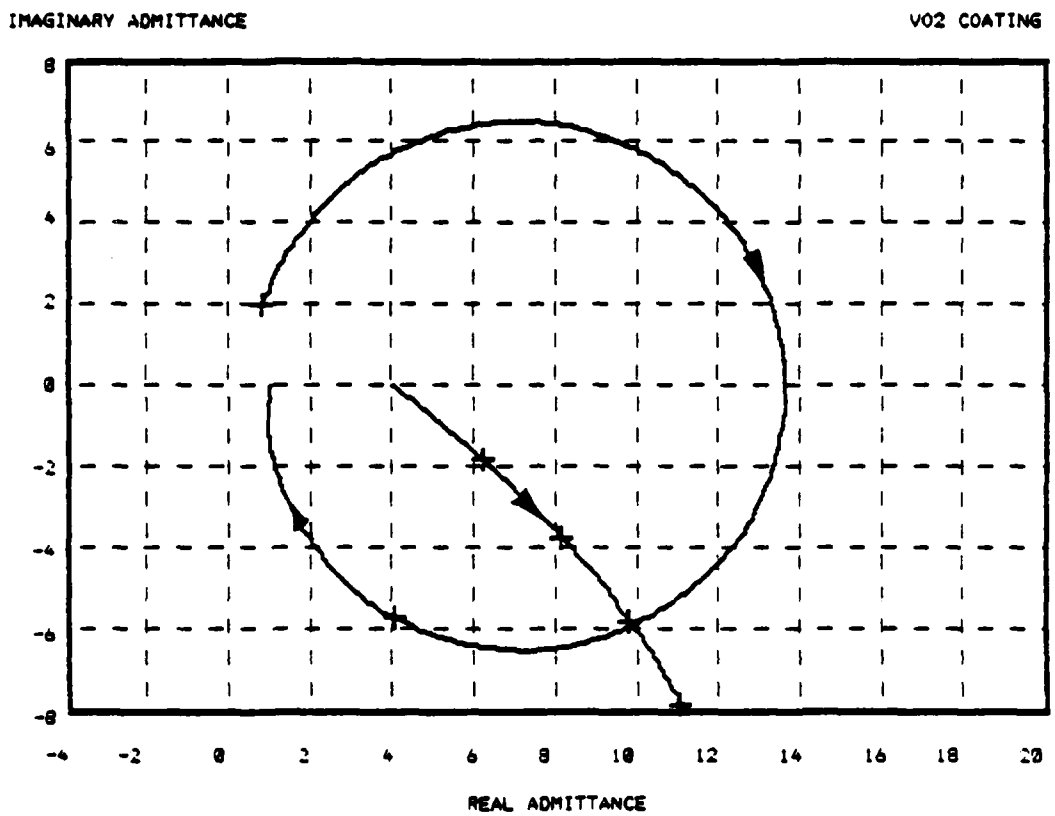

Fig. 13. Admittance locus of titanium superimposed on inverse locus of VO_2

Titanium n-ik = 9.1 - i 17.8

the optimum 700-nm thickness and so a rather greater thickness has to be used in the final design for the matching to be effective:

Air |VO_2(815nm) Ti(34.4nm) | Ge .

The performance of this design is shown in Fig. 14.

Now let us consider the addition of extra layers above the VO_2 layer to exceed the maximum possible reflectance obtained with the VO_2 outermost. The most straightforward arrangement is to retain the 700-nm thickness of the VO_2, which will look much like bulk material when switched to the hot state, and to add a two-layer boosting combination of a low-index matching layer and a quarterwave high-index layer. This combination can be calculated to be:

Air | H 0.832 L .

When, however, one tries to achieve zero reflectance in the cold state with this configuration above the VO_2, there is complete failure. Its reverse admittance locus reveals why. Figure 15 is the relevant locus, and it can clearly be seen that the end point of the VO_2 layer is in the part of the complex plane corresponding to the negative real part of the admittance. This is a forbidden region, so we can deduce immediately that there is no possible combination that can be used between the substrate and the VO_2 layer to reduce the cold-state reflectance to

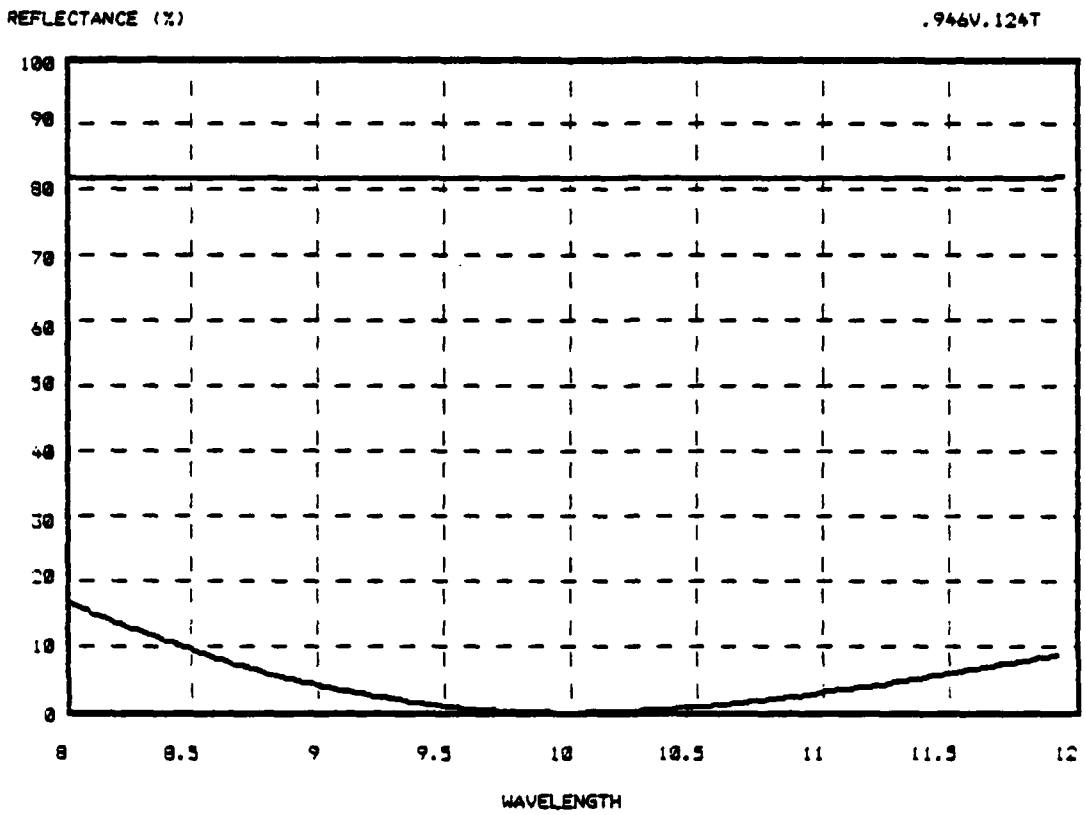

Fig. 14. Air | VO_2 – 615nm | Ti – 34.4nm | Ge

Ti – Titanium n–ik = 9.1 – i 17.8

Switched (upper) and unswitched (lower) performance

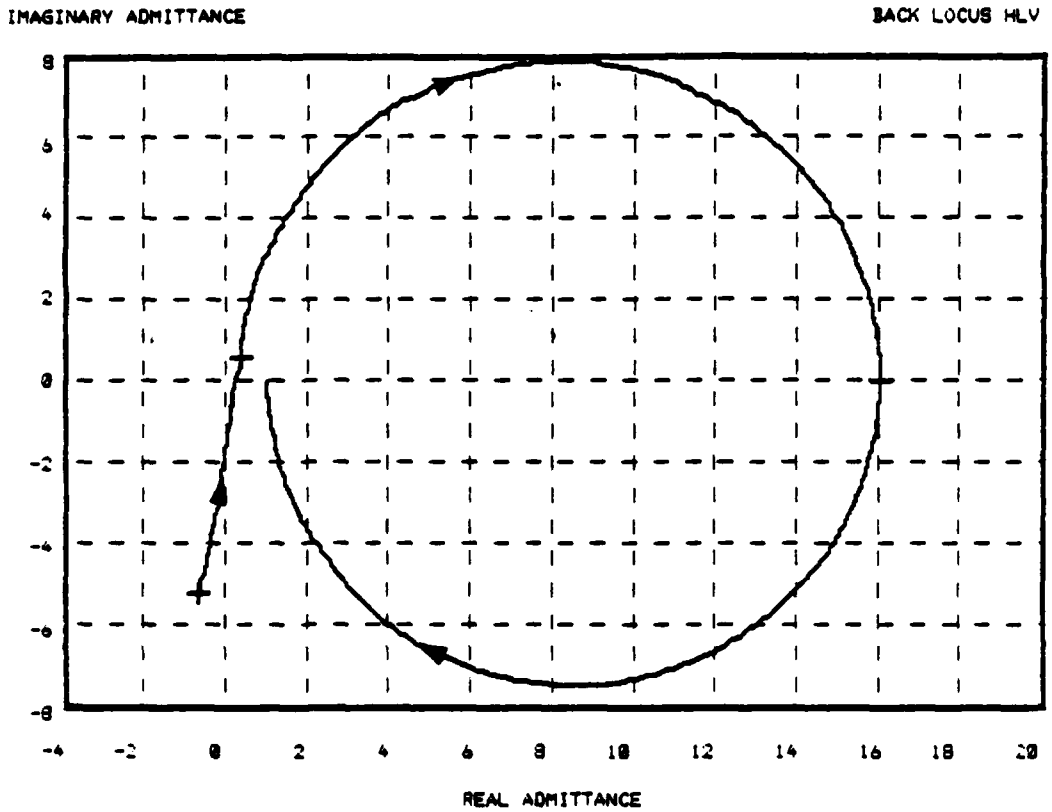

Fig. 15. Reverse admittance locus of

Air | H 0.832L | VO_2 - 700nm |

H - Ge n = 4.0

L - ZnS n = 2.2

zero. A detuning of the boosting layers to give a somewhat lower reflectance of 90% in the hot state results in an acceptable reverse locus and the design:

Air | 0.6H 1.424L VO_2(700nm) 1.58H 0.308L HLHL | Ge ;

Figure 16 shows its performance.

VI.3. Zero Reflectance with High Transmittance in the Cold State

This type of coating can most readily be designed using the same techniques as the previous section and employing the curve in Fig. 8, showing transmittance in the cold state. For high transmittance the VO_2 layer should be made thinner than the optimum 700 nm, which can be done without any great penalty in lost reflectance in the hot state since the reflectance curve is very flat.

VI.4. Zero Reflectance in the Hot State

This coating involves the design of an antireflection coating for the VO_2 in the switched hot state. Optical constants of 3.0-i7.0 make it exceedingly difficult to match a thick layer of VO_2 with a simple coating, and although zero reflectance is not impossible, the performance would be good over only a narrow region. The admittance locus shows that a much better arrangement is a thinner layer of VO_2 under a single matching layer of as high an index as possible, so that

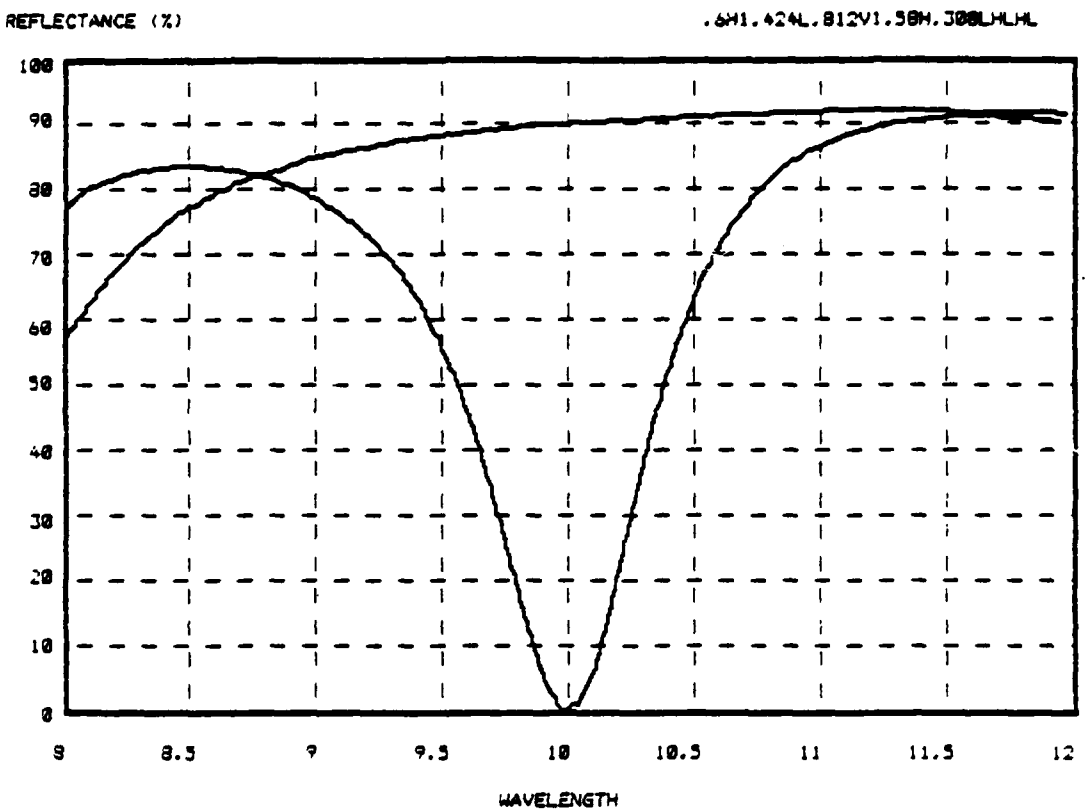

Fig. 16. Air | 0.6H 1.424L | VO_2 - 700nm | -
- 1.58H .308L HLHL | Ge

H - Ge n = 4.0
L - ZnS n = 2.2

Switched (upper) and unswitched (lower) performance

the vanadium dioxide is as thick as it can be without jeopardizing the design. Lead telluride (PbTe) was chosen due to its index of around 5.7 in the 10-μm region. The admittance locus is shown in Fig. 17. The design is:

$$\text{Air} \mid 0.604P\ VO_2(700\text{nm}) \mid \text{Ge}\ .$$

Since the matching is optimized for the hot state, it will be far from ideal in the cold state: High reflectance will result as indicated in the performance curve of Fig. 18.

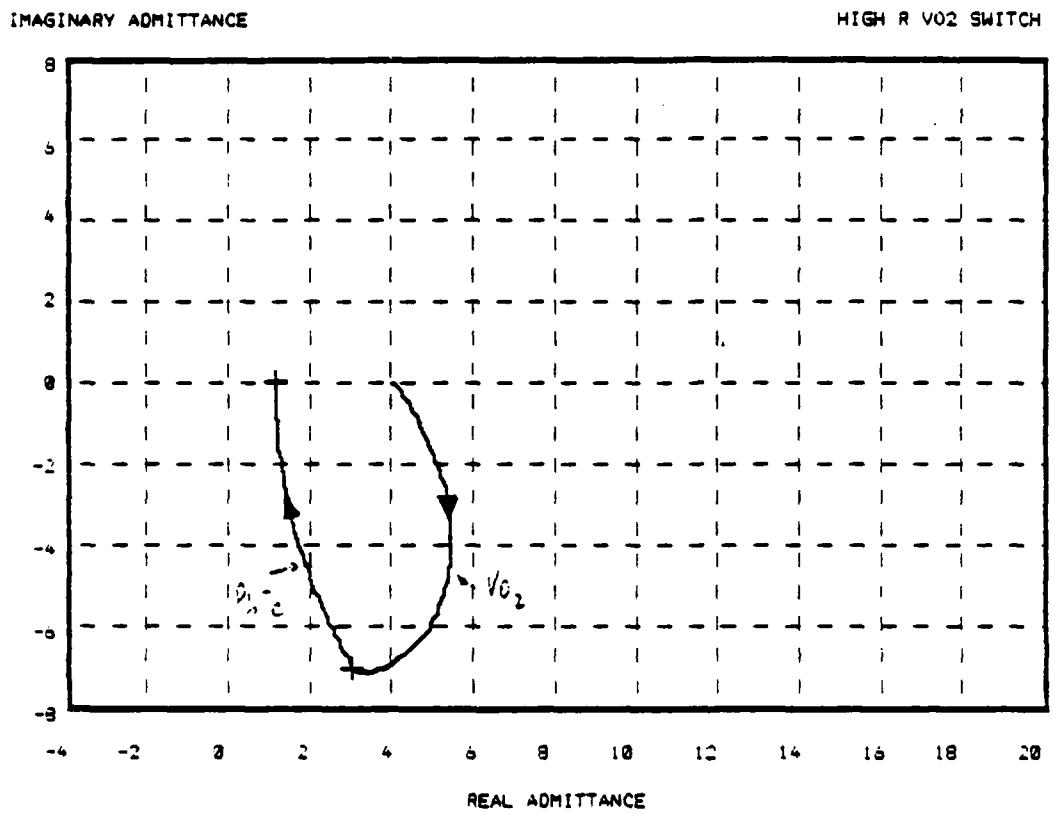

Fig. 17. Admittance locus of

Air | 0.604P | VO_2 – 700nm | Ge

P – PbTe n = 5.7

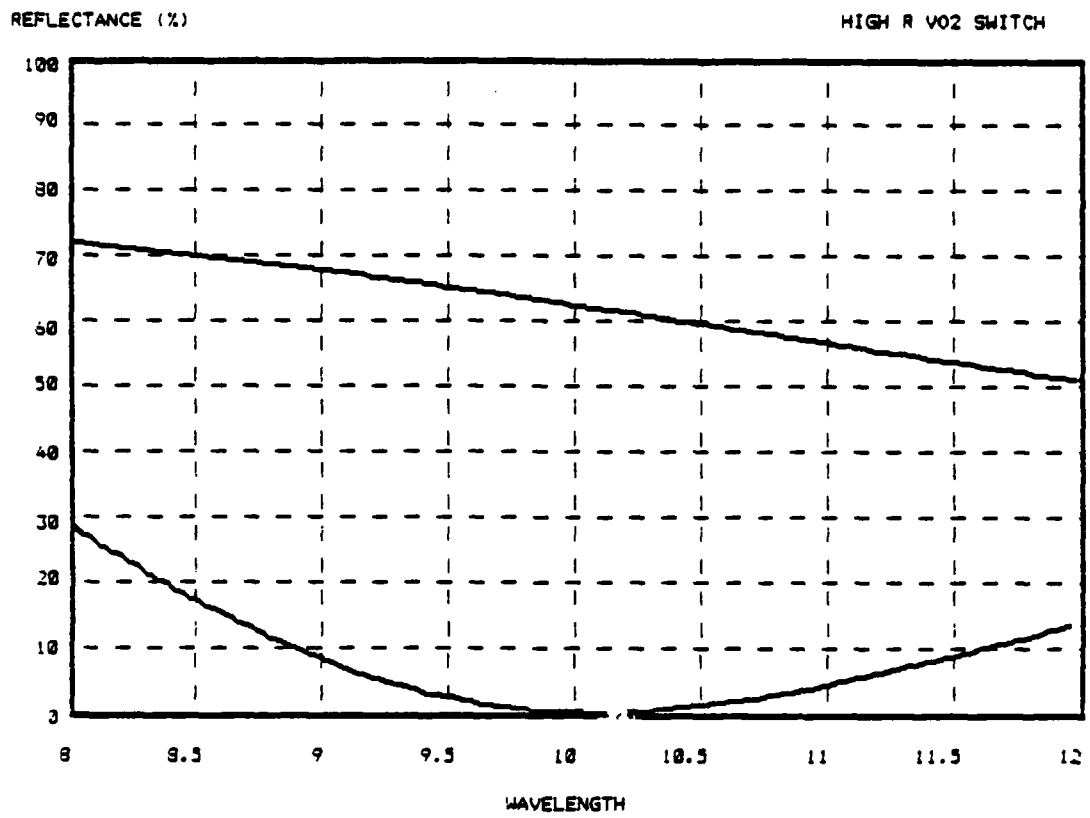

Fig. 18. Air | 0.604P | VO_2 - 700nm | Ge

P - PbTe n = 5.7

Switched (lower) and unswitched (upper) performance

VII. SUMMARY, CONCLUSIONS, AND RECOMMENDATIONS

Our three-year effort has produced negative results in the sense that we have not deposited the material we intended. Such outcomes are common in many projects where high-risk research is performed in areas where little prior experience or information is available. However, if the work has been executed competently, systematically and consistently, conclusions can be drawn that may guide future efforts aimed at the same objective. The evaluation and exclusion of previous approaches by subsequent research teams will save valuable time and resources and enjoy a greater chance of success.

We realize that we invested much time and effort over the past three years in approaches that hindsight reveals to have been unworkable. When we began, however, we did not have the necessary information; it came from the unsuccessful implementation of those approaches.

Nonetheless, the properties of SmS could still contribute to several optical technologies, so the search for means of depositing acceptable films should continue. For the immediate future, the research effort would perhaps be best deployed to modify or innovate PVD techniques. Should these methods not produce promising SmS films, we would recommend a second look at CVD. Despite our difficulties, we in no way exhausted the range of starting materials, reactor configurations, and process parameters that might lead to the successful CVD of SmS. Until several additional processes are tried, the CVD of

SmS cannot be considered impossible. Toward this end, we have compiled several recommendations from our recent experience.

VII.1. Choice of the Reactant Material

1. Organometallic compounds are prone to decomposition at several molecular loci. If Sm remains bound to several other atoms, the resulting fraction may either react with H_2S and become incorporated in the film, not react with H_2S and still enter the film, or simply proceed out of the chamber. None of these scenarios leads to the desired product; the first two include atoms from the ligand, notably O and C, in the film. One way to reduce the problem is to create a source material that is rich in S. Samarium dithiocarbamate is such a candidate if it can be made to react with H_2S. Under the conditions of our last few runs, the material simply recrystallized on the vessel walls. If conditions that promoted the reaction can be identified, such sulfur-rich materials may mitigate the consequences of unpredictable breakup of organometallic molecules in the CVD environment.

2. Samarium trihalides should be reconsidered as reactant materials. In particular, the tribromide of Sm, according to recent publications, appears to have a higher vapor pressure than previously reported. It is here that our original approach, based on a naive striving for flexibility in arranging gas flow, limited our range of reaction temperatures. Now that we have eliminated Teflon, we could operate our system at the temperatures necessary to dissociate samarium

tribromide. At these temperatures, Sm_2S_3 may be preferentially formed, but perhaps this tendency could be countered by manipulating other process parameters, or by post-deposition anneal.

3. Chemical vapor transport should be investigated more fully. In a closed system where highly purified solid samarium, sulfur, and iodine are carefully sealed in a quartz ampule, contamination should be minimal, and equilibrium reactions would promote growth under minimum stress. Our models of this process indicate its thermodynamic feasibility.

VII.2. Recommendations Concerning the Reaction Vessel and Process Parameters

1. Our preference for atmospheric-pressure deposition may have limited our options significantly. At the start of the program, our previous success with other CVD materials, operational convenience, and the exclusion of impurities by working at positive pressures recommended this environment. We are now aware of other data that suggest operation at reduced pressures where many of the critical reactions proceed in a more favorable direction.

2. Our attempt to build a reactor that could deposit a variety of different materials with a minimal reconfiguring of the reactor plumbing indicated the use of Teflon. This decision restricted the temperature range and led to leaks and tedious leak hunting. We have learned that it is better to design a system for a specific material than to strive

for versatility at all costs. Six other lessons were to minimize the number of joints and fittings, maximize the fluid conductance of lines between system components, avoid particulate transport in the source lines, eliminate hot spots along the source lines and in the reaction chamber, promote turbulence in the reaction chamber, and design all components for convenient cleaning and adjustment.

VII.3. Recommendations Concerning the Analysis of the Films

Film analysis required that we strike a balance among the relevancy, accuracy, availability, efficiency, and affordability of the technique. Relevancy was the first aspect. The sequence of measurement had to yield useful information on structure as well as composition, since we had to determine the presence of the SmS phase. Accuracy of the measurement was somewhat less important in our attempt to simply produce the material. Availability and efficiency were both important. The instruments not only had to be convenient to us, but they had to be managed in such a way that rapid turnaround was possible. Finally, affordability was a factor, since our resources were not unlimited.

We believe that our analysis program was rather successful, in view of the constraints under which we operated. In this regard, we can make several recommendations toward improving analysis of SmS films, regardless of deposition method. First, x-ray analysis is extremely important and should not be handicapped by inadequate or non-existent software. The only on-line data analysis capabilities in Arizona are at two local research laboratories for the copper industry, and their

ability to accommodate us was extremely limited. We had a very well managed Siemens x-ray diffractometer available to us on campus, but it produced strip chart records that required tedious attempts at interpretation "by hand." Had this machine been purchased with a computer and software, we would probably know much more about our films, since a computer can search the 35,000 or more XRD files in minutes, while update hardcopies of that data were not even extant on campus. Nonetheless, XRD identified the Sm_2O_2S constituent, and informed us consistently that we were not producing SmS, despite encouraging, if misleading data from purely compositional techniques that indicated an Sm:S ratio close to unity. XRD should remain a central analytical technique.

We found scanning electron microprobe and Rutherford backscattering helpful for determining composition, although we needed a technique for reliably detecting and comparing O and C levels. Perhaps SIMS would have been helpful, especially if depth profiling were possible. We were able to have very limited Auger analysis done, which revealed that our films were uniform with depth in terms of Sm, S, C, and O ratios. Future workers should, then augment SEMQ and RBS with SIMS and Auger. Perhaps SEMQ and/or RBS could be replaced with SIMS and/or Auger. The latter techniques were not readily available or affordable to us on this project, but their absence was not critical, since SEMQ and RBS revealed our critical C and O contamination, and we were not able to reduce it to the point that more sensitive techniques were necessary.

VII.4. Recommendations Concerning the Determination of the Physical Properties of the Films

The intimate and inseparable influences of the substrate on the film makes a calibrated measurement of the pressure-induced changes in thin films a questionable prospect at best. The best approach to determining the intrinsic properties of coatings appears to be deposition on a soluble substrate, so that the latter can be dissolved snf the unsupported film can be tested.

Optical measurements of such a film should be possible in an anvil such as Jayaraman's, which employs a small sapphire anvil to apply hydrostatic pressure to the sample. Calibration at these low pressures must be made by extrapolating a high-pressure calibration of the shift of the ruby fluorescence, as the small size of the cell precludes other methods. The measurement of resistivity under pressure can probably be achieved in a conventional bomb with the use of suitable contact materials, but only on a substrate-supported film. At present, it is not clear how to make this measurement on an unsupported film.

VIII. REFERENCES

The list presented here refers to publications specifically cited in the text. A more complete list is cited in references 6 and 7.

1. A. Jayaraman, V. Narayanamurti, E. Bucher, and R. G. Maines, Phys. Rev. Lett. 25, 1430 (1970).

2. J. L. Kirk, K. Vedam, V. Narayanamurti, A. Jayaraman, and E. Bucher, Phys. Rev. B6, 3023 (1972).

3. E. Kaldis, A. Schlegel, P. Wachter, and Ch. Zurcher, J. Magn. Magn. Mat. 3, 1 (1976).

4. A. Jayaraman, P. Dernier, and L. D. Longinotti, Phys. Rev. B11, 2783 (1975).

5. P. D. Hillman, Ph.D. Thesis, University of Arizona (1983).

6. M. R. Jacobson, P. D. Hillman, A. L. Phillips, and U. J. Gibson, Proc. SPIE 428 (1983).

7. P. D. Hillman, A. L. Phillips, M. R. Jacobson, and U. J. Gibson, Proceedings of the IX International Conference on CVD (The Electrochemical Society 1984) p. 517.

8. H. A. Eick, Chem. Properties of Rare Earth Mono-Thio Oxides, 43-44, January 5, 1958.

IX. APPENDICES: XRD, SEMQ, and RBS ANALYSES

The following tables document x-ray diffraction [XRD], scanning electron microprobe quantometer [SEMQ], and Rutherford backscattering [RBS] data for the third year of the program. Earlier XRD data and the Auger information are summarized in the annual reports for the first and second years. The same general format is used for all three methods.

XRD ANALYSIS

To present the XRD data, a number of codes and abbreviations are used to condense the information. The table is organized into sections, beginning with coatings from other laboratories, followed by our own as-deposited samples, presented by batch, bare substrates submitted to XRD, and annealed samples shown by anneal run. Sample numbers, such as 49-7, represent batch and serial number within the batch. Samples which have been annealed are awarded prefixes, such as A1, which denotes the first anneal. At the beginning of each data line are two lines of code, which identifies substrate and the lab and operator responsible for the trace. The code is translated below:

Substrate Codes: SiO_2=Q,Si=Si,CaF_2=CF,Si_3N_4=SN,Glass=G.
Instrument Codes: Physics/Phillips=PP,Duval/Phillips=DP,
Anaconda/Phillips=AP,Geosciences/Siemens=GS.
Operator Codes: Messerly=M,Davidson=D;Thorpe=T;Bilodeau=B.

Looking across each page header, a list of compounds and their strong x-ray lines is shown. The aluminum from the sampleholder, the substrates, and the film are included. The x-ray lines are identified by their 2θ angles for Cu(Kα) radiation and are rounded to the next lowest integer angle in degrees. Identifications are listed below each heading angle with an x. Very strong lines are given an x!, unsure identifications as x?, and very weak lines as (x). Note that the header usually has two lines in the same column: identification of both lines is shown by a column of two x's in the data line. Comments may follow the data line; additional identifications are listed simply by the 2θ angle rounded down.

Sample/Substrate	Holder Al	Substrates CF	SN	Si	Q	Films Sm_2O_2S					SmS		Sm_2S_3	
Inst./Oper./Date	38 65	28	28	33 69	24	26 37 46	54	61	26	43	26	39		
	44 78	59	59	56		29 40 48	56	76	30	51	33			
SmS SAMPLES FROM OTHER LABORATORIES														
Bell/Sa									x	x				
DP/D/1-13-84									x	x				
Three other SmS lines.														
Little/G									x	x				
AP/T/2-22-84									x	x				
AS-DEPOSITED SAMPLES														
36-11/Si												x?		
DP/D/1-6-84												x?		
Strong lines at 43, 58, 72, 74, 88. Very strong, narrow line at 40.														
36-17/Si												x?		
DP/D/1-6/84				x!								x?		
Strong lines at 58, 66, 66.5, 72, 74, 88. Very strong, narrow line at 40.														
39-13/CF														
PP/M/2-3-84	Check													
GS/B/3-28-84	x	x	x!											
	x	x	x!											
CaF_2 at 55. Unknown line at 31.														
41-8/Si														
DP/D/2-2-84					x!	x!								
Strong lines at 41, 48, 66, 66.5, 71, 72.														
GS/B/3-28-84	x	x			(x)	x!								
	x	x												
41-13/CF														
PP/M/2-3-84					x!									
AP/T/2-22-84			x!											
			x!											
GS/B/3-29-84	x	x	x!											
	x	x	x!											

Sample/Substrate	Holder	Substrates				Films							
	Al	CF	SN	Si	Q	Sm_2O_2S					SmS	Sm_2S_3	
Inst./Oper./Date	38 65	28	28	33 69	24	26 37	46	54	61		26 43	26	39
	44 78	59	59	56		29 40	48	56	76		30 51	33	
44-4/Si PP/M/2-20-84 Line at 31.				x									
45-6/Si PP/M/2-20-84 No lines. AP/T/2-22-84 Line at 66.													
46-13/SN PP/M/3-16/84 No lines, amorphous background.													
47-6/SN PP/M/3-16-84 No lines, amorphous background.													
48-6/Si	x	(x)		x	x							x	x
GS/B/4-6-84	x	x										x?	
48-10/SN	x	x										x?	
GS/B/4-6-84	x	x											
49-7/CF	x	x	x!	x?									
GS/B/4-11-84	x	x	x!										
49-12/SN	x	x		x									
GS/B/4-11-84 Wide amorphous zone 25-30.	x	x											
50-2/CF	x	x	x										
GS/B/4-20-84	x	x											
50-5/Si	x	x		x	x!								
GS/B/4-20-84 Wide amorphous zone 25-30 as sample number 49-12.	x	x											
51-2/CF	x	x	x										
GS/B/4-26-84	x	x											
51-5/SN	x	x		x									
GS/B/4-26-84	x	x											
53-1/SN GS/B/6-7-84 Line at 53.			x!										
53-2/Si GS/B/6-7-84 SiO_2 at 26.				x	x								

X-RAY DIFFRACTION ANALYSIS

Sample/Substrate	Holder	Substrates					Films							
	Al	CF	SN	Si		Q	Sm_2O_2S					SmS		Sm_2S_3
Inst./Oper./Date	38	65	29	28	33	69	24	26	37	46	54	61	26	43	26	39
	44	78	59	59	56			29	40	48	56	76	30	51	33	
55-1/SN	x	x?		x											x?	
GS/B/6-14-84	x	x		x												
Line at 95.																
55-3/Si	x	x	x	x				x	x							
GS/B/6-14-84	x	x														
SiO_2 at 26.																
57-1/SN	x	x		x												
GS/B/6-25-84	x	x														
57-2/Si																
GS/B/6-25-84					x	x	x?									
58-1/SN																
GS/B/6-28-84																
58-2/Si																
GS/B/6-28-84					x	x										

SUBSTRATES

Substrate/CF	x	x	x													
GS/B/4-26-84	x	x	x													
Substrate/SN	x	x		x												
GS/B/4-26-84	x	x														
Substrate/Si	x	x			x	x										
GS/B/4-26-84	x	x														

	Holder	Substrates					Films								
mple/Substrate	Al	CF	SN	Si		Q	Sm_2O_2S					SmS		Sm_2S_3	
nst./Oper./Date	38	65	28	28	33	69	24	26	37	46	54	61	26	43	26	39
	44	78	59	59	56			29	40	48	56	76	30	51	33	

NNEALED SAMPLES

1-41-6/SN	x	x		x	x			x	x							
S/B/5-16-84	x	x						x	x							
1-48-5/CF	x	x	x					x	x		x					
S/B/5-16-84	x	x	x	x				x	x		x					
Huge line at 94.																
1-48-8/Si	x	x			x	x		x	x		x	x				
S/B/5-16-84	x	x	x	x	x			x	x	x		x				
Line at 13.																
1-49-10/SN	x	x?		x				x	x		x					
S/B/5-16-84	x	x						x	x	x		x				
1-50-5/Si								x	x		x	x				
S/B/5-16-84	x?				x	x		x	x	x		x				
1-51-5/SN	x?			x?				x	x?							
S/B/5-16-84	x	x						x								
1-52-6/Si																
S/B/5-16-84					x											
Lines at 26 and 46? Line at 58.																
2-48-7/SiO_2	x	x					x	x	x	x	x	x				
S/B/6-5-84	x	x						x	x	x	x	x				
2-49-3/SiO_2	x	x					x	x	x	x	x					
S/B/6-5/84	x	x						x			x	x				
2-49-11/Si	x	x			x	x		x	x	x	x	x				
S/B/6-5-84	x	x						x		x		x				
2-50-3/SiO_2	x	x					x	x	x	x	x	x				
S/B/6-6-84	x	x						x	x	x		x				
2-50-5/Si	x	x			x	x		x	x	x	x	x				
S/B/6-6-84	x	x						x	x	x		x				
2-51-5/SN	x	x		x				x	x	x	x					
S/B/6-6-84	x	x						x		x	x					
3-55-1/SN								x	x	x	x					
S/B/6-21-84								x		x	x	x				
Lines at 28 and 58. Molybdenum from getter powder?																
3-55-3/Si	x	x						x	x	x	x	x				
S/B/6-20-84	x	x						x		x	x	x				

The format is similar to the previous table. Six elements are arrayed across the top of each page, and atomic percents are given in each data line. Thicknesses, given in Angstrom units under the sample number and substrate type, were determined by weight and density.

Sample Thickness A Comment	Substrate	Method Comment	Date	Sm	S	C	O	Si	Ca
AS-DEPOSITED SAMPLES									
36-15 1300 Pre-Anneal	Si_3N_4	Auger		25	26	20	30		
		SEMQ		16	22	61	~0		
36-15 Post-anneal	Si_3N_4	Auger		27	18	23	32		
		SEMQ		18	15	52	15		
37-18 1200	CaF_2	Auger		24	26	26	24		
		SEMQ		20	21	60	~0		
41-1 900	SiO_2	SEMQ Strange Black Appearance	03/02/84	1	16	10	64	10	
41-4 1300	Si	SEMQ	03/02/84	17	16	11	22	34	
41-10 1900	CaF_2	SEMQ	03/02/84	27	30	14	29	00	
44-2 900	Si	SEMQ	03/02/84	10	9	15	21	45	
44-5 1200	SiO_2	SEMQ	03/02/84	3	3	15	6	73	
44-11 600	Si_3N_4	SEMQ	03/02/84	4	3	10	12	71	
44-14 300	Graphite	RBS		16	19	47	18		
45-1 400	SiO_2	SEMQ	02/16/84	4	4	23	69		
		Include Si	02/16/84	3	3	17	51	26	--
			03/02/84	3	3	13	56	25	

Sample Thickness Å Comment	Substrate	Method Comment	Date	Sm	S	C	O	Si	Ca
45-2 600	Si	SEMQ	02/16/84	12	12	75	0		
			02/16/84	3	3	18	0	76	
		Include Si							
			03/02/84	3	3	15	10	69	
45-3 600	Si_3N_4/Si	SEMQ	02/16/84	13	14	73	0		
			02/16/84	4	4	21	0	70	
		Include Si							
			03/02/84	4	4	18	7	67	
45-4 300	CaF_2	SEMQ	02/16/84	14	29	57	0		
			02/16/84	8	15	34	0	1	42
		Include Si							
			03/02/84	0	60	27	13	0	
45-5 700	Graphite	RBS Very similar to 44-14		16	19	47	18		
46-5 Near Zero	CaF_2	SEMQ	03/02/84	12	1	87	0	0	
				1	1	12	1	0	86
		Include Ca							
46-4	Graphite	RBS At 0°	3/05/84	14	18	39	27	Fluorine-2	
46-6	Graphite	RBS At 0°	03/05/84	14	18	36	30	Fluorine-2	
		At 45°		13	17	33	36	Fluorine-2	
46-7 200	Si	SEMQ	03/02/84	3	1	7	11	78	
46-12 600	SiO_2	SEMQ	03/02/84	0	3	5	59	33	
46-13 500	Si_3N_4	SEMQ	03/02/84	4	2	8	11	74	

Sample Thickness A Comment	Substrate	Method Comment	Date	Sm	S	C	O	Si	Ca
47-1	SiO_2	SEMQ	03/23/84	17	26	19	38	1	
		Center of fringe pattern							
				11	9	13	51	16	
		Mid-slope on red fringe							
				3	2	6	62	26	
		Outer edge on orange fringe							
48-6	Si	SEMQ	04/11/84	21	21	16	42	1	
		One position							
				19	19	16	44	1	
		Another position							
48-10	Si_3N_4	SEMQ	04/11/84	21	22	16	41	0	
		One position							
				20	21	16	42	1	
		Another position							
49-7	CaF_2	SEMQ	04/11/84	29	29	16	25		
		Normal position							
				16	15	9	18	0	43
		Computed with Ca							
				18	19	62	1	0	
		After hour of C buildup due to beam irradiation							
49-12	Si_3N_4	SEMQ	04/11/84	25	25	14	19	17	
		Normal position							
				22	21	13	18	26	
		At yellow spot/defect							
				12	9	10	14	55	
		At purple spot/defect							
50-1	Si_3N_4	SEMQ	04/25/84	27	27	13	23	9	
50-2	CaF_2	THIS DATA IS UNRELIABLE DUE TO COMPUTER PROBLEMS							
50-3	SiO_2								
50-5	Si	SEMQ	04/25/84	32	32	12	23	1	

Sample	Substrate	Method	Date	Sm	S	C	O	Si	Ca
Thickness A		Comment							
Comment									
SmS SAMPLES FROM OTHER LABORATORIES									
BTL	Sapphire	Auger		30	59	2	8		
		SEMQ	02/16/84	44	46	10	~0		
		SEMQ	03/02/84	45	43	12	0	0	
SmS	Bulk	SEMQ	03/02/84	41	38	21	0	0	

APPENDIX D

FINAL REPORT

THE JOHNS HOPKINS UNIVERSITY
APPLIED PHYSICS LABORATORY
LAUREL, MARYLAND 20707

FACULTY PARTICIPANTS:

T. O. POEHLER
R. POTEMBER
T. PHILLIPS

TABLE OF CONTENTS

I. Organo Metallic Switching..... 3

II. Electrical and Optical.....29

III. Publications and Talks.....90

Abstract

We have demonstrated reproducible optical and optoelectronic switching between two states in polycrystalline organo-metallic semiconductor films using radiation from several visible and infrared lasers. Although the optical measurements have largely concerned films of copper or silver complexed with the electronic acceptor tetracyanoquinodimethane (TCNQ), results on a wide range of acceptors indicate similar effects. It has been shown that the effect of the applied electric field on the initial charge-transfer salt (e.g., CuTCNQ) is to induce a phase transition resulting in the formation of a non-stoichiometric complex salt containing neutral TCNQ.

These results have been extended to show that regions of an optically switched AgTCNQ or CuTCNQ film can be reversed (i.e., erased) using a CO_2 laser as a source of thermal energy. The effect can be observed by Raman spectroscopy and direct observation. Results on the wavelength and irradiance dependence of the optical switching threshold show the optical switching occurs over a wide spectral range and can be interpreted in light of a reversible switching mechanism in these organic materials. Associated with these results are dramatic changes in absorption, reflection and transmission in these materials.

These organo-metallic compounds appear to be most promising as: (1) optical and optoelectronic switching materials, (2) erasable optical storage systems, and (3) nonlinear optical materials. The results obtained in this work have significant immediate potential for applications in laser hardening, erasable optical recording, and optical processing.

We have demonstrated significant modifications to the electrical, optical, and microwave switching properties of VO_2 through incorporation of

other ions. Thin films of Ti and W doped VO_2 were prepared and their electrical resistivities, optical transmission properties (0.4μ-2.5μ), and microwave transmission properties were measured as a function of temperature. The Ti dependence of the electrical resistivity and the single transition is consistent with a model in which the Ti ions are, in part, incorporated as interstitial impurities leading to an increased e^- concentration the π^* band. The occupation of the band is manifested in the decreasing temperature of the transition and the decreasing resistivities. Vanadium dioxide films prepared in this work had optical switching ratio of 4 to 8 higher than those prepared on similar substrates. A controlled reduction of switching temperatures was obtained for VO_2 films containing Ti and W ions. The former was accompanied by a reduction in the hysteresis at the phase transition. Significant increases of the optical and microwave transmission switching ratios was achieved in these mixed composition films.

I. Organo Metallic Switching

Introduction

The electron acceptor molecules 7,7,8,8-tetracyanoquinodimethane (TCNQ) and 11,11,12,12-tetracyano-2,6-napthoquinodimethane (TNAP) have been shown to produce electrically conducting solids with aromatic heterocyclics, as well as with alkali, and divalent transition metal counter ions.[1,2] We have observed a reversible electric field induced phase transition in polycrystalline organo-metallic semiconductor films incorporating these acceptors. The transitions are observed in films of either copper or silver complexed with the electron acceptors tetracyanonapthoquinodimethane (TNAP),[3] tetracyanoquinodimethane (TCNQ),[4] or other TCNQ derivatives.[5] This phase transition is accompanied by an abrupt increase in the electrical conductivity of the organic semiconductor when the applied field surpasses a threshold value. This highly conductive state remains intact as long as the field is present. When the applied field is removed, the system can either return to the high-impedance state, or in cases where a voltage significantly higher than the threshold voltage is used to induce the highly conductive state, the material will remain in the low-impedance state after the applied field has been removed.[6] The character of the switching in going from a high to a low-impedance state in these organic charge-transfer complexes is believed to be superior in many respects to existing inorganic materials.[7,8]

Optical Properties

We have investigated the effects of electric fields at optical frequencies on thin organo-metallic films in this family and have reported the observation of switching between the two stable phases as a result of the redox reaction induced by optical fields. These observations of switching between

the two states in these films have been made by both Raman spectroscopic methods and by direct observation of the electrical properties of the organometallic films.[9]

Since non-integral oxidation states are common in solids, it is difficult to predict exact stoichiometry of the equilibrium equation, but the equation which best describes switching in Cu-TCNQ is

$$[Cu^{+}(TCNQ^{\bullet})]_n \rightleftharpoons Cu^{0}_{x} + [Cu^{+}(TCNQ^{\bullet})]_{n-x} + (TCNQ^{0})_{x}. \qquad (1)$$

In addition, an ionic or a molecular displacement associated with this equilibrium would explain the observed memory phenomena and the fact that all the devices show only two stable resistive states.

For electrical measurements, a top metal electrode of aluminum or chromium was evaporated or sputtered directly on the organic film, and contacts made to the top metal electrode and the underlying metallic substrate. For the optical and electro-optical experiments, the top metal electrode was either omitted or prepared with a thickness that permitted partial transmission of optical radiation. Depending on the specific material involved, the field strengths required to cause switching transitions varies between 2×10^3 V/cm and 2×10^4 V/cm. Fields of this magnitude are easily obtained near focus in many moderate power laser beams. We have irradiated a number of CuTCNQ and AgTCNQ specimens with the 488 nm and 458 nm lines from an argon ion laser. The effects of this radiation have been observed both by Raman spectra and by electrical measurements made on specimens of the conventional two terminal switching geometry.

There have been a number of measurements reported on Raman spectra of

TCNQ and a number of the simple TCNQ salts.[10-16] Strong Raman bands are observed in these materials as is illustrated in Figure 1 for both TCNQ and a CuTCNQ film. It is apparent from this figure that a number of the Raman modes are strongly affected by the electronic structure of the TCNQ particularly ν_4, ν_6, ν_7, and ν_2. For example, the TCNQ ν_4 (C=C stretching) shows a frequency shift from approximately 1375 cm^{-1} for the fully charged transfer species to 1451 cm^{-1} for the neutral species. It is apparent from the Raman spectrum of this CuTCNQ film presented in Figure 1(b) that the film contains essentially no neutral TCNQ. This spectrum was observed using an incident laser beam power which does not perturb the equilibrium state of the film. If the incident optical beam intensity is increased above a certain threshold value, however, the Raman spectrum of the CuTCNQ film changes dramatically. A typical spectrum is shown in Figure 1(c). It is apparent that the system now contains a substantial quantity of neutral TCNQ as evidenced by the appearance of the strong band at 1450 cm^{-1} that is characteristic of neutral TCNQ. Since this effect depends directly on field strength, the actual power required to cause the switching between these two states depends on the beam size at the film surface in the case of optical excitation. For the particular case illustrated in Figure 1(c) the irradiance required to cause optical switching was approximately 600 W/cm^2.

Large changes in the Raman spectrum of an irradiated film can be observed as illustrated in Figure 1 without any apparent change in the macroscopic properties of the film in the visible region. However, with intensified radiation, lines or patterns can easily be observed being generated at the surface of the film. These patterns are optically visible as a result of the

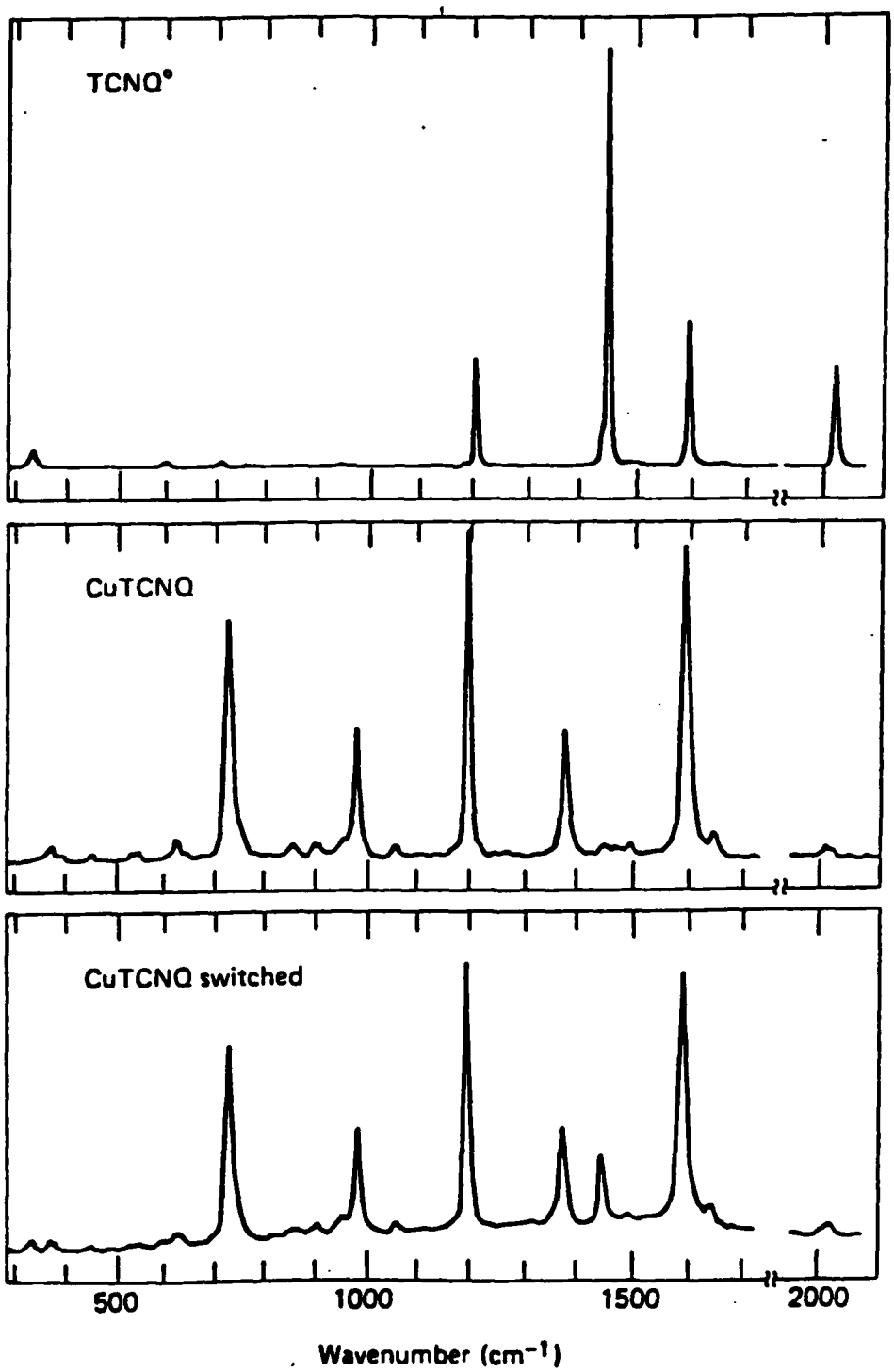

Figure 1. Raman bands

(a) Raman spectrum of neutral TCNQ
(b) Raman spectrum of CuTCNQ film
(c) Raman spectrum of CuTCNQ film after exposure to Ar laser

mation of macroscopic regions of neutral TCNQ. A high contrast pattern nerated by optical beam exposure of AgTCNQ film is shown in Figure 2. By eeping a modulated laser beam across the film surface it has been found that llisecond exposures are sufficient to write this type of line.

These optical effects can be observed in many copper and silver TCNQ rivatives as reported previously for the electrical switching. As in the se of low frequency electric fields, the details of the changes between able states of the films vary according to the materials. For example, in TCNQ changes in the Raman spectrum are observed at lower optical field rengths than in CuTCNQ. Another major difference is the appearance of a oad feature in the 1050-1800 cm^{-1} region of the Raman spectrum of AgTCNQ at ser powers well above that required for switching. This signal was not served under similar conditions for CuTCNQ nor for neutral TCNQ.

In addition to measuring the transition between the two stable states of ese films by changes in the Raman spectra, measurements of the changes in e electrical resistance induced by optical fields were measured in several lms. A conventional AgTCNQ switching structure with a partially transparent uminum top metal electrode was subjected to laser radiation at 488 nm and e changes in the electrical resistance were measured. The film was biased th a dc electric field of approximately 5 volts across the aluminum/AgTCNQ/ lver structure where the AgTCNQ film thickness was approximately 5 μm. The field was adjusted so that the film remained in the high resistance state ist below the threshold for electrical switching. Application of the argon ser beam induced the film to rapidly change state into the low resistance gime. This is illustrated in Figure 3. Rapid cycling of the optical beam used the device to respond by rapidly switching between the high and low

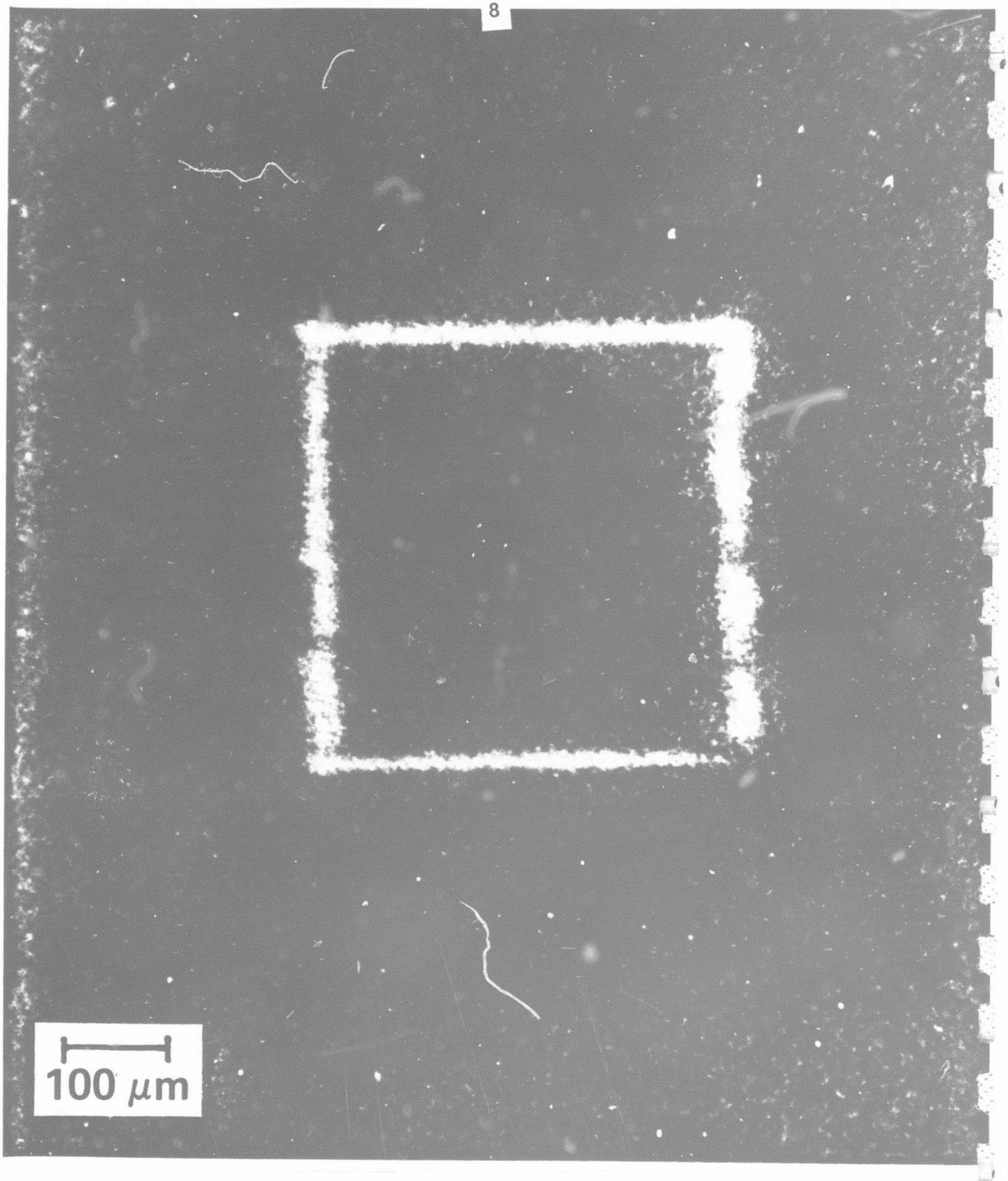

Figure 2. High contrast pattern generated by optical beam exposure of AgTCNQ film.

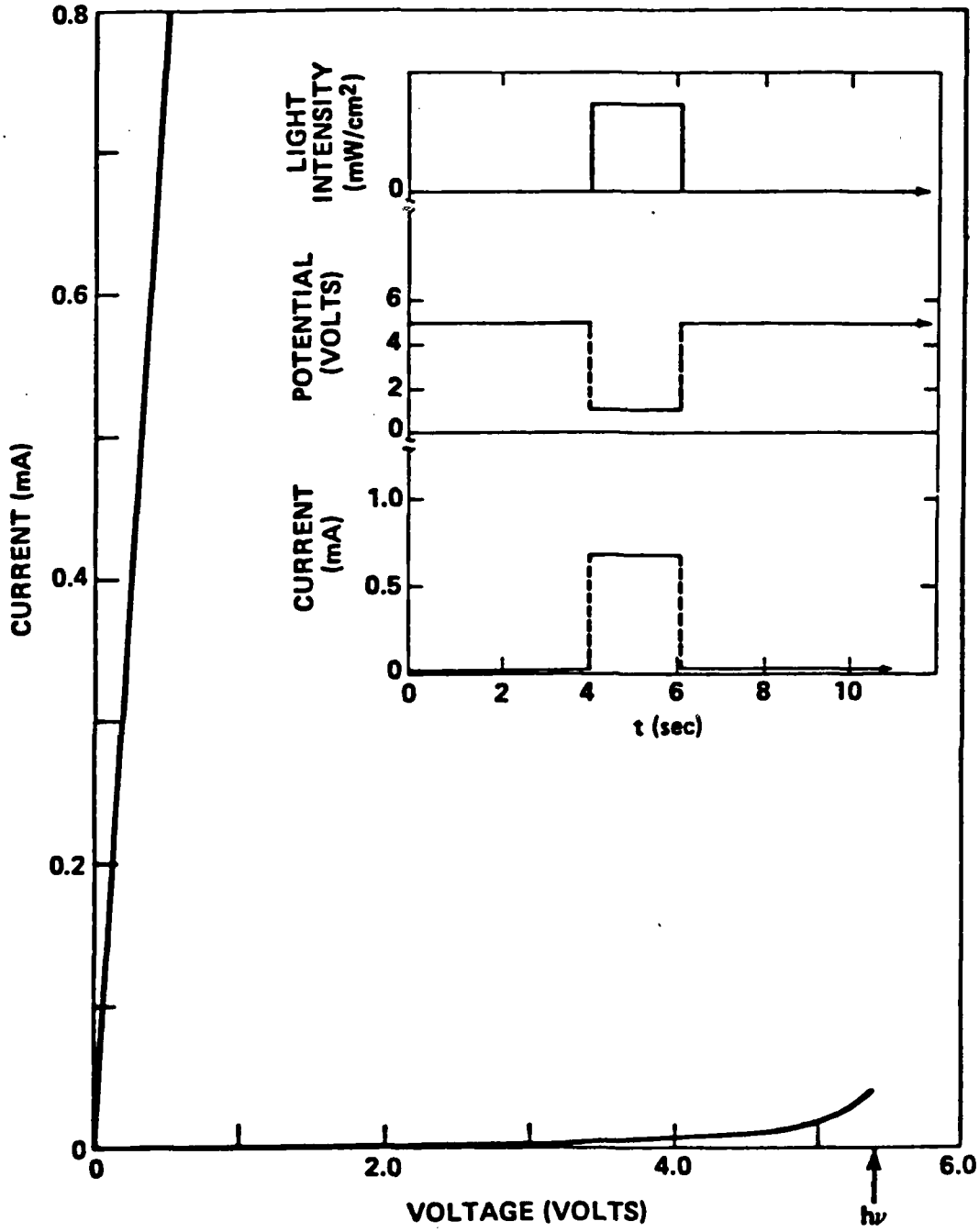

gure 3. Switching characteristic of AgTCNQ induced by application of argon laser beam showing (a) high- and (b) low-impedance states.

Insert: Time variation of current when laser beam was periodically interrupted. The laser power was 25 mW and the beam diameter was 100 μm.

resistance states. When the optical beam was removed and the electrical bias was reduced to zero, the film returned to its equilibrium high resistance state. Thus it is apparent that the irradiation of these films by optical fields can cause transitions which are observable via optical and electrical techniques.

Erasable Optical Switching

We have also demonstrated that a CO_2 laser can be used as a source of thermal energy to reverse or erase switched regions of the film.[17] The reaction shown in Eq. (1) is reversible and the initial phase can be easily reformed by heating the film. The reaction proceeds readily because the simple $Cu^+(TCNQ^{\cdot-})$ has been shown to be thermodynamically more stable than the complex salt containing neutral TCNQ (TCNQ°), shown on the right-hand side of Eq. (1).[7] Shown in Figure 4 are the results on reversing the optoelectronic switching. The high and low impedance states exhibit marked differences in the Raman spectrum, especially in the 1300-1500 cm^{-1} region due to the ν_4 band (C=C stretching). In this spectral region, the initial charge-transfer complex in the high impedance (insulating) state has only one strong Raman band at 1375 cm^{-1} corresponding to the TCNQ anion species (Fig. 4a). In all cases, the laser power of the probe beam was sufficiently low that the equilibrium state of the film was not perturbed. After irradiation with an argon laser, the film is switched to the low impedance (conducting) state, and an additional band is observed at 1450 cm^{-1} corresponding to neutral TCNQ (Fig. 4b). The film in the conducting state can be driven back to the original insulating state using defocused CO_2 laser radiation as shown in Figure 4c. For thin CuTCNQ films on a copper substrate, the CO_2 laser irradiance required to

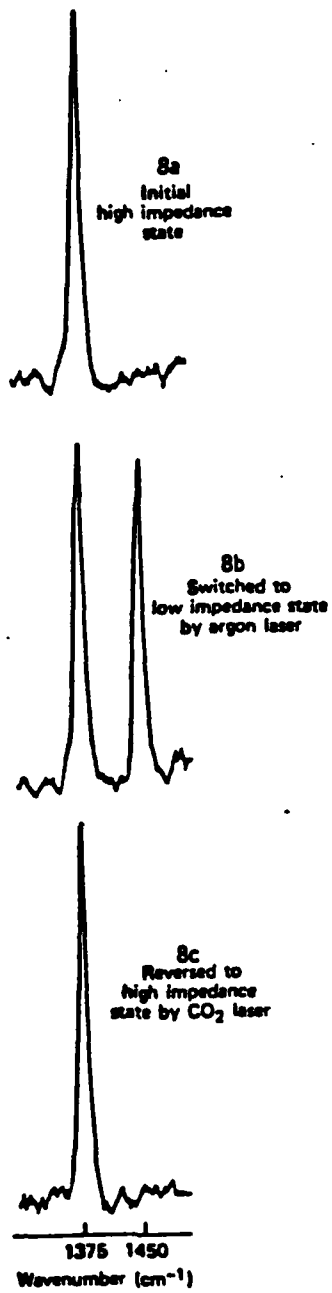

Figure 4. Raman spectra in the 1300-1500 cm^{-1} region demonstrating the use of CO_2 laser radiation to reverse the optoelectronic switching. The band at 1375 cm^{-1} corresponds to the TCNQ anion species and the band at 1450 cm^{-1} corresponds to neutral TCNQ.

reverse the film state was approximately 200 W/cm^2. It should be emphasized that this exposure was necessary because of the efficient heat dissipation from the film to the metal substrate. Much lower exposures, however, can be used when the films are on thermally insulating substrates.

CO_2 laser radiation can also be used to erase high-contrast patterns which contain macroscopic amounts of TCNQ°. This effect for AgTCNQ on a glass substrate is shown in Figure 5 where an array of nine spots was produced by a focused CO_2 laser beam and the central spot was almost entirely erased by a defocused CO_2 laser beam. Each spot was initially produced by a 50 msec exposure from a 1W CO_2 laser; the laser irradiance at the sample was approximately 600 W/cm^2. The central spot was erased by defocusing the lens to achieve a beam diameter of 2 mm at the sample and then irradiating at a power of 2W ($I \sim 60$ W/cm^2).

Wavelength Dependence of Optical Switching

The wavelength dependence of the optical switching threshold for CuTCNQ and AgTCNQ was studied to obtain information about the switching mechanism.[17] Wavelengths from three different CW lasers were used: 457.9, 488.0, and 514.5 nm from an argon ion laser; 632.8 nm from a helium-neon laser; and 10,600 nm from a carbon dioxide laser. At each wavelength, the metal-organic films were irradiated at various laser powers and at several locations on the film. The switching threshold (i.e., the laser irradiance at which neutral TCNQ was produced) was measured by Raman spectroscopy. By varying the laser spot size, it was determined that the threshold was dependent on the laser irradiance and not on the power. The results are presented in Table I. Variations in the observed thresholds are due largely to spatial inhomogeneities in the film,

with the exception of the value at 10,600 nm for CuTCNQ. It is evident that the optical switching threshold for AgTCNQ is approximately one-half the value for CuTCNQ. The threshold for AgTCNQ is essentially independent of wavelength, while the threshold for CuTCNQ is relatively constant in the visible spectral region, but is approximately four times higher in the infrared.

We have compared the spectral variation of optical switching threshold of CuTCNQ to the variation in absorption coefficient and showed that there was little variation in switching threshold over a range from 458 nm to 10600 nm. In contrast the absorption coefficient differed sharply at those extremes. The AgTCNQ complex provides an even more significant example of constant switching threshold in the visible portion of the sepctrum where there are significant variations in absorption coefficient. As shown in Figure 6, the

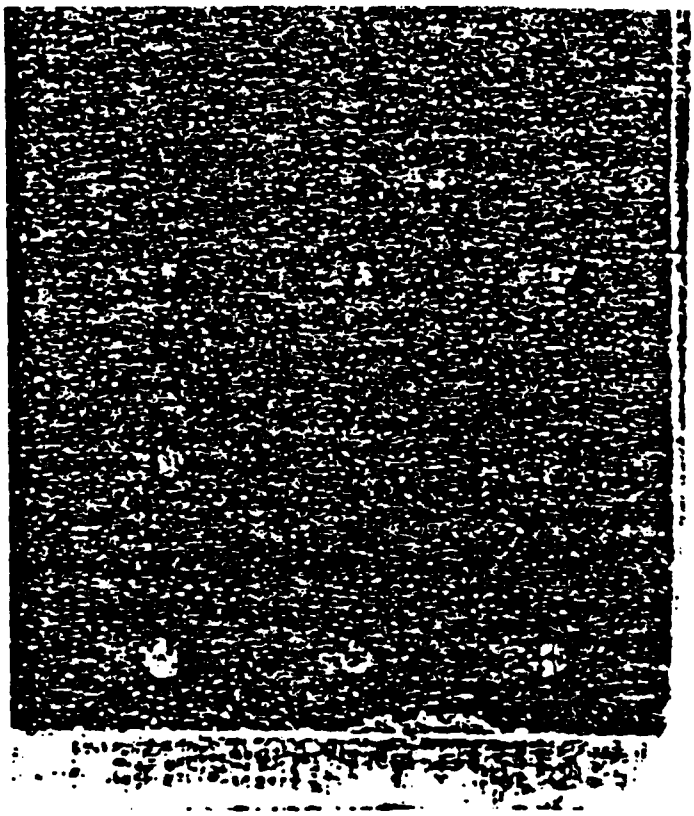

Figure 5. High contrast spots produced on AgTCNQ by a focused CO_2 laser. The central spot was erased using defocused CO_2 laser radiation.

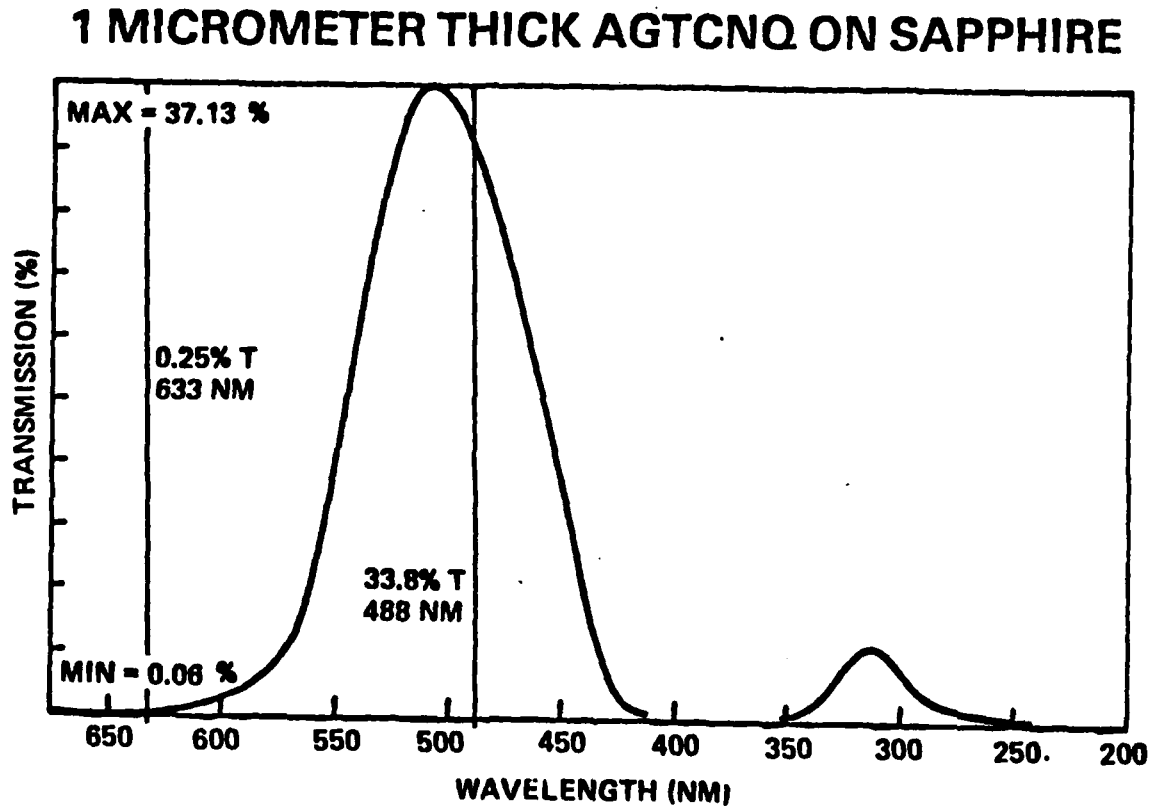
1 MICROMETER THICK AGTCNQ ON SAPPHIRE
MAX = 37.13 %
0.25% T
633 NM
33.8% T
488 NM
MIN = 0.06 %
TRANSMISSION (%)
650
600
550
500
450
400
350
300
250.
200
WAVELENGTH (NM)

Figure 6

Table I Optical Switching threshold for AgTCNQ and CuTCNQ at various wavelengths

Laser Source	Wavelength nm	Photon Energy eV	Incident Laser Irradiance at Threshold (W/cm^2)[a]	
			AgTCNQ	CuTCNQ
Argon Ion	457.9	2.71	800	1500
	488.0	2.54	600	1500
	514.5	2.41	1000	1500
Helium-Neon	632.8	1.96	1100	2000
Carbon Dioxide	10600.0	0.12	600	8000

absorbance of a 1 μm thick AgTCNQ film in the vicinity of the 488 nm argon ion laser line is approximately 0.32, while at 632.8 nm the absorbance is approximately 2.2. Despite this large variation in absorption coefficient, the threshold intensity for switching at $\lambda = 488$ nm was approximately 1200 W/cm^2 while at $\lambda = 632.8$ nm the threshold intensity for switching was about 1100 W/cm^2. This is a clear demonstration of the insensitivity of optical switching threshold to optical absorption coefficients and is a further indication that the origin of phase transition being a field effect rather than an optical transition.

Optical Transmission Associated with Switching

An area of significant interest is the change in macroscopic optical

[a] For the visible wavelengths, the irradiated area was 2×10^{-5} cm^2 and the incident power ranged from 12 to 40 mW. For the infrared wavelength, the irradiated area was 1.7×10^{-3} cm^2.

properties of the CuTCNQ films in a radiation field. The potential for large changes in transmission and reflection in CuTCNQ and other members of this family under intense radiation fields are of significant practical interest. A very preliminary investigation of this process is beginning. It is, of course, obvious that the macroscopic properties of CuTCNQ and AgTCNQ films, when irradiated, are dramatically changed in that the films undergo a change from their respective blue and violet colors to a rather pale yellow, characteristic of neutral TCNQ. The transmission spectra of regions which exhibit this color change should show also significant changes in their transmission properties. We have begun to investigate the transmission spectra of irradiated thin films formed on glass substrates. As shown in Figure 7, a typical CuTCNQ film formed by solid state diffusion is rather poorly transmitting from the mid-visible into the near infrared in the vicinity of 1100 nm, and there is a substantial increase in transmission extending into the infrared. Upon irradiating the CuTCNQ film with a Nd:YAG laser at 532 nm scanned over a sufficient region to perform simple transmission measurements, one observes a large change in the transmission as also shown on Figure 7. A significant increase in transmission throughout the spectrum from the mid-visible to the IR is observed. Extremely dramatic increases are observed in the red end of the spectrum and the near IR, particularly those regions which are of interest with respect to many of the principal laser sources. These preliminary transmission measurements demonstrate a very large change in the optical transmission which is clearly of practical interest.

The transmission properties of an AgTCNQ film are shown in Figure 8. In contrast to the changes observed in CuTCNQ, the switched and unswitched films are quite similar in the infrared portion of the spectrum. However, large

TYPICAL CuTCNQ TRANSMISSION SWITCH

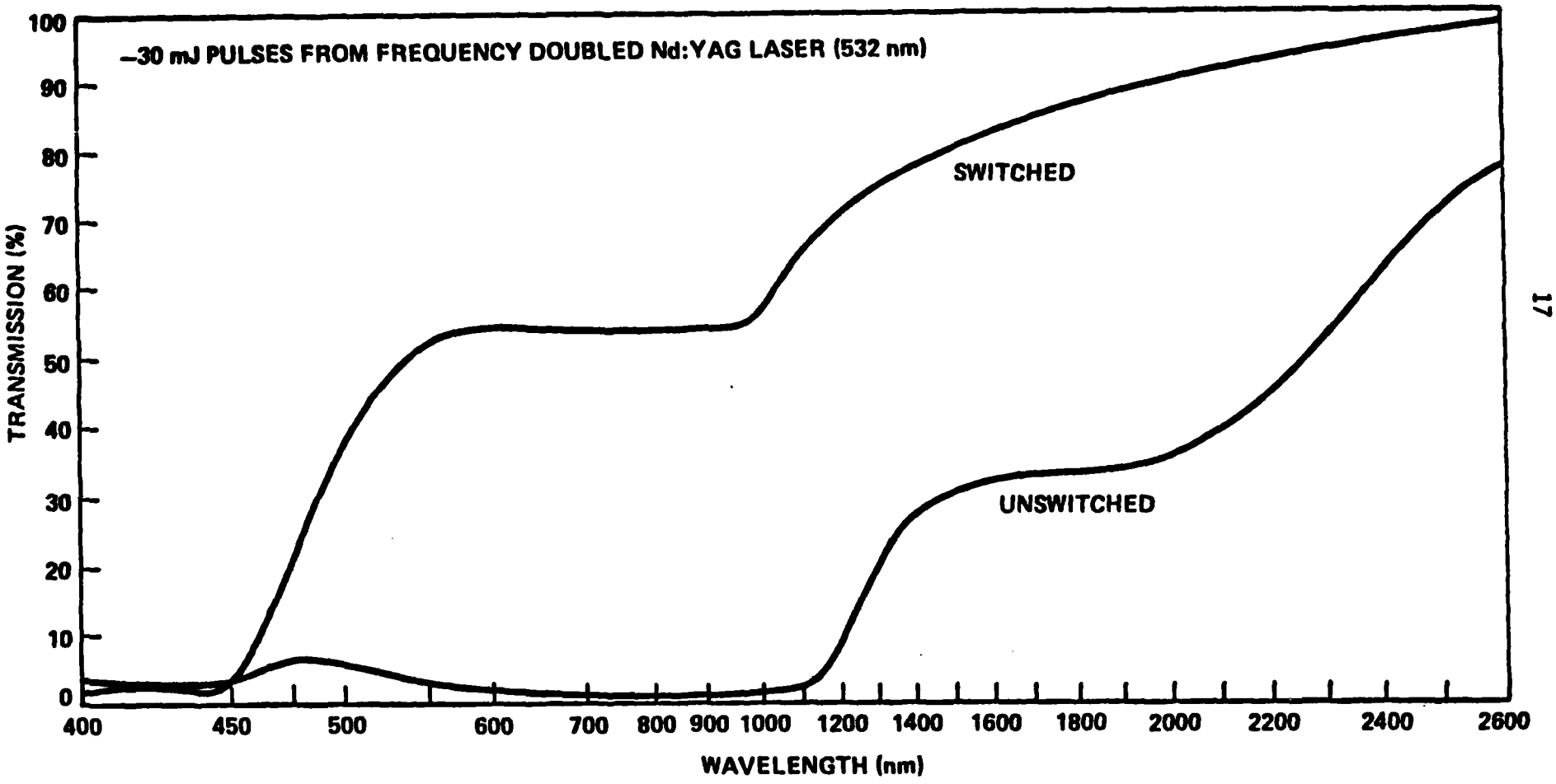

Figure 7

TYPICAL AgTCNQ TRANSMISSION SWITCH

–45 mJ PULSES FROM FREQUENCY DOUBLED Nd:YAG LASER (532 NM)

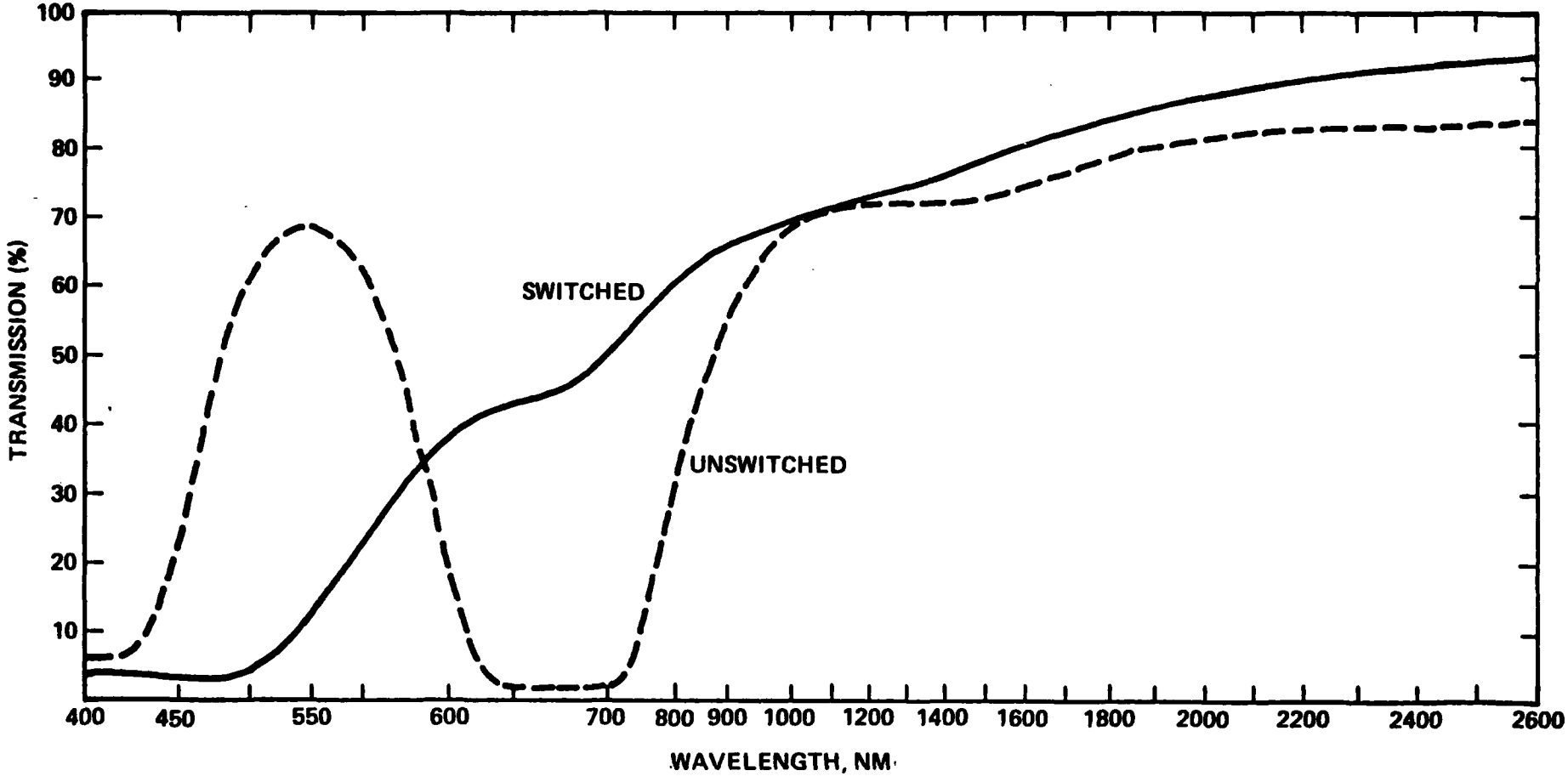

Figure 8

changes in transmission are noted in the visible part of the spectrum between 400 and 600 nm. The switched AgTCNQ becomes strongly transmitting in a band centered at 500 nm while the unirradiated film is poorly transmitting in the same region.

Solid-State Diffusion Process

Considerable progress has recently been made in the aspects of this program related to film formation and processing. We have discovered that these organometallic charge-transfer complexes can be produced in thin film form by a solid-state diffusion process. Various metal-organic crystalline films are prepared by this solid-state diffusion process in a two-step procedure. First, the organic compound is vacuum condensed or sublimed onto a suitable metal substrate or transparent substrate containing a thin metal film. Second, the formation of the complex salt is completed when the thin film deposited on a substrate is heated to initiate a topotatic electron transfer reaction between the metal film and the organic compound.

The optical parameters of these films made by solid-state diffusion exhibit enhanced optical properties. Scanning electron microscopy reveals that these films are very uniform with a smooth featureless surface down to the micron level. An example of films produced by this process is shown in Figure 9 and 10. Figure 10 shows on the left a film where no structure is discernible.

Work is in progress to use this new material preparation process to make thin films on quartz, glass, and sapphire for optical studies. Transmission and reflection data recently made on these films in the switched and unswitched states is now being used to calculate these materials as potential visible and infrared optical switching elements.

1 min TCNQ Deposition

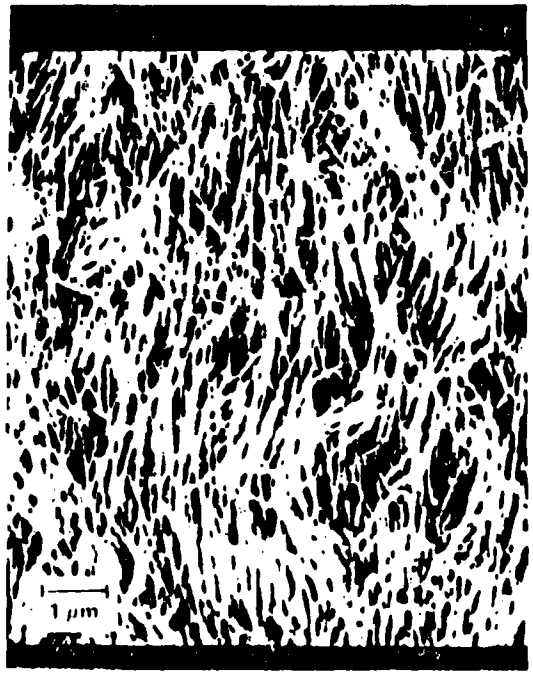

45 sec TCNQ° Deposition

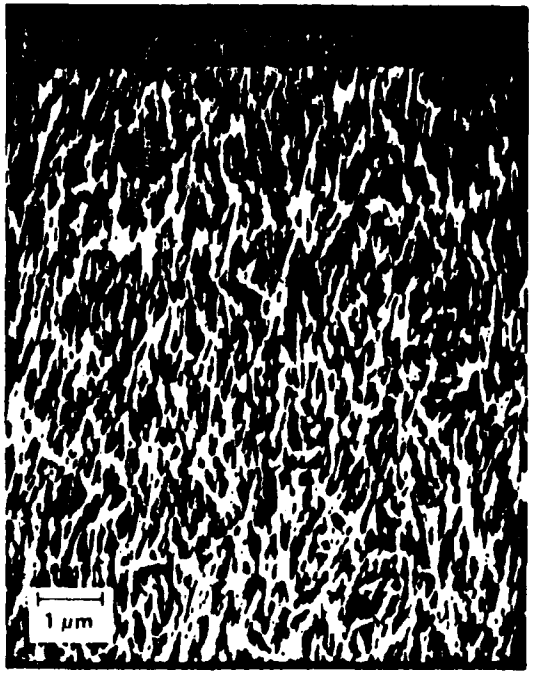

30 sec TCNQ° Deposition

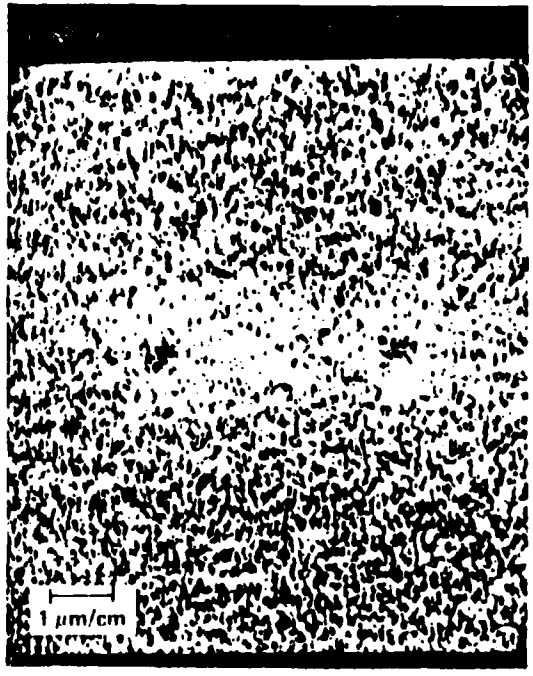

CuTCNQ

Figure 9

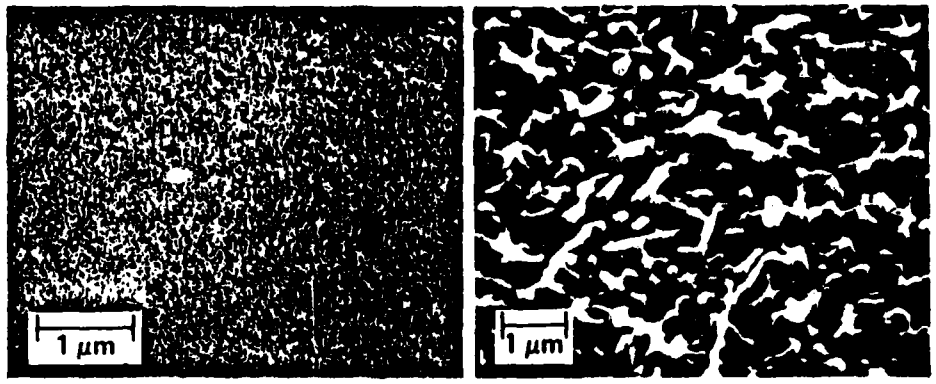

Figure 10

NEW MATERIALS

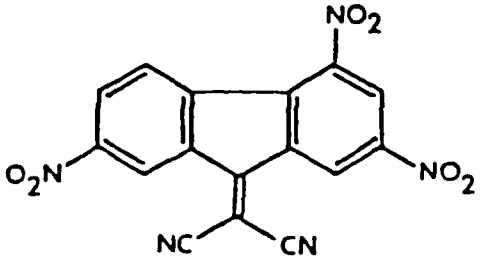

DTF

NOMETHYLENE-2,4,7-TRINITROFLUORENE

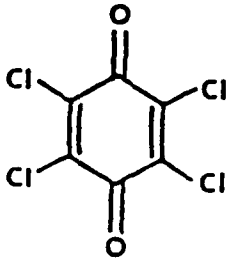

TCBQ

TETRACHLORO-P-BENZOQUINONE

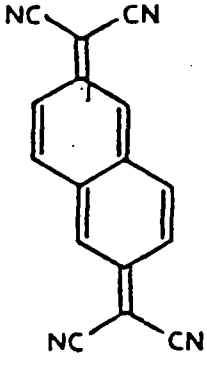

TNAP

TRACYANONAPTHOQUINODIMETHANE

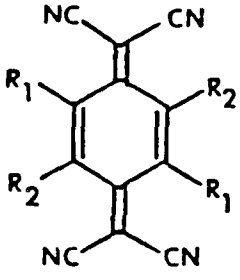

TCNQ(R_1)(R_2)

TETRACYANOQUINODIMETHANE

R_1=$CH(CH_3)_2$ R_2=H
R_1=OCH_2CH_3 R_2=H
R_1=OCH_3 R_2=$OCH(CH_3)_2$
R_1=R_2=H
R_1=R_2=F

Figure 11

w Materials

Work in progress has also involved a variety of thin films of miconducting charge transfer complexes different from the typical AgTCNQ and iTCNQ for which many of the previous results have been reported. Other salts iich are members of the class are those formed of metal donor atoms and the ·ganic acceptor molecules such as TCNE, TCNQ, methyl TCNQ, and TNAP. Many of iese new materials are illustrated in Figure 11. Work is in progress on valuating the specta observed in a variety of these complexes and the rela- ive merits of the various donor/acceptor complexes both in regard to switch- ıg performance and to film formation. An entirely new acceptor, dicyano- ethylenetrinitrofluorine (DTF), is an acceptor which had not previously been nvestigated for switching behavior in donor/acceptor complexes. We have egun to investigate the switching behavior of the CuDTF complex. The Raman ands of the neutral DTF and neutral TCNQ are compared in Table II. The rincipal bands of interest in TCNQ with regard to optical switching are the $_4$ band at 1451 cm^{-1} and the ν_3 band at 1598 cm^{-1}. In DTF, typical bands are bserved at 1342 and 1600 cm^{-1}. On forming the complex CuTCNQ, the ν_4 band is hifted from 1451 cm^{-1} to 1375 cm^{-1} when the species changes from a neutral to fully charge transferred one. In CuDTF, a similar change is observed from 327 cm^{-1} to 1342 cm^{-1}.

Upon irradiation by an Ar laser, the spectrum of CuTCNQ, of course, egins to exhibit an increase in the line at 1451 cm^{-1} associated with neutral CNQ, and a concomitant reduction of the line at 1375 cm^{-1} as more of the TCNQ ons become neutral species. In the CuDTF compound, quite a different ehavior is observed. There is a slight change in the prominent lines of the pectrum upon Ar laser irradiation, but more significant is the appearance of

Table II

Raman Spectrum of TCNQ, CuTCNQ; DTF, CuDTF

TCNQ, cm^{-1}	CuTCNQ, cm^{-1}	DTF, cm^{-1}	CuDTF, cm^{-1}
2223	2205		
1598	1603	1598	1600
1451	1375	1372	1342
1204	1203	1298	
948	980	1107	
710	734	866	

a broad fluorescence extending from 500 to 600 nm with a peak at about 525 nm. Apparently the creation of a certain number of neutral species by the laser beam is followed by a relaxation process and emission of radiation so that the neutral species are not themselves directly observed. This result is interesting, both in regard to potential applications, and in suggesting that real time spectroscopy of this process may be able to follow the transition from the fully charge transferred species to the neutral and into the radiative state.

Many copper complexes are observed to exhibit switching behavior with thresholds varying over almost two orders of magnitude (Table III). Complexes such as CuTNAP and CuTCNQ (OM_e) (O-JPR) switch at irradiances similar to that required for CuTCNQ. On the other hand, CuTCNQ $(OET)_2$ exhibits a switching threshold at least one order of magnitude lower then CuTCNQ. Finally, there is observed in CuTCNQ $(i\text{-}pr)_2$ a unique switching behavior (Fig. 12). At an input power of 20mw (@458 nm) the spectral line associated with TCNQ $(i\text{-}pr)_2^0$ appears. As the incident power is increased to 40 mw, the line associated with $TCNQ^0$ is observed. The observation of these two lines associated with

OPTICAL SWITCHING THRESHOLDS OF VARIOUS COPPER COMPLEXES

COMPOUND	WAVELENGTH NM	INCIDENT POWER mW	IRRADIANCE W/cm^2	REMARKS
$CuTCNQ(OEt)_2$	458	3	150	
$CuTCNQ(OEt)_2$	458	15	750	COMPRESSED FILM
CuTNAP	488	30	1500	
CuTCNQ(OMe)(O-ipr)	488	30	1500	
CuDTF	458	15	750	SOME DECOMPOSITION AT HIGH POWER LEVEL; FLUORESCENCE
$CuTCNQ(i\text{-}pr)_2$	488	40	2000	
$CuTCNQF_4$	488	150	7500	SOME DECOMPOSITION

BEAM AREA APPROXIMATELY 2×10^{-5} cm^2

Table III

STEPWISE SWITCHING OF CuTCNQ SALTS AND CuTCNQ(i-pr)2

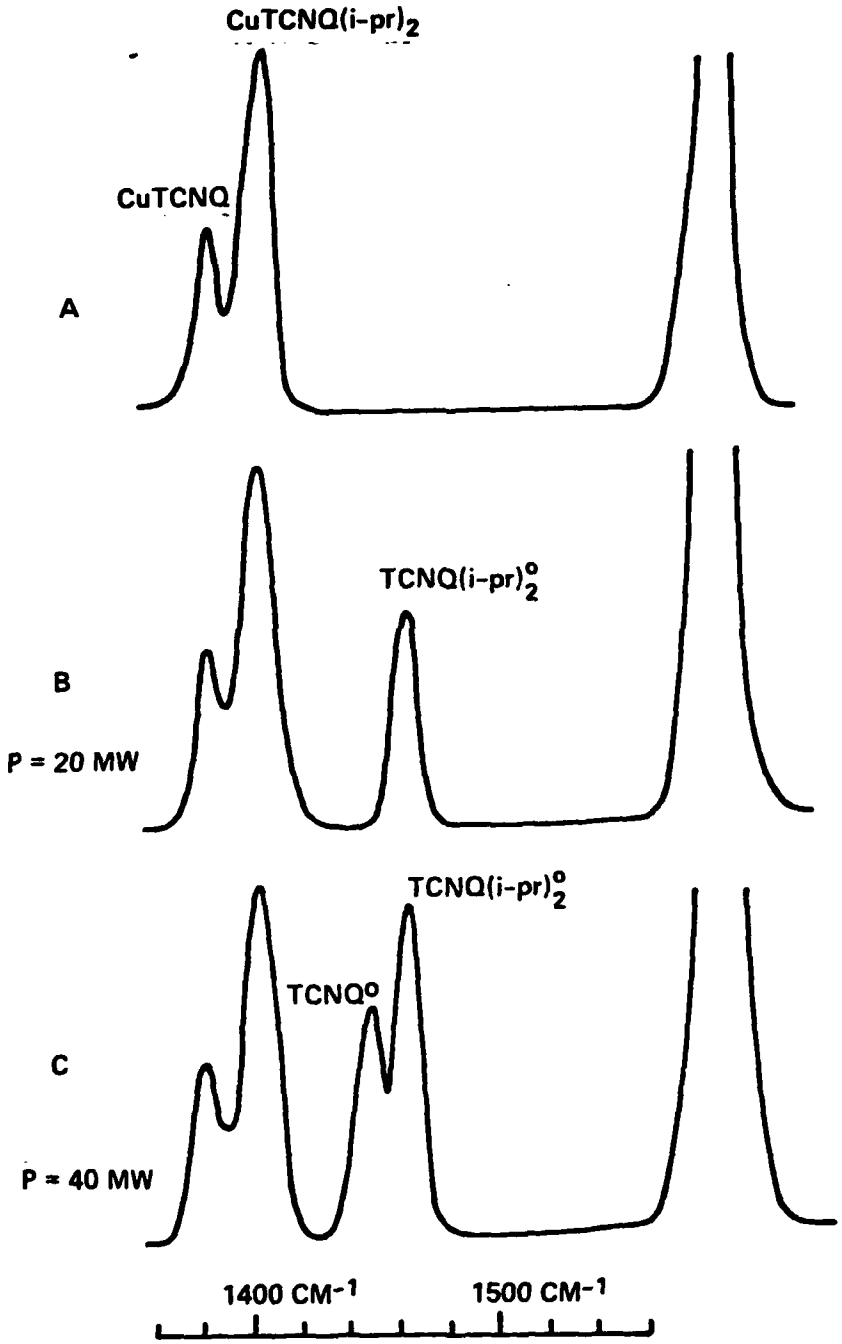

Figure 12

TCNQ ν_4 (C = C stretching) and TCNQ(i-pr) ν_4 modes suggests the storage of multiple bits of information in the same molecular species.

Conclusion

We have demonstrated reproducible optical and optoelectronic switching between two states in polycrystalline organo-metallic semiconductor films using radiation from a variety of visible and infrared lasers. The results are observed on a wide range of acceptors related to the electronic acceptor tetracyanoquinodimethane (TCNQ) complexed with copper or silver. It has been shown that the effect of the applied electric field on the initial charge-transfer salt (e.g., CuTCNQ) is to induce a phase transition resulting in the formation of a non-stoichiometric complex salt containing neutral TCNQ.

These results have been extended to show that regions of an optically switched AgTCNQ or CuTCNQ film can be reversed (i.e., erased) using defocused lasers as sources of thermal energy. The effect can be observed by Raman spectroscopy and direct observation. Results on the wavelength and irradiance dependence of the optical switching threshold show the optical switching occurs over a wide spectral range and can be interpreted in light of a reversible switching mechanism in these organic materials. Associated with these results are dramatic changes in absorption, reflection and transmission in these materials.

These organo-metallic compounds are most promising as: (1) optical and optoelectronic switching materials, (2) erasable optical storage systems, and (3) nonlinear optical materials. The results obtained in this work have significant potential for applications in laser hardening, erasable optical recording, and optical processing and are recommended as candidates for substantial further development.

References

1. G. R. Johnson, M. G. Miles, and J. O. Wilson, Mol. Cyrst. Liq. Cryst. 33, 67 (1976).

2. H. H. Afify, F. M. Abdel-Kerim, H. F. Aly, and A. A. Shabaka, Z. Naturforsch 33a, 344 (1978) and Y. J. Iida, Phys. Phys. Soc. Japan 30, 583 (1971).

3. R. S. Potember, T. O. Poehler, A. Rappa, D. O. Cowan, and A. N. Bloch, J. Am. Chem. Soc. 102, 3659 (1980).

4. R. S. Potember, T. O. Poehler, and D. O. Cowan, Appl. Phys. Lett. 34, 405 (1979).

5. R. S. Potember, T. O. Poehler, D. O. Cowan, and A. N. Bloch, Proceedings of the NATO Conf. on Chemistry and Physics of One-Dimensional Materials, Luis Alcácer, Ed. (D. Reidel Publishing Co., Boston, 1980), pp. 419-428.

6. S. R. Ovshinsky and H. Fritzsche, IEEE Trans. Electron. Dev. ED-20, 91 (1973).

7. S. R. Ovshinsky, Phys. Rev. Lett. 21, 1450 (1968).

8. See, for example, A. Adler, H. K. Henisch, and Sir N. Mott, Rev. Mod. Phys. 50, 209 (1978).

9. R. S. Potember, T. O. Poehler, and R. C. Benson, "Optical Switching in Semiconductor Organic Thin Films," Appl. Phys. Ltrs. 41, 548 (1982).

10. T. Takenaka, Spectrochim Acta 27A, 1735 (1971).

11. A. Girlando and C. Pecile, Spectrochim. Acta 29A, 1859 (1973).

12. R. Bozio, A. Girlando, and C. Pecile, J. Chem. Soc., Farad. Trns. II 71, 1237 (1975).

13. C. Chi and E. R. Nixon, Spectrochim. Acta 31A, 1739 (1975).

14. D. L. Jeanmaire and R. P. VanDuyne, J. Am. Chem. Soc. 98, 4029 (1976).

15. M. S. Khatkale and J. P. Devlin, J. Chem. Phys. 70, 1851 (1979).

16. E. I. Kamitsos, C. H. Tzinis, and W. M. Risen, Jr., Solid-State Comm. 42, 561 (1982).

17. R. C. Benson, R. C. Hoffman, R. S. Potember, E. Bourkoff, and T. O. Poehler, Appl. Phys. Lett. 42, 855 (1983).

II. Electrical and Optical

INTRODUCTION

Vanadium dioxide, VO_2, is a transition metal oxide which undergoes a semiconductor to metal phase transition[1] at approximately 67°C. Over the years, considerable effort has been expended in studying the changes in the electrical resistivity, magnetic susceptibility, optical properties (UV, visible, IR, Raman), and crystal structure associated with this phase transition.[2,3,4] There are several other transition metal oxides which also exhibit similar behavior, though none do so at such a convenient temperature.

Paralleling the investigation of pure VO_2, there have been numerous studies[4] involving the incorporation of various dopant ions into VO_2. It was believed that changes seen in the properties of these doped-VO_2 could be correlated to the electronic structure of the impurity ions. These correlations then yielded information regarding the nature of the transition in pure VO_2. Most of the impurity studies centered around the measurement of the electrical resistivity changes, in which it was observed that the transition temperature could be increased or decreased depending on the nature of the dopant, and, in some cases, semiconductor to semiconductor transitions were observed. The resistivity ratio, if altered, was always depressed by doping.

Because of the pronounced physical changes observed in VO_2, it has been of considerable interest, not only from a theoretical standpoint, but also from an applications viewpoint. These properties have already been utilized in the successful production of thermal switches at submillimeter to optical wavelengths, and optical storage devices.

Few of the impurity-based studies were very comprehensive with respect to the examination of an adequate impurity composition range for any particular ion and very few examined the optical properties of these materials. Most of these doped-VO_2 studies were performed on single crystals and powders, very few were performed on thin films. In many aspects, thin films are more desirable than single crystals or powders. Single crystals often crack when they are temperature cycled, whereas thin films appear to be almost indefinitely cycleable without any degradation in properties. R.f. reactive sputtering , a process used to make thin films, is capable of producing materials, alloys etc., that are not normally accessible by the thermodynamic equilibrium driven techniques used to make single crystals and powders. Consequently, possibly new materials are obtainable in the form of thin films. And from a practical standpoint, any application involving VO_2 will most likely be with the material deposited in some form of thin film.

There are a number of ions that could be examined as potential candidates for study in the form of thin films of which we chose Ti and W for somewhat different reasons. Although Ti-doped VO_2 has been the subject of a number of reports, including one thin film based study, the results were often quite contradictory. This behavior was quite unusual and we were interested to see if our efforts could aid in resolving the problem. The W-doped VO_2 thin film study chosen because of the very large effect that W has on the transition temperature of VO_2 in single crystals and powders. It was therefore of interest to see if similar or additional properties were observed in thin film preparations. It was our intent to systematically examine the properties of Ti-doped VO_2 thin films as a function of Ti concentration at the low end (< 20%) of the composition range and similarly the W-doped VO_2 in the < 2% W

range. The evaluation of these materials was centered principally on the examination of the electrical and optical (visible to near IR) properties, with a secondary intent of determining if these properties could be optimized at some impurity concentration.

EXPERIMENTAL PROCEDURES

Film Growth Procedure

Films of VO_2, Ti-doped VO_2, and W-doped VO_2 were prepared by a r.f. reactive sputtering technique, using a floating diode bridge configuration. The substrate, a 1"x0.5"x0.32 Pyrex 7052 glass slide, was held to the upper electrode by a 2"x2"x0.01" alumina mask with a 0.5" hole in the center. The upper electrode consisted of a 2.5" diameter stainless steel cup, which was radiantly heated from the rear by a 1000W tungsten-halogen projection bulb. The power to the bulb was manually controlled by means of a variable transformer. The temperature of the electrode was monitored by a chromel/alumel thermocouple which was inserted into a hole drilled near and parallel to the polished front surface of the electrode. Because of the strong electrical coupling between the electrode and the thermocouple, neither temperature measurement nor control was attempted while the r.f. power was applied. The electrode, and presumably the substrate temperatures were typically maintained at 600°C. Some samples were prepared at 520°C and 630°C to investigate the effects on the films' properties.

The target consisted of a 2.5" diameter vanadium cup with 0.375" sidewalls. The cup was filled with metal powder consisting of approximately 25 gms of -20 mesh vanadium and the appropriate amounts of -100 mesh titanium or -100 mesh tungsten powder. The combined powders were thoroughly mixed

before being added to the target cup. The electrode separation was 1.3" and the input r.f. power was approximately 400 watts. The rectified voltage across the electrodes was typically 1200V.

The deposition procedure is as follows. The bell jar containing the sputtering apparatus was evacuated to a minimum of $1x10^{-7}$ torr, with an oil diffusion pump. The substrate heater was turned on and the substrate was brought up to the desired temperature. As the substrate was heating, high purity oxygen was allowed to flow into the system via a needle valve while the vacuum system continued to pump on the bell jar through a 1" opening. The flow rate was adjusted such that the dynamically obtained equilibrium pressure was typically 0.22 microns. O_2 pressures from 0.15 to 0.45 microns were also examined. When the O_2 pressure had stabilized, high purity Argon was then similarily leaked into the system and the Argon flow was adjusted such that the combined O_2 and Ar pressures was 25±3 microns. In order to clean the target, a grounded shutter was placed between the target and substrate electrodes and r.f. power was applied resulting in the sputtering of the target onto the underside of the shutter surface. This presputtering target-cleansing process was continued until the powdered target surface was of a uniform bright metallic appearance, with a minimum time of 10 minutes. The shutter was then removed and when the substrate temperature had reached an equilibrium value, the metal powder was reactively sputtered onto the heated glass substrate for times ranging from 45 minutes to 3.0 hours. At the completion of the sputtering process, the r.f. power was turned off and the electrode/substrate temperature was remeasured. The Ar supply was shut off and the O_2 pressure was also remeasured to insure that the O_2 pressure remained constant, at least in the beginning and the end of the deposition

procedure. When problems with a film's physical appearance did occur, it was often accompanied by differences in the starting and ending O_2 pressures. The O_2 flow and substrate heater were then turned off and the thin film sample was allowed to cool while the system was being re-evacuated. In approximately 45 minutes to 1 hour, the sample had cooled to 100°C at which time the system was purged to the ambient atmosphere and the sample was removed.

VO_2 Doped Composition

The titanium-doped VO_2 films were prepared in the following compositions (wt% Ti); 0.2, 0.41, 0.82, 1.2, 2.0, 3.0, 4.9, 6.6, 8.8, 12.5. These percentages represent the titanium content in the mixed V/Ti powder target. The titanium content in the films is expected to be somewhat less, as the sputtering rate of titanium is generally lower than that of vanadium.

The tungsten-doped VO_2 films were prepared in the following compositions (wt% W); 0.1, 0.3, 0.6, 1.0. As explained above for the titanium doped VO_2 films, the actual tungsten content in the VO_2 films is expected to be less than the starting compositions. One group of W-doped VO_2 films were prepared by a slightly different technique than that described above. Because of wide variation of properties seen in the W-doped VO_2, vide infra, some films were reactively sputtered from a solid target of V/W. This target was previously prepared by sputtering, in the absence of O_2, a V/W (0.6% W) powder onto a solid V foil cup for 24 hours. This V foil cup which contains a V/W film estimated to be 25 microns thick, was then used as the target in the general procedure detailed above.

The starting composition of the powders used to produce the Ti and W doped VO_2 thin films will be used to identify the various films in discussions

of their measured properties. Based on the various properties of the W films produced from the solid V/W target it was assumed that they were equivalent to films that would have been produced from 0.4% W powdered targets and will be identified as such.

Alloy Composition Determination

It was attempted to determine the composition of the doped VO_2 through the use of an energy dispersive detector. The detector was an accessory to a scanning electron microscope. The procedure employed was to measure the energy profile of the secondary X-rays emitted by the film in response to the scanning electron beam. In the case of the Ti doped films the analysis was complicated by two factors. First, the K_β peak of Ti overlaps the K_α peak of V. This rather minor problem was further complicated by the presence of barium in the glass substrate. Barium has, among others, X-ray emissions that are very close in energy to the K_α and K_β of V and Ti.

Consequently, in order to determine the concentration of V and especially Ti from the individual peaks corresponding to the respective K_α and K_β peaks, it is necessary to know the Ba contribution. This was attempted by measuring the intensity of a fourth Ba peak which has a previously determined intensity relationship with the three other interfering emissions. With this information, the amount of Ti and V were calculated and this data is presented in Table 1. Also tabulated are estimates of error based on the estimated precision of the data. As can be seen, the size of the errors precludes the determination of the low Ti content films. Only for the films with the larger amounts of Ti could this analysis be of any utility. The thin films that started with 8.8% Ti were analysed to contain ~ 6% Ti, indicating that the

films contain about 75% of the starting composition. It is reasonable to assume that this scaling factor applies throughout the various thin film compositions. It should be noted that for the purpose of this study it is not necessary to know the absolute Ti concentration. It is only important that the relative amount of Ti be known, and this is assumed to be proportional to the weight composition of the powdered targets.

With the W-doped VO_2 films, the small amount of W in the VO_2 films was below the limit that could be reliably determined by the energy dispersive technique. Although the absolute amount of W is not known, as in the Ti-doped films, the relative amount is assumed to be given by the starting composition.

Film Thickness Measurements

The thickness of the thin films was measured by the Tolansky multiple beam Fizeau fringe technique. In order to use this interferometric technique, a moderately sharp edge had to be etched in the film. This was accomplished by masking all but a small 2mm section at the perimeter of the film with wax. The unmasked area was etched with aqua-regia and the excess wax was [illegible]h a combination of heat and hexane. It should be noted that the masking was not performed until after the electrical, optical and microwave measurements were performed. Random checks, though, indicated that the film's properties were not noticeably affected by the masking and mask removal procedure.

In addition to examining the Ti and W doped VO_2 thin films as a function of composition, most compositions were also examined at two different thicknesses. Each composition was prepared with a deposition time of 1.5 hours

which produced films of 1100Å to 1800Å. Another group of films were prepared with a deposition time of 3.0 hours. The thicknesses of these films varied from 2100Å to 4200Å. When it is appropriate to distinguish between the two groups of films, the films will be designated by the respective deposition times.

Sample Holder

In all of the measurements that were made as a function of temperature, the thin film samples were held sandwiched between two aluminum cylinders (1." dia x 1.75"). Each cylinder had a 0.25" hole through its length for the optical and microwave transmission measurements. One cylinder had 4 additional holes equally spaced around and parallel to the central hole. Thin insulated tungsten wires (#36) were inserted through these holes and provided the electrical contacts for the four-probe electrical resistivity measurements. The wire ends contacting the film surface were formed into small bulbs to minimize film damage. Each cylinder was wrapped with 23 turns of (#24) nichrome wire, and the windings were powered in series by a proportional controlled 25 VAC source. A copper-constantan thermocouple (dia. 0.005") was positioned in a shallow groove at the end of a heating cylinder and made contact with the glass substrate and cylinder.

Electrical Measurements

The electrical resistivity measurements were performed by a four-probe a.c. technique using a slightly modified version of a device previously described.[5] The modifications allowed the apparatus to be controlled by a computer. The frequency of the a.c. controlled current source was 23Hz. The

signal from the two voltage probes was processed by a lockin amplifier and the resulting d.c. voltage was digitized and recorded. A.C. phase-locked techniques were used to avoid the problems associated with drift, offset potentials, and thermoelectric potentials which can occur in d.c. measurements. The current varied in decade steps from 0.1 μA to 1 mA r.m.s. The current was selected so as to present a maximum of 0.5V to the lockin amplifier from across the voltage probes. If the compliance voltage of the current source exceeded 5 volts, the gain of the instrumentation amplifier was increased by a power of 10, correspondingly reducing the requirements of the voltage drop across the voltage probes. The maximum error in temperature due to resistive heating is calculated to be 0.05°C. The temperature of the thin film samples was cycled from ambient to 100°C and back to ambient, at approximately 1C° per minute. Datum was recorded when one of two criteria were met; either a 0.3° change in temperature or a 7% change in resistance. This later criterion insures that a reasonable number of data points are collected in the temperature regime of the semiconductor-metal transition. The resistivity ratio was arbitrarily defined as the quotient of the resistance of 35°C divided by the resistance of 90°C. The resistance values used were averages of 4-6 resistance readings in immediate vicinity of the two temperatures.

The transition temperatures were obtained from the zero-crossing point of the log (resistance) vs temperature second derivative curve. The second derivative was numerically determined by performing a 19 pt moving linear least-squares regression analysis on the data and the subsequently calculated first derivative curve.

Optical Transmission Measurements

Concurrent with the temperature dependent resistance measurement, the optical transmission (%T) of the thin films was measured at 2.5μ, by placing the film holder in the sample beam of a modified Beckman DK-2. The transition temperatures for the optical transitions were obtained in a manner identical to that described for the electrical resistance transition temperatures. The %T for all films was also measured at 0.9μ and 1.1μ at 35°C and 90°C. A select number of films, with a minimum of two at each composition were subject to a complete spectral scan from 0.4μ to 2.5μ at 35°C and 90°C.

The measured %T's were corrected for film and substrate reflection loss, film thickness and interference effects. The refractive index for air and the glass substrate was assumed to be 1.0 and 1.5 respectively. The values for the complex refractive index of the VO_2 films were taken from Verleur et al.[6] In order to correct the %T data obtained from the doped VO_2 films for reflection and interference effects, the real part of the refractive index was held constant and equal to that of pure VO_2, and the imaginary component was allowed to vary. It was assumed that the real part of refractive index would not change significantly upon the substitution of similar Ti ions for the V ions. In order to account for the %T changes seen in the 12.5% Ti VO_2 films, and holding the imaginary part constant, the real part would have to drop to 1.7-1.8, which is an unreasonably low value. Consequently it was felt that fixing the real part of the refractive index and varying the imaginary was not unreasonable.

Microwave Transmission Measurements

A single-beam microwave transmission spectrometer was constructed for the

measurement of the thin films' microwave transmission properties as a function of temperature. Electrical resistivity measurements were made simultaneously with the microwave transmission measurements. The microwave spectrometer consists of a 29-31 GHz klystron microwave generator, variable attenuator and frequency meter connected to a -20 db directional coupler and another variable attenuator. The output of the second attenuator is fed directly into the heated sample holder. The sample holder is the same one used in the combined electrical resistivity/optical transmission measurements described above. The transmitted microwave radiation was detected by a HP power meter which was positioned as close as possible to the sample holder. No attempt was made to achieve any degree of impedence matching between the second attenuator output and the sample holder, or within the sample holder itself. As a consequence of this arrangement some power was reflected back to the source. In order to check for problems associated with this reflected power, the output of the -20db directional coupler, which looks at the microwave generator, was connected to a crystal diode detector. The diode output was monitored with a voltmeter during the course of the heating and cooling measurement cycle. This was done to ensure that the klystron output power was not varying with time and that changes in the reflected power from the sample/sample holder were not disturbing the source output power.

The spectrometer was calibrated by placing a clean glass slide in the sample holder and adjusting the two attenuators till the power meter read 0.1 mW full scale. The output of crystal diode was adjusted to be within the range of 30 → 50 millivolts. With the glass slide removed, the transmitted power is approximately 0.3 mW, indicating that approximately 0.2 mW is being reflected and/or absorbed by the substrate. When the blank glass slide is

replaced by a one with a deposited thin film, the transmitted power is 98±4% of full scale. The variations from 100% transmission are caused primarily by the sensitivity of the experimental setup to assembly and disassembly.

R.F. Reactive Sputtering Parameters

The optimum sputtering parameters; substrate temperature, O_2 partial pressure, and Ar partial pressure used in this work were determined examining the effect of each on the electrical properties of VO_2. The film's physical appearance was also a good indicator of the film's quality. The Ar operating pressure is primarily determined by characteristics of sputtering equipment. It must be high enough to sustain a reasonable plasma and dark zone, yet not too high so as to allow destructive discharging to occur. Within this constraint, it was found that 25μ of Ar yielded a stable plasma and also produced films which visually appeared to be clear and homogeneous. With the Ar partial pressure held at 25μ, a series of VO_2 films were made at three substrate temperatures; nominally 520°C, 600°C and 630°C. At each temperature, the O_2 partial pressure was varied from 0.15 to 0.45μ. Very few films made at 630°C though were measured because the substrates tended to crack during the sputtering process.

It should be noted that this study was actually performed after all the Ti and W doped VO_2 films were made. It was undertaken because the sputtering parameters determined in an earlier study, the ones used to make the doped VO_2 films, did not appear to work after some major repairs were made to the sputtering equipment. It appears now that we simply did not wait long enough for the repaired sputtering equipment to reach some apparent state of equilibrium, because the optimum sputtering parameters have remained

unchanged. This exercise though did allow us to document the effects of the sputtering parameters on the thin film properties and to lend reassurance that the originally determined parameters were optimized. The data from the initial work is not as complete as that presented in this work for two reasons. First, the optimum sputtering parameters were found much more quickly and there was no need to explore the prameters space for obviously less than optimum values. Secondly the experimental equipment for making the detailed temperature dependent data was still under construction. Resistance measurements were made by simple two probe measurements, and were not automated.

A detailed study of the effects of the sputtering parameters on the deposited VO_2 films has been published earlier by Griffits and Eastwood.[7] In this paper, they too examined variations of film properties with respect to substrate temperature and O_2 partial pressure in more detail. In order to put the results obtained in our study in perspective with respect to the problems and unknowns that can be encountered with reactively sputtered VO_2 films, the current results will be presented and compared with those of Griffiths et al. There are some significant differences in the range of experimental conditions under which acceptable films were made, and also in the results obtained. Experimentally, Griffiths et al used conditions, some of which, were considerably different than that used in the current work. They used crystalline sapphire and amorphous fused quartz for substrates. The fused quartz ought to yield results comparable to those obtained from glass substrates.

They used much lower substrate temperatures of 275°C to 450°C with higher O_2 partial pressures varying from 0.5 to 2μ. In their study, the Ar partial

pressure was adjusted so that the total pressure was 7.5μ. Interestingly though, within these limits they obtained films which compared roughly with the films made in this study. When samples were prepared in our reactive sputtering equipment using their parameters, the resulting films were green or yellow in color and showed no switching behavior.

Their deposition time was adjusted to yield films with thicknesses of 2000Å±10%. They did observe that the deposition rate was strongly dependent on the O_2 partial pressure with the rate dropping rapidly at higher partial pressures. In our study the deposition rate was relatively uneffected by the O_2 partial pressure except at the very lowest pressures where the rate increased by a factor of 1.6. The thickness of films made in this study were 2750Å±20%.

The resistance of the monoclinic semiconducting phase, measured at 35°C (R_{35}), differed between films made at the three substrate temperatures. The films made at 600°C and 630°C have R_{35}'s approximately 6 times that of the films made at 520°C. There may be some dependence (with changes of approximately a factor of 10) on the O_2 partial pressure, but it is not entirely evident given the variance of the data. Griffths et. al., in contrast observed the R_{35} dropped very rapidly, by a factor of 1000 as the O_2 partial pressure was lowered from 2.0μ to 0.25μ.

The behavior of the R_{90} values, on the other hand were more in agreement between the two studies. As the O_2 partial pressure was lowered, the R_{90} dropped by approximately a factor of 30 over the respective O_2 partial pressure limits. At any O_2 partial pressure, the films made at 600°C and 630°C had R_{90}'s that were approximately 6 times higher than the films made at 520°C.

The resistivity ratio (R_{35}/R_{90}) for films made at the three substrate temperatures increased slowly with decreasing O_2 partial pressure down to approximately 0.3μ. Resistivity ratios of 50-200 were typical for 0.3μ $\leq$ O_2 partial pressure $\leq$ 0.45μ. Below 0.3μ, the resistivity ratios reach a maximum at 0.2-0.25μ, and fall again at O_2 partial pressures $\leq$ 0.2μ. Typical values in the vicinity of the optimum O_2 partial pressure are 2500-3500 for the films made at 600°C and 630°C and 1200-1700 for the films made at 520°C.

Griffths et. al. observed that the transition temperatures were effected by the O_2 partial pressure. Although it was not explicitly stated, it is assumed that the upper transition temperature (going from semiconductor to metallic phase was lowered from 67°C to 62°C for the films on fused quartz substrates. In the present study, the upper transition temperature was uneffected by the O_2 partial pressure, remaining constant at 61.5(1.1)°C for all three substrate temperatures.

It should be noted that this value of 61.5°C for the upper transition temperature is not at all in agreement with previously obtained data, and it is not clear why. In spite of this inconsistency, it is believed the behavior exhibited in the electrical measurements is reasonable and consistent with the behavior observed in the doped films.

Doped-VO_2: Effects on the Electrical Resistivity

Titanium-Doped VO_2

The general form of the resistivity verses temperature behavior of all the films examined is depicted in Figure 1. At temperatures below the transition temperature, the resistivity exhibits an activated response with energies $= d(\ln\rho)/d(kT)^{-1}$ in the general range of ~20 to 0.30 eV. As the temperature is increased, the material undergoes the semiconductor/metal transition at a

temperature nominally about 68°C, which is dependent on the composition and is known as the upper transition temperature. Beyond the upper transition temperature the resistivity is still activated but with a much lower activation energy in the range of 0.08 to 0.15 eV. The activated resistivity observed in the high temperature phase is consistent with most published data on VO_2 thin film resistivity measurements. One can see from this published data that the resistivity is activated, though there is no mention of the energy nor are the plots sufficiently detailed to extract the energy accurately. Single crystals of VO_2 on the other hand possess a metallic-like resistivity at temperatures above the upper transition temperature. It is possible then that the activated resistivity observed in the metallic state arises from grain boundary effects in the thin films.

When the film temperature is lowered the material undergoes the reverse metal/semiconductor transition at a temperature (lower transition temperature) usually 5-10°C lower than the upper transition temperature with a concomitant rise in resistivity back to the starting values. Unlike single crystals, films can be switched repeatedly without any change in their properties.

The low temperature resistivities (R35) and high temperature resistivities (R90) of Ti-doped VO_2 thin films are presented as a function in Figure 2 and Figure 3, respectively, of the Ti concentration. The deposition time for these films was 1.5 hr. The variation within any one particular composition for both the semiconducting and metallic phases can be as much as a factor of 10. This variation is presumably due to the sensitivity of semiconducting and metallic phase resistivities to small changes in the film growth parameters.[3,7,8] In the low temperature phase, the R_{35} drops, on an overall average by about a factor of 15 over the Ti concentration range

examined. The resistivity values obtained for the high temperature phase also appear to drop, though only by about a factor of 2-4.

Historically it is not so much the absolute values of the low and high temperature resistivities that are taken as the measure of a film's quality, but rather it is the ratio of these two values which appear to yield a better and somewhat normalized index of the film's switching properties. The resistivity ratio, defined as the ratio of the resistance at 35°C divided by the resistance at 90°C (R35/R90), is a sensitive measure of a VO_2 film's properties, reflecting differences in texture (preferred crystallite orientation), grain size, stoichiometry, impurity concentration and presumably other additional factors. The presence of texturing in a film, induced by depositing the film on an oriented substrate, is known to significantly improve the resistivity ratio. Increased grain size is also presumed to improve the resistivity ratio. Stoichiometry of the film too, is going to play an important role in determining the resistivity ratio, in particular through its effect on the transport properties, and possibly also through more subtle avenues, such as its effect[3,9] on the grain size and crystallite orientation.

The transport properties of the film are also going to be significantly effected by the concentration of impurities, and depending on the nature of the impurity and where it is located in the lattice, the impurity will certainly affect the transport properties of the two phases quite differently.

Presented in Figure 4 is the resistivity ratio of the 1.5 hr Ti-doped VO_2 thin films, plotted as a function of the powdered sputtering target's Ti wt percent. At 0% Ti, i.e. pure VO_2, the resistivity ratio is on the order of 500 to 750. As small amounts of Ti are added, there is a rise in the resis-

tivity ratio with a maximum occurring at approximately 1 to 1.5% Ti. This maximum resistivity ratio is about 3 to 4 times that of VO_2. The values of 500 to 750 for VO_2 are in fact quite high with respect to previous reports of[7,8,9] resistivity ratios obtained for VO_2 thin films deposited on glass substrates. This fact gives some confidence to the belief that the sputtering parameters have truly been optimized to yield high quality films. And it also suggests that the increased resistivity seen in the Ti-doped VO_2 is really due to the Ti, and not some unrelated change in the sputtering conditions. Beyond the maximum at 1-1.5%, the resistivity ratio drops with a continued increase in the Ti concentration, till at 6.6% Ti there is another sharp rise. Unfortunately there aren't any film compositions in the vicinity of 6.6% that can support or otherwise indicate that this resistivity ratio maximum is real. Although on the other hand, the variance in the data at and beyond 3% Ti and including the 3-6.6% samples is relatively low, and the data are therefore probably quite reliable. The reliability of the data in conjunction with some interesting X-ray measurements to be presented later, do suggest that this lone resistivity maximum at 6.6% may in fact be genuine. As the Ti concentration increases beyond 6.6%, the resistivity ratio falls rapidly to values of 300-500.

With the behavior of the resistivity ratio in mind, Figures 2 and 3 can be examined with a slightly different perspective. Both of the two resistivity ratio maxima at 1.2% and 6.6% are primarily due to a drop in the R_{90} values. The size of the resistivity ratio maximum at 6.6% is substantially attenuated by the rapid roll-off in the R_{35} values beyond 4.9% Ti. At 12.5% the R_{90} values are in general lower than those at 6.6%, but the more rapidly decreasing R_{35} values continues to lower the resistivity ratio at the higher

Ti concentrations. Figure 5 presents the equivalent data for the Ti-alloy VO_2 films with a deposition time of 3 hrs. Even though the number in data points is smaller, the general features seen in Figure 4 are observed in Figure 5, with some variation. The first resistivity ratio maximum is obviously present, but its center is not well-defined because there are only two data points in the 2-5% regime. The second resistivity ratio maximum at 6.6% is not at all evident, again because of the small number of data in the 2-5% Ti concentration region. Given the difficulties caused by the sparseness of data, the overall behavior is approximately the same.

There is a significant difference though that is quite interesting. The magnitude of the resistivity ratio for the thicker 3 hr films is about twice that observed for the 1.5 hr films. One would expect to find differences in the measured resistances for the two series of films as a consequence of the difference in thickness, but the resistivity ratio should remain unchanged. Figures 6 and 7 show the R_{35} and R_{90} for the 3 hr Ti-doped VO_2 films. When compared to the corresponding Figures 2 and 3, it can be seen, with some difficulty, that the larger resistivity ratios are primarily a consequence of the 3 hr films possessing slightly higher values of R_{35}.

Transition Temperatures

The temperatures of which the semiconductor/metal and metal/semiconductor occur in the Ti-doped VO_2 films as a function of Ti concentration is shown in Figure 8. The upper transition temperature is approximately 69-70°C for VO_2 and decreases as the Ti concentration is increased at a rate of approximately -0.35C°/% Ti. At 8.8%, the decrease in the transition temperature reverses direction and begins to increase at 12.5% Ti.

The temperature at which the metal/semiconductor transition occurs is approximately 61.5°C for the VO_2 thin films and does not appear to change noticeably as Ti is doped into the system in the range 0% to 8.8%. From 8.8% to 12.5% the transition temperature begins to rise along with the upper transition temperature. The transition temperatures of the 3 hr Ti-doped films behave similarly including the upturn from 8.8% to 12.5% Ti.

Tungsten-doped VO_2

The effect of tungsten on the semiconducting resistivity of VO_2 is very pronounced as evidenced by Figure 9 in which R_{35} versus W concentration is plotted. With the addition of 1% W, the resistivity of the semiconducting phase drops by 2 orders of magnitude. The metallic phase resistivity (Figure 10) also decreases, but not as rapidly. There appears to be a minimum at 0.6% W and then rises again at 1% W. And as in the case of thin film VO_2 and Ti doped VO_2, the metallic phase resistivity was activated with an activation energy of approximately 0.1eV. The resistivity ratio obtained for the W-doped VO_2 is seen in Figure 11, and as one would expect from Figures 9 and 10, there appears to be a minor rise in the resistivity ratio at 0.1% W of questionable significance, followed by a definite decline throughout the remaining composition range. Studies[10,11] performed on W-doped single crystals reported nearly identical findings with respect to the effect of W on the resistivities of the two phases. Actually this agreement is somewhat surprising as it is usually found that there is a strong difference between the results of single crystal and thin film studies of VO_2 on amorphous substrates.

When the films were first made, their electrical and optical transmission

properties were measured. Approximately 3-6 months later, the electrical properties were remeasured when the microwave transmission characteristics were determined. It was observed that in this span of time the resistivities of some W-doped films changed by as much as a factor of 5. The change occurred in both the semiconducting phase and the metallic phase, and was most evident in the 0.6% W films.

Transition Temperatures

The temperatures at which the semiconductor/metal and metal/semiconductor transitions occur are shown in Figure 12. From 0 to ~ 0.3%, the transition temperatures are approximately equal to that of VO_2. Beyond 0.3%, both transition temperatues decrease rapidly at a rate of -21C°/% W. The shape of the resistivity curve is also affected by the W content, with the 1% W thin films exhibiting a very broad transition between the two phases.

The single crystal W-doped VO_2 exhibited[10] a similar decrease in transition temperature with W content. A difference is noted in that, unlike the present study, the decrease was already apparent at 0.3% W. There is another curious difference between the two studies that should be mentioned, and that deals with the shape of the transition. In the single crystal study, the transition is still well-defined at 1.0% W, and becomes broadened at 1.7% W. Data presented for the single crystal reflectance measurements appears to suggest that the transition again becomes well defined again at 2.0% W, though resistance data is not presented.

Optical Transmission

The optical transmission of the VO_2 and doped VO_2 thin films was measured

from 0.40 μ to 2.5 μ in the semiconducting phase at 35°C and in the metallic phase at 90°C. This spectral window was determined by the strong absorption coefficient of both phases at the short wavelength limit and by the substrate absorption at the long wavelength limit.

The extraction of a material's underlying optical parameters (complex index of refraction) from the optical measurements on a thin film of the material is usually complicated by interference effects. These interference effects are most evident when the wavelength of the optical probe is, as in the present case, on the order of 0.1 to 5 times the optical thickness of the thin film. The complex index of refraction contains a real part denoted by n and an imaginary component k which is related to the extinction coefficient (α) by the relationship $\alpha = \frac{4\pi k}{\lambda}$. In order to determine both n and k, it would be necessary to determine both the transmission and reflection properties of a thin film. As reflection measurements were not performed, it was necessary to constrain one of the complex refractive index elements while allowing the other to vary in order to fit the measured transmission data. The real component n was chosen to remain fixed as it was felt that the substitution of Ti for V would have a negligible effect on n. Similarly it was also assumed that the very small amounts of W also would not have a large effect on n. The value of n was assumed to be equal to that of VO_2 and was taken from the data presented by Verleur[6] et al.

Two wavelengths, 0.9μ and 2.5μ, were chosen to monitor the effect of Ti and W on the absorption coefficient of VO_2 and 2.5μ represents the upper wavelength limit of the spectral measurements, and 0.9μ is approximately a lower limit, below which there is little difference between the transmission characteristics of the two phases. The values of n used to determine the

absorption coefficient for the semiconducting phase were 3.20, and 2.92 for 2.5μ, and 0.9μ respectively. The corresponding values of n for the metallic phase were 2.88, and 1.78.

The absorption coefficient (k) of the semiconducting phase for the Ti doped VO_2 thin films at 0.9 and .5μ is presented in Figure 13. As can be seen in this figure, the absorption coefficient at 0.9 μ remains approximately constant from 0% Ti to 8.8% Ti with a small decrease evident at 12.5% Ti. The relatively low absorption coefficient at 2.5μ (VO_2; k = 0.12) makes it difficult to observe small variations effected by the Ti content. The variation in the k's and in particular the negative values calculated for the data obtained at 2.5 μ reflect the difficulties associated with determining optical constants from thin films. On the average though, the absorption coefficient is within one standard deviation of Verleur's data.

It is felt that the predominate source of error in obtaining the optical constants lies in the area of film thickness determination. The thickness used in this study was determined at the outer 1-2 mm of the circular film, in order to preserve the films for future studies. Some films were examined for deposition homogeneity by successive etchings towards the center of the film and it was found that variations of ±10% were not uncommon. This inhomogeneity in film thickness can easily account for the variation seen in the absorption coefficients.

The absorption coefficient of the metallic phase at 0.9 μ and 2.5 μ is shown in Figure 14. At 2.5 μ the decline in absorption coefficient begins to become evident at 8.8% to 12.5% Ti. The absorption coefficient at 0.9 μ also shows a similar decline. Both absorption coefficients at 0.9 μ and 2.5 μ are approximately 21% below the average absorption coefficient observed for VO_2

films containing lesser Ti concentrations.

The analysis of the optical properties of W-doped VO_2 thin films was complicated by the presence of a larger than normal crystallite VO_2 formation around the perimeter of the thin films. This feature gave the films a hazy appearance which decreased the transmission of the films. This hazy appearance was variable to the extent that it affected the films, and consequently it was not possible to calculate the intrinsic absorption coefficient. Despite this problem, it can be said though that there were not any large changes in the transmission effected by the W content. It should be mentioned that the appearance of the haze was not characteristic of just the W-doped VO_2 films. It appears to be more a consequence of the condition of the sputtering equipment which was exhibiting some errant behavior in the time interval that the W-doped films were being prepared.

In addition to measuring the transmission at two discrete temperatures, the optical transmission was monitored at 2.5 μ as a function of temperature simultaneously with the electrical resistivity measurements. Since the optical characteristics at 2.5 μ are determined by free carrier effects, it should be possible to relate the optical transmission to the electrical resistivity. This was done by Verleur[6] et. al. for VO_2 (at 4μ) and they calculated that the transmission curve should undergo an abrupt discontinuity at very nearly the temperature of the resistance continuity. Experimentally though, they found that the optical transmission transition occured 4°C before the resistivity transition. The explanation given is that the small regions of the film switch before 68°C causing the transmission to decrease, but the resistivity transition is not observed till there is a significant overlap of these metallic regions. In the present study, it was also observed that the

optical transition occurred before the resistive transition (for increasing temperatures), but the difference between the two transition temperatures was only 1.0 (±.75)°C. This was observed for Ti and W doped VO_2 films and did not appear to have any dependence on the amount of dopant. Following from the explanation offered by Verleur et. al., it would appear that the domains are more uniform in the current films.

Microwave Transmission

The microwave transmission of the Ti and W doped VO_2 films was measured as a function of temperature at 30 GHz. Also the electrical resistivity of the films was measured simultaneously with microwave transmission measurement. The microwave reflection characteristics were not measured because of a large impedence mismatch that was present between the microwave source and the sample holder. This mismatch generated a substantial amount of reflected power, and it was felt that reflected power from the film could not be reliably measured in the presence of such a large background.

The microwave transmission of the films is given by the equation:

$$T = {}^{-ad\rho^{-1/2}}(1-R)$$

where T is the measured power transmission, d is the film thickness in Å, ρ is the resistivity of the film, a is a proportionality constant, and R is the power reflection coefficient. At 25°C, in the semiconducting phase, the resistivity of all the films was high enough that a film had a negligible effect on the transmission. The observed transmissions were typically 98% with a standard deviation of 4%. The uncertainty is due to the sensitivity of

the experimental setup to minor changes in the positioning of the substrate. As the temperature is increased to values that are still below the transition temperature, the transmisison does not change despite a typical change in resistivity of approximately 3. This suggests that the measured transmission coefficient of 98% is primarily the result of a reflection coefficient of 2%.

Above the semiconductor/metal transition where the resistivities are on the order of 10^{-3} ohm cm, the microwave transmission is seen to drop significantly. Transmission coefficients of 0.10 to 0.90 were observed, and were related to the resistivity of the metallic phase. A logarithmic transform of the equation above indicates that there should be a linear relationship between $\log_e$ (transmission coefficient) and $d \cdot \rho^{-1/2}$, assuming the reflection coefficient remains constant. This relationship is plotted in Figure 15 for the 1.5 hr Ti-doped VO_2 films. It can be seen that there is a definite correlation between $\log_e$ (transmission coefficient) and $d \cdot \rho^{-1/2}$, but it is not exactly linear as the $\log_e$ (transmission coefficient) decreases more rapidly at higher values of $d \cdot \rho^{-1/2}$. It is not unreasonable to assume that the reflectivity is not a constant, but rather is increasing with increasing values of $\rho^{-1/2}$. This would then account for the observed deviation from linearily. For most of the 1.5 hr Ti-doped VO_2 thin films examined, the dependence of the metallic phase microwave transmission coefficient on the Ti concentration is indirectly related to the dependence of the resistivity on the Ti content. This was demonstrated in Figure 3, where there is seen a modest decrease in R_{90} with an increasing Ti concentration. Consequently the lower transmission coefficients are usually found with the films containing larger concentrations of Ti. This observation is generally true for the Ti compositions from 0% to 8.8%, but at 12.5% a very curious anomoly occurs. In

Figure 15, there can be seen 4 points that are significantly removed from the cluster of data points. These 4 points were all obtained from 12.5% Ti-doped VO_2 thin films. From Figure 3, it is seen that the high temperature resistivity of these 12.5% Ti films are among the lowest of all the films, yet the measured transmission coefficient is much higher than one would expect from such low resistivities.

The data obtained from the 3.0 hr Ti doped VO_2 thin films in Figure 16 behaves in a similar fashion in regards to the relationship between $\log_e$ (transmission coefficient) and $d \cdot \rho^{-1/2}$. The smaller number of data points and larger variance in the data make it somewhat difficult to see that there is a similar downward curvature in the plot as was seen in the 1.5 hr Ti doped VO_2 thin films. This curvature appears to occur at approximately the same value of $\rho^{-1/2}$; which is found at twice the value $d \cdot \rho^{-1/2}$ as that observed in the 1.5 hr films, because of the nominal two fold increase in the thickness of the 3.0 hrs films.

Unlike the 1.5 hrs Ti doped VO_2 films, there is nothing unusual about the behavior of the 3.0 hr 12.5% Ti doped films. There are though three samples that are somewhat out of agreement with the majority of the other data points. These data points were obtained from 0.2, 0.41 and 1.2 % Ti films. Like the 1.5 hr 12.5% Ti doped films, the resistivity of these films are also among the lowest of the 3.0 hr Ti-doped films. As a point of comparison, the deviation of the data from 1.5 hr 12.5% Ti doped VO_2 films is much larger than the deviation of the three 3.0 hr Ti-doped films.

A similar presentation of the W-doped VO_2 thin film derived data is shown in Figure 17. In this case the relationship between $\log_e$(transmission coefficient) and $d \cdot \rho^{-1/2}$ appears to be entirely linear. The reason that there is

no apparent deviation from linearity is most likely due to the higher resistivity of the W-doped VO_2 films in the metallic phase, which results in little or no change in the reflection coefficient.

The temperature dependence of the microwave transmission of the Ti and W-doped VO_2 thin films is, as expected, determined by the temperature depndence of the electrical resistivity. In all cases the temperature at which the microwave transmission occurs is 2 to 4°C higher than the corresponding resistivity discontinuity.

DISCUSSION

There have been a number of studies[4,12] in which the effects of different transition metal ions on the various properties of VO_2 have been examined; six of them dealing with the electrical properties of Ti-doped VO_2. Of these six, one was performed on thin films of VO_2[13], another with powders[14] and the rest were done on single crystals[12,15,16,17]. Interestingly, in these studies there is indicated a diverse variation of properties observed from what is nominally the same material. In three[15,16,17] of the four studies performed on single crystals, two resistivity transitions were observed; a semiconductor/semiconductor transition in the vicinity of 53°C-65°C and a semiconductor/metal transition near 68°C-70°C. The semiconductor/semiconductor transition decreased in temperature with and the more pronounced semiconductor/metal transition temperature increased slightly with increasing Ti content.

The other single crystal study[12] and the powder based study[14] observed just one metal/semiconductor transition that decreased in temperature with increasing Ti concentration. The present thin film study also demonstrated

similar behavior. In the only other thin film-based study[13] reported, there was observed just one semiconductor/metal transition that increased quite rapidly in temperature with increasing concentrations of Ti. In addition to the differences observed in the number of transitions and the Ti concentration dependence of the temperature at which they occur, there is also some differences observed in the effect that Ti has on the resistivity of the various phases. In most cases the resistivity of both phases decreases upon the addition of Ti with the largest fractional change occuring in the semiconducting phase, but in two of the reports[12,13], an increase in resistivity was noted, primarily for the metallic phase.

The existence of two phases, their temperature dependences and changes in the resistivity of the phases of doped VO_2 can all be, to varying degrees, individually accounted for within the framework of a model proposed by Goodenough.[4] But the confusing and contradictory patterns of behavior exhibited in the different Ti-doped VO_2 studies obviously make it difficult to see how the Ti-doped VO_2 system fits into this model, or whether the model is adequate to describe the material. Briefly, Goodenough proposed that there are two mechanisms that contribute to the semiconductor/metal transition. The dominate one is an antiferroelectric/paraelectric transition effected by a shifting of V^{+4} ions within an oxygen octahedra. When the system is in the antiferroelectric state, another V^{+4} ion translational shift can occur effecting a change from equally spaced V ions to a homopolar V-V bonding pairs. These two transitions occur similtaneously in pure VO_2. Through the addition of foreign entities, the energetics of these two transitions can be altered significantly and in some cases they become separate and identifiable. Also the additional ions usually influence the carrier concentration and mobility

of the different phases which is reflected in the respective resistivity changes. Similar behavior can also be affected by small variations in the stoichiometry of the VO_2[7]. In addition to the numerous atomic and molecular parameters which effect VO_2 and doped-VO_2, there are also parameters that are more macroscopic in scale which manifest their presence in the observed properties, such as crystallinity, crystallite orientation, grain size and possible internal stress. This later parameter may have a significant effect on thin film properties[18]. All of these parameters come together in some fashion to determine the overall behavior. It is not entirely unreasonable to believe that the variations observed in the behavior of the different Ti-doped VO_2 reports is in some part due to the collective interaction of all these parameters, of which the substitution of Ti for V is only one aspect.

The results of this study and of previous reports must be viewed in this context. According to Goodenough, the ionic radius of the Ti^{+4} is just slightly larger than V^{+4}, but it is large enough that it will not initiate a ferroelectric-type distortion. The $3d^0$ orbitals of Ti^{+4} though, do allow it to interact with the π orbitals of the oxygen octahedra and therefore can participate in the antiferroelectric distortion driven by neighboring vanadium ions. This modest destabilization of the antiferroelectric distrotion causes the transition to occur at lower temperatures. The secondary homopolar V-V bonding/metallic V-V bonding transition, is also effected by the Ti substitution because the $3d^0$ configuration precludes any V-Ti "homopolar bonding". This transition is therefore also destablized and its temperature coefficient is presumably greater than that of the antiferroelectric transition. Overall then, the result of adding Ti to VO_2 would be separate the single semiconductor/metal transition of VO_2 into a semiconductor/semiconductor and a semicon-

ductor/metal transition. Both of which decrease in temperature as the Ti concentration increases, with the electrically less-pronounced semiconductor/semiconductor phase transition decreasing somewhat more rapidly.

In the present study, a single semiconductor/metal transition is observed to decrease at the rate of approximately -0.35°C/% Ti, with no evidence of the second transition. It is not known what factors determine the strength of the effect that Ti has on these two distortions which in turn ultimately determines their temperature dependence. If the temperature dependence of the homopolar bonding distortion was somehow reduced in the Ti-doped VO_2 thin film it would then be driven by the antiferroelectric transition much like VO_2, leading to a single transition, which decreases in temperature as the Ti concentration increases.

Such an effect might come about if one were to assume that some of the Ti ions are incorporated into the lattice as $3d^1Ti^{+3}$. It might be argued that the solution determined negative reduction potential of Ti^{+4} would indicate otherwise, though the relative ion stabilities and consequently the reduction potentials in the solid state are certainly different than in solution. It is not inconceivable that the stability of Ti^{+3} ion might be enhanced relative to Ti^{+4} in the solid state, through such features as the homopolar V-V bonding interactions. The $3d^1$ configuration would allow the Ti^{+3} ion to participate in the homopolar bonding distortion, consequently stabilizing itself and the distortion, reducing the dependence that the transition temperature has on the Ti concentration. The Ti^{+3} ion will undoubtedly have an effect on the antiferroelectric distortion, but it is not clear whether the overall effect will be stabilizing or destabilizing. The ion itself would certainly destabilize it more than the Ti^{+4} because of the increased ionic radius and the extra d

electron. On the other hand, it must be realized that along with the Ti^{+3} ions there will be some charge compensating V^{+5} ions, and the small size of these ions is thought to substantially increase the stability of the antiferroelectric distortion, raising the temperature at which it occurs. Note also that the concentration of V^{+5} ions can also be increased by a nonstoichiometric increase in the oxygen concentration. Thus, depending on the concentrations and the relative strength of the contrary effects of Ti^{+3} and V^{+5} on antiferroelectric distortion, it is possible to explain or at least to conceive that one could have the different types of behavior observed in the transition temperatures of the Ti-doped VO_2 studies.

In most of the Ti-doped VO_2 studies, the resistivity of both phases dropped as the Ti content was decreased, with the semiconductor resistivity dropping more rapidly. It could be argued that this is the result of an increased carrier concentration effected by the presence of V^{+5}. The increased carrier concentration would have more of an effect in the semiconducting phase, where the total number of carriers is lower than in the metallic phase. This of course assumes that the V^{+5} is mobile. There are two metal^{+3} ion (Al^{+3},Cr^{+3}) systems in which the resulting V^{+5} is not considered to be mobile and thus could not contribute to the overall carrier concentration. In fact, in such systems the resistivity of the metallic phase is actually increased, presumably because the V^{+5} ion perturbs the carrier mobility in the $\pi^*/d_{\parallel}$ conduction band. But V^{+5} holes apparently are not always localized, as the decreased resistivities in systems which are oxygen rich and presumably possess the extra V^{+5} ions, is accounted for by the presence of partially mobile holes[4,7]. Other phases such as V_6O_{13}, though, should also be considered.

In systems which are not oxygen rich and do not show the double transition, the decreased resistivities must be explained differently. It is possible that in these systems some Ti is incorporated interstitially[7] which would introduce extra electrons into the V 3d bands via the compensating V^{+3} ions. It should be mentioned that the extra electrons would not only lower the resistivity of both phases, but their presence in the π^* band would also destablize the antiferroelectric distortion, and therefore lower the temperatures of that transition. Of the two possibilities presented, the later appears to be a more likely explanation for the current thin film study, as the O_2 concentration was maintained on the low side of the interval between V_2O_3 and V_2O_5.

In the other thin film study, it was observed that there was one transition and it increased in temperature with increasing Ti, which at first seems quite contrary to the current thin film results. The lowest concentration that they reported in their study was 15% Ti which is just above the highest Ti concentration used in the current study. In Figure 8, it can be seen that in this study, the transition temperature does start to increase in the range of 8.8% to 12.5% Ti, which is the highest concentration examined. It's possible that this reversal is in fact real and the consequence of a different mechanism coming to play at the higher concentrations of Ti.

Overall, the Ti-doped VO_2 thin films exhibited a decreasing resistivity of both phases which can tentatively be explained by the explanation given above. It was also observed that this decrease was not entirely linear, as there were two Ti concentration regimes in which a peak in the resistivity ratio was observed. The one at 1%-1.5% %T: is quite obvious and the one at 6.6% Ti is a bit more tenuous. Both of these resistivity ratio peaks are

apparently due to a more rapid drop in the metallic resistivity relative to the semiconducting resistivity, though the variation in the data makes it difficult to say conclusively that there isn't also an increase in the semiconducting resistivity.

Earlier it was stated that stress may play a significant role in the behavior of these materials and it is possible that the existence of these two resistivity ratio peaks is evidence of this role. In Figure 18, the cell volume/metal oxide unit is plotted for some Ti doped VO_2 powders at different Ti concentrations in the semiconducting and metal phase. At two compositions, it can be seen that the cell volume change is zero when the material is taken through the transition. These two compositions are quite near the compositions in which the resistivity ratio peaks are observed. It's reasonable to assume that minimizing the internal stress that occurs at the transition due to a cell volume change would certainly have an effect on the properties of these materials. The influence of stress could be felt at the molecular level, effecting the mobility of the carriers, or the number of carriers via some impurity defect production. At a more macroscopic level, the minimization of the cell volume change may also result in improved and more consistent contacts between the various grains, domains and crystallites. In this case the effect would probably be more evident in the metallic phase, where some of the measured high temperature resistivity is due to the interdomain or intergrain contact resistance.

The 3 hr Ti-doped VO_2 films exhibited similar behavior within the limits of the data quality. The 3 hr films also exhibited higher values of the resistivity ratio at any given Ti composition which was primarily due to an increase in the semiconductor resistivity. It was thought that the crystal-

line orientation of the 3 hr films might be increased over that of the 1.5 hr films, since oriented crystalline films obtained from crystalline substrates typically have higher resistivity ratios than films produced on amorphous substrates. Although the 3 hr films were produced on glass substrates, it was felt that the film growth rates of the initially random orientations might eventually lead to a preferred orientation if the film deposition were continued long enough. Though this is possible, the difference between films grown on amorphous substrates and crystalline substrates is primarily found in the metallic state resistivity, unlike that of the 1.5 and 3.0 hr Ti-doped VO_2 films, where the difference was found in the semiconductor resistivity.

The electrical properties observed with the W-doped VO_2 films are rather straight forward and can be explained by Goodenough's model of VO_2. Given the similarity of the low temperature structues of VO_2 and WO_2 one would think that the W would be incorporated into the lattice as W^{+4}. Horlin[11] et al have pointed out that the net magnetic moment/W is actually more consistent with a formal charge distribution of $V_2^{+2}W^{+6}O_2$. This higher valence W is also suggested by the electrical resistivity behavior as interpreted by Goodenough. In systems containing higher valence ions, the extra electrons of the compensating V^{+3} ions are deposited on the π^* band. As described earlier, the antiferroelectric distortion, which raises the π^* band in energy, is significantly destabilized by the presence of any electrons in that band. The rapid drop in temperature of that transition with increasing tungsten content is a consequence of these electrons, as is the equally rapid drop in the resistivity of the semiconducting phase. It is not clear though why the transition temperature does not drop immediately with the addition of W as was seen in the single crystals.

The activation energy of the W-doped VO_2 thin films in the semiconducting phase did decrease somewhat with the addition of W, but the values of 0.13-0.20 eV are much higher than those reported for single crystals[10,11]. For nearly equivalent W concentrations, values of 0.054 to 0.096 eV were observed. It is conceivable that the temperature dependence of the intergrain and interdomain contact resistance in the thin films is responsible for the differences in the observed activation energies. One could reasonably assume that the activation energy observed in the thin films is the simple sum of the intrinsic activation energy, given by that reported for the single crystals, and some activation energy characteristic of the contact resistance. If the intrinsic activation energy is subtracted from the observed activation energy, the value obtained is nearly equal to that observed in the metallic phase of the thin films which to a zeroth order approximation, should be just the activation energy of the intergrain contact resistance.

The optical transmission of the Ti-doped VO_2 films does not appear to be significantly affected by the Ti over most of the composition range examined. It should be emphasized that the optical transmission spectra from 0.4 μ to 2.5 μ were not corrected for multiple reflections and interference effects and consequently were examined only for moderately large Ti dependent features. Subtle effects would probably not have been noticed. The optical transmission at 0.9 μ and 2.5 μ, on the other hand, was corrected for the thin film effects of multiple reflections and interference, but we were required to use the real part of the refractive index from VO_2 and hold it constant when the experimental data was inverted. In both phases and at both wavelengths, the addition of Ti caused the absorption coefficient to decrease. Because of the variance, the decline is only noticeable at the higher Ti concentrations,

where the absorption coefficient decreases by about 10% in the semiconducting phase and approximately 21% in the metallic phase, compared to VO_2. It is not clear if the dependence is linear, or if it occurs only at the higher Ti concentrations. Because it appears throughout the spectral region examined and in both phases, the decrease in the absorption coefficient is probably the result of the optically inactive (in the 0.9-2.5 μ region) "TiO_2" diluting the optical absorption of the VO_2.

The 10% decline in the semiconducting phase absorption coefficient is consistent with a dilution by 12.5%, given the standard deviation of the data. In the metallic phase, the 21% decrease implies that the Ti is doing more than simply diluting the VO_2. Since the optical absorptions of metallic VO_2 in this region are primarily determined by free-carrier effects, it is not unreasonable to assume that the Ti is also disturbing the band structure of VO_2 in such a manner so as to reduce the free carrier absorption.

The microwave transmission characteristics of the Ti and W doped VO_2 are governed principally by the resistivity of the materials. There seems to be little attenuation in the semiconducting phase. In the metallic phase, where the resistivity is low, there is a definite correlation between the resistivity and the transmission. There were some curious anomalies in the Ti-doped VO_2 where some low resistivity samples exhibited some unusually high transmission coefficients. This was especially evident for the 4 12.5% Ti 1.5 hr films. To a lesser extent similar behavior was observed for some lower Ti content 3.0 hr films. It is not clear if this behavior is in some way characteristic of films of low resistivity or if possibly the Ti concentration is in some way responsible.

CONCLUSIONS

Thin films of Ti and W doped VO_2 were prepared and their electrical resistivities, optical transmission properties (0.4μ-2.5μ), and microwave transmission properties were measured as a function of temperature. The Ti dependence of the electrical resistivity and the single transition is consistent with a model in which the Ti ions are, in part, incorporated as interstitial impurities leading to an increased e^- concentration the π^* band. The occupation of the band is manifested in the decreasing temperature of the transition and the decreasing resistivities. It is also suggested that the resistivity of the metallic phase is further influenced by a second order effect which involves the minimization of the cell volume change of the transition in two Ti composition regimes, 1%-1.5° Ti and 6.6% Ti. This factor is assumed to be responsible for two maxima observed in the resistivity ratio at these same compositions.

The W-doped VO_2 films are believed to contain the W^{+6} ion and compensating V^{+3} ions. In a manner similar to that observed in the Ti-doped VO_2 films, the transition temperature and resistivity is depressed. The effect of the W, though, is many times that of the Ti.

The optical absorption of the semiconducting phase of VO_2 is diluted by the Ti, such that the absorption coefficient is decreased by an amount equal to that of the Ti concentration. The absorption coefficient of high temperatue metallic phase is also decreased, but by more than that observed in the low temperature phase. This suggests that the Ti is in some way altering the band structure of VO_2, but the effect is certainly not obvious in the electrical measurements.

The microwave transmission coefficient was determined for all the films

examined. It was observed that in the semiconducting phase the resistivity was high enough that there was no measureable microwave absorption. In the metallic phase, the transmission coefficient was a direct function of the films resistivity, and this relationship was observed for almost all of the films examined. There was an anomaly observed at the highest Ti concentration studied, in which the transmission coefficient was much higher than the films respective resistivity would indicate.

References

1. Morin, F. J., Phys. Rev. Lett., 3, 34 (1959)

2. Paul, W., Mat. Res. Bull., 5, 691 (1970).

3. Berglund, C. N. and Guggenheim, H. J., Phys. Rev., 185, 1022 (1969).

4. Goodenough, J. B., J. Sol. St. Chem., 3, 490 (1971).

5. Phillips, T. E., Anderson, J. R., Schramm, C. J., and Hoffman, B. M., Rev. Sci. Instrum., 50, (1979).

6. Verleur, H. W., Barker, A. S., Jr., and Berglund, C. N., Phys. Rev., 172, 172 (1968).

7. Griffiths, C. H., and Eastwood, H. K., J. Appl. Phys., 45, 2201 (1974).

8. Kavanagh, K. L., and Naguib, H. M., Thin Solid Films, 91, 231 (1982).

9. Rozgonyi, G. A., and Hensler, D. H., J. Vac. Sci. Tech., 5, 194 (1968).

10. Reyes, J. M., Lynch, G. F., Sayer, M., McBride, S. L., and Hutchinson, T. S., J. Can. Cer. Soc., 41, 69 (1972).

11. Hörlin, T., Niklewski, T., and Nygren, M., Mat. Res. Bull., 7, 1515 (1972).

12. MacChesney, J. B., and Guggenheim, H. J., J. Phys. Chem. Solids, 30, 225 (1969).

13. Balberg, I., Abeles, B., and Arie, Y., Thin Solid Films, 24, 307 (1974).

14. Rudorff, W., Walter, G., and Stadler, J., Z. Anorg. Allg. Chem., 297, 1 (1958).

15. Mitsuishi, T., Jap. J. Appl. Phys., 6, 1060 (1967).

16. Chase, L. L., Phys. Lett., 46A, 215 (1973).

17. Hölin, T., Niklewski, T., and Nygren, M., Acta. Chem. Scand. 30A, 619 (1976).

18. Hensler, D. H., J. Appl. Phys., 39, 2354 (1968).

19. Perlyoyev, V. A., Zh. Neorg. Khim. 25, 3193 (1980).

Figure Legends

1) Typical electrical response (log(resistance)) of a VO_2 thin film on a glass substrate as a function of temperature, identifying the semiconducting resistance (R_{35}, metallic resistance (R_{90}) and the two transition temperatures.

2) Semiconducting resistivity ($\log(R_{35})$) as a function of the Ti concentration for the 1.5 hr Ti-doped VO_2 thin films.

3) Metallic resistivity ($\log(R_{90})$) as a function of the Ti concentration for the 1.5 hr Ti-doped VO_2 thin films.

4) Resistivity ratio (R_{35}/R_{90}) as a function of the Ti concentration for the 1.5 hr Ti-doped VO_2 thin films.

5) Resistivity ratio (R_{35}/R_{90}) as a function of the Ti concentration for the 3.0 hr Ti-doped VO_2 thin films.

6) Semiconducting resistivity ($\log(R_{35})$) as a function of the Ti concentration for the 3.0 hr Ti-doped VO_2 thin films.

7) Metallic resistivity ($\log(R_{90})$) as a function of the Ti concentration for the 3.0 hr Ti-doped VO_2 thin films.

8) Upper and lower transition temperatures observed for the electrical resistivity response as a function of the Ti concentration for the 1.5 hr Ti-doped VO_2 thin films.

9) Semiconducting resistivity ($\log(R_{35})$) as a function of the W concentration for the W-doped VO_2 thin films.

10) Metallic resistivity ($\log(R_{90})$) as a function of the W concentration for the W-doped VO_2 thin films.

11) Resistivity ratio (R_{35}/R_{90}) as a function of the W concentration for the W-doped VO_2 thin films.

12) Upper and lower transition temperatures observed for the electrical resistivity response as a function of the W concentration for the W-doped VO_2 thin films.

13) Absorption coefficient (k) at 0.9μ and 2.5μ as a function of the Ti concentration for the 1.5 hr Ti-doped VO_2 thin films at 35°C.

14) Absorption coefficient (k) at 0.9μ and 2.5μ as a function of the Ti concentration for the 1.5 hr Ti-doped VO_2 thin films at 90°C.

15) Log_e (microwave transmission coefficient @30 GHz) verses film thickness/resistivity$^{1/2}$ for the 1.5 hr Ti-doped VO_2 thin films.

16) Log_e (microwave transmission coefficient @30 GHz) verses film thickness/resistivity$^{1/2}$ for the 3.0 hr Ti-doped VO_2 thin films.

17) Log_e (microwave transmission coefficient @30 GHz) verses film thickness/resistivity$^{1/2}$ for the W-doped VO_2 thin films.

18) Plot of the metal oxide (MO_2) volume as a function of the Ti concentration in Ti-doped VO_2 powders, in both the semiconducting monoclinic and metallic tetragonal phases. Data was taken from reference 19.

Table I

Starting Composition %TI	%Ti Determined by EDS
0.0	1.2 (4.5)
0.0	5.3 (3.9)
0.2	2.8 (4.3)
0.41	3.5 (4.1)
0.82	2.7 (4.2)
1.20	2.3 (4.3)
1.20	3.9 (4.1)
3.0	3.8 (4.1)
4.9	6.0 (3.8)
4.9	5.2 (3.9)
6.6	3.4 (4.1)
6.6	1.8 (4.4)
6.6	2.7 (4.3)
8.8	6.6 (3.8)
8.8	6.7 (3.8)

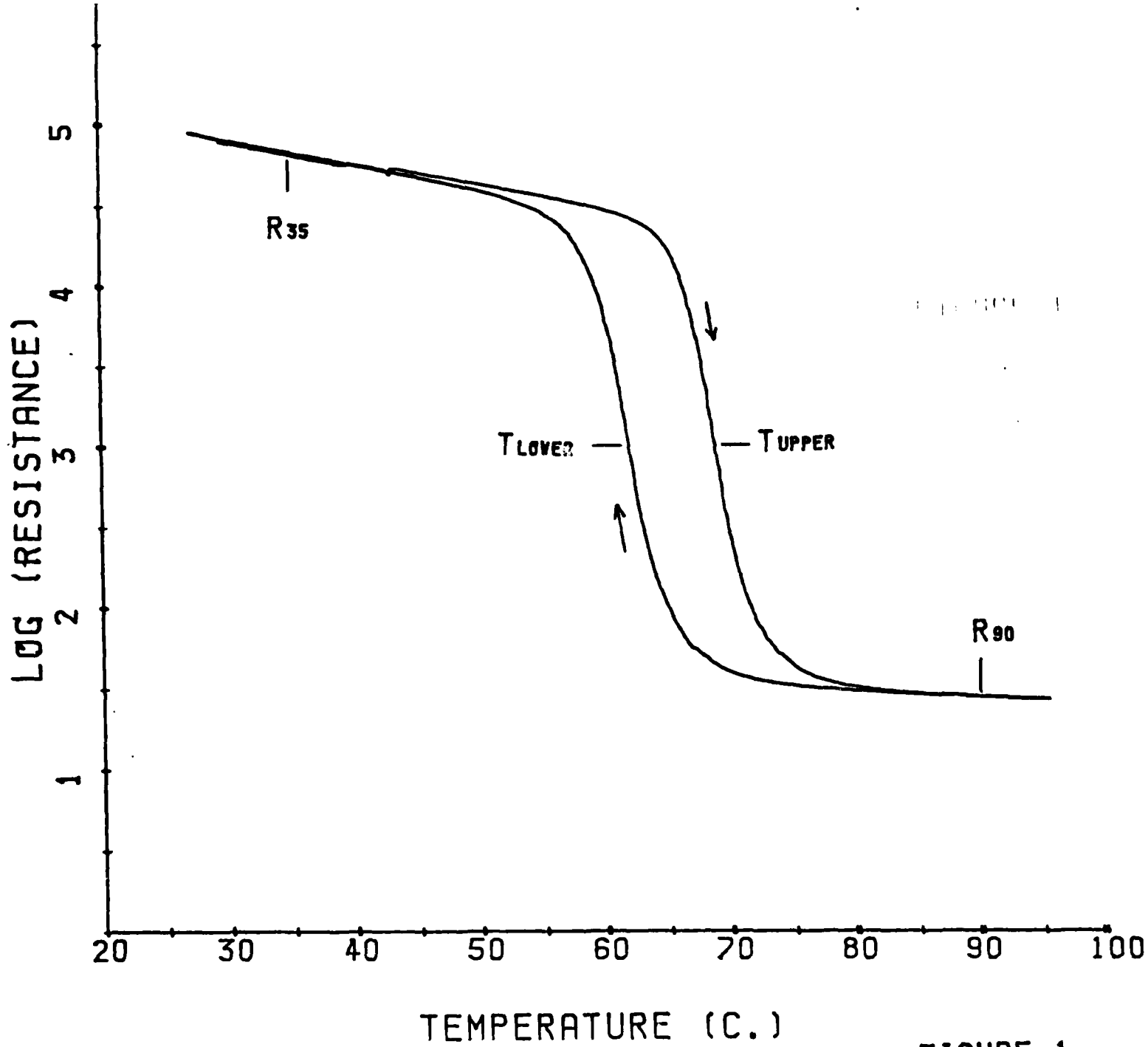
LOG (RESISTANCE)
1
2
3
4
5
R35
TLOWER
TUPPER
R90
20
30
40
50
60
70
80
90
100
TEMPERATURE (C.)

FIGURE 1

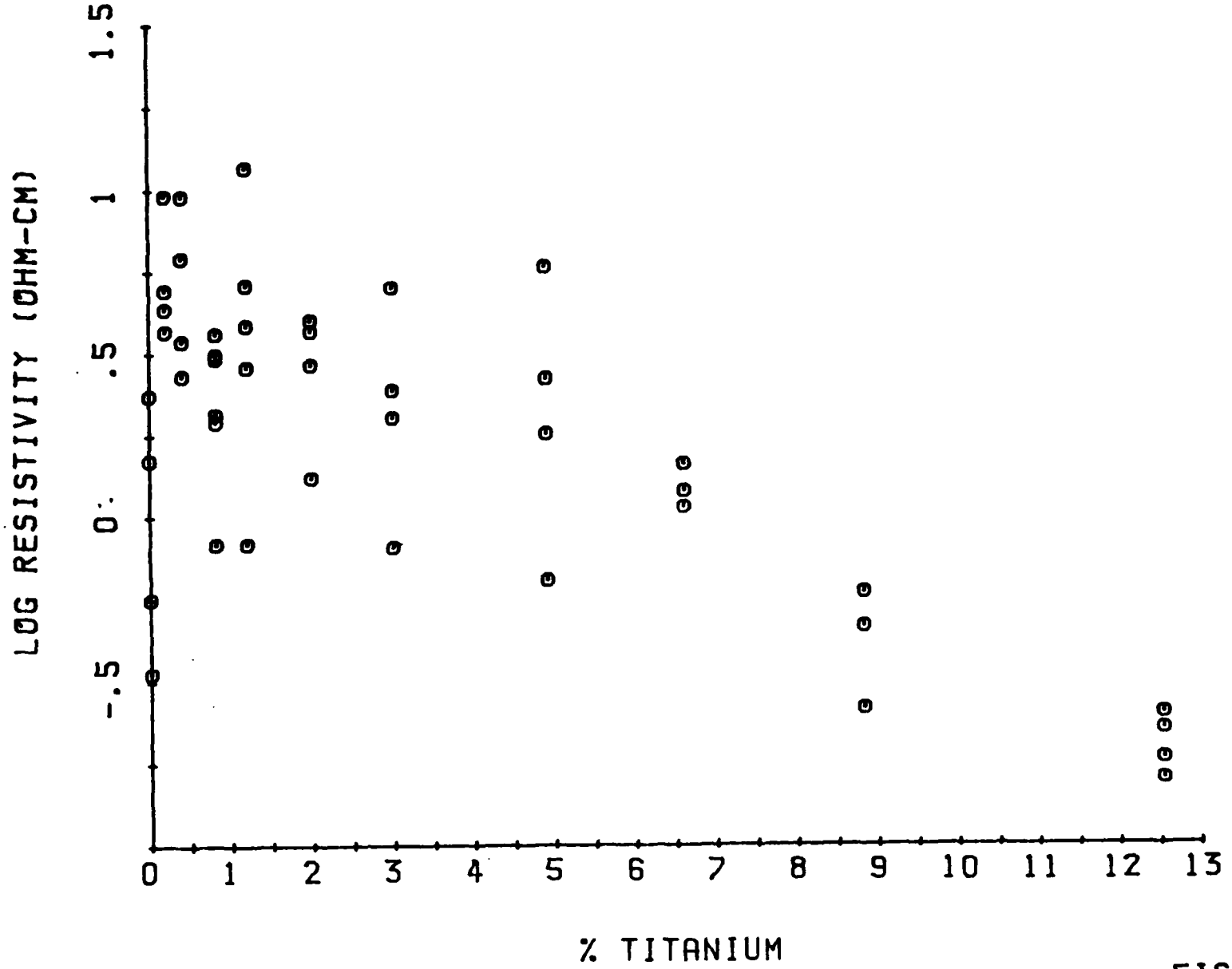
LOG RESISTIVITY (OHM-CM)
1.5
1
.5
0
-.5
0
1
2
3
4
5
6
7
8
9
10
11
12
13
% TITANIUM

FIGURE 2

LOG RESISTIVITY (OHM-CM)
-1.5
-2
-2.5
-3
-3.5
% TITANIUM
0
1
2
3
4
5
6
7
8
9
10
11
12
13

FIGURE 3

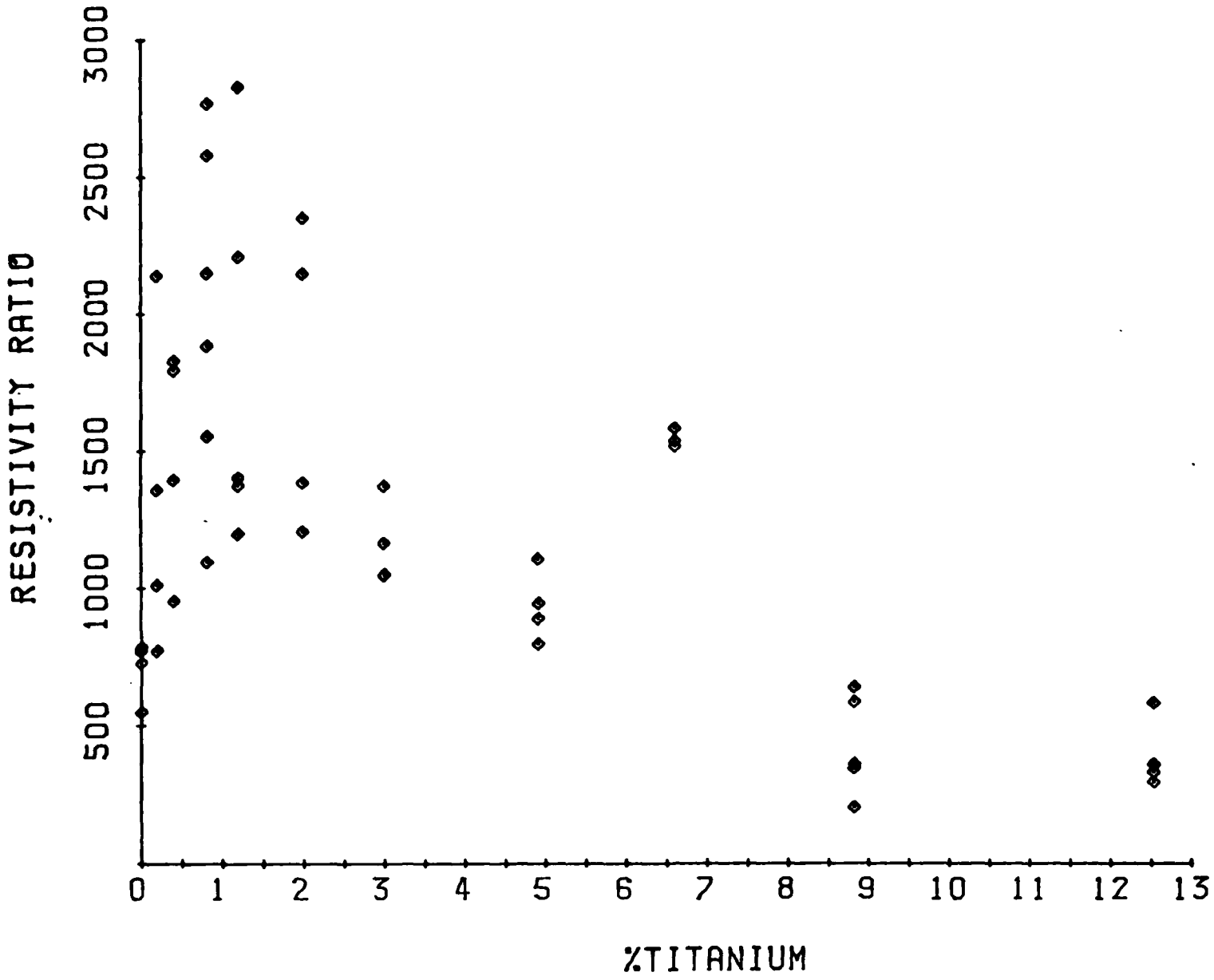
RESISTIVITY RATIO
500
1000
1500
2000
2500
3000
0
1
2
3
4
5
6
7
8
9
10
11
12
13
%TITANIUM

FIGURE 4

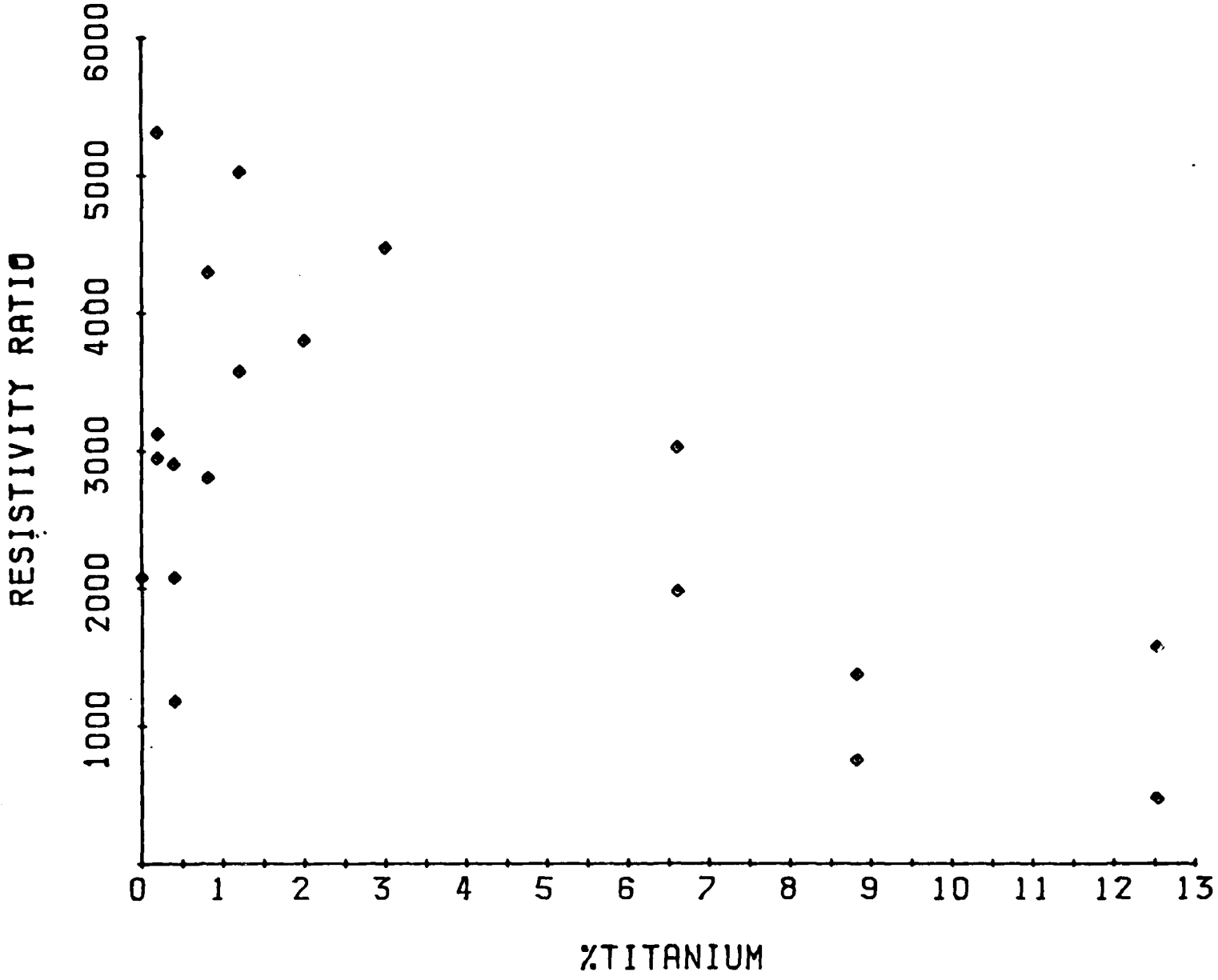
RESISTIVITY RATIO
1000
2000
3000
4000
5000
6000
0
1
2
3
4
5
6
7
8
9
10
11
12
13
%TITANIUM

FIGURE 5

LOG RESISTIVITY (OHM-CM)
1.5
1
.5
0
-.5
0
1
2
3
4
5
6
7
8
9
10
11
12
13
% TITANIUM

FIGURE 6

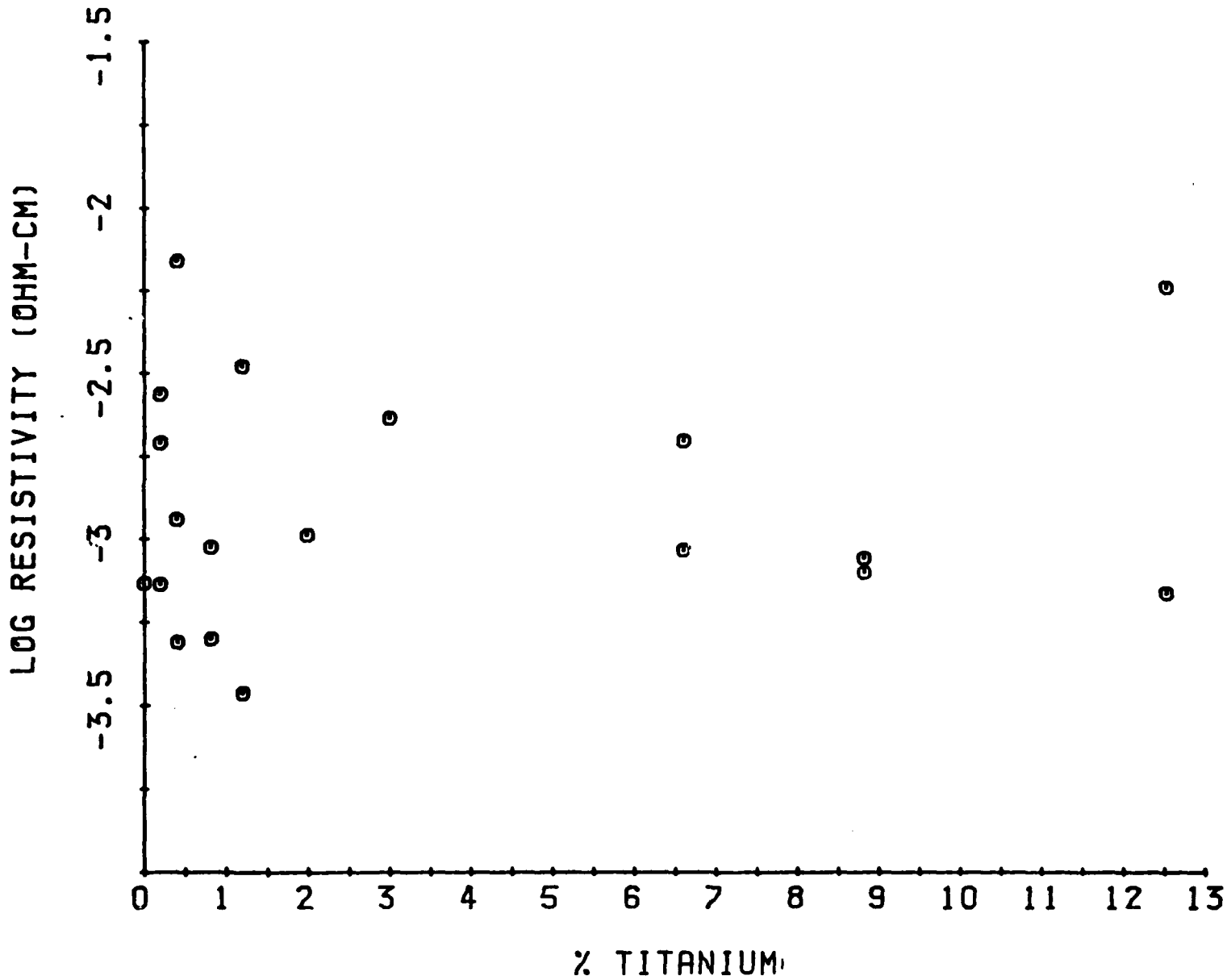
LOG RESISTIVITY (OHM-CM)
-1.5
-2
-2.5
-3
-3.5
0
1
2
3
4
5
6
7
8
9
10
11
12
13
% TITANIUM

FIGURE 7

TRANSITION TEMPERATURE (°C)
58
60
62
64
66
68
70
72
74
%TITANIUM
0
1
2
3
4
5
6
7
8
9
10
11
12
13

FIGURE 8

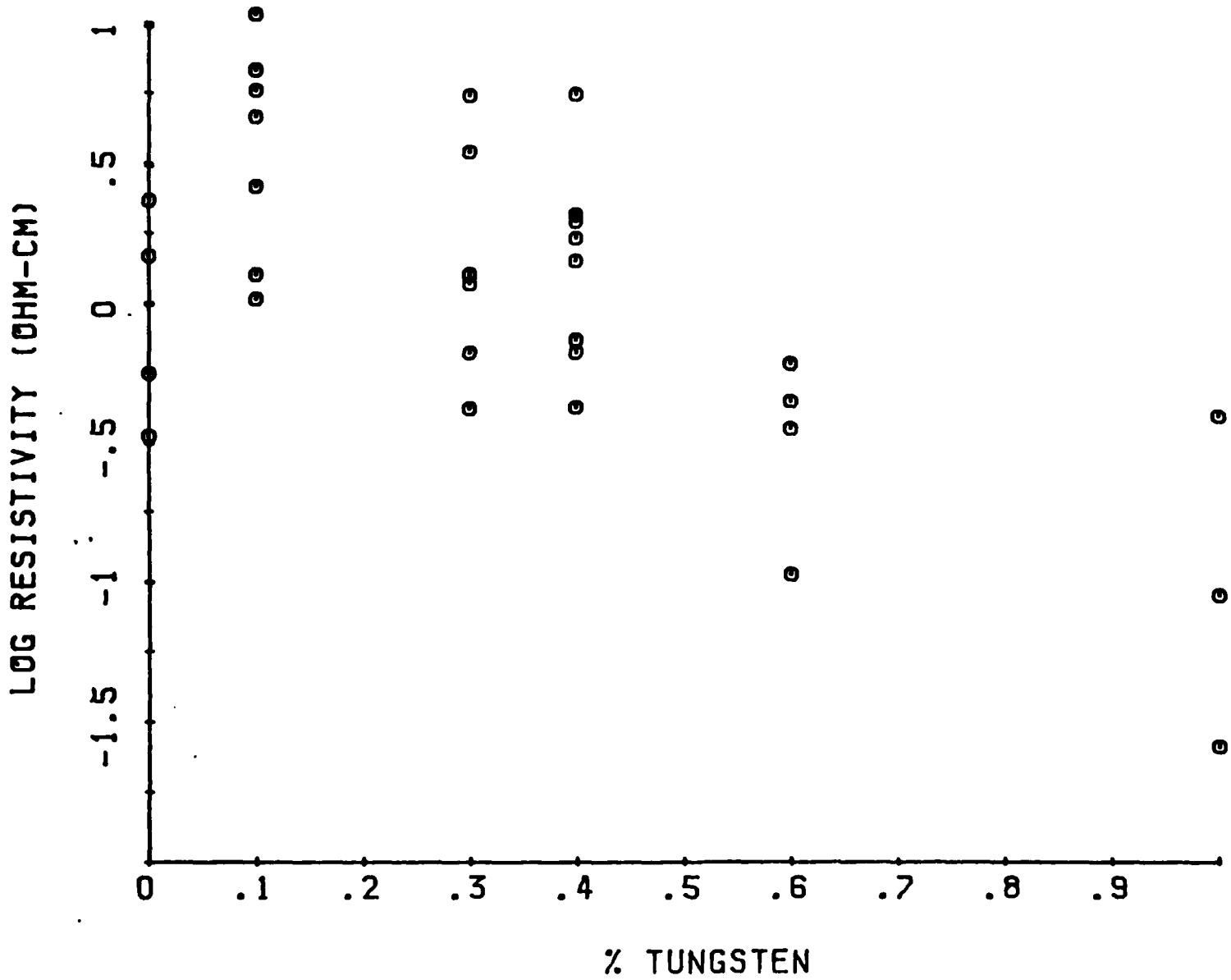

FIGURE 9

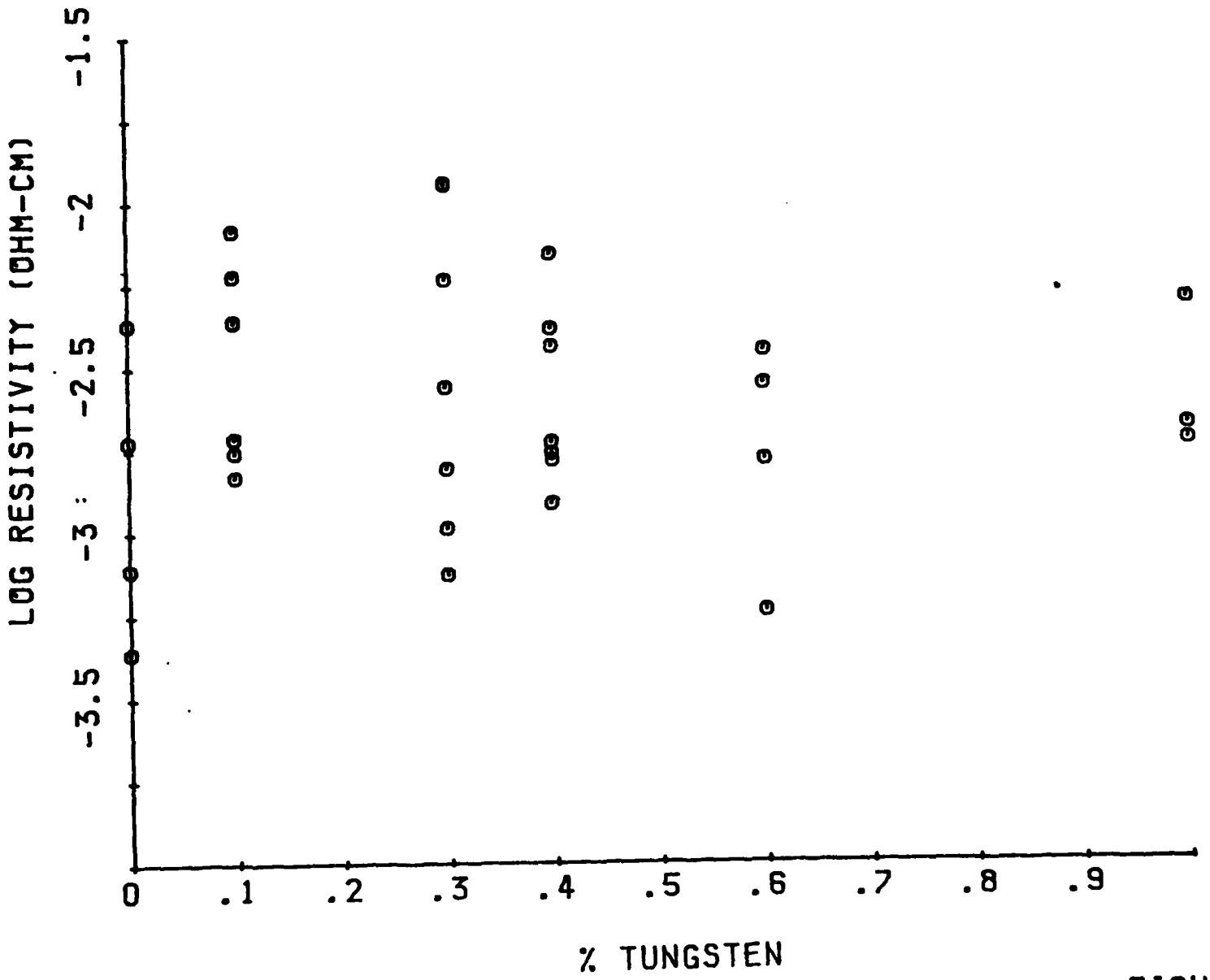

FIGURE 10

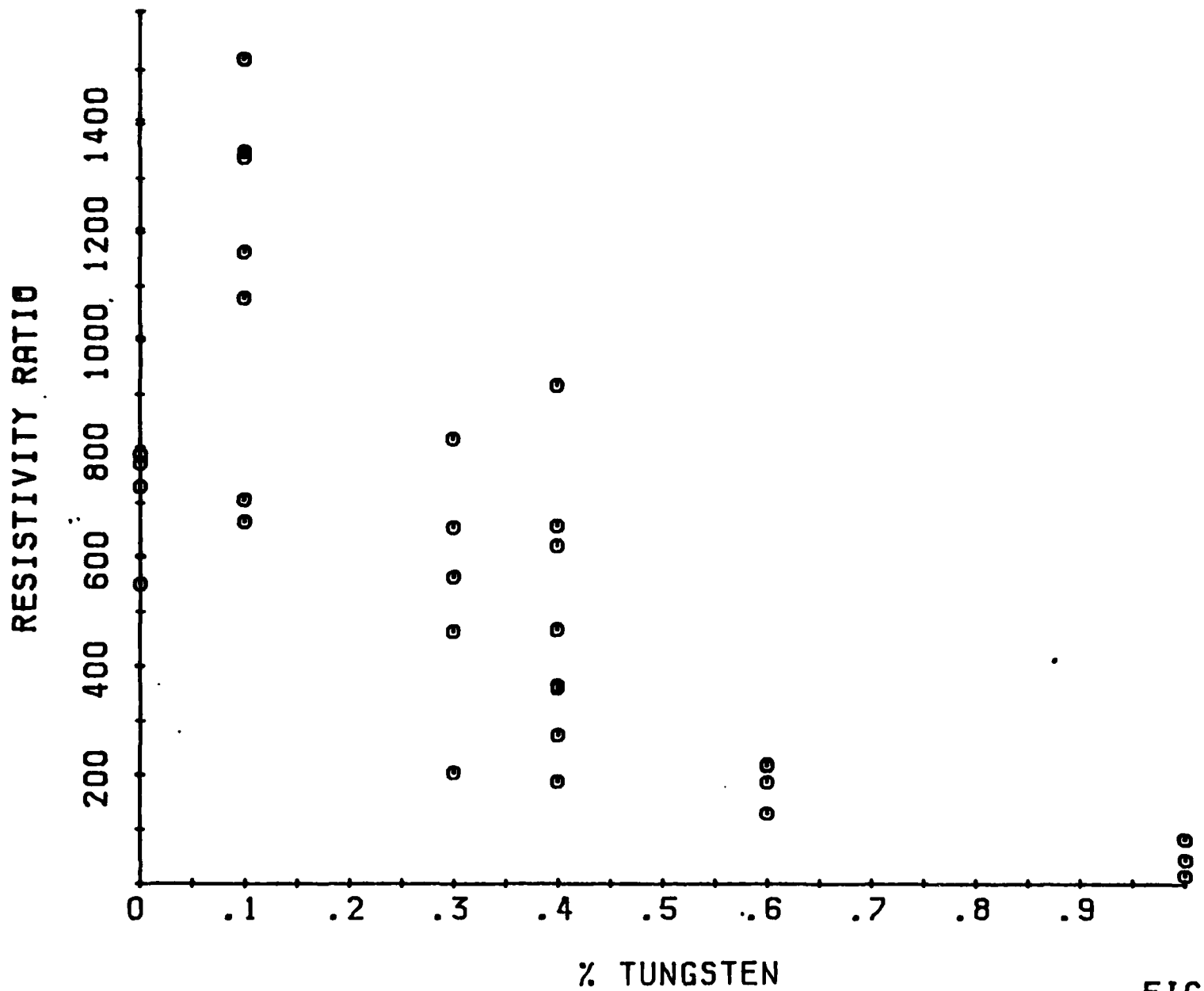
RESISTIVITY RATIO
200
400
600
800
1000
1200
1400
0
.1
.2
.3
.4
.5
.6
.7
.8
.9
% TUNGSTEN

FIGURE 11

TRANSITION TEMPERATURE (°C)
45
50
55
60
65
70
75
% TUNGSTEN
0
.1
.2
.3
.4
.5
.6
.7
.8
.9

FIGURE 12

ABSORPTION COEFFICIENT (@35 C)
0
.25
.5
0
1
2
3
4
5
6
7
8
9
10
11
12
13
%TITANIUM
@2.5 MICRONS
@0.9 MICRONS

FIGURE 13

ABSORPTION COEFFICIENT (@90 C)
1
2
3
4
5
6
7
0
1
2
3
4
5
6
7
8
9
10
11
12
13
%TITANIUM
@0.9 MICRONS
@2.5 MICRONS

FIGURE 14

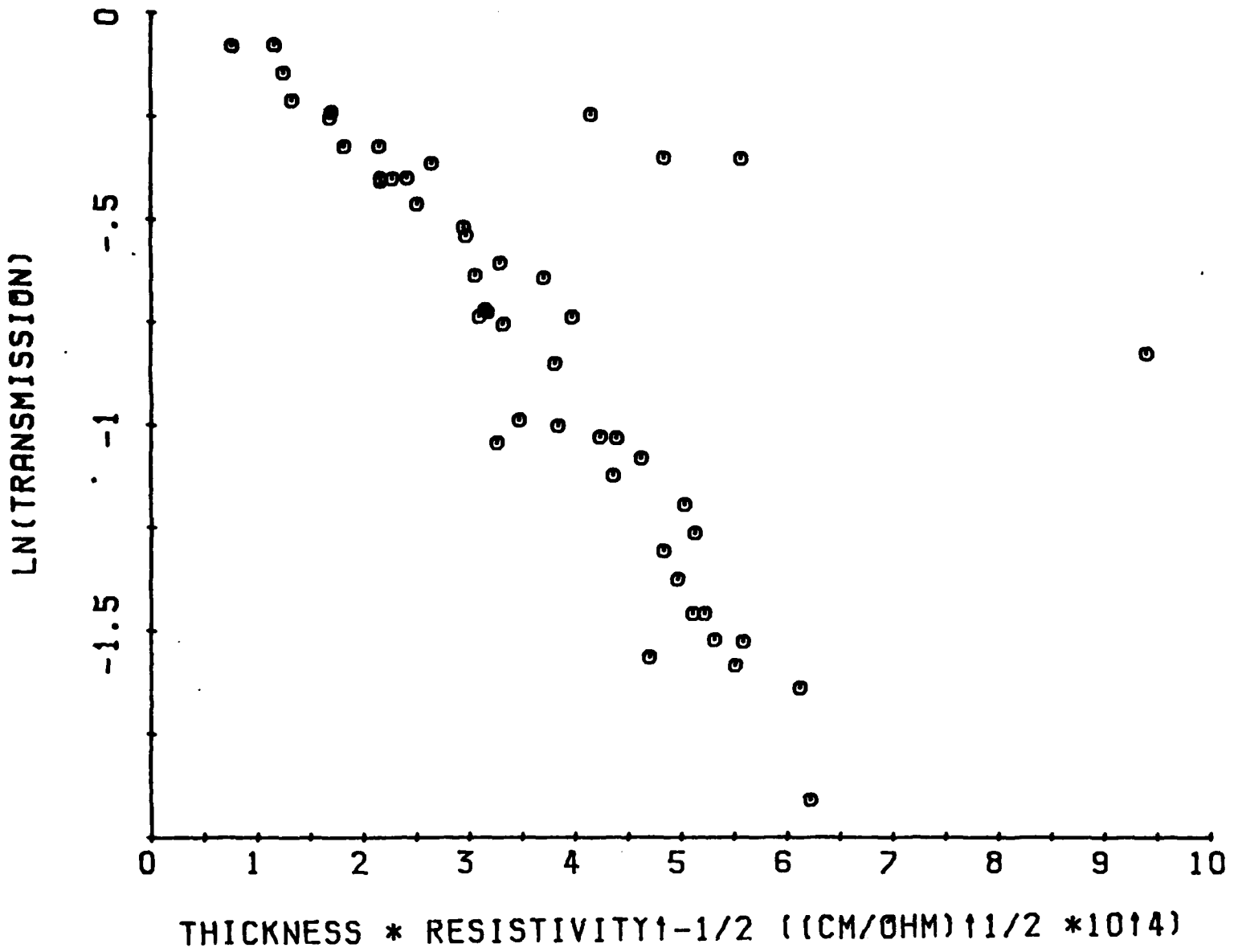
LN(TRANSMISSION)
0
-.5
-1
-1.5
0
1
2
3
4
5
6
7
8
9
10
THICKNESS * RESISTIVITY↑-1/2 ((CM/OHM)↑1/2 *10↑4)

FIGURE 15

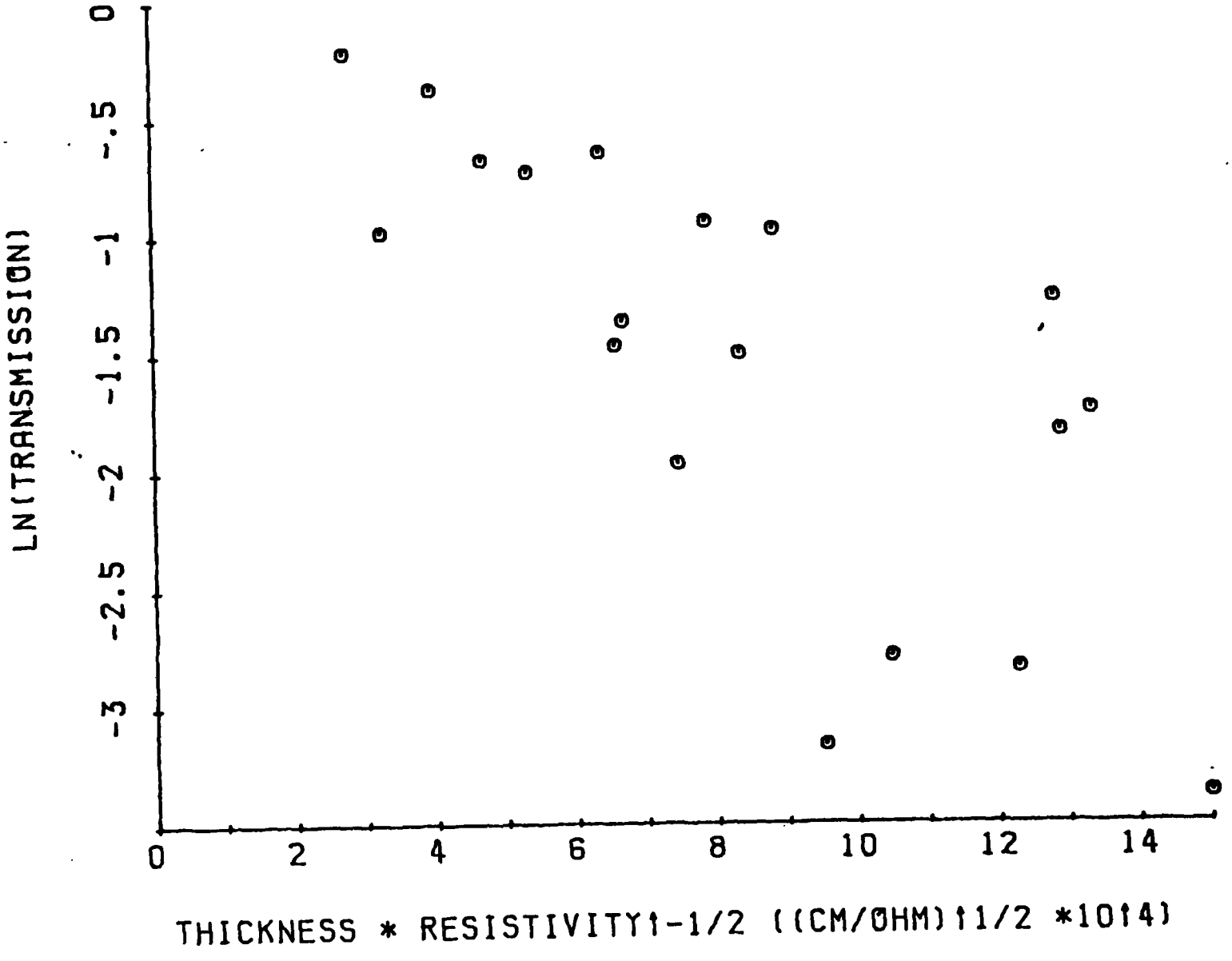
LN(TRANSMISSION)
0
-.5
-1
-1.5
-2
-2.5
-3
0
2
4
6
8
10
12
14
THICKNESS * RESISTIVITY↑-1/2 ((CM/OHM)↑1/2 *10↑4)

FIGURE 16

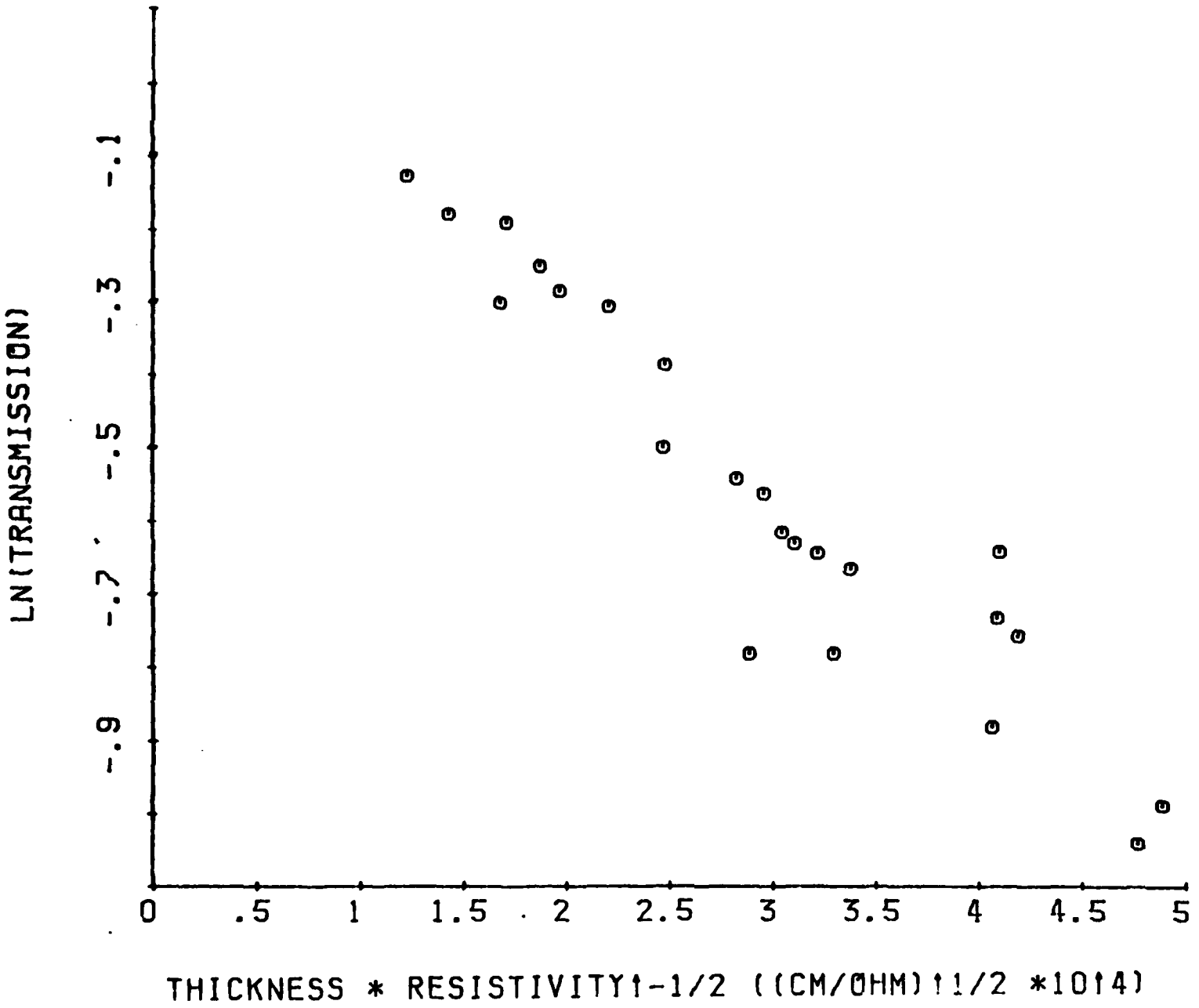
LN(TRANSMISSION)
-.1
-.3
-.5
-.7
-.9
0
.5
1
1.5
2
2.5
3
3.5
4
4.5
5
THICKNESS * RESISTIVITY↑-1/2 ((CM/OHM)↑1/2 *10↑4)

FIGURE 17

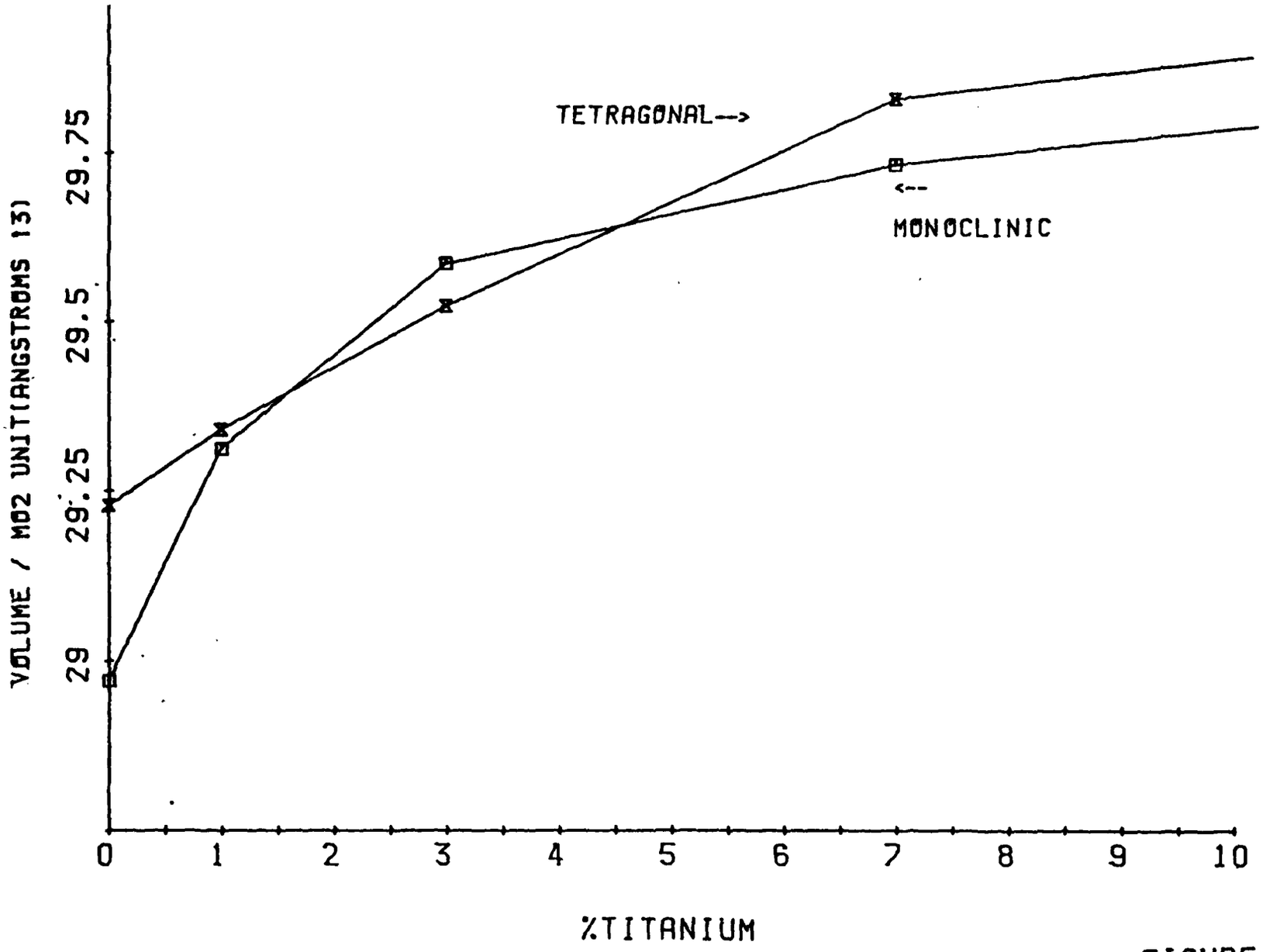
VOLUME / MO2 UNIT(ANGSTROMS 13)
29
29.25
29.5
29.75
TETRAGONAL-->
<--
MONOCLINIC
0
1
2
3
4
5
6
7
8
9
10
%TITANIUM

FIGURE 18

III. Publications and Talks

Publications

1. R. S. Potember, T. O. Poehler, and R. C. Benson, "Optical Switching in Semiconductor Organic Thin Films," Appl. Phys. Lett. 41, 548 (1982).

2. R. C. Benson, R. C. Hoffman, R. S. Potember, E. Bourkoff, and T. O. Poehler, "Spectral Dependence of Reversible Optically Induced Transitions in Organometallic Compounds," Appl. Phys. Lett. 42, 855 (1983).

3. R. S. Potember, R. C. Hoffman, R. C. Benson, and T. O. Poehler, "Erasable Optical Switching in Semiconductor Organic Charge-Transfer Complexes," Proc. of International CNRS Colloquium on Physics and Chemistry of Synthetic and Organic Metals, J. Phys. (Paris) Vol. 44, pp. C3-1597-C31604 (1983).

4. R. S. Potember, T. O. Poehler, R. C. Hoffman, and R. C. Benson, "Optical Switching in Semiconductor Thin Films," Proc. of International Congress on Application of Lasers and Optics (to be published, 1983).

5. R. S. Potember, T. O. Poehler, R. C. Hoffman, and R. C. Benson, "Erasable Optical Switching in Semiconductor Thin Films," in Proc. of Second International Workshop on Molecular Electronic Devices (to be published, 1983).

6. T. O. Poehler, R. S. Potember, R. C. Hoffman, and R. C. Benson, "Erasable Optical Switching in Semiconductor Organic Thin Films," Bull. Am. Phys. Soc. 28, 447 (1983).

7. R. S. Potember, T. O. Poehler, R. C. Hoffman, R. B. Givens, and R. C. Benson, "Electron Beam Induced Switching in Thin Films Organo-metallic Charge Transfer Complexes," Bull. Am. Phys. Soc. 28, 55 (1983).

8. T. O. Poehler, R. S. Potember, R. C. Benson, and R. C. Hoffman, "Optical Phase Transitions in Organo-Metallic Charge-Transfer Complexes," Symposium on Solid-State Chemistry at the 35th Southeastern Regional Meeting of the American Chemical Society (SERMACS-35) in Charlotte, NC, Nov. 9-11, 1983, Molecular Crystals and Liquid Crystals, Vol. 107, pp. 91-101 (1984).

9. R. S. Potember, T. O. Poehler, R. C. Hoffman and R. C. Benson, "Erasable Optical Switching in Organic Charge Transfer Complexes", Molecular Crystals and Liquid Crystals (to be published)

Talks

1. R. S. Potember, "Optical Switching in Organic Charge-Transfer Complexes," Colloquium, IBM Research Center, Yorktowne Heights, NY, November 19, 1982.

2. R. S. Potember, "Optical Switching in Organic Semiconductor Complexes,"

International Conference on the Physics and Chemistry of Synthetic and Organic Metals, Les Arcs, France, December 15, 1982.

T. O. Poehler, "Optical Switching and Memory of Organometallic Charge Transfer Materials," Martin Marietta, Baltimore, MD, January 7, 1983.

R. S. Potember, T. O. Poehler, R. C. Hoffman, and R. C. Benson, "Erasable Optical Switching in Semiconductor Thin Films," Second International Workshop on Moelcular Electronic Devices, Naval Research Laboratory, Washington, DC, March 13, 1983.

T. O. Poehler, R. S. Potember, R. C. Hoffman, and R. C. Benson, "Erasable Optical Switching in Semiconductor Organic Thin Films," American Physical Society Meeting, Los Angeles, CA, March 23, 1983.

R. S. Potember, T. O. Poehler, R. C. Hoffman, R. B. Givens, and R. C. Benson, "Electron Beam Induced Switching in Thin Films Organo-metallic Charge Transfer Complexes," American Physical Society Meeting, Los Angeles, CA, March 25, 1983.

R. C. Benson, R. C. Hoffman, R. S. Potember, and T. O. Poehler, "Optical Switching in Organometallic Films," Conf. on Lasers and Electro-Optics, Baltimore, MD, May 1983, p. 110.

T. E. Phillips, K. Moorjani, J. C. Murphy and T. O. Poehler, "Photo-electrochemical Properties of Iron-Titanium Oxide Thin Films," American Chemical Society Meeting, Washington, DC, August 29-September 2, 1983.

T. E. Phillips, R. C. Hoffman, and T. O. Poehler, "Electrical and Optical Switching Behavior of Thin VO_2 Films Doped with Titanium," American Chemical Society Meeting, Washington, DC, August 29-September 2, 1983.

). T. O. Poehler, R. S. Potember, R. C. Benson, and R. C. Hoffman, "Optical Phase Transitions in Organo-Metallic Charge-Transfer," Southeastern Regional Meeting of the American Chemical Society (SERMACS-35) in Charlotte, NC, Nov. 9-11, 1983.

l. R. S. Potember, "Electronic Devices from Conductive Organics," 1983 Summer Institute for Polymer Science and Technology, Lake Mohonk, New Paltz, NY, June 17, 1983.

2. R. S. Potember, "Optical Switching in Organic Charge Transfer Complexes," Wright-Patterson Air Force Base, Dayton, OH, July 8, 1983.

3. R. S. Potember, T. O. Poehler, R. C. Hoffman, and R. C. Benson, "Laser-Induced Optical Changes in Organometallic Thin Films," American Physical Society, Detroit, MI, March 29, 1984.

4. R. S. Potember, T. O. Poehler, R. C. Hoffman, and R. C. Benson, "Erasable Optical Switching in Organnic Charge Transfer Complexes," ICSM 84, Albano Terme, Italy, June 20, 1984.

15. T. O. Poehler, R. S. Potember, R. C. Benson, and R. C. Hoffman, "The Electronic and Vibrational Spectra of Electric Field-Induced Phase Transitions in Metal-TCNQ Complexes," American Physical Society, Detroit, MI, March 29, 1984.